

*NASA CR-168, 935*

NASA-CR-168935  
19820017216

# The Telecommunications and Data Acquisition Progress Report 42-68

January and February 1982

N. A. Renzetti  
Editor

**LIBRARY COPY**

APR 19 1982

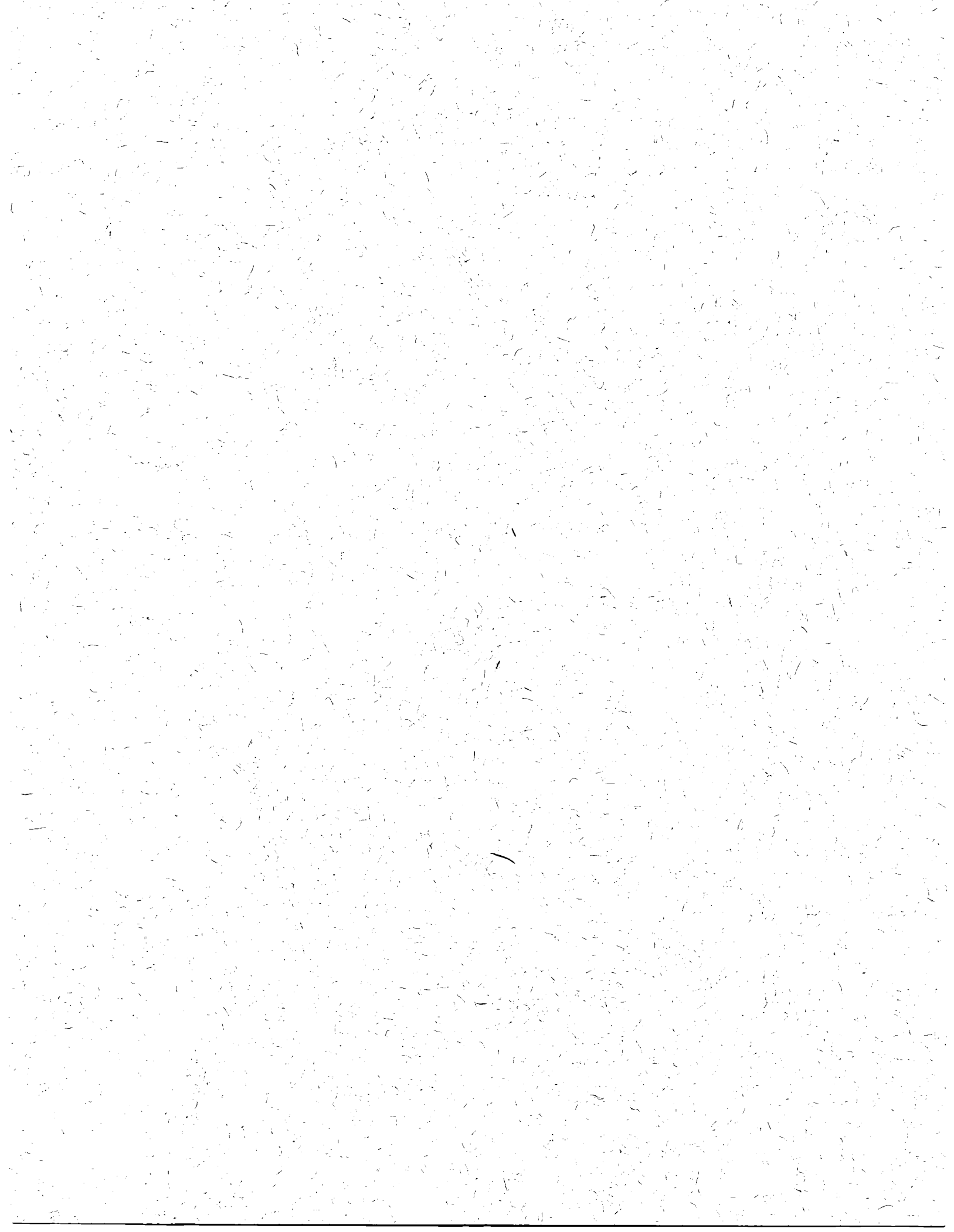
LANGLEY RESEARCH CENTER  
LIBRARY, NASA  
HAMPTON, VIRGINIA

April 15, 1982

**NASA**

National Aeronautics and  
Space Administration

Jet Propulsion Laboratory  
California Institute of Technology  
Pasadena, California



# The Telecommunications and Data Acquisition Progress Report 42-68

January and February 1982

N. A. Renzetti  
Editor

April 15, 1982

**NASA**

National Aeronautics and  
Space Administration

Jet Propulsion Laboratory  
California Institute of Technology  
Pasadena, California

*N82-25092 #*  
*+HR #*  
*N82-25111 #*

The research described in this publication was carried out by the Jet Propulsion Laboratory, California Institute of Technology, under contract with the National Aeronautics and Space Administration.

## Preface

This publication provides reports on developments in Earth-based radio technology with applications to several programs. In space communications it reports on activities of the Deep Space Network. In geodynamics it reports on the application of radio interferometry at microwave frequencies for geodynamic measurements. In the field of astrophysics the Deep Space Stations individually and in pairs as an interferometer have been applied to direct observation of celestial radio sources.

Each succeeding issue of this report will present material in some, but not necessarily all, of the following categories:

### Radio Astronomy

#### Radio Interferometry at Microwave Frequencies

- Geodetic Techniques Development

- Spacecraft Navigation

- Orbiting Very Long Baseline Interferometry

### Deep Space Network

- Description

- Program Planning

- Advanced Systems

- Network and Facility Engineering and Implementation

- Operations

- Spacecraft Radio Science

- Planetary Radar

In each issue, there will be a report on the current configuration of one of the seven DSN systems (Tracking, Telemetry, Command, Monitor and Control, Test Support, Radio Science, and Very Long Baseline Interferometry).

The work described in this report series is either performed or managed by the Telecommunications and Data Acquisition organization of JPL.



# Contents

## THE DEEP SPACE NETWORK DESCRIPTION OF THE DSN

<b>Description of the Deep Space Network</b> .....	1
N. A. Renzetti	

### ADVANCED SYSTEMS

#### Tracking and Ground-Based Navigation

<b>An Efficient Sampling Technique for Sums of Bandpass Functions</b> .....	3
W. M. Lawton	
NASA Code 310-10-63-55	
<b>An Experimental Investigation of the Changes of VLBI Time Delays Due to Antenna Structural Deformations</b> .....	8
T. Y. Otoshi and L. E. Young	
NASA Code 310-10-60-05	

#### Communications

<b>The Effects of Viterbi Decoder Node Synchronization Losses on the Telemetry Receiving System</b> .....	17
L. J. Deutsch and R. L. Miller	
NASA Code 310-20-67-60	
<b>Electronic Beam Steering of Semiconductor Injection Lasers</b> .....	25
J. Katz	
NASA Code 310-20-67-59	
<b>Phase Control and Beam Steering of Semiconductor Laser Arrays</b> .....	42
J. Katz	
NASA Code 310-20-67-59	
<b>A PPM Modulator and Demodulator for the 2.5-Bit/Detected Photon Demonstration</b> .....	50
W. K. Marshall	
NASA Code 310-20-67-59	
<b>A Statistical Model of the Photomultiplier Gain Process With Applications to Optical Pulse Detection</b> .....	55
H. H. Tan	
NASA Code 310-20-67-13	
<b>Evaluation of Waveguide Coating Materials</b> .....	68
W. C. J. Chen and B. W. Baker	
NASA Code 310-20-61-10	

#### Network Data Processing and Productivity

<b>Error Probabilities in Optical PPM Receivers With Gaussian Mixture Densities</b> .....	72
R. M. Gagliardi	
NASA Code 310-40-73-55	
<b>An Automated FORTRAN Documenter</b> .....	78
T. Erickson	
NASA Code 310-40-73-64	

# NETWORK AND FACILITY ENGINEERING AND IMPLEMENTATION

## Network

<b>New CCIR Papers on Telecommunications for Deep Space Research</b> .....	86
N. F. de Groot NASA Code 311-06-50-00	
<b>DSN RFI Susceptibility Models Development Program Overview</b> .....	103
M. K. Sue NASA Code 311-06-50-00	
<b>RFI Measurement Survey at Goldstone in November and December 1981</b> .....	110
R. M. Taylor NASA Code 311-06-50-00	

## Ground Communications

<b>Operations of the Reconfigured Ground Communications Facility Central Communications Terminal and the Network Operations Control Center</b> .....	122
J. C. Santana and L. E. Jennings NASA Code 311-06-11-20	

## Deep Space Stations

<b>Mark IV-A DSCC Telemetry System Description</b> .....	130
R. Burt NASA Code 311-03-41-81	

## OPERATIONS

### Network Operations

<b>Analysis of DSN PPM Support During Voyager 2 Saturn Encounter</b> .....	139
C. D. Bartok NASA Code 311-03-12-30	

## ENERGY

<b>Potential Reduction of DSN Uplink Energy Cost</b> .....	151
S. Dolinsky and N. F. de Groot NASA Code 311-03-31-30	
<b>A Simplified Solar Cell Array Modelling Program</b> .....	167
R. D. Hughes NASA Code 311-03-44-08	

# Description of the Deep Space Network

N. A. Renzetti  
TDA Mission Support

*The facilities, functions, and operations capabilities of the Deep Space Network are summarized. Network activities in support of planned future as well as ongoing deep space missions are described as are activities in support of radio astronomy experiments and the Astronomical Radio Interferometric Earth Surveying (ARIES) Network.*

## I. General

The Deep Space Network has facilities in the California desert near Barstow, in the mountain area west of Madrid, Spain, and in the mountain area west of Canberra, Australia, each facility consisting of several large-antenna space communication stations. These sites are approximately  $120^\circ$  in longitude apart, which allows for continuous communication between the earth and the spacecraft exploring the solar system.

The Network is developed, implemented, maintained and operated by the Jet Propulsion Laboratory for the Office of Space Tracking and Data Systems of NASA. Much of the implementation and operations activities are contracted to industry. The Network carries out several functions in providing communications to spacecraft — it transmits commands, receives scientific and engineering telemetry data, and generates radio science and navigation data.

The Network maintains communication with 11 spacecraft in various orbits. Four of these spacecraft are on trajectories which will cause them to leave our solar system during the next decade. Two of them, Pioneers 10 and 11, are the respon-

sibility of the Ames Research Center, with JPL being responsible for commands to and telemetry from the spacecraft and for navigation using data generated by the network. Both spacecraft flew by Jupiter, with Pioneer 11 also encountering Saturn, on their way out of the solar system. The other spacecraft are Voyagers 1 and 2, which flew by Jupiter and Saturn. Voyager 2 is now on a trajectory for an encounter with Uranus in 1986 and Neptune in 1989.

Pioneers 6 through 9, also the responsibility of Ames, were launched in the 1960's and continue to provide data as interplanetary solar monitors. Pioneer 12 is orbiting Venus and making measurements of that planet.

The Helios Project is a joint NASA-West Germany venture exploring the Sun. The one remaining spacecraft continues to investigate the solar wind, the magnetic field, solar and galactic cosmic rays, electromagnetic waves, micrometeoroids, and zodiacal light. The Project is managed by the Goddard Space Flight Center for NASA. Of the four Viking spacecraft launched to Mars and originally the responsibility of the Langley Research Center, one continues to return meteorological data on the surface of Mars, and data generated by the Network are providing increased knowledge on Earth-Mars dynamics.

The Network is actively engaged in preparations for the support of the Galileo mission to Jupiter and its satellites and for the joint NASA-European Space Agency International Solar Polar Mission. The latter mission will examine the unexplored polar regions of the Sun.

The Network will provide support to the European Space Agency for Giotto, which will intercept Halley's Comet, and the Network is negotiating with Japan's Institute of Space and Aeronautical Sciences for support of the Planet A and MS-T5 missions to Halley's Comet.

The Network is undergoing a major implementation which will result in the consolidation of its ground stations with those of the Space Flight Tracking Data Network of the Goddard Space Flight Center. It will then be the only NASA ground-based network providing support to those missions which cannot be supported by the Tracking and Data Relay Satellite System.

Primarily using the facilities at Goldstone, California, the Network supports planetary radar astronomy experiments. These experiments provide information on the topography and character of the surfaces of the planets, asteroids, and comets.

Because it works at the state-of-the-art of deep space communications, the Network provides unique experiment capabilities in radio astronomy. These experiments study the character of pulsars and compact radio sources. In the latter case, the angular resolution of the long baseline between the deep space stations provides new information on the structure of these radio sources.

## **II. Astronomical Radio Interferometric Earth Surveying (ARIES) Network**

The ARIES Network consists of several sites in Southern California that are visited by mobile VLBI (very long baseline interferometry) facilities which use extragalactic radio sources to provide vector baseline determinations between the sites. The changes of these baselines are expected to provide direct evidence of plate motion and the relationship of crustal strain to earthquakes. Each mobile VLBI facility consists of a transportable instrument which conducts radio interferometric observations at microwave frequencies. JPL has three of these transportable instrument systems which visit the sites and operate with the fixed telescopes of the DSN at Goldstone and the Owens Valley Radio Observatory of the Caltech Radio Astronomy group.

# An Efficient Sampling Technique for Sums of Bandpass Functions

W. M. Lawton  
Navigation Systems Section

*A well known sampling theorem states that a bandlimited function can be completely determined by its values at a uniformly placed set of points whose density is at least twice the highest frequency component of the function (Nyquist rate). A less familiar but important sampling theorem states that a bandlimited narrowband function can be completely determined by its values at a properly chosen, nonuniformly placed set of points whose density is at least twice the passband width. This allows for efficient digital demodulation of narrowband signals, which are common in sonar, radar and radio interferometry, without the side effect of signal group delay from an analog demodulator. This paper extends this theorem by developing a technique which allows a finite sum of bandlimited narrowband functions to be determined by its values at a properly chosen, nonuniformly placed set of points whose density can be made arbitrarily close to the sum of the passband widths. Applications and a multidimensional extension of this technique will be discussed in a future paper.*

## I. Introduction and Statement of Result

A set  $S$  of real numbers is *bounded* if it is contained in a finite interval. The *content* of a bounded set  $S$  is the unique real number, denoted by  $\text{cont}(S)$ , which satisfies the following two conditions:

*Condition 1:* Whenever  $\{[a_i, b_i] : i = 1, \dots, M\}$  is a finite collection of closed intervals such that

$$S \subset \bigcup_{i=1}^M [a_i, b_i] \quad (1)$$

then

$$\text{cont}(S) \leq \sum_{i=1}^M (b_i - a_i) \quad (2)$$

*Condition 2:*  $\text{cont}(S)$  is the largest number which satisfies condition 1.

In particular, if  $S$  is a finite union of finite intervals, then  $S$  is bounded and  $\text{cont}(S)$  is the sum of the lengths of the intervals.

A function  $f(t)$  is called *bandlimited* if its Fourier transform  $F(x)$  defined by

$$F(x) = \int_{-\infty}^{\infty} f(t) \exp(-2\pi i x t) dt \quad (3)$$

satisfies the following property:

$$S = \{x \text{ such that } F(x) \neq 0\} \text{ is bounded} \quad (4)$$

The *frequency content* of a bandlimited function  $f$  is the content of the set  $S$  in (4).

The object of this paper is to prove the following result:

**Theorem 1:** Given any bounded set  $S$  of real numbers and any real number  $\epsilon > 0$ , there exists an integer  $P$ , real numbers  $T_i$  for  $1 \leq i \leq P$ , a real number  $T > 0$ , and functions  $s_i(t)$  for  $1 \leq i \leq P$  such that, for every function  $f(t)$  whose Fourier transform vanishes outside of  $S$ , the following equation is valid:

$$f(t) = \sum_{i=1}^P \sum_{N=-\infty}^{+\infty} f(NT + T_i) s_i(t - NT - T_i) \quad (5)$$

and furthermore

$$\text{cont}(S) + \epsilon > P/T \quad (6)$$

Equation (5) expresses the fact that  $f(t)$  can be determined by its values on (or *sampled* on) a set of points  $\{NT + T_i\}$ , called a *sampling set*, whose average *density*, which is  $P/T$ , can be chosen to be arbitrarily close to the frequency content of  $f(t)$ . In the proof of theorem 1 the *order*  $P$ , *step size*  $T$ , *phases*  $T_i$ , and *sampling functions*  $s_i(t)$  will be specified. The following observations place theorem 1 in a historical perspective.

The classical sampling in Refs. 1 and 2 corresponds to theorem 1 where

$$S = [-W, W], P = 1, T_1 = 0, T = 1/2W$$

and

$$s_1(t) = \text{Sin}(2\pi Wt)/(2\pi Wt)$$

In this case, the sampling set has density =  $\text{cont}(S) = 2W$  and consists of uniformly placed points.

Kohlenberg's sampling theorem in Ref. 3 for narrowband functions corresponds to theorem 1 where

$$W_0 > 0, S = [-W_0 - W, -W_0] \cup [W_0, W_0 + W], P = 2,$$

$$T_1 = 0$$

$T_2$  is subject to weak restrictions,  $T = 1/W$  and  $s_1(t)$  and  $s_2(t)$  are rather complicated. In this case, the sampling set has

density =  $\text{cont}(S) = 2W$  and consists of nonuniformly placed points. Applications of this sampling technique (and of the more restrictive phase quadrature technique) to radar, sonar and radio interferometry are discussed in Refs. 4-6.

Any function  $f(t)$  which represents a single channel electronic signal will be real valued; hence its Fourier transform  $F(x)$  will satisfy the relation  $F(-x) = \text{complex conjugate of } F(x)$  and the set  $S$  in (4) will be symmetric about the origin. For this reason, the passband of a narrowband signal is usually specified by the set

$$[W_0, W_0 + W]$$

rather than the set

$$S = [-W_0, -W_0 - W] \cup [W_0, -W_0 + W].$$

However, this paper treats complex valued functions because the analysis involved is simpler and because complex random processes are of interest in applied analysis (see Ref. 7). Also, it should be noted that theorem 1 can easily be extended to wide sense stationary random processes whose spectral densities satisfy the hypothesis of theorem 1.

Many signals which occur in spread spectrum communication, navigation and remote sensing (radar, sonar, laser scanning) can be modelled as finite sums of narrowband functions whose passbands are widely separated with respect to their widths. A special example, in which each of the passbands is extremely narrow, arises for the Mobil Automated Field Instrument System (MAFIS) navigation system being developed at the Jet Propulsion Laboratory (communicated by Dr. William Hurd). In this system, four nearly pure frequency tones are transmitted simultaneously and the received signal is digitally sampled. The calculated phases associated with each tone are converted to navigation ranging data. This phase estimation problem is a special case of the problem discussed in Ref. 8. However, for the more general case where the passbands are wider, theorem 1 is appropriate.

Applications of theorem 1 and of a multivariable extension of theorem 1 will be discussed in a sequel to this paper. The latter applications include digital sampling strategies for imaging radar and optical systems.

## II. Derivation of Main Result

The proof of theorem 1 requires the following formula which was known to Gauss (Ref. 9).

If  $F(x)$  is the Fourier transform of  $f(t)$  then for every value of  $T, x$ , and  $y$ :

$$T^{1/2} \exp(\pi i x y) \sum_{N=-\infty}^{+\infty} f(NT + y) \exp(2\pi i NT x) = \quad (7)$$

$$T^{-1/2} \exp(-\pi i x y) \sum_{N=-\infty}^{+\infty} F(NT^{-1} - x) \exp(2\pi i NT^{-1} y)$$

(note that the left side of Eq. (7) is transformed to the right side by the substitution  $T \rightarrow T^{-1}$ ,  $x \rightarrow y$ ,  $y \rightarrow -x$  and  $f \rightarrow F$ ; the beauty of this symmetry is reflected in Gauss' title to Ref. 9). This formula has (mistakenly) acquired the name of the Poisson summation formula under which it is to be found in most serious books on signal processing (Ref. 10) and Fourier analysis (Refs. 11 and 12).

The proof of theorem 1 also requires the Fourier inversion theorem (see Refs. 10-12), which states that a function  $f(t)$  can be determined by its Fourier transform  $F(x)$  as follows:

$$f(t) = \int_{-\infty}^{+\infty} F(x) \exp(2\pi i x t) dx \quad (8)$$

Now, let  $S$  be a bounded set of real numbers and let  $\epsilon > 0$  as in the hypothesis of theorem 1. From the definition of the content of  $S$  an integer  $M$  and closed intervals  $[a_i, b_i]$ ,  $1 \leq i \leq M$  can be chosen such that;

$$S \subset J = \bigcup_{i=1}^M [a_i, b_i] \quad (9)$$

and

$$\text{cont}(S) + \frac{\epsilon}{2} > L = \sum_{i=1}^M (b_i - a_i) \quad (10)$$

Choose  $T > 2M/\epsilon$ ; therefore,

$$M/T < \epsilon/2 \quad (11)$$

For any real number  $x$  define the set  $N(x)$  of integers by

$$N(x) = \{N \text{ such that } NT^{-1} - x \in I\} \quad (12)$$

and define

$$n(x) = \text{number of elements in } N(x) \quad (13)$$

and define

$$P = \max \{n(x): x \text{ is real}\} \quad (14)$$

Now, choose real numbers  $T_i$ ,  $1 \leq i \leq P$  to be arbitrary but fixed. Sufficient restrictions on the set  $\{T_i: 1 \leq i \leq P\}$  will be formulated which imply the conclusion of theorem 1 (where  $S, \epsilon, P, T_i$  and  $T$  in theorem 1 coincide with the parameters chosen above).

Since  $\{NT^{-1} - x \in I; N \text{ an integer}\}$  consists of a set of points pairwise spaced at a distance at least  $T^{-1}$  and lying within a union of  $M$  intervals whose lengths sum to  $L$ , a simple combinatoric argument implies the inequality

$$P/T \leq M/T + L \quad (15)$$

which, together with inequality (11) implies

$$P/T \leq \epsilon/2 + L \quad (16)$$

Finally, combining inequalities (10) and (16) yields

$$\text{cont}(S) + \epsilon > P/T \quad (17)$$

which establishes inequality (6).

In order to determine  $f(t)$  from sample values as in Eq. (5), Eq. (8) suggests that first the function  $F(x)$  should be determined from sample values of  $f(t)$ . The relationship between  $F(x)$  and sample values of  $f(t)$  is exactly described by Eq. (7). Define, for every real number  $x$ , the  $P$  by  $n(x)$  size matrix  $B(x)$  as follows:

$$B(x) = [b_{ij}(x)], 1 \leq i \leq P, 1 \leq j \leq n(x) \quad (18)$$

where (of course the non subscript  $i$  is  $\sqrt{-1}$ )

$$b_{ij}(x) = \exp(2\pi i N_j(x) T^{-1} T_i) \quad (19)$$

and  $N_j(x)$  is the  $j$ th element, in ascending order, of the set  $N(x)$  in (12). Define, for every real number  $x$ , a  $P$  size column vector  $V(x)$  by

$$V(x) = [v_i(x)], 1 \leq i \leq P \quad (20)$$

where

$$v_i(x) = T \sum_{N=-\infty}^{+\infty} f(NT + T_i) \exp [2\pi i x(NT + T_i)] \quad (21)$$

and a  $n(x)$  size column vector  $W(x)$  by

$$W(x) = [w_j(x)], 1 \leq j \leq n(x) \quad (22)$$

where (with  $N_j(x)$  defined as in (19))

$$w_j(x) = F(N_j(x)T^{-1} - x) \quad (23)$$

Then the set of equations obtained by substituting the value  $y = T_i$  for  $1 \leq i \leq P$  into Eq. (7) can be written in matrix form as:

$$V(x) = B(x) W(x) \quad (24)$$

Clearly, in order to determine  $F(x)$  it suffices to determine  $W(x)$  for values of  $x$  in the interval  $[0, T^{-1}]$ . As  $x$  ranges from 0 to  $T^{-1}$  the set of values  $N_j(x)$  ( $1 \leq j \leq n(x)$ ) form a finite set of integers  $\{K_j : 1 \leq j \leq g\}$  where  $g \geq P$ . Now, the set of exponential functions  $\exp(2\pi i K_j u) : 1 \leq j \leq g$  are orthogonal and hence linearly independent functions of the variable  $u$ . Therefore, there exists a set of real numbers  $\{u_i : 1 \leq i \leq g\}$  such that the  $g$  by  $g$  matrix  $Q = [\exp(2\pi i K_j u_i)]$  has rank  $g$ . Then choose  $T_i = Tu_i$  for  $1 \leq i \leq P$ . Since any choice of  $n(x) \leq P \leq g$  columns of  $Q$  results in a  $P$  by  $n(x)$  matrix having rank  $n(x)$  and  $B(x)$  arises by choosing the first  $n(x)$  columns of  $Q$ , it follows that such a choice of  $T_i$ ,  $1 \leq i \leq P$  will imply that for any value of  $x$  between 0 and  $T^{-1}$  the  $n(x)$  by  $n(x)$  matrix  $B^*(x) B(x)$  (where  $*$  denotes the transpose of a matrix) has rank  $n(x)$  and is therefore invertible. Hence Eq. (24) can be solved for  $W(x)$  to yield a (generalized inverse) solution.

$$W(x) = [B^*(x) B(x)]^{-1} B^*(x) V(x) \quad (25)$$

Furthermore, the complicated matrix valued function preceding  $V(x)$  in (25) is, by (18), (19), and the definition of  $N_j(x)$ , constant over each of a finite number of intervals. Therefore, there exists an integer  $r$ , real numbers  $x_1 < x_2 < \dots < x_r$ , and a set of coefficients  $\{c_{ij} : 1 \leq i \leq P, 1 \leq j \leq r\}$  such that

$$F(x) = \begin{cases} \sum_{i=1}^P c_{ij} v_i(-x) \text{ for } x_j < x < x_{j+1} \text{ (for } j < r) \\ 0 \text{ for } x > x_r \text{ or } x < x_1 \\ \text{unspecified otherwise} \end{cases} \quad (26)$$

Finally, applying Eq. (8) yields

$$f(t) = \int_{-\infty}^{\infty} F(x) \exp(2\pi i x t) dx \quad (27)$$

$$\begin{aligned} &= T \sum_{j=1}^{r-1} \sum_{i=1}^P c_{ij} \sum_{N=-\infty}^{+\infty} f(NT \\ &\quad + T_i) \int_{x_j}^{x_{j+1}} \exp[2\pi i x (t - NT - T_i)] dx \\ &= \sum_{i=1}^P \sum_{N=-\infty}^{+\infty} f(NT + T_i) s_i(t - NT - T_i) \end{aligned}$$

where

$$s_i(t) = T \sum_{j=1}^{r-1} \frac{\exp(2\pi i x_{j+1} t) - \exp(2\pi i x_j t)}{2\pi i t} c_{ij} \quad (28)$$

are the sampling functions in Eq. (5). The proof of theorem 1 is concluded.

## References

1. Nyquist, H., "Certain Topics in Telegraph Transmission Theory," *AIEE Trans.*, p. 617, 1928.
2. Whittaker, J. M., *Interpolatory Function Theory*, Cambridge Tracts in Mathematics and Mathematical Physics, No. 33, Cambridge University Press, 1935.
3. Kohlenberg, A. W., "Exact Interpolation of Bandlimited Functions," *J. Appl. Phys.* 24, p. 1432-1436, 1953.
4. Grace, O. D., and Pitt, S. P., "Quadrature Sampling of High-Frequency Waveforms," *J. Acous. Soc., A.*, 44, No. 5, pp. 1453-1454, 1968.
5. Hurd, W. J., "Preliminary Demonstration of Precision DSN Clock Synchronization by Radio Interferometry," *DSN Progress Report 42-37*, pp. 57-68, Jet Propulsion Laboratory, Pasadena, Calif., 1977.
6. Milenkovic, P. H., "Recovering the Spectrum of a Narrowband Process from Syncopated Samples," *DSN Progress Report 42-51*, pp. 47-50, Jet Propulsion Laboratory, Calif., 1979.
7. Miller, K. S., *Complex Stochastic Processes*, Addison-Wesley, Reading, Mass., 1974.
8. Boorstyn R. R., and Rife, D. C., "Multiple Tone Parameter Estimation from Discrete-Time Observations," *Bell System Tech. J.*, 55 No. 9, 1389-1410, 1976.
9. Gauss, C. F., "Schönes Theorem der Wahrscheinlichkeitsrechnung," in *Werke 8*, pp. 88-89, B. G. Teubnerin, Leipzig, 1900.
10. Papoulis, A., *Signal Analysis*, McGraw-Hill, N. Y., 1977.
11. Dym, H., and McKean, H. P., *Fourier Series and Integrals*, Academic Press, N. Y., 1972.
12. Rudin, W., *Real and Complex Analysis*, McGraw-Hill, N. Y., 1974.

## Acknowledgements

The author wishes to express his appreciation to J. Ellis, W. Hurd, R. Nichols, E. Posner, L. Rauch, and C. Solloway for helpful discussions about this paper.

# An Experimental Investigation of the Changes of VLBI Time Delays Due to Antenna Structural Deformations

T. Y. Otoshi

Radio Frequency and Microwave Subsystems Section

L. E. Young

Tracking Systems and Applications Section

*An experimental investigation was conducted on the 64-m antenna at DSS 14 to study the effects of antenna structural deformations on VLBI time delays at S-band. Structural deformations primarily occur as functions of antenna elevation angle due to gravity loading. For a Cassegrain antenna, one of the major effects of structural deformation on measured VLBI time delays are those delay changes associated with axial subreflector displacement from its nominal position. Two types of time delay changes that occur when the subreflector is axially defocused are (1) a change which is a linear function of subreflector defocus position and (2) a cyclical change caused by multipath. Test results showed that for the 64-m DSN antenna, the linear change is 1.8 times the subreflector defocus position, while the peak-to-peak change in cyclical variation is about  $\pm 3$  cm when a spanned bandwidth of 38 MHz at 2290 MHz is used.*

## I. Introduction

When a large antenna is used to track a signal coming from a spacecraft or VLBI radio source, gravity loading causes deformations of the antenna structure as functions of antenna pointing angles. If the resulting changes in antenna time delays are not properly taken into account, significant errors could occur in the determination of spacecraft position, station location, or other uses of VLBI data such as for studies of earth crustal movements.

It was shown in a structural deformation study by Katow (Ref. 1) that when the antenna points at elevation angles dif-

ferent from optimum 45 deg, structural deformation of the antenna will occur due to gravity loading. Four structural deformation variables that affect time delay changes were shown to be displacements of the best-fit paraboloid focal point, paraboloid vertex, feed horn phase center, and subreflector vertex. The displacements were analyzed as functions of elevation angle relative to the optimum 45-deg elevation angle parameters which in turn are referenced back to the station location (intersection of Az-El axes). Of the various displacements mentioned, defocusing (and refocusing) of the subreflector was shown to contribute the largest changes in VLBI time delays as functions of elevation angles.

On August 23, 1980, VLBI experiments were performed on the 64-m antenna at DSS 14 (Fig. 1) for purposes of simulating gravity loading and measuring associated time delay changes. One of the simulation experiments performed was to isolate and measure the time delay changes associated with axial subreflector defocusing. This article will describe the experimental procedure and also the data processing methods involved in obtaining the 1- to 2-cm accuracy required to observe the multipath effects when using VLBI bandwidth synthesis (BWS) channel separations of about 40 MHz. The experiment described in this article is believed to be the first use of VLBI data taken specifically for comparison to antenna multipathing theory.

## II. Discussion of the Antenna Multipath Phenomenon

Figure 2 shows the geometry of the DSS 14 Cassegrain antenna with a reflex-dichroic system which enables simultaneous receptions of both S- and X-band frequencies. A signal originating from the far field is collected by the parabolic reflector, reflected to the subreflector, re-reflected, and arrives at the receive horn via the ray paths of the dual-band system. If the antenna is ideal, all signals follow geometric optics (GO) ray paths so that they all have the same delay (path length) from the paraboloid focal plane to the system feed horn focal point. In practice numerous factors such as blockage, mechanical supports, imperfect reflector surfaces, mechanical distortions, and defocusing cause departure from the ideal Cassegrain antenna. Furthermore, two known types of multipath signals are generated within the antenna optics medium of practical Cassegrain antennas. The first type is caused by a portion of the illuminating plane wave signal becoming blocked by the large subreflector and subreflector support struts. Diffraction around the edges of the subreflector and struts will occur and a portion of these diffracted fields propagates directly into the receive horn. Another type of multipath phenomenon that occurs is that generated by unwanted multiple reflections between the subreflector and feedcone surfaces as illustrated in Fig. 3.

When the subreflector of a Cassegrain antenna defocuses in the axial direction, two types of VLBI time delay changes occur, namely: (1) a linear time delay change due to geometric path length changes related to the subreflector displacement and (2) a cyclical time delay change due to multiple reflection multipath signals of the type depicted in Fig. 3. Both types of changes were previously analyzed theoretically through the use of electromagnetic theory principles and antenna computer programs developed specifically to study the effects of defocusing and multiple reflections between the subreflector and feedcone support surfaces (Ref. 2). A typical

theoretical curve showing the linear and cyclical variation is depicted in Fig. 4.

If one desires a quick estimate of the effects of subreflector defocusing, the following approximate formula can be used to compute the delay change in nanoseconds.

$$\Delta\tau_{BWS} = \frac{K_1 \Delta S}{c} + \frac{A}{\pi \Delta f} \sin \left[ \frac{\pi \Delta f x}{c} \right] \cos \left[ \frac{2\pi f_0 x}{c} - \psi \right] \quad (1)$$

where

$$x = \ell_2 - \ell_1 \cong 2d + (K_2 - K_1) \Delta S \quad (2)$$

and

$K_1, K_2$  = constants relating pathlength changes to subreflector movement for the primary and secondary signals, respectively, and are approximately equal to 1.8 and 3.8, respectively.

$\Delta S$  = subreflector defocus position relative to the nominal position, cm

$c$  = speed of light (29.97925 cm/ns)

$A$  = voltage ratio of the multipath signal to the primary signal

$\Delta f$  = spanned bandwidth =  $(f_B - f_A)$

$f_0$  = center frequency =  $(f_B + f_A)/2$

$f_B$  = upper frequency used in VLBI BWS measurement, GHz

$f_A$  = lower frequency used in the VLBI BWS measurement, GHz

$\ell_1, \ell_2$  = path lengths of the primary and secondary signals, respectively, cm

$d$  = nominal distance between the subreflector vertex and cone platform surface creating the multipath signal, cm

$\psi$  = phase angle which establishes where the multipath cyclical pattern begins, radians

Equation (1) was derived by first taking the phase term given in Ref. 3 and applying it to the BWS equation (Ref. 4) at the two channel frequencies involved in the BWS measurements. Then assuming that the multipath signal is small, i.e.  $A < 0.1$  and using trigonometric identities, the approximate formula given by Eq. (1) was obtained.

The approximate formula given above will yield a theoretical multipath amplitude ripple that is slightly larger than those obtained from the Rusch Computer Program (Ref. 2). Since this approximate formula does not account for edge diffractions, it does not give sufficient damping of the sinusoidal features. However, the approximate formula can be very useful for obtaining quick estimates of error bounds and for making quick comparisons to experimental subreflector defocus data. The formula is also useful for clearly showing that multipath error (the cyclical term) decreases as spanned bandwidth is increased.

### III. Description of Experiment

One of the major experiments performed on the 64-m antenna at DSS 14 was to isolate and measure the time delay changes associated with axial subreflector defocusing. The experiment consisted of observing a radio source simultaneously with the 26-m antenna at DSS 13 and the 64-m antenna at DSS 14. The signal outputs from three 1.8-MHz-wide channels were recorded on magnetic tape at each station. Hydrogen masers provided the basic frequency standards at each station and provided the clock (timing) signals. At each station, phase calibration signals were injected into the incoming signal stream at an injection port close to the output of the feed horn assembly. As discussed in Ref. 4, the phase calibration signals are used to remove instrumental delay changes that occur below the injection port at each station. Removal of these instrumental delays enables the isolation and measurement of only those delay changes caused by antenna optics structural deformations and changes in the transmission media above the antenna. Since the DSS 13-14 baseline is short (21.6 km), the assumption is made that the transmission media (consisting of troposphere, ionosphere, and plasma) are similar above the two stations. Any delay changes in this transmission media during the experiment should cancel out in the VLBI correlation processing because of common-mode rejection. The shortness of the baseline also affords the additional advantages of reduced sensitivity to errors in source position, universal time, and polar motion.

The experiment was performed with a 2290-MHz center frequency and at various spanned bandwidths (SBW), with the largest SBW being 38 MHz. The 26-m antenna at DSS 13 was used as the reference antenna, with its subreflector fixed in the nominal position throughout the test. Only the subreflector on the 64-m antenna was defocused. For this experiment to be valid, the DSS 13 antenna delay must not vary radically with antenna pointing angles. An X-band test performed by Freily (Ref. 6) showed that the DSS 13 antenna gain changes were small as functions of elevation angle. If the reported small gain changes for this antenna were due primarily to structural deformations, it is reasonable to expect that phase and group

delay changes for the DSS 13 antenna would also be small. If slowly varying group delay changes do occur on the DSS 13 antenna, most of the effects of this drift are later removed by polynomial curve fits performed on repeated points taken under nominal conditions.

The VLBI experiments for the results of this article were specifically designed to enable accurate measurements of multipath-caused delay changes as functions of axial subreflector defocusing. First, in order to minimize the delay changes contributed by the ionosphere and temperature variations, the experiments were purposely scheduled to be performed during local nighttime hours. Secondly, a radio source was selected on the basis that it would (1) provide adequate signal-to-noise ratio, (2) be essentially unresolved (unstructured) over the DSS 13 – DSS 14 baseline and (3) remain at nearly constant elevation angles in the region of 45 to 60 deg throughout the major portion of test times. It was desirable that the antenna be pointed at nearly constant elevation angles so that gravity loading would be constant and not cause unknown or unwanted subreflector movements.

A factor which must be considered in an experiment of this type is the wind velocity and its direction relative to the paraboloid reflector surface. It was fortunate that for this particular experiment the wind velocity was less than 9.7 kph (6 mph) throughout the test period. Using the wind study results reported by R. Levy (Ref. 5), it could be concluded that only negligible errors could be contributed to this experiment by 9.7-kph wind loading or wind gusts.

The experimental procedure for the axial subreflector test was to move the subreflector sequentially from a positive defocus position on one side of nominal setting, then to a negative defocus position (of nearly equal increment) on the other side of nominal setting, and then back to nominal setting. At each of these subreflector positions, a measurement was made for a period of about 2 minutes duration. All data were purposely taken in this manner relative to the nominal setting so that polynomial curve fits could later be performed on the nominal points to enable removal of long-term drifts (such as those due to clock frequency offsets, antenna elevation angle dependence, geometric delay modeling errors, etc.). The total range of defocus of the subreflector from its nominal position for this test was plus/minus 6 cm. Three separate runs were made using the above described test procedure.

Postprocessing of the data consisted of the following five steps:

- (1) Performing a correlation of the data recorded on magnetic tapes through the use of the Caltech/JPL Block 0 VLBI correlator giving the total time delay of the DSS 13 – 14 baseline

- (2) Applying phase calibrator corrections for each station to remove instrumental delay part of the total delay
- (3) Using the VLBI Fit Delay Program to remove the geometric delays, long-term drifts, and residual clock errors so that the remaining delay changes could be attributed to changes occurring only in the antenna optics region
- (4) Performing further data reduction necessary to express the results in terms of antenna test parameters
- (5) Correlating the final processed data with antenna theory.

#### IV. Test Results

Figure 5 shows a plot of nominal point test data after correlations on the VLBI data recorded on magnetic tapes were performed. The purpose of showing this plot is to show the magnitude of long-term drift due to residual clock errors, and to show that most of this drift will be ultimately removed by the Fit Delay Program. An unweighted third-order polynomial curve was fitted to the points and shows that the drift is of the order of 140 cm over the test period of about 8 hours. Also indicated on the plot are the time periods of the axial subreflector test runs and the corresponding antenna elevation angles.

Figure 6 shows a plot of the scatter of the nominal points when the Fit Delay Program was used to perform a *weighted* polynomial curve fit routine on the nominal data points. The weights were based on error estimates derived directly from the outputs of the VLBI correlator. It should be mentioned that the residual errors shown in Fig. 6 were arrived at by judiciously dividing the total test time into three sections and performing separate fit delay second-order polynomial curve fits to the nominal points in each section. Division into three sections was necessary because the long-term drifts over 8 hours could not be accurately characterized by a single second-order polynomial. The deviations of the nominal points were computed by the Fit Delay Program to have an rms value of 1.5 cm, which is a useful value for estimating the type of accuracy that can be achieved by this experiment.

After deriving the best-fit curve to the nominal points, the Fit Delay Program then computes deviations of nonnominal points from the curve. These deviations are the test data of interest and are shown plotted in Fig. 7 for the three subreflector defocusing tests performed within the same 8-hour time span. These data have been corrected with phase calibration data for both DSS 13 and 14. The vertical scale is shown in units of equivalent freespace path length units, while

the horizontal axis is the axial subreflector defocus position (relative to the nominal position).

Since it is known from theory (see Section II of this article) that the delay changes caused by axial subreflector defocusing will consist of a linear term and a cyclical term, it is desirable to perform a least squares fit using a theoretical model that contains both terms. However, it is difficult to perform a least squares fit using the more accurate theoretical model developed by Rusch (Ref. 2) because numerical solutions from his analysis are arrived at by an iterative process that cannot be expressed in closed form. A study is currently being made to perform a least squares fit using the approximate expression given in Eq. (1). The results of this work will be reported in a future TDA Progress Report.

The alternative data reduction approach that was used for the results of this article was to do the curve fitting in a sequential manner. First a linear fit was performed on the total data and then a multipath curve fit was made to the residuals. Although this alternate procedure is not as theoretically rigorous as curve fitting to both linear and cyclical terms simultaneously, it did enable results to be obtained in an expedient manner using available computer programs. A weighted linear curve was fitted to the test data from all three subreflector tests using weights based on error estimates of each test data point and the rms error of the nominal points shown in Fig. 6. Figure 7 shows the resulting linear curve together with its standard error limits as indicated by the edges of the shaded area. The standard error is a function of subreflector setting and is the largest ( $\pm 0.4$  cm) at the outer edges ( $\pm 6.6$  cm) of the plot. The slope of the best fit linear curve to experimental data is 1.77, which is in excellent agreement with the theoretical slope value of 1.76 reported in Ref. 2. This agreement is fortuitous because of the apparent cancellation of the multipathing signature.

It is important to emphasize that the slope of the linear curve is about 1.8 and not the 2.0 value most often used for crude estimates. The actual slope will generally be less than 2.0 and will be different for each Cassegrain antenna. The 2.0 slope applies only to a single ray on the paraboloid axis of symmetry, while the true slope is dependent upon the total primary feed amplitude pattern, the subreflector scattered patterns at the different defocus positions, and the corresponding changes in the amplitude and phase over the entire paraboloidal aperture. These dependent factors are all taken into account in the Rusch program (Ref. 2), when integrations are performed over the entire paraboloidal antenna aperture.

Figure 8 shows the residuals after the best fit linear curve was subtracted from the data points shown in Fig. 7. For purposes of comparison with antenna theory, a theoretical multipath curve was generated by the Rusch program for the multi-

path geometry on the 64-m antenna at 2290 MHz and 38 MHz SBW. The theoretical curve is shown as the dashed line and was "eye-ball" fitted by lining up the peak of the theoretical curve with the peak data points at about the negative 2-cm defocus position on the X-axis and centering the curve symmetrically about the Y-axis. The solid line theoretical curve shown in the same plot was generated from use of the second term of the approximate equation given in Eq. (1), assuming that the multipath signal was -36 dB (corresponding to  $A = 0.016$ ) down from the primary signal. Other parameters used to generate this solid curve were  $d = 1657$  cm,  $K_1 = 1.8$ ,  $K_2 = 3.8$ ,  $\psi = -1.016$  radians, and the experiment VLBI channel frequencies of 2.271 and 2.309 GHz. It can be seen in Fig. 8 that the two theoretical curves differ mainly in the amplitude damping features, as was explained in Section II of this article.

It can further be seen that for both theoretical curves and experimental data, the peak-to-peak values are approximately plus/minus 3 cm. Although peak-to-peak values are in reasonable agreement between theory and experiment, the periodicity is not in good agreement. This disagreement might partially be explained by the fact that the theoretical curve accounts only for the multipath signal produced by multiple bounces between the subreflector and flat surfaces behind the feed-

horn. The experimental data include multipath errors over the entire antenna, including the quadripod supports.

## V. Conclusions

The experiment to determine the effects of subreflector defocusing was successfully performed at an S-band frequency of 2290 MHz. It was determined that for the 64-m DSN antenna, axial subreflector defocusing results in a linear component of VLBI delay change equal to 1.8 times the axial defocus position. This information will be very useful for (1) correcting for unintentional subreflector movement due to gravity and/or (2) correcting for delay changes due to intentional or automatic refocusing which is sometimes purposely done to maximize antenna gain.

The observed peak-to-peak change of cyclical variation was about plus/minus 3 cm at 2290 MHz using a 38-MHz SBW. The cyclical variations are attributed to the multipath phenomenon. Although the measured delay changes due to multipath do not agree in detail with the relatively simple theoretical curves, the agreement achieved on error bounds between theory and experiment is a noteworthy achievement. The data presented in this article should be helpful in establishing worst-case error limits on VLBI measurements due to structural deformation of the antenna.

## References

1. Katow, M. S., "DSS 14 64-m Antenna-Computed RF Pathlength Changes Under Gravity Loadings," *TDA Progress Report 42-64*, pp. 123-131, Jet Propulsion Laboratory, Pasadena, Calif., Aug. 15, 1981.
2. Otoshi, T. Y., and Rusch, W. V. T., "Multipath Effects on the Time Delays of Microwave Cassegrainian Antennas," *DSN Progress Report 42-50*, pp. 52-55, Jet Propulsion Laboratory, Pasadena, Calif., Apr. 15, 1979.
3. Otoshi, T. Y., "S/X Band Experiment: A Study of the Effects of Multipath on Group Delay," *Deep Space Network Progress Report 42-24*, pp. 40-50, Jet Propulsion Laboratory, Pasadena, Calif., Dec. 15, 1974. (See the Appendix entitled "Derivation of Equations for Phase and Group Delay Errors Caused by Multipath," Eqs. (A-11) and (A-12), p. 48.)
4. Thomas, J. B., "The Tone Generator and Phase Calibration in VLBI Measurements," in *The DSN Progress Report 42-44*, pp. 63-74, Jet Propulsion Laboratory, Pasadena, Calif., Apr. 15, 1978.
5. Levy, R., "VLBI Antenna Mechanical Calibration Work Unit," in *OSTDS Advanced Systems Review at JPL (DSN Advanced Systems Review)*, p. 92, June 24-26, 1980 (JPL/NASA document).
6. Freily, A. J., "Performance of DSS 13 26-m Antenna at X-Band," *DSN Progress Report 42-30*, pp. 113-118, Jet Propulsion Laboratory, Pasadena, Calif., Dec. 15, 1975.

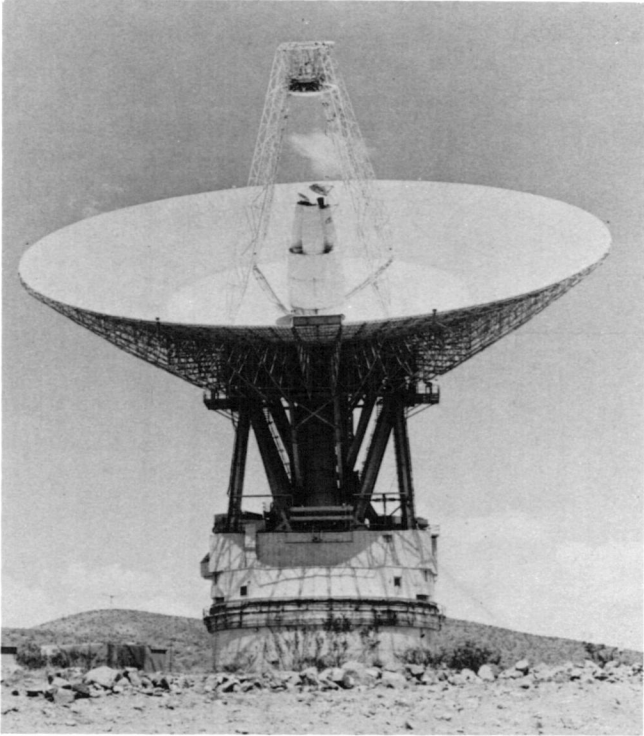


Fig. 1. DSN 64-m Cassegrain antenna at Goldstone, California

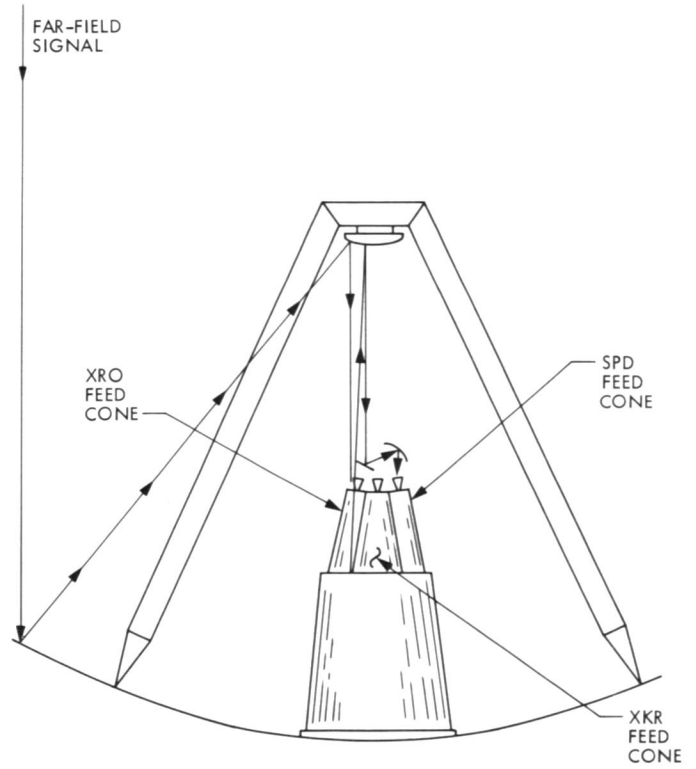


Fig. 3. A secondary propagation ray path on DSN 64-m antenna

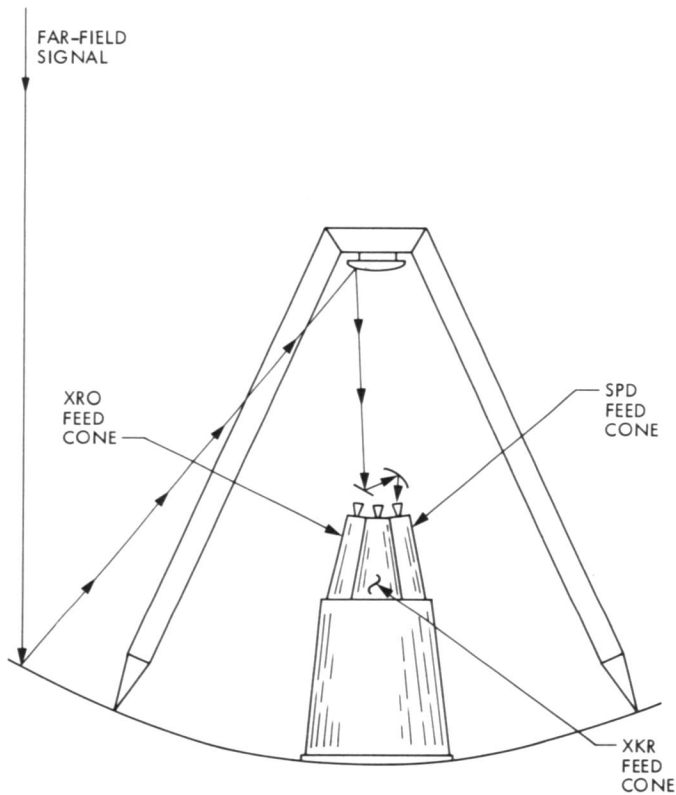


Fig. 2. Typical ray path for primary signal on DSN 64-m antenna

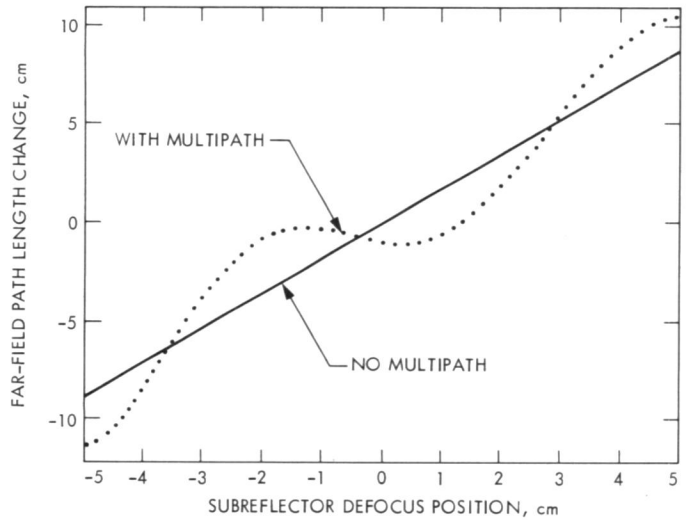
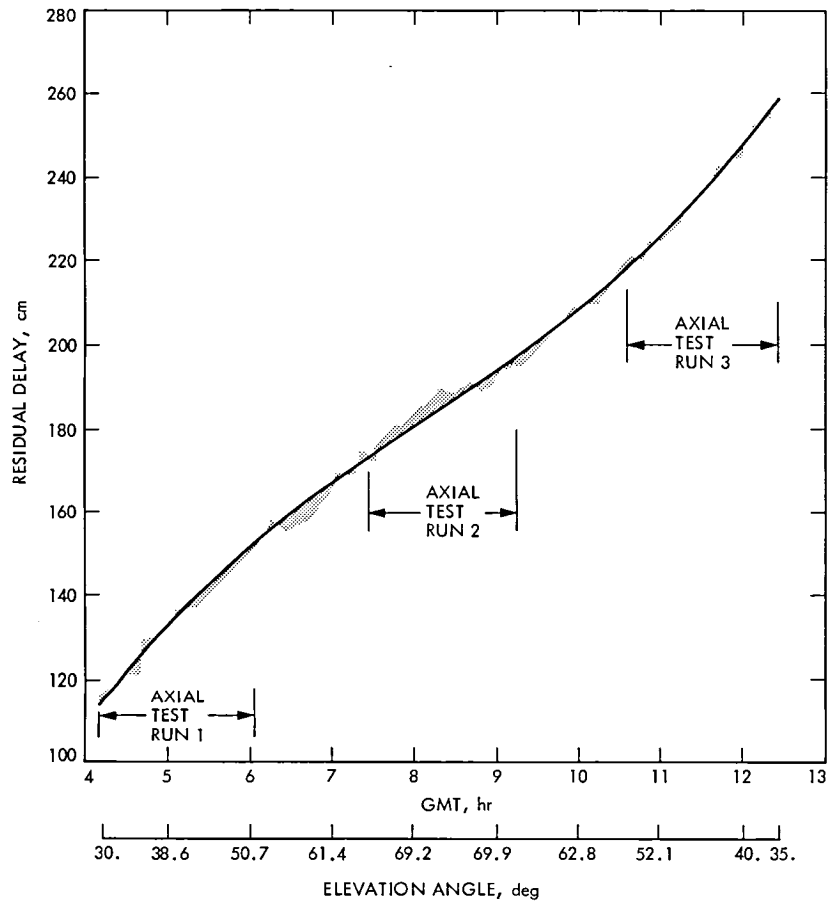
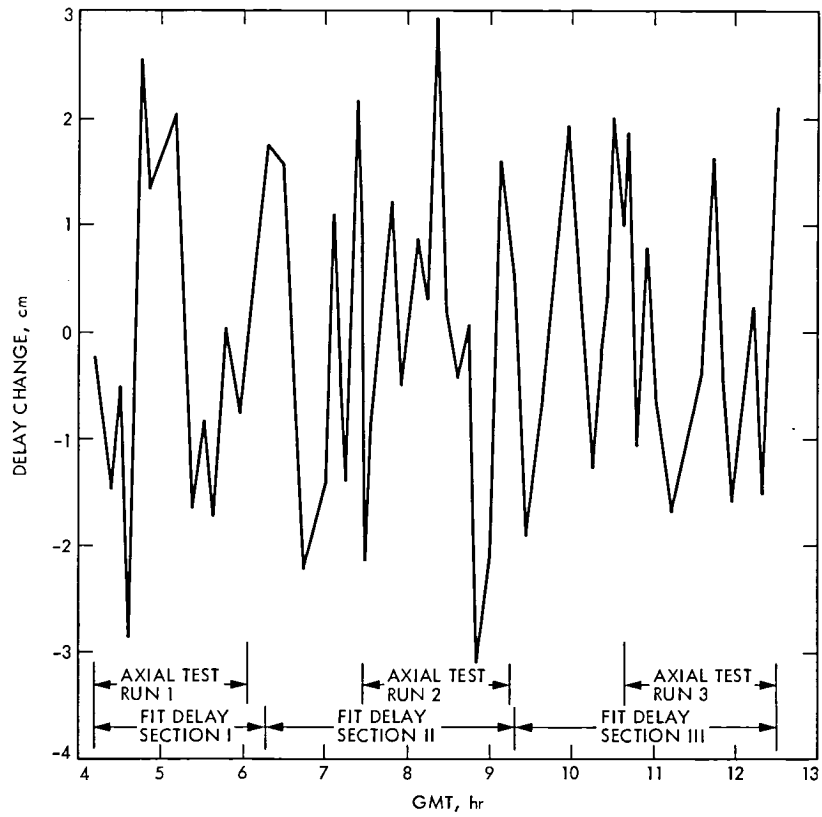


Fig. 4. Sample theoretical curve showing far-field delay changes due to subreflector defocusing on 64-m antenna at 2285-MHz and 40-MHz spanned bandwidth (from Ref. 2)



**Fig. 5. Polynomial curve fit to nominal points after correlation to DSS 13-DSS 14 baseline is performed**



**Fig. 6. Residuals of nominal points after residual clock errors and instrumental drift are removed**

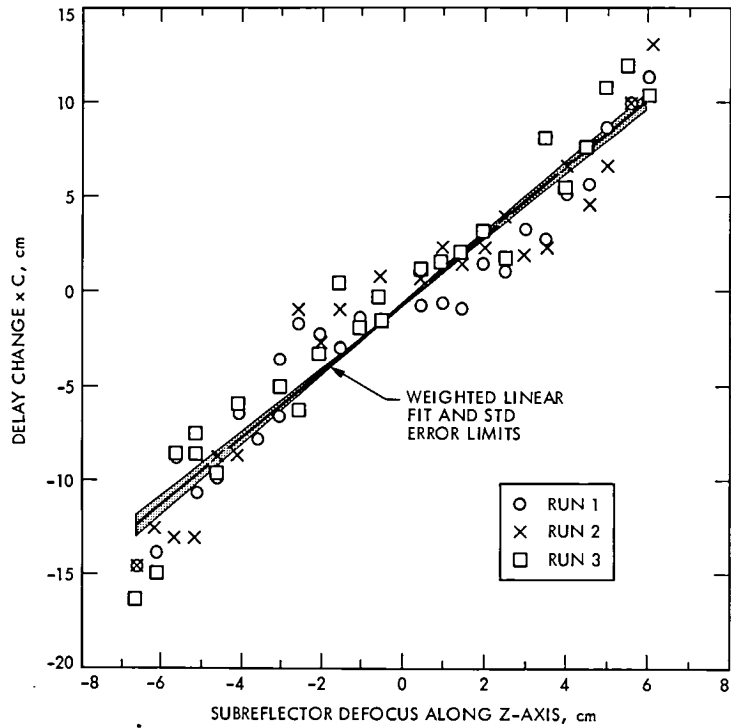


Fig. 7. Weighted least squares linear fit to processed VLBI data from axial subreflector tests on 64-m antenna at 2290 MHz

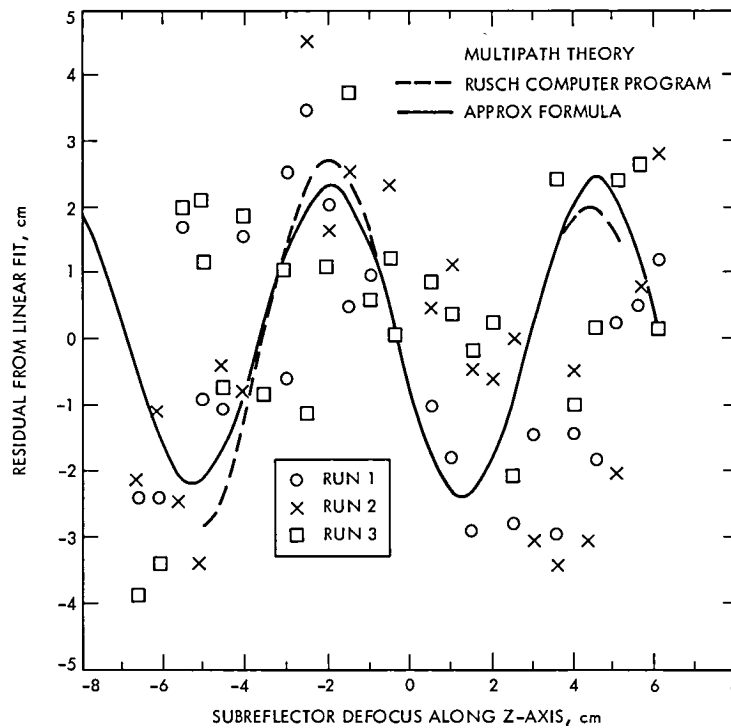


Fig. 8. Comparisons of multipath theoretical curves to experimental data which were derived by subtracting linear fit from VLBI data points (see Fig. 7)

# The Effects of Viterbi Decoder Node Synchronization Losses on the Telemetry Receiving System

L. J. Deutsch and R. L. Miller  
Communications Systems Research Section

*The Viterbi decoders currently used by the Deep Space Network (DSN) use an algorithm for maintaining node synchronization that breaks down at bit signal-to-noise ratios (SNRs) of about 2.0 dB. In this report, it is shown that this can become an important consideration when the effects of noisy carrier referencing are combined with the lower SNRs that are expected at Voyager 2 Uranus and Neptune encounters. Depending on the available carrier power, node synchronization losses of between 0.85 and 1.25 dB can be expected in addition to the radio loss.*

## I. Introduction

Most present and all planned deep space missions make use of convolutional coding. The NASA standard (7, 1/2) convolutional code is used in conjunction with Viterbi, or "maximum likelihood", decoding. Figure 1 shows an encoder for this convolutional code. The input information bits  $i_1 i_2 i_3 \dots$  are shifted into a register. This register is used to generate two parity checks each time a new information bit is entered. A commutator interleaves these parity checks to produce the coded output stream  $a_1 b_1 a_2 b_2 a_3 b_3 \dots$ .

One advantage to convolutional coding is that decoding may begin at any symbol  $a_j$  in the output stream. This is in contrast to block coding in which the decoder must be aligned with codeword boundaries. A convolutional decoding system must, however, be capable of distinguishing between the  $a_j$ s and the  $b_j$ s in order to function properly. The process of deter-

mining which of the symbols are the  $a_j$ s is called "node synchronization".

The Viterbi decoders that are currently used by the DSN have internal hardware for determining node synchronization. The algorithm that is used was optimized for the larger bit SNRs that were being considered at the time they were built. Tests conducted in 1979 in the Telecommunications Development Laboratory (TDL) have shown that this node synchronization algorithm breaks down at a bit SNR of about 2.5 dB when the carrier tracking loop SNR is 16 dB (Ref. 1). At bit SNRs below this value, the Viterbi decoder always decides that it is out of synchronization — regardless of whether it really is. This means that it oscillates between proper and improper node synchronization.

With the advent of concatenated Reed-Solomon/convolutional coding, poor node synchronization will become

a more critical factor in overall channel performance. This is due to the fact that the Viterbi decoders will be operated at bit error rates of about  $10^{-2}$  to achieve a concatenated bit error rate of  $10^{-5}$  (Ref. 2). This corresponds to an  $E_b/N_0$  of about 2 dB at the input of the Viterbi decoder, which means that the telemetry receiving system will be operating in the region of poor node synchronization.

The theory developed in this article predicts that between 0.85 and 1.25 dB will be lost due to the poor performance of the current DSN Viterbi decoders' node synchronization algorithm (for the convolutional-only channel) at SNRs that are typical of the Voyager 2 Uranus encounter. One solution to this problem is to disable the internal node synchronization hardware in the existing Viterbi decoders. A new external node synchronization logic could then be implemented. One such algorithm is described in Ref. 3. Another algorithm which makes use of frame headers in the data stream was analyzed by Laif Swanson, Section 331 (personal correspondence).

## II. The Model

A simplified block diagram of a DSN telemetry system is shown in Fig. 2. Information bits produced by the spacecraft instruments are first convolutionally encoded. The encoded bits, which will be referred to as "channel symbols" are amplitude-modulated on a square wave subcarrier. The resulting signal phase-modulates a high-frequency sinusoidal carrier which is amplified and transmitted over the space channel. The channel is assumed to add an independent white Gaussian noise to this signal. On the ground, the carrier is demodulated in the receiver, and the subcarrier is stripped off by the Sub-carrier Demodulation Assembly (SDA). The Symbol Synchronizer Assembly (SSA) recovers a noisy version of the channel symbol stream, which is sent to the Viterbi decoder for decoding. The decoder performs its own node synchronization.

For modeling purposes, only losses occurring in the space channel, receiver, and decoder were considered for this report. These are certainly the most important losses since the loop SNRs of the SDA and SSA are typically much higher than that of the receiver.

Suppose that the bit SNR of the signal incident on the ground antenna is  $E_b/N_0$ . The result of a phase estimate error  $\phi$  in the receiver tracking loop would be an output SNR of  $(E_b/N_0) \cos^2\phi$  (Ref. 5). Suppose also that the bit error rate at the output of the Viterbi decoder is  $f(x)$  when the input bit SNR to the decoder is  $x$ . Then a constant phase error of  $\phi$  in the receiver will produce an average decoded bit error rate of  $f[(E_b/N_0) \cos^2\phi]$ .

Assume now that the phase error  $\phi$  is changing slowly compared to the decision length of the Viterbi decoder. Then the overall average decoded bit error rate of the system is given by

$$P_b = \int_{-\pi}^{\pi} f[(E_b/N_0) \cos^2\phi] p(\phi) d\phi \quad (1)$$

where  $p(\phi)$  is the density of the phase error  $\phi$ . This is known as the high rate model.

To illustrate the applicability of the high rate model assumption, consider a typical Voyager 2 Uranus encounter scenario. A typical data rate would be  $R_b = 19.2$  kbps. The bandwidth of a Block IV receiver for the encounter would be 30 Hz. This means that a phase error  $\phi$  would remain relatively constant over a period of about 600 bits – much longer than the path memory in the present Viterbi decoders.

The density  $p(\phi)$  is derived in Ref. 6 to be

$$p(\phi) = \frac{\exp(\rho \cos \phi)}{2\pi I_0(\rho)}$$

where  $\rho$  is the loop SNR of the receiver tracking loop, and  $I_0$  is the zero order modified Bessel function.

The Viterbi decoder error function  $f(x)$  will be taken to be the ideal performance curve exhibited in Ref. 4 with the exception that  $f(x) = 1/2$  whenever  $x$  is below some value  $T$ , the Viterbi decoder node synchronization threshold. In this region, it is assumed that the decoder is continuously resynchronizing and hence produces random output.

## III. Numerical Results

Numerical methods were used to calculate the Viterbi bit error rate as a function of  $E_b/N_0$ , carrier tracking loop SNR, and node synchronization threshold using Eq. (1). It was observed that the performance predicted by the model for a node synchronization threshold of 2.0 dB and a carrier tracking loop SNR of 16 dB closely approximates the actual performance data generated in the TDL (Ref. 1). This evidence supports the hypothesis that the present Viterbi decoders do not maintain proper node synchronization below 2.0 dB of  $E_b/N_0$  in a perfect carrier tracking environment. Figure 3 shows the TDL data points as well as the performance predicted by the model. A bit error rate curve for a loop SNR of 16 dB but with perfect node synchronization is included for comparison.

Graphs of Viterbi decoder bit error rate performance for node synchronization thresholds of 0.0 and 2.0 dB appear in Figs. 4 and 5, respectively. The 0.0-dB curves agree very well with the data that are exhibited in Ref. 4 for a single aperture and perfect node synchronization. The curves of Figs. 4 and 5 were used to generate the two radio loss curves shown in Fig. 6. Radio loss is defined to be the ratio of the bit SNR needed to achieve some predetermined bit error rate in a degraded system to that required in an ideal system. In this case, the ideal system is taken to be the ideal Viterbi decoder performance as given in Ref. 4, and the fixed bit error rate is 0.005, the generally accepted upper bound for uncompressed image transmission. The difference between the two curves represents the incremental SNR loss due to poor node synchronization performance. Data from design control tables predict that for Voyager 2 Uranus encounter (at a data rate of 19.2 kbps, a modulation index of  $76^\circ$  and 90% weather), a 64-meter antenna would have an associated carrier tracking loop SNR of about 13 dB, while a 34-meter antenna would have one of about 11 dB. The associated node synchronization losses for these unarrayed antennas would therefore be 0.85 and 1.25 dB, respectively.

Plots of the loss due to poor node synchronization as a function of node synchronization threshold appear in Fig. 7 for various carrier tracking loop SNRs. These represent the

additional degradations over the carrier phase jitter losses. It is easily seen from these graphs how much can be gained by improving the node synchronization algorithm of the Viterbi decoders.

#### IV. Conclusions

The model developed in this article predicts that as much as 0.85 dB may be gained at Voyager 2 Uranus encounter in a 64-meter-aperture receiving system by lowering the current Viterbi decoder node synchronization threshold from 2.0 to 0.0 dB. This can be accomplished in three ways. One is to replace the current Viterbi decoders with new decoders that could be designed to work well in the low SNR environment that will exist in Voyager's far planetary encounters. The other two ways involve modifying the current decoders so that they no longer determine their node synchronization internally. If this modification is done, then either the scheme described in Ref. 3 or a scheme that uses frame header information in the symbol stream may be implemented.

In the immediate future, this model will be extended to the concatenated Reed-Solomon/convolutional channel where the effects of poor node synchronization are expected to be even more pronounced than in the convolutional-only channel.

## References

1. Liu, K. Y., and Lee, J. J., "An Experimental Study of the Concatenated Reed-Solomon/Viterbi Channel Coding System and Its Impact on Space Communications," Publication 81-58, Jet Propulsion Laboratory, Pasadena, Calif., Aug. 15, 1981.
2. Miller, R. L., Deutsch, L. J., and Butman, S. A., "On the Error Statistics of Viterbi Decoding and the Performance of Concatenated Codes," Publication 81-9, Jet Propulsion Laboratory, Pasadena, Calif., Sep. 1, 1981.
3. Greenhall, C. A., Miller, R. L., and Butman, S. A., "A Quick-Look Decoder with Isolated Error Correction and Node Synchronization," *IEEE Trans. Comm.*, Vol. COM-29, No. 7, July 1981.
4. Divsalar, D., and Yuen, J. H., "Improved Carrier Tracking Performance with Coupled Phase-Locked Loops," in *TDA Progress Report 42-66*, Jet Propulsion Laboratory, Pasadena, Calif., Dec. 15, 1981.
5. Deutsch, L. J., Miller, R. L., and Butman, S. A., "New Results on Antenna Arraying: Part 1," *TDA Progress Report 42-62, January and February 1981*, Jet Propulsion Laboratory, Pasadena, Calif.
6. Lindsey, W. C., and Simon, M. K., *Telecommunications Systems Engineering*, Prentice Hall, Inc., N. J., 1973.

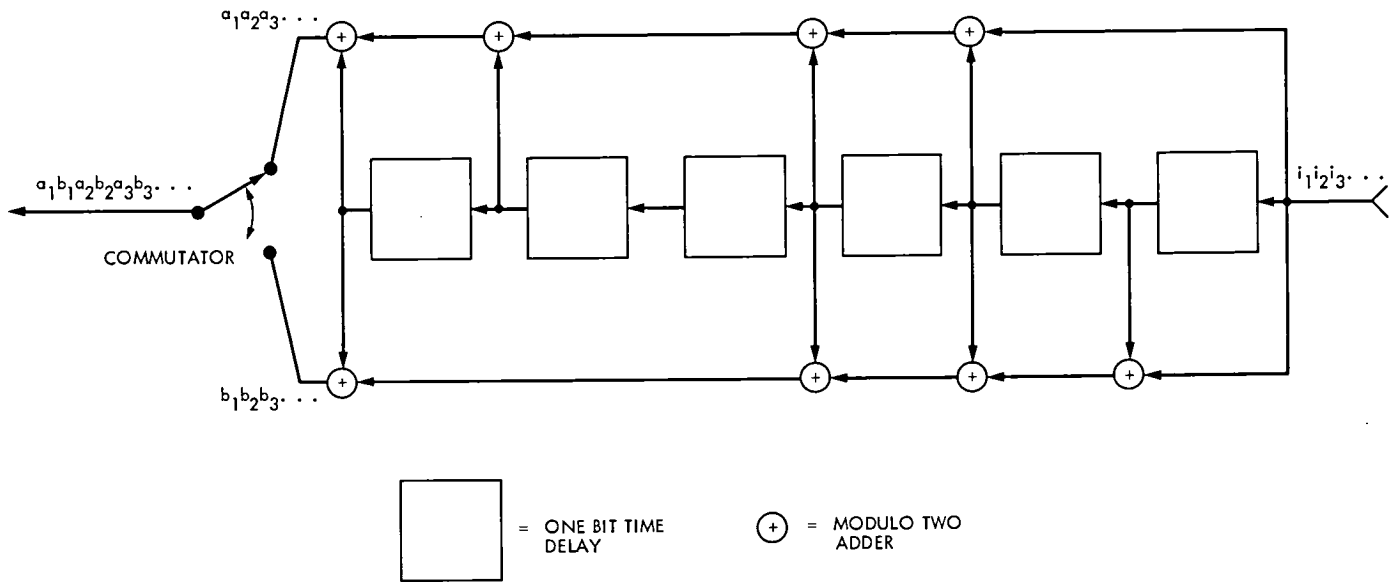


**Fig. 1. Conceptual diagram of a (7 1/2) convolutional encoder**

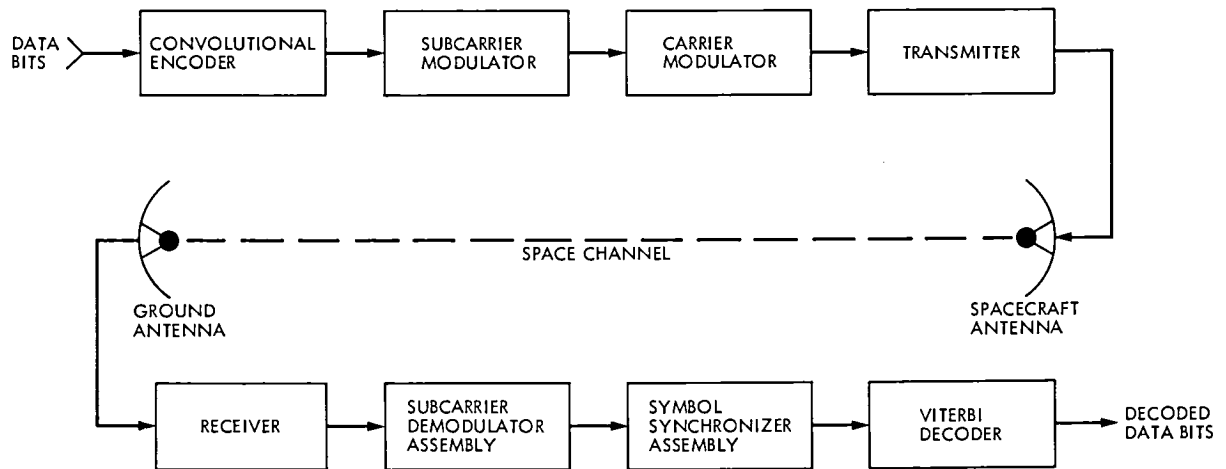


**Fig. 2. Simplified block diagram of the DSN telemetry system**

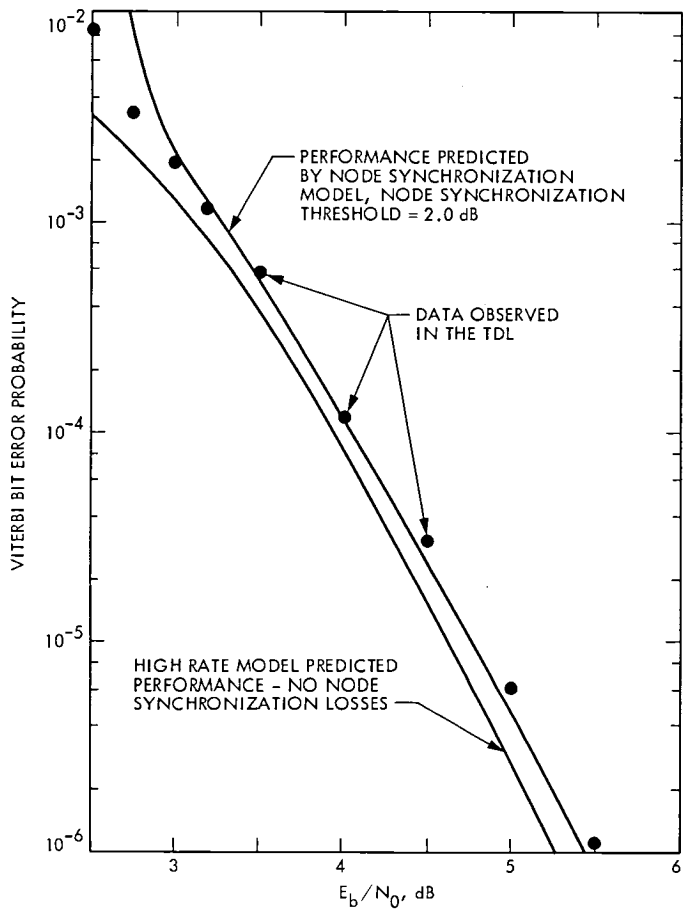


Fig. 3. Viterbi-decoder bit error rate performance with a carrier tracking loop SNR of 16 dB

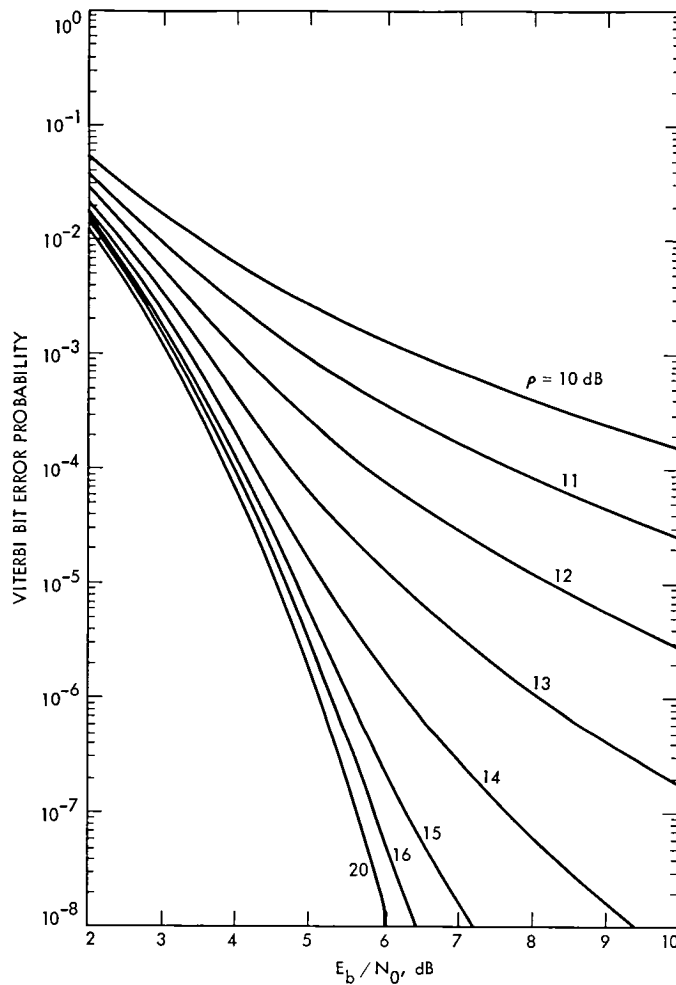


Fig. 4. Viterbi-decoded bit error rate for various carrier tracking loop SNRs, node synchronization threshold = 0.0 dB

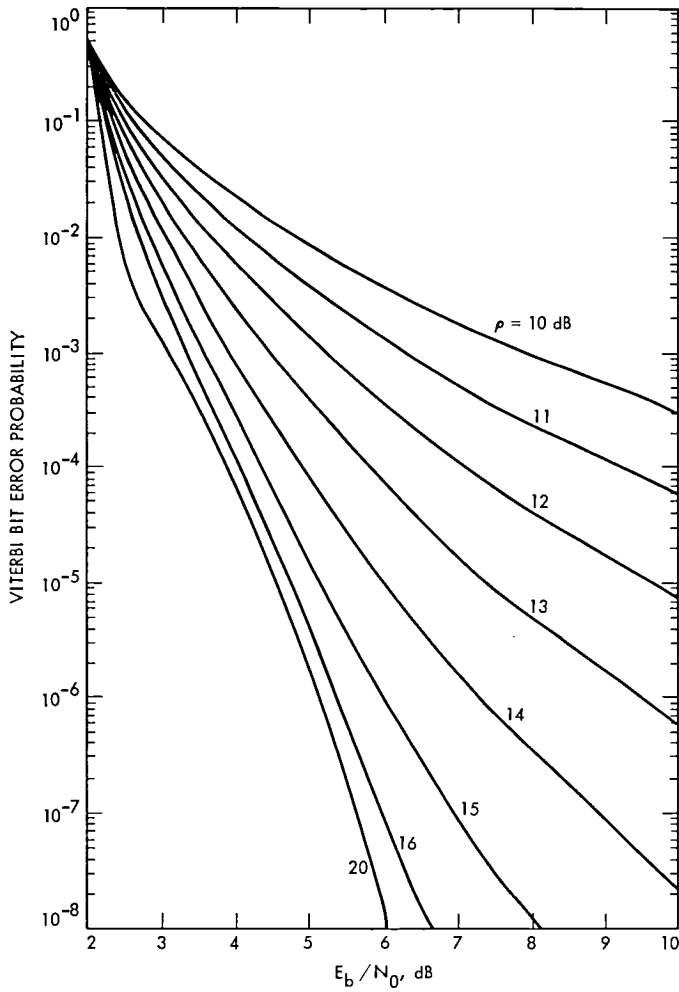


Fig. 5. Viterbi-decoded bit error rate for various carrier tracking loop SNRs, node synchronization threshold = 2.0 dB

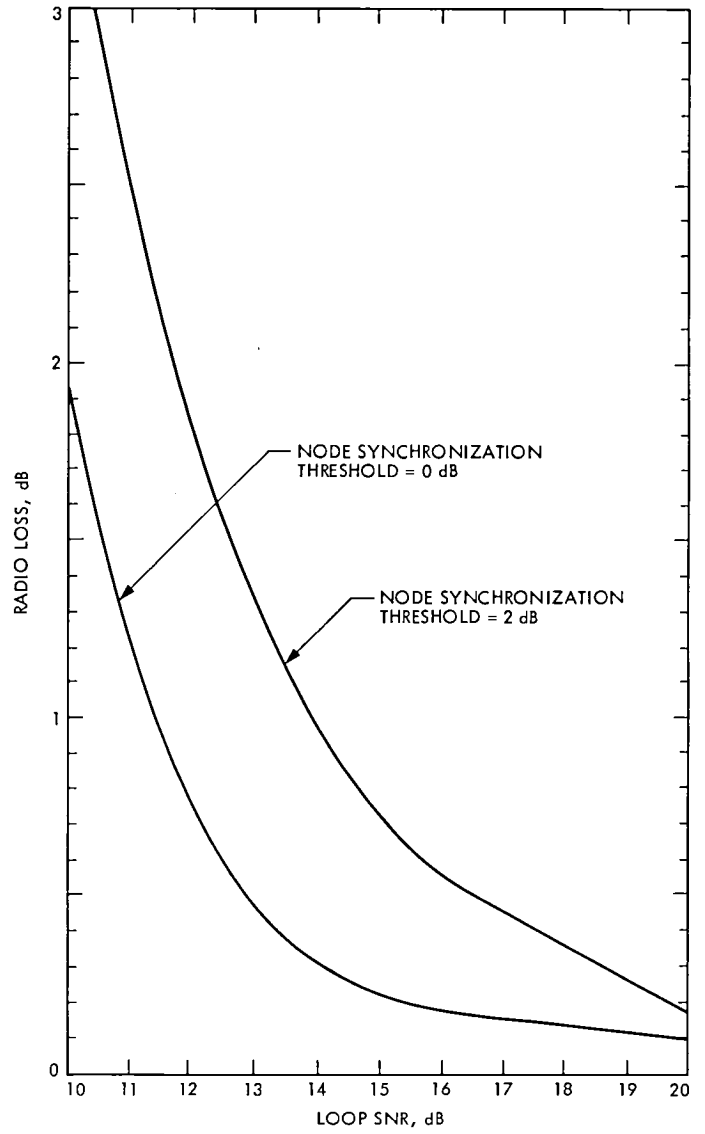
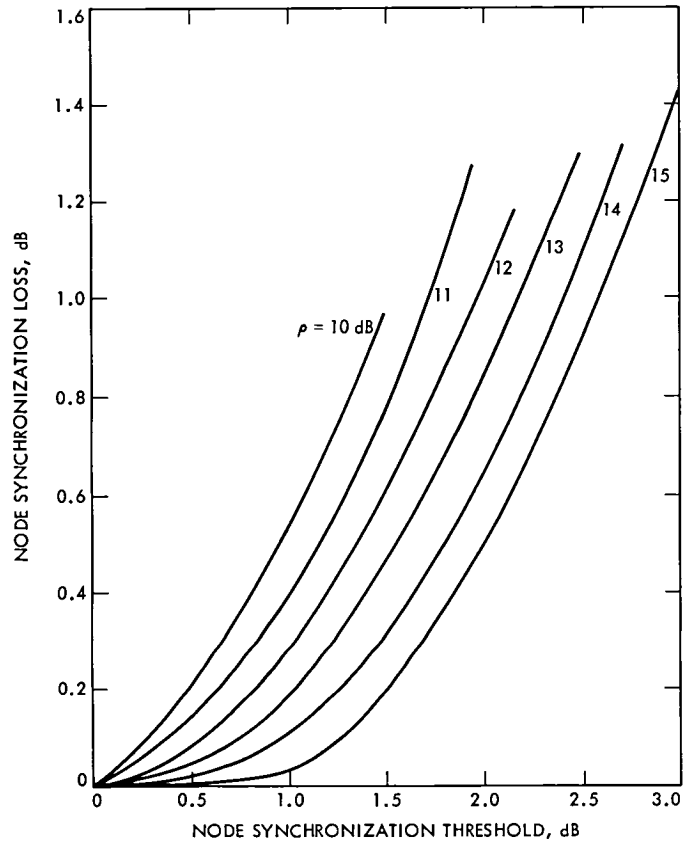


Fig. 6. Radio loss at BER = .005 at node synchronization thresholds of 0.0 dB and 2.0 dB



**Fig. 7. Node synchronization loss for various carrier tracking loop SNRs**

# Electronic Beam Steering of Semiconductor Injection Lasers

J. Katz

Communications Systems Research Section

*A theoretical analysis of the problem of beam steering of semiconductor injection lasers is presented. The required modifications of the dielectric constant profile of the laser structure are derived, and a practical method for implementing the needed modifications is outlined.*

## I. Introduction

Many applications of lasers in general, and semiconductor injection lasers in particular, call for the controlled deflection, or steering, of the radiation pattern emitted by them. That is the case, for example, in pointing and tracking subsystems of optical communication links or optical radars and in systems for optical data recording and retrieval.

In many cases the beam steering is performed by optical-mechanical systems of mirrors, lenses and scanners. Several physical phenomena such as the electrooptic, acoustooptic or piezoelectric effects can also be utilized for building beam deflectors (Ref. 1). In this paper we present a theoretical analysis of yet another important way of achieving this goal by incorporating the steering mechanism within the semiconductor laser itself via the modification of its index of refraction. Such a monolithic configuration has the potential advantages of higher reliability and considerable savings in size and weight of the system. Another method, which is a subject of a separate publication, is by controlling the individual phases of lasers in a phase-locked array configuration, in a similar fashion to microwave phased arrays (Ref. 2).

In a paper published recently (Ref. 3) electronic steering of a semiconductor laser beam via the modification of the dielectric constant has been demonstrated. The radiation pattern was deflected  $\pm 14^\circ$  with respect to the normal of the laser facet. Since the far field radiation pattern was about  $6^\circ$ , this represents deflection of about  $\pm 2$  beamwidths.

The purpose of this paper is twofold: first, to provide a theoretical analysis of the problem, and second, to outline the approach for implementing the beam steering method.

Section II reviews the relation between the far-field radiation pattern of the laser (i.e., the beam to be deflected) and the near-field pattern (i.e., the field distribution at the laser facet), which is basically a Fourier transform relation. Then the wave equations for the modified laser field are derived, establishing the general relation between the unperturbed dielectric constant profile of the laser cavity, the desired amount of beam deflection and the specific modifications of the dielectric constant profile that must be implemented. Section III gives several specific examples of dielectric constant profiles which represent several types of semiconductor

lasers. In all cases it is found that an antisymmetric modification of the imaginary part of the dielectric constant can cause beam deflection. Finally, Section IV outlines a method for achieving the desired modification of the dielectric constant profile, thus serving as a general guideline for this application.

## II. Modification of the Laser Field and Dielectric Constant Needed for Beam Deflection

In this section we establish the relations between the desired beam deflection and the modifications of the laser field that need to be employed for this purpose. The schematic configuration (Fig. 1) shows a top view of a semiconductor injection laser and its emitted radiation pattern. Deflection of the beam by angle  $\theta$  is equivalent to shifting the far-field pattern by this angle.

The relation between the far-field radiation pattern and the near-field radiation pattern (i.e., the field distribution at the laser facet – the  $(xy)$  plane) has been thoroughly investigated (Refs. 4-9). Basically it is found that the far-field pattern is the Fourier transform of the near-field pattern times an obliquity function  $g(\phi)$ :

$$U(\phi) \propto g(\phi) \int_{-\infty}^{\infty} E(y) e^{-ik(\phi)y} dy \quad (1)$$

where  $\phi$  is a general angle in the  $(yz)$  plane (see Fig. 1),  $E$  and  $U$  are the near-and far-field patterns, respectively, and  $k(\phi)$  is given by

$$k(\phi) = \frac{2\pi}{\lambda} \sin \phi \quad (2)$$

The different works cited above give different forms for  $g(\phi)$ . A good approximation, commonly used in the literature (Ref. 10) is  $g(\phi) \sim \cos \phi$ . In the following analysis we will not take this factor into account since the additional attenuation caused by it when the beam is deflected can be compensated, in principle, by increasing the total current through the device.

The equation governing the near-field distribution of the laser near field  $E$  is the Helmholtz equation:

$$\frac{d^2 E}{dy^2} + (\epsilon k^2 - \beta^2) E = 0 \quad (3)$$

where  $\epsilon$  is the dielectric constant profile along the  $y$  direction,

$\beta$  is the propagation constant,  $k = 2\pi/\lambda$  and  $\lambda$  is the wavelength of the radiation in vacuum. The notations needed in this paper and the relations between the dielectric constant, index of refraction and gain and loss coefficients of a particular material are summarized in Appendix A. The reduction of the general three-dimensional formulation of the wave equation in the laser structure to the one-dimensional problem considered here (as implied by Eq. 3) is outlined in Appendix B. In all the following analysis, the superscript 0 indicates the value of the unperturbed parameter, i.e., its value when the laser beam is not deflected, and all unsuperscripted parameters are valued in the deflected case. Also the subscripts  $r$  and  $i$  refer to the real and imaginary parts, respectively, of the parameter.

Using the well-known rules of the Fourier transform we know that in order to obtain a beam deflection by an angle  $\theta$ , i.e.,

$$U[k(\phi)] = U^0 [k(\phi) - k(\theta)] \quad (4)$$

the near-field pattern has to be multiplied by a phase factor, namely,

$$E(y) = E^0(y) e^{ik(\theta)y} \quad (5)$$

It is clear that in order for such an operation to take place, the dielectric constant profile of the laser has to be modified, so that the modified waveguide will support the modified near-field pattern. The magnitude and shape of the modification are derived below:

Using Eq. (5) in Eq. (3), noting that  $E^0$  by definition satisfies the following equation:

$$\frac{d^2 E^0}{dy^2} + [\epsilon^0 k^2 - (\beta^0)^2] E^0 = 0 \quad (6)$$

we obtain

$$\epsilon k^2 - \beta^2 = \frac{[\epsilon^0 k^2 - (\beta^0)^2 + k^2(\theta)] E^0(y) - 2ik(\theta) \frac{dE^0}{dy}}{E^0(y)} \quad (7)$$

Equating the real and imaginary parts of Eq. (7) and using the results of Appendix C which establishes the relations

between the propagation constants of the optical mode in the laser waveguide and the field distribution, we obtain the following basic equations, relating the needed modification of the real and imaginary parts of the dielectric constant to the desired amount of beam deflection:

$$\Delta\epsilon_r + \frac{\int_{-\infty}^{\infty} \Delta\epsilon_r |E^0|^2 dy}{\int_{-\infty}^{\infty} |E^0|^2 dy} = - \frac{2k(\theta)}{k^2} \frac{\frac{dE_r^0}{dy} E_i^0 - E_r^0 \frac{dE_i^0}{dy}}{(E_r^0)^2 + (E_i^0)^2} \quad (8)$$

and

$$\Delta\epsilon_i = \frac{2}{k^2} [\beta_r^0 \Delta\beta_i + \beta_i^0 \Delta\beta_r] - \frac{2k(\theta)}{k^2} \frac{\frac{dE_r^0}{dy} E_r^0 + \frac{dE_i^0}{dy} E_i^0}{(E_r^0)^2 + (E_i^0)^2} \quad (9)$$

where

$$\Delta\epsilon_r = \epsilon_r - \epsilon_r^0 \quad (10a)$$

$$\Delta\epsilon_i = \epsilon_i - \epsilon_i^0 \quad (10b)$$

$$\Delta\beta_r = \beta_r - \beta_r^0 \quad (10c)$$

$$\Delta\beta_i = \beta_i - \beta_i^0 \quad (10d)$$

are the changes of the corresponding parameters from the unmodified case.

As noted in Appendix C, significant simplification of Eqs. (8) and (9) results if the modifications of the dielectric function is an antisymmetric function; i.e.,

$$\Delta\epsilon_r(y) = - \Delta\epsilon_r(-y) \quad (11a)$$

$$\Delta\epsilon_i(y) = - \Delta\epsilon_i(-y) \quad (11b)$$

In this case Eq. (8) is reduced to

$$\Delta\epsilon_r = - \frac{2k(\theta)}{k^2} \frac{\frac{dE_r^0}{dy} E_i^0 - E_r^0 \frac{dE_i^0}{dy}}{(E_r^0)^2 + (E_i^0)^2} \quad (12)$$

while Eq. (9) is reduced to

$$\Delta\epsilon_i = - \frac{2k(\theta)}{k^2} \frac{\frac{dE_r^0}{dy} E_r^0 + \frac{dE_i^0}{dy} E_i^0}{(E_r^0)^2 + (E_i^0)^2} \quad (13)$$

Equations (12) and (13) give explicit expressions for  $\Delta\epsilon_r$  and  $\Delta\epsilon_i$ , respectively, while Eqs. (8) and (9) are integral equations for these quantities.

In the following section we will apply Eqs. (12) and (13) to several specific examples of semiconductor laser waveguides.

### III. Specific Examples of Dielectric Constant Modification

In this section we present three examples of beam-steering in one-dimensional waveguide structures. In the first example the unperturbed waveguide has a pure real index guiding; in the second case, a pure imaginary index guiding, and in the last example, a general complex index guiding. It is found that in all cases the beam deflection can be achieved by establishing an antisymmetric modification of the imaginary part of the dielectric constant profile along the laser junction plane (i.e.,  $y$  direction in Fig. 1).

#### A. Pure Real Index Guiding — the “Sech<sup>2</sup>” Profile

We consider the following dielectric constant profile, shown in Fig 2a:

$$\epsilon^0(y) = \tilde{\epsilon} \left[ 1 + \delta \cdot \left( \operatorname{sech}^2 \sqrt{\frac{\delta \cdot \tilde{\epsilon}}{2}} ky \right) \right] \quad (14)$$

where  $\tilde{\epsilon}$  is the dielectric constant at  $y \rightarrow \pm\infty$  and  $\delta$  is a constant. Although this profile represents only a first-order approximation to real life devices, it is analyzed here since the simple analytic solution that one obtains in this case serves to illuminate the basic underlying requirements of beam steering.

Defining the dimensionless coordinate

$$\zeta \equiv \sqrt{\frac{\delta \cdot \tilde{\epsilon}}{2}} ky \quad (15)$$

the wave equation (6) is reduced to

$$\frac{d^2 E^0}{d\zeta^2} + 2 \operatorname{sech}^2(\zeta) E^0(\zeta) = \frac{2}{\delta \cdot \tilde{\epsilon}} \left[ \frac{(\beta^0)^2}{k^2} - \tilde{\epsilon} \right] E^0(\zeta) \quad (16)$$

which is known to have a solution of the form

$$E^0(y) = \text{sech}(\xi) = \text{sech}\left(\sqrt{\frac{\delta\tilde{\epsilon}}{2}}ky\right) \quad (17)$$

with the propagation constant  $\beta^0$  given by

$$(\beta^0)^2 = k^2 \tilde{\epsilon} \left(1 + \frac{\delta}{2}\right) \quad (18)$$

Using Eqs. (17) and (18) in Eqs. (12) and (13) we obtain

$$\Delta\epsilon_r = 0 \quad (19)$$

$$\Delta\epsilon_i(y) = \sqrt{2\delta\tilde{\epsilon}} \frac{k(\theta)}{k} \tanh\left(\sqrt{\frac{\delta\tilde{\epsilon}}{2}}ky\right) \quad (20)$$

or, using the definition of Eq. (2):

$$\Delta\epsilon_i(y) = \sqrt{2\delta\tilde{\epsilon}} (\sin\theta) \tanh\left(\sqrt{\frac{\delta\tilde{\epsilon}}{2}}ky\right) \quad (21)$$

The profile of  $\Delta\epsilon_i$  (Eq. 21) is shown in Fig. 2b. It is an antisymmetric function, as expected. In this case there is no change in the real part of the dielectric constant profile.

## B. Pure Imaginary Index Guiding — the Quadratic Profile

We consider the following dielectric constant profile:

$$\epsilon^0(y) = \begin{cases} \epsilon(0) - a^2 y^2 & |y| < \frac{S}{2} \\ \epsilon(0) - a^2 \left(\frac{S}{2}\right)^2 & |y| > \frac{S}{2} \end{cases} \quad (22)$$

This example describes with a reasonable accuracy the guiding mechanism of a contact-stripe laser with “medium” stripe widths  $S$  (Ref. 10, Ch. 7.10). In the following we will neglect the effects of the field distribution tails at  $|y| > S/2$ , which is a good approximation for not too narrow stripe widths.

The complex parameter  $a$  is given by Ref. 10, Ch. 7.10

$$a = a_r + ia_i = (1+i) \sqrt{\frac{\lambda \sqrt{\epsilon_r^0} g_m}{\pi S^2}} \quad (23)$$

where  $g_m$  is the gain in the center of the laser stripe. The parameters in Eq. (23) are depicted in Figs. 3a and 3b.

The fundamental mode of the electric field in this waveguide is given by

$$E^0(y) = e^{-K^2 y^2 (1+i)} \quad |y| > \frac{S}{2} \quad (24)$$

where  $K$  is defined by

$$K^4 \equiv \frac{k \sqrt{\epsilon_r^0} g_m}{2S^2} \quad (25)$$

Using the results of Appendix C, we find the real and imaginary parts of the wave propagation constant:

$$(\beta_r^0)^2 = k^2 \epsilon_r^0 - \frac{K^2}{2} \quad (26)$$

$$\beta_i^0 = \frac{k \sqrt{\epsilon_r^0} g_m - K^2}{2\beta_r^0} \quad (27)$$

It is interesting to note from Eq. (26) that because of the gain guiding, a wave can propagate although its velocity is higher than the velocity of light in the material, a phenomenon that is impossible in real index waveguides.

Using Eqs. (2), (24)-(27) in Eqs. (12), (13) we obtain the needed modification in the dielectric profile:

$$\Delta\epsilon_r = -4 \left(\frac{K^2}{k}\right) \cdot (\sin\theta) \cdot y \quad |y| < \frac{S}{2} \quad (28)$$

and

$$\Delta\epsilon_i = -\Delta\epsilon_r = 4 \left(\frac{K^2}{k}\right) \cdot (\sin\theta) \cdot y \quad |y| < \frac{S}{2} \quad (29)$$

We note again that antisymmetrical modifications of the index of refraction are needed. Another interesting feature is that in this case the modification in the real part of the dielectric constant has the same magnitude and the opposite sign as the modification of the imaginary part of the dielectric constant.

## C. Complex Index Guiding — Slab Waveguide Profile

This example can be used to describe the behavior of many generic types of lasers such as the Buried-Heterostructure laser (Ref. 11), the Channelled-Substrate-Planar laser (Ref. 12), and

the Deep Diffusion Stripe laser (Ref. 13). The dielectric constant profile in such structures, as shown in Fig. 4, is given by

$$\epsilon_r = \begin{cases} \epsilon_{r2} & |y| < \frac{S}{2} \\ \epsilon_{r1} & |y| > \frac{S}{2} \end{cases} \quad (30a)$$

$$\epsilon_i = \begin{cases} \epsilon_{i2} & |y| < \frac{S}{2} \\ \epsilon_{i1} & |y| > \frac{S}{2} \end{cases} \quad (30c)$$

where  $\epsilon_{r1}$ ,  $\epsilon_{r2}$ ,  $\epsilon_{i1}$  and  $\epsilon_{i2}$  are constants. Typical stripe widths in lasers of these types are usually – although not always – narrower than in gain-guided lasers described in the previous example (2-5  $\mu\text{m}$  vs 5-15  $\mu\text{m}$ ).

In this case the field solutions are given by

$$E^0(y) = \begin{cases} \cos h^0 y & (31a) \\ \cos\left(h^0 \frac{S}{2}\right) e^{q^0 S/2} e^{-q^0 |y|} & (31b) \end{cases}$$

where  $h$  and  $q$  are, in general, complex numbers, and their values are determined by the eigenvalue equation (Ref. 1, Ch. 19):

$$\left(h^0 \frac{S}{2}\right) \tan\left(h^0 \frac{S}{2}\right) = \left(q^0 \frac{S}{2}\right) \quad (32)$$

Following the calculations outlined in Appendix C, the propagation constant is given by

$$(\beta_r^0)^2 = \epsilon_{r2} k^2 - (h_r^0)^2 = \epsilon_{r1} k^2 + (q_r^0)^2 \quad (33)$$

$$\beta_i^0 = \frac{k^2}{2\beta_r^0} [\epsilon_{i1} + (\epsilon_{i2} - \epsilon_{i1}) \Gamma_y] \quad (34)$$

where  $\Gamma_y$  is the fraction of the mode energy contained under the stripe width  $S$ .

Using Eqs. (33), (34) in Eqs. (12), (13) we obtain

$$\Delta\epsilon_r = \begin{cases} -\frac{2k(\theta)h_i^0}{k^2 \cos^2(h_r^0 y)} \left[ (h_r^0 y) + \frac{1}{2} \sin(2h_r^0 y) \right] & |y| < \frac{S}{2} \\ \pm \frac{2q_i^0 k(\theta)}{k^2} & |y| > \frac{S}{2} \end{cases} \quad (35a, 35b)$$

and

$$\Delta\epsilon_i = \begin{cases} \frac{2k(\theta)h_r^0}{k^2} \tan(h_r^0 y) & |y| < \frac{S}{2} \\ \mp \frac{2q_r^0 k(\theta)}{k^2} & |y| > \frac{S}{2} \end{cases} \quad (36a, 36b)$$

Note that in this case the modification of the real part of the dielectric constant is much smaller than the modification of the imaginary part of the dielectric constant, since  $|h_i^0| \ll h_r^0$  and  $|q_i^0| \ll q_r^0$ .

#### IV. Implementation of Beam Steering via Asymmetric Current Injection Across the Laser Stripe

In the last sections it has been shown that antisymmetric modifications of the dielectric constant have to be established across the laser structure if its beam is to be deflected. The major contribution to the beam deflection comes from modifying the imaginary part of the dielectric constant, since it is a well-known fact that Fourier transform of real functions are always symmetric, regardless of the nature of the (real) function. As shown in Appendix A (Eq. A-6), the imaginary part of the dielectric constant  $\epsilon_i$  is related to the gain in the laser medium  $g$ :

$$g = \frac{2\pi}{\lambda} \frac{\epsilon_i}{\sqrt{\epsilon_r}} = k \frac{\epsilon_i}{\sqrt{\epsilon_r}} \quad (37)$$

In addition, it is known that the gain in the laser medium is related to the carrier density  $N$  in its active layer. A commonly used formula is (Ref. 14)

$$g(N) = \frac{A}{\beta_r^0} (N - N_{om}) \quad (38)$$

where  $A$  is a proportionality constant and  $N_{om}$  is the carrier density needed for transparency (i.e.,  $g = 0$ ). For GaAs at

room temperature  $A \cong 1.6 \cdot 10^{-6} \text{ cm}^3\text{-sec}^{-1}$  and  $N_{om} \cong 7.5 \cdot 10^{17} \text{ cm}^{-3}$ .

Equations (37), (38) suggest a possible method for modifying the dielectric constant via modifying the distribution of the carrier density across the laser structure. This can be done by splitting the stripe contact of the laser to several parallel stripes, and passing different amounts of current through each stripe, as shown schematically in Fig. 5. Although the exact formulas are quite lengthy (Ref. 10, Ch. 7.7), the carrier density profile in the active region due to current injection in a stripe contact is basically a bell-shaped function whose width and height are roughly proportional to the stripe width and to the current density through the stripe, respectively.

An example of carrier distribution is shown in Fig. 6, where the total current of 250 mA is divided between two stripe contacts whose width is  $2 \mu\text{m}$  and whose center-to-center separation is  $8 \mu\text{m}$  (the diffusion length is taken to be  $3.6 \mu\text{m}$ ). The currents ratio in the two stripes is  $\gamma:(1 - \gamma)$ . For  $\gamma = 0.5$ , the distribution is symmetric and no beam deflection is expected. However, for  $\gamma < 1/2$ , an antisymmetric component whose shape is shown in Fig. 7 is established across the structure, resulting in a beam deflection. If we approximate the laser structure by the quadratic gain medium (example 2 of previous section), and assume that we want to deflect the beam by  $0.1 \text{ rad}$  ( $5.7^\circ$ ), and that  $g_m = 100 \text{ cm}^{-1}$ ,  $\sqrt{\epsilon_r} = 3.6$  and  $\lambda = 0.9 \mu\text{m}$ , then we need a gain difference between the two edges of the stripe of (see Eqs. 25, 29 and 37)

$$\begin{aligned} \Delta g &= g\left(y = \frac{S}{2}\right) - g\left(y = -\frac{S}{2}\right) \\ &= \sqrt{\frac{k \cdot g_m}{\sqrt{\epsilon_r}}} \sin \theta \cong 140 \text{ cm}^{-1} \end{aligned} \quad (39)$$

From Eq. (38) we see that the requirement of Eq. (39) corresponds to establishing a carrier density difference of about  $\Delta N = 8 \cdot 10^{17} \text{ cm}^{-3}$ . Using the results of Figs. 6 and 7 we see that a current splitting ratio of approximately 3:7 is needed (see Appendix D for a detailed derivation). From Eq. (28) we see that a change in the real part of the dielectric constant has also to be established. This change may be automatically effected through the plasma effect, where, for GaAs we have (Ref. 10, Ch 2):

$$\delta\epsilon_r \cong -1.1 \cdot 10^{-20} \Delta N \quad (40)$$

It is seen that  $\Delta N = 8 \cdot 10^{17}$  translates to  $\delta\epsilon_r \approx 9 \cdot 10^{-3}$ , which reasonably compares with the needed value of  $\delta\epsilon_r \cong 2 \cdot 10^{-2}$ .

In other structures, such as the slab waveguide (example 3 in the previous section), the requirements for beam deflection are even less stringent in terms of the gain and carrier gradients that need to be established across the laser structure, and thus larger beam deflection angles are feasible.

As a final note it should be emphasized that it is virtually impossible to achieve the exact modification, as required by equations such as (28), (29), (35), (36), since we do not have a direct local access and control to the active region. Furthermore, the above equations were derived using simplified laser models and thus are also not exact. However, the experimental results reported in Ref. 3, where beam deflection was obtained using only a double-stripe contact, indicate that practical structures which adequately approximate the exact theoretical requirements are feasible. Since the results of Ref. 3 also show that the amount of beam deflection depends on both the current ratio and magnitude, a more refined model of the laser operation above threshold (see, for example, Ref. 15) must also be incorporated into the analysis.

## V. Conclusions

Electronic beam steering of semiconductor lasers is very useful in many applications, and thus it is important to understand the underlying relationships between the physical parameters of the device and the amount of deflection of its radiation pattern.

In this report the problem of beam deflection of semiconductor injection lasers has been theoretically investigated. It was found that beam deflection can be achieved by tailoring the profile of the current injected into the laser active region via the modifications in the dielectric constant that accompany such current distribution changes. The magnitude of the modifications possible are sufficient for beam deflections of several degrees and in certain laser structures even more. Among the systems that could greatly benefit – in terms of size and weight reduction – from the application of electronic beam steering are pointing and tracking subsystems of optical communication links, optical radars, and optical data recording/retrieval systems.

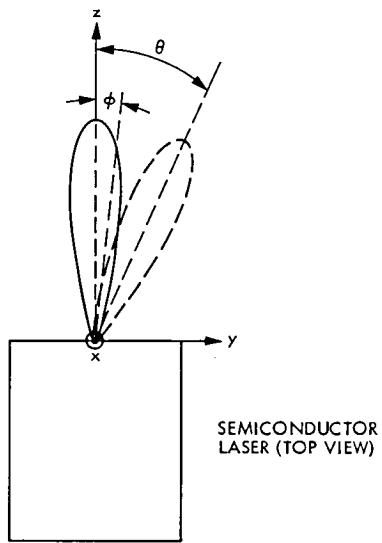


Fig. 1. Schematic configuration of semiconductor laser beam steering

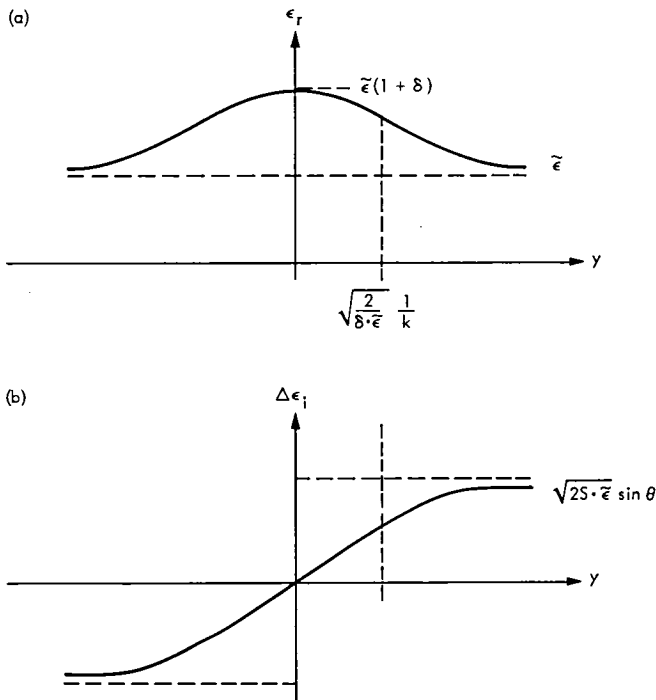


Fig. 2. (a) A  $\text{sech}^2$ -law dielectric constant distribution; (b) modification of the dielectric constant needed for a beam deflection of an angle  $\theta$

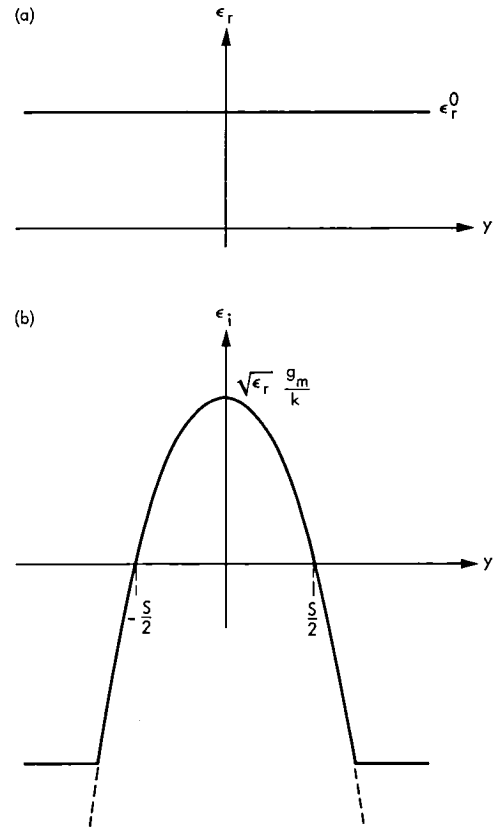


Fig. 3. Dielectric constant distribution in a quadratic index pure gain guiding medium: (a) real part, (b) imaginary part

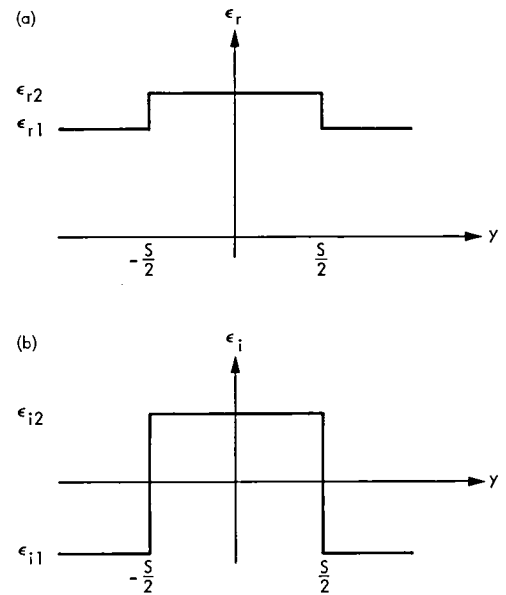


Fig. 4. Dielectric constant distribution in a one-dimensional three-layer slab waveguide: (a) real part, (b) imaginary part

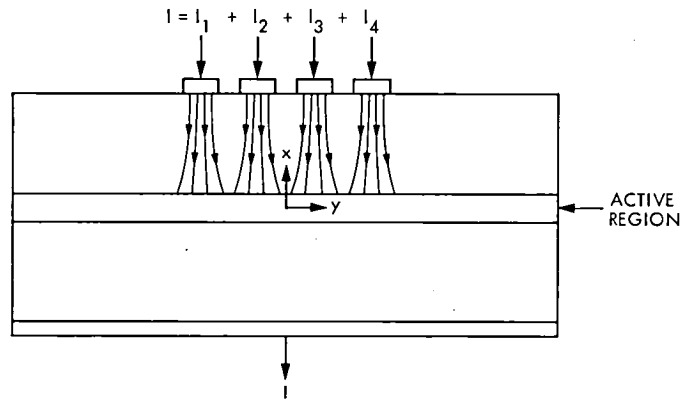


Fig. 5. Schematic configuration of multiple stripe laser structure which makes carrier density profiling possible

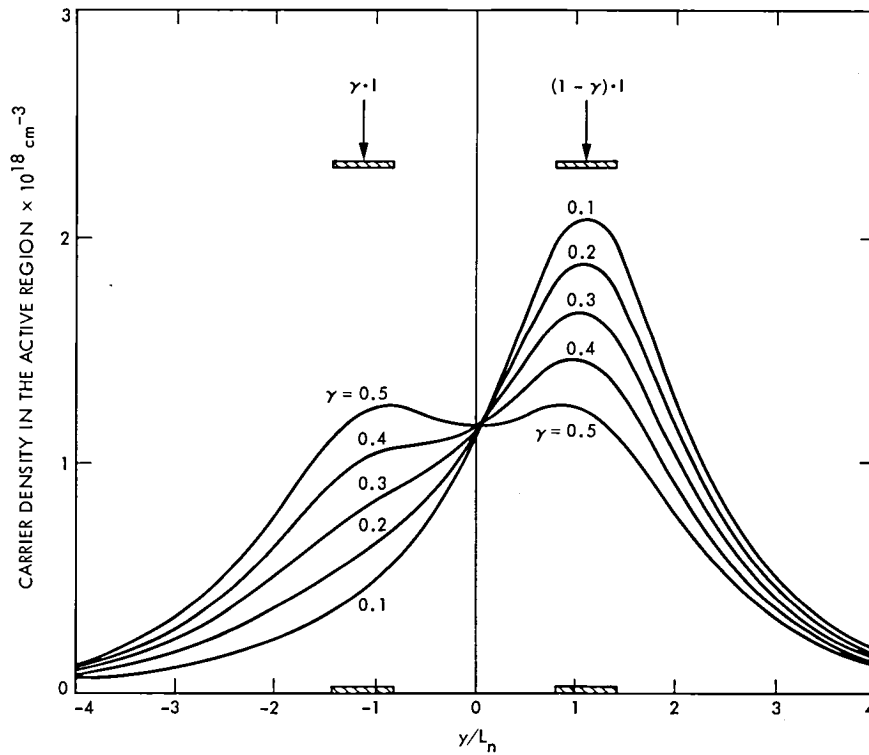
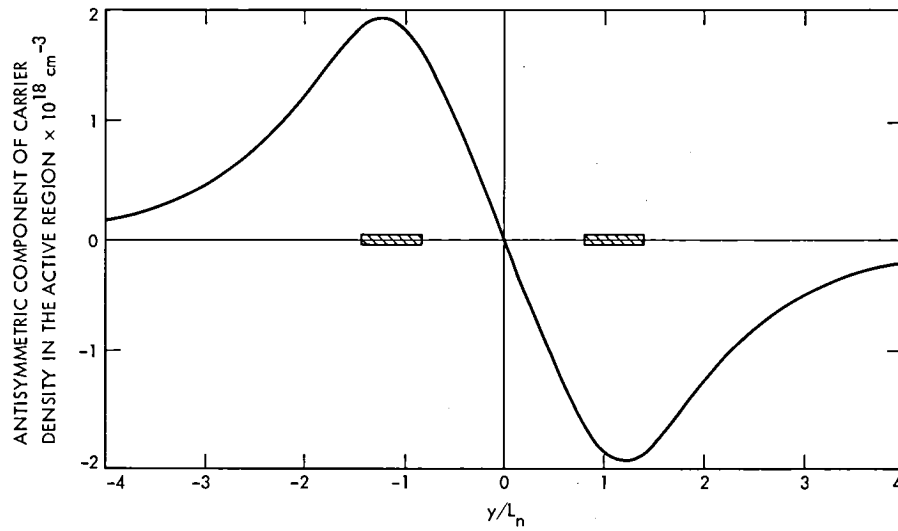


Fig. 6. Distribution of the carrier density in the GaAs active region due to current injection in a double-stripe structure; the currents ratio is  $\gamma:(1-\gamma)$



**Fig. 7. Distribution of the antisymmetric component of the carrier density in the case of maximum asymmetry (i.e.,  $\gamma \rightarrow 0$ )**

## Appendix A

In this appendix we establish the notations used in the text for describing the dielectric properties of the material. A material is characterized by a dielectric constant  $\epsilon$ , whose relation to the index of refraction  $n$  of the material is given by

$$\epsilon = n^2 \quad (\text{A-1})$$

Since both  $\epsilon$  and  $n$  are generally complex quantities, Eq. (A-1) can be rewritten as

$$\epsilon_r + i\epsilon_i = (n_r + in_i)^2 \quad (\text{A-2})$$

where the subscripts  $r$  and  $i$  refer to the real and imaginary parts, respectively, of each quantity. Since in virtually all the relevant applications involving dielectric waveguides the condition  $|\epsilon_i| \ll \epsilon_r$  (and hence also  $|n_i| \ll n_r$ ) is met, we can use the following approximate relations between the real and imaginary part of  $\epsilon$  and  $n$ :

$$n_r \cong \sqrt{\epsilon_r} \quad (\text{A-3a})$$

$$n_i \cong \frac{\epsilon_i}{2\sqrt{\epsilon_r}} \quad (\text{A-3b})$$

and

$$\epsilon_r \cong n_r^2 \quad (\text{A-4a})$$

$$\epsilon_i \cong 2n_r n_i \quad (\text{A-4b})$$

The meaning of the imaginary part of the index of refraction is readily understood when the propagation of a plane wave through a medium with an index of refraction  $n$  along the  $Z$  direction is considered)

$$E = e^{j(\omega t - knZ)} = e^{kn_i Z} e^{i(\omega t - kn_r Z)} \quad (\text{A-5})$$

where  $k \equiv \omega/c$ . We see that  $n_r$  determines the phase velocity of the wave, and  $n_i$  determines if the medium is lossy ( $n_i < 0$ ) or with gain ( $n_i > 0$ ).

The magnitude of the power gain (or loss) coefficients, expressed in units of ( $\text{length}^{-1}$ ), is given by

$$g = 2 \cdot kn_i = \frac{4\pi}{\lambda} n_i = \frac{2\pi}{\lambda} \frac{\epsilon_i}{\sqrt{\epsilon_r}} \quad (\text{A-6})$$

## Appendix B

In this appendix we briefly outline the derivation of the wave equation (3) used in this paper. This outline also serves as a good demonstration on how real life three-dimensional problems, which usually do not have analytic solutions, can be reduced to tractable one-dimensional problems. Here we follow the treatment of Ref. 10, Ch. 7.10.

The laser structure cross-section is depicted in Fig. B-1. Its active region has a width  $d$  and a dielectric constant  $\epsilon(y)$ . It is sandwiched between two low index of refraction cladding layers whose dielectric constant is assumed to be fixed at  $\epsilon_{clad}$ . The laser cavity is along the  $z$  axis. Since we are interested in variations along the  $y$  direction, we want to factor out the  $x$  and  $z$  dependence in the problem. In the following we explain how this is done.

We start with the general three-dimensional wave equation. Since semiconductor lasers are known to emit light predominantly in the TE modes, only the equation for  $\mathcal{E}_y$  is considered:

$$\nabla^2 \mathcal{E}_y = \frac{\epsilon}{c^2} \frac{\partial^2 \mathcal{E}_y}{\partial t^2} \quad (\text{B-1})$$

where  $\epsilon$  is the dielectric constant of the medium and  $c$  is the light velocity in vacuum.

Next we assume solutions with harmonic time dependence that are propagating along the laser cavity  $z$  with a propagation constant  $\beta$ :

$$\mathcal{E}_y(x, y, z, t) = \tilde{\mathcal{E}}_y(x, y) e^{i(\omega t - \beta z)} \quad (\text{B-2})$$

Using Eq. (B-2) in Eq. (B-1), with the definition

$$k \equiv \frac{\omega}{c}$$

we obtain the following equation, which does not contain any  $z$  dependence:

$$\nabla_t^2 \tilde{\mathcal{E}}_y(x, y) + (\epsilon k^2 - \beta^2) \tilde{\mathcal{E}}_y(x, y) = 0 \quad (\text{B-3})$$

where

$$\nabla_t^2 \equiv \frac{\partial^2}{\partial x^2} + \frac{\partial^2}{\partial y^2} .$$

In order to factor out the  $x$  dependence, we can, to a first approximation, assume field solutions of the form:

$$\tilde{\mathcal{E}}_y(x, y) = E_y^x(x) E_y^y(y) \quad (\text{B-4})$$

This approximation is good for modes that are not too close to cutoff (i.e., modes that are "reasonably" well guided). Furthermore, since the variation of  $\epsilon$  along the  $x$  direction occurs over distances much shorter than along the  $y$  direction (typically fractions of a micron vs several microns), we can neglect the small  $y$  dependence of  $E_y^x$  [as implied in Eq. (B-4)], and use separation of variables and write the following equation for  $E_y^x(x)$ :

$$\frac{\partial^2 E_y^x(x)}{\partial x^2} + \beta_x^2 E_y^x(x) = 0 \quad (\text{B-5})$$

where  $\beta_x^2$  is a separation constant. Using Eqs. (B-4), (B-5) in (B-3), multiplying the resulting equation by  $[E_y^x(x)]^*$  (where  $*$  denotes complex conjugation) and integrating over  $x$ , results in the following equation:

$$\frac{d^2 E_y^y(y)}{dy^2} + [k^2 \Gamma_x \epsilon(y) + (1 - \Gamma_x) \epsilon_{clad} - \beta_z^2 - \beta_x^2] E_y^y(y) = 0 \quad (\text{B-6})$$

where  $\Gamma$  is the fraction of the field intensity confined to the active region, i.e.,

$$\Gamma_x \equiv \frac{\int_{-d/2}^{d/2} |E_y^x(x)|^2 dx}{\int_{-\infty}^{\infty} |E_y^x(x)|^2 dx} \quad (\text{B-7})$$

Equation (B-6) is the desired one-dimensional wave equation. The following few notational changes are employed in order to bring it to the form used in the text (Eq. 3). First, we drop the subscript and the superscript from the field notation since it is clear to which component we are referring. Second, we scale the actual dielectric constant of the active region and

use the effective quantity:  $\epsilon(y)$  in the text refer to  $\epsilon_{eff}$  of this appendix, where

$$\epsilon_{eff} \equiv \Gamma_x \epsilon(y) + (1 - \Gamma_x) \epsilon_{clad} \quad (\text{B-8})$$

and last, the propagation constant  $\beta$  in the text is given by

$$\beta^2 = \beta_z^2 + \beta_x^2 \quad (\text{B-9})$$

It is worthwhile noting that as the mode becomes more confined to the active region (either by increasing  $d$  or by increasing the difference between  $\epsilon(y)$  and  $\epsilon_{clad}$ ),  $\Gamma$  approaches unity, and then  $\epsilon_{eff} \rightarrow \epsilon(y)$  and  $\beta \rightarrow \beta_z$ .

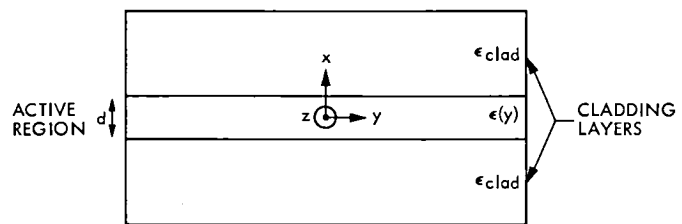


**Fig. B-1. Schematic cross section of a semiconductor injection laser**

## Appendix C

In this appendix we derive the relations between the propagation constants and the field distributions. These relations are required for evaluating some of the effects of the modification of the dielectric constant  $\epsilon_x$  that are needed for beam steering.

We start with the wave equation for the unperturbed field  $E^0$  (Eq. 6):

$$\frac{d^2 E^0}{dy^2} + [\epsilon^0 k^2 - (\beta^0)^2] E^0 = 0 \quad (\text{C-1})$$

where the superscript 0 denotes the unperturbed quantities. Multiplying Eq. (C-1) by  $(E^0)^*$ , integrating over  $y$  and assuming along the reasoning of Appendix A that

$$(\beta^0)^2 \equiv (\beta_r^0 + i\beta_i^0)^2 \cong (\beta_r^0)^2 + 2i\beta_r^0\beta_i^0 \quad (\text{C-2})$$

we obtain

$$(\beta_r^0)^2 = \frac{k^2 \int_{-\infty}^{\infty} \epsilon_r^0 |E^0|^2 dy - \int_{-\infty}^{\infty} \left| \frac{dE^0}{dy} \right|^2 dy}{\int_{-\infty}^{\infty} |E^0|^2 dy} \quad (\text{C-3})$$

and

$$\beta_i^0 = \frac{k^2 \int_{-\infty}^{\infty} \epsilon_i^0 |E^0|^2 dy}{2\beta_r^0 \int_{-\infty}^{\infty} |E^0|^2 dy} \quad (\text{C-4})$$

where  $\epsilon^0 = \epsilon_r^0 + i\epsilon_i^0$  is the unperturbed dielectric constant of the medium.

The modified (perturbed) field is given by [Eq. (5)]

$$E = E^0 e^{ik(\theta)y} \quad (\text{C-5})$$

From Eq. (C-5) we see that

$$|E|^2 = |E^0|^2 \quad (\text{C-6})$$

(i.e., the magnitude of the field is not changed), and that

$$\left| \frac{dE}{dy} \right|^2 = k^2(\theta) |E^0|^2 + \left| \frac{dE^0}{dy} \right|^2 \quad (\text{C-7})$$

From Eqs. (C-3), (C-4) we can write equivalent equations for  $\beta_r$  and  $\beta_i$ ,

$$\beta_r^2 = \frac{k^2 \int_{-\infty}^{\infty} \epsilon_r |E|^2 dy - \int_{-\infty}^{\infty} \left| \frac{dE}{dy} \right|^2 dy}{\int_{-\infty}^{\infty} |E|^2 dy} \quad (\text{C-8})$$

$$\beta_i = \frac{k^2 \int_{-\infty}^{\infty} \epsilon_i |E|^2 dy}{2\beta_r \int_{-\infty}^{\infty} |E|^2 dy} \quad (\text{C-9})$$

Using Eqs. (C-3), (C-4), (C-6) and (C-7) in Eqs. (C-8), (C-9), we obtain:

$$\beta_r^2 = (\beta_r^0)^2 - k^2(\theta) + k^2 \frac{\int_{-\infty}^{\infty} \Delta\epsilon_r |E^0|^2 dy}{\int_{-\infty}^{\infty} |E^0|^2 dy} \quad (\text{C-10})$$

and

$$\beta_i = \left( 1 - \frac{\Delta\beta_r}{\beta_r^0} \right) \left[ \beta_i^0 + \frac{\int_{-\infty}^{\infty} \Delta\epsilon_i |E^0|^2 dy}{\int_{-\infty}^{\infty} |E^0|^2 dy} \right] \quad (\text{C-11})$$

where

$$\Delta\epsilon = \epsilon - \epsilon^0 = (\epsilon_r - \epsilon_r^0) + i(\epsilon_i - \epsilon_i^0) \equiv \Delta\epsilon_r + i\Delta\epsilon_i \quad (\text{C-12})$$

is the perturbation on the dielectric constant, and  $\Delta\beta_r$  can be calculated from Eq. (C-10) using the approximation  $\beta_r^2 - (\beta_r^0)^2 \cong 2\beta_r^0 \Delta\beta_r$ :

$$\Delta\beta_r \equiv \beta_r - \beta_r^0 \cong \frac{1}{2\beta_r^0} \left[ k^2 \frac{\int_{-\infty}^{\infty} \Delta\epsilon_r |E^0|^2 dy}{\int_{-\infty}^{\infty} |E^0|^2 dy} - k^2(\theta) \right] \quad (\text{C-13})$$

A special case is when the real and/or the imaginary parts of the perturbation on the dielectric constant are antisymmetric functions.

First, if

$$\Delta\epsilon_r(y) = -\Delta\epsilon_r(-y) \quad (\text{C-14})$$

then, from Eq. (C-13) we see that

$$\Delta\beta_r \cong -\frac{k^2(\theta)}{2\beta_r^0} \quad (\text{C-15})$$

If furthermore we also have

$$\Delta\epsilon_i(y) = -\Delta\epsilon_i(-y), \quad (\text{C-16})$$

then from Eq. (C-11) we see that

$$\Delta\beta_i = \beta_i^0 \frac{k^2\theta}{2(\beta_r^0)^2} \quad (\text{C-17})$$

## Appendix D

In this appendix we derive the current ratio needed to establish a given antisymmetric carrier density. Let us denote by  $F(\xi)$  the carrier profile resulting from current injection through a single stripe centered at  $\xi = 0$ . From Ref. 10 Ch. 7.7 we can see that

$$F(\xi) = F(-\xi) \quad (\text{D-1})$$

As a first approximation we assume that the problem is linear (for a detailed analysis, refer to Ref. 10, Ch. 7.7) and thus we have two stripes whose centers are separated a distance of  $2a$  apart and the currents ratio through the stripes is  $\gamma:(1 - \gamma)$ , then the resulting carrier profile is

$$f(y) = \gamma F(y - a) + (1 - \gamma) F(y + a) \quad (\text{D-2})$$

Decomposing  $f(y)$  into its symmetric and antisymmetric components, making use of Eq. (D-1), we obtain

$$f(y) = f_{sym}(y) + f_{anti\ sym.}(y) \quad (\text{D-3})$$

where

$$f_{sym} = \frac{1}{2} [F(y + a) + F(y - a)] \quad (\text{D-4})$$

$$f_{anti\ sym.} = \left(\frac{1}{2} - \gamma\right) [F(y + a) - F(y - a)] \quad (\text{D-5})$$

From Fig. 7 we see that

$$\max |F(y + a) - F(y - a)| \cong 4 \cdot 10^{18} \text{ cm}^{-3} \quad (\text{D-6})$$

and from the discussion following Eq. (39) we see that we need  $\Delta N \cong 8 \cdot 10^{17} \text{ cm}^{-3}$ . Solving

$$8 \cdot 10^{17} \cong \left(\frac{1}{2} - \gamma\right) 4 \cdot 10^{18}$$

we obtain  $\gamma \cong 0.3$ .

## References

1. See, for example, A. Yariv, *Quantum Electronics*, 2nd Edition, Wiley, N.Y., 1975.
2. Katz, J., "Phase Control and Beam Steering of Semiconductor Laser Arrays", *TDA Progress Report 42-68*, Jet Propulsion Laboratory, Pasadena, Calif. (this issue).
3. Scifres, D. R., Streifer, W., and Burnham, R. D., "Beam Scanning with Twin-Stripe Injection Lasers," *Appl. Phys. Lett.*, **33**, pp. 702-704, 1978.
4. Hockham, G. A., "Radiation from a Solid-State Laser," *Electron. Lett.*, **9**, pp. 389-391, 1973.
5. Lewin, L., "Obliquity Factor for Radiation from Solid State Laser," *Electron. Lett.*, **10**, pp. 134-135, 1974.
6. Butler, J. K., and Zoroofchi, J., "Radiation Fields of GaAs-(AlGa)As Injection Lasers," *IEEE J. Quant. Electron.*, *QE-10*, pp. 809-815, 1974.
7. Lewin, L., "Obliquity-Factor Correction to Solid-State Radiation Patterns," *J. Appl. Phys.*, **46**, pp. 2323-2324, 1975.
8. Lewin, L., "A Method for Calculation of the Radiation Pattern and Mode Conversion Properties of a Solid State Heterojunction Laser," *IEEE Trans. Microwave Theory Tech.*, *MTT-23*, pp. 516-535, 1975.
9. Dias, P., Portnoi, E. L., Raikh, M. E., and Ryvkin, B. S., "Far-Field Radiation of a Heteroepitaxial Waveguide with Smooth Refractive Index Profile," *Sov. Tech. Phy. Lett.*, **2**, pp. 424-425, 1976.
10. Casey, H. C., Jr., and Panish, M. B., *Heterostructure Lasers*, Academic Press, N.Y., 1978, Ch. 2.7.
11. Tsukada, T., "GaAs -  $\text{Ga}_{1-x}\text{Al}_x\text{As}$  Buried Heterostructure Injection Lasers," *J. Appl. Phys.* **45**, pp. 4899-4906, 1974.
12. Aiki, K., Nakamura, M., Kuroda, T., Umeda, J., Ito, R., Chinone, N., and Maeda, M., "Transverse Mode Stabilized  $\text{Al}_x\text{Ga}_{1-x}\text{As}$  Injection Lasers with Channeled-Substrate-Planar Structure," *IEEE J. Quant. Electron.*, *QE-14*, pp. 89-94, 1978.
13. Ueno, M., and Yonezu, H., "Stable Transverse Mode Oscillation in Planar Stripe Laser with Deep Zn Diffusion," *IEEE J. Quant. Electron.*, *QE-15*, pp. 1189-1196, 1979.
14. Kressel, H., and Butler J. K., *Semiconductor Lasers and Heterojunction LEDs*, Academic Press, N.Y., 1977, ch. 17.
15. Wilt, D., and Yariv, A., "A Self-Consistent Static Model of the Double-Heterostructure Laser," *IEEE J. Quant Electron.*, *QE-17*, pp. 1941-1949, 1981.

# Phase Control and Beam Steering of Semiconductor Laser Arrays

J. Katz

Communications Systems Research Section

*The operational principles and a possible device configuration of one-dimensional monolithically integrated semiconductor laser arrays are described. The output beam of the array can be electronically steered. Devices of the type described in this report can find applications in optical communication systems where the power levels needed are above the capability of a single laser device.*

## I. Introduction

Among the most promising candidates for light emitters in optical communication systems are semiconductor injection lasers (Ref. 1). These lasers are far more reliable than other laser types. In addition, they are much more efficient, and possess the small size and ruggedness typical of semiconductor devices. These advantages are offset by the relatively low levels of power that can be emitted by them in a stable radiation pattern (typically a few milliwatts in CW operation and about an order of magnitude more in a low duty cycle operation). Although research efforts are currently being conducted in order to improve this limitation (Refs. 2-4), it is conceivable that some applications, such as communication links for deep space missions (Ref. 5), will still require more power than is available from a single device.

A possible solution to this problem is to combine, coherently (Refs. 6-9) or incoherently (Refs. 10-14), the power of several lasers. Coherent power combining, via phase locking of the lasers, has several advantages over noncoherent power combining. First, when the power of the lasers is combined incoherently, each laser emits light in its individual spectrum. Thus it is necessary to have an optical filter with a wider band-

width at the receiver, with the penalty of increased detected background noise radiation. Secondly, the locking of the lasers causes a reduction in the far-field beam divergence angle. This makes the task of subsequent beam narrowing simpler (e.g., by requiring an optical telescope with a smaller magnification). As will be described in a subsequent section, coherent power combining also makes monolithic beam steering of the laser array possible.

As pointed out in a recent report (Ref. 15), the requirement for maintaining phase locking among the lasers in the array is quite stringent. Roughly speaking, the intrinsic frequencies of oscillation of the individual lasers must be maintained within a very close proximity of each other, typically within a relative deviation of a few tens of ppm. Modifying the oscillation frequency by changing the amount of current flowing through the laser is possible but not desirable, since it is better to be able to independently control both the amplitude and the frequency of each laser. Section II of this report describes a method to achieve a moderate amount of frequency control by incorporating an intracavity electrooptic modulator into the laser cavity, thus mitigating the problem of achieving phase-lock condition among the lasers of the array.

In addition, some applications, which involve operations such as beam pointing and tracking, can benefit from the incorporation of electronic beam steering, in a similar fashion to the microwave phased arrays. Section III of this report describes two methods of implementation: one which utilizes a discrete beam deflector element external to the array (and thus can be used also with incoherent arrays or single lasers), and a second method which monolithically incorporates an individual phase-shifter in tandem with every laser in the array. By controlling the phase shift of each device, we can first bring the array to oscillate in the fundamental, well-behaved mode, and also deflect the radiation pattern by the desired amount.

Although several physical phenomena can be used to control light waves, the use of the linear electrooptic (EO) effect is considered here (Ref. 16). In the most basic form of the linear EO effect, the change in the index of refraction of the material is proportional to the electric field applied on it. (Because of the anisotropy of actual crystals, the relation is a tensorial, not a scalar one.) The reason for considering this particular effect is twofold. First, since it involves the application of voltages, the power consumption can be minimal (unless the voltage is applied on medium or low resistivity materials, or when dealing with high frequency operation). Secondly, since GaAs, which is the intended substrate material of the injection lasers used in our application is also a quite strong electrooptic material, monolithic integration of lasers and modulators is possible, as described below.

Whereas Sections II and III review the application of the internal and external phase shifters to the individual laser devices, Section IV briefly addresses the specific problems of implementing the phase control mechanisms in the densely packed array configurations.

## II. Frequency Control of Semiconductor Lasers Using an Intracavity Electrooptic Modulator

Consider a laser cavity that is made of two sections, as shown in Fig. 1. The first section is a regular laser-amplifier section. The length of this section is  $l_a$ , and the electromagnetic mode of the laser propagates in it with a propagation constant  $\beta = kn_a$ , where  $k = 2\pi/\lambda$  and  $n_a$  is the effective index of refraction. In the second (modulator) section, of length  $l_m$ , the effective index of refraction  $n_m$ , seen by the laser radiation mode, is a function of the applied electric field  $\mathcal{E}$ .

The phase condition for oscillations, which demands that the round-trip phase delay of the laser mode in the cavity

is an integer ( $p$ ) multiple of  $2\pi$  (Ref. 16, Ch. 9), can be written as:

$$\frac{\omega_p}{c} [l_a n_a + l_m n_m(\mathcal{E})] = p\pi \quad (1)$$

where  $\omega_p$  is the (radian) frequency of the  $p$ th mode. Differentiating Eq. (1) with respect to  $n_m$  yields

$$\frac{\Delta\omega_p}{\omega_p} = - \frac{1}{1 + \frac{l_a n_a}{l_m n_m}} \frac{\Delta n_m}{n_m} \quad (2)$$

i.e., the relative change in the frequency is proportional to the relative change in the index of refraction in the modulator section.

The change of the index of refraction with the electric field is explained with the help of Fig. 2, which shows a GaAs crystal cleaved in the orientation used in fabricating semiconductor injection lasers.  $(x, y, z)$  and  $(x', y', z')$  are the principal coordinate systems for  $\mathcal{E} = 0$  and  $\mathcal{E} \neq 0$ , respectively (Ref. 16). The mode of the semiconductor laser is predominantly TE polarized; i.e., the electric field of the optical wave is parallel to the  $y'$  axis. In this configuration the index of refraction seen by the laser field propagating in the modulator section is changed from  $n_m$  by an amount  $\Delta n_m$  given by (Ref. 16):

$$\Delta n_m = - \frac{1}{2} n_m^3 r \mathcal{E} \quad (3)$$

where  $r$  is the electrooptic tensor element relevant to this configuration. The largest field  $\mathcal{E}_m$  that can be applied is the one beyond which phenomena such as avalanche set in. For GaAs  $\mathcal{E}_m \gtrsim 3 \cdot 10^5$  volts/cm (depending on the doping),  $n_m \cong 3.6$  and  $r \cong -1.5 \cdot 10^{-10}$  cm/V. Several assumptions are implied in the above analysis. It is assumed that the modulator section is a depletion region of a reverse biased pn junction. Furthermore, by properly designing the doping concentrations and the dimensions of the device, and utilizing heterojunctions, the electric field can be made to be uniform over the region occupied by the optical mode, and the optical mode itself will have its characteristics virtually unchanged when the voltage imposed on the device is varied. A possible design is depicted in Fig. 3.

Using the above numbers, we find that the maximum relative change in index of refraction that can be modified via the linear EO effect is

$$\frac{\Delta n_m}{n_m} \cong 3 \cdot 10^{-4} \quad (4)$$

As will be discussed later, the modulator section is fabricated of GaAlAs so that the light that is generated in the GaAs active region of the laser-amplifier section can propagate in it without being strongly absorbed. Although the various parameters in Eq. (3) are different in GaAlAs and GaAs, the results of Eq. (4) still approximately hold.

Using Eq. (4) in Eq. (2), it is seen that the laser frequency can be modified by a fractional change of about  $10^{-4}$ . Since  $\Delta\omega/\omega = \Delta\lambda/\lambda$ , this means changing the wavelength by up to about 1 Å ( $\lambda \cong 0.8 - 0.9 \mu\text{m}$ ).

Such a device – which combines on the same substrate the operation of an injection laser and the intracavity modulator – has been demonstrated (Ref. 17). The voltage was applied to the modulator section in the configuration of a reverse biased junction, and wavelength modulation of up to 0.4 Å was obtained. Using a different device configuration, still better performance may be achieved, in particular with respect to the threshold current density and amount of frequency modulation. This subject will be further discussed in the next section.

### III. External Phase Control of Semiconductor Lasers Using Electrooptical Modulators

The electrooptic effect which was described in the last section, can also be utilized for controlling the phase of the light wave emitted from the laser. The first application is the deflection of the radiation pattern (Ref. 16). By placing a prism which is made of an electrooptical material (e.g., KDP) in the path of the light beam (which can come from either a single laser or an array), as shown in Fig. 4, the beam is deflected by an amount  $\Delta\theta$  equal to

$$\Delta\theta = \frac{\ell}{D} n^3 r \mathcal{E} \quad (5)$$

where  $\ell$  is the length of the prism,  $D$  is its width and  $n$  is its index of refraction. The dynamic range of the beam deflection, measured in beamwidths, is proportional to  $\ell$ . A typical value is 1 beamwidth for a 1-cm-long prism.

The second possible application of the electrooptic effect is the fabrication of an electrooptic modulator on the same substrate with the laser, but external to the laser cavity. A cross section of a possible device is shown in Fig. 5. The amount of additional phase shift  $\Delta\phi$  introduced to the laser radiation field is approximately given by

$$\Delta\phi = \frac{2\pi}{\lambda} \ell_x \frac{1}{2} n_m^3 r \frac{V}{d} \quad (6)$$

where  $d$  is the thickness of the region on which the voltage  $V$  is applied, and  $\ell_x$  is the length of the external phase shifter (see Fig. 5). From Eq. (6) it is seen that the amount of phase shift is proportional to  $\ell_x$ . Typical values that can be obtained are 1 radian for  $\ell_x = 100 \mu\text{m}$ .

Of course, applying a phase shift to a single laser is of no significance to our application. However, if we have a phase-locked array of semiconductor lasers, then by individually controlling the relative phase shifts among the various lasers, we can obtain a controlled beam deflection of the entire array, in a similar fashion to microwave phased arrays. Operation of a semiconductor laser device on similar principles has been recently demonstrated (Ref. 18). We should also note that the dynamic range of the beam steering in this case is contained within the far-field radiation pattern of the individual lasers of the array.

### IV. One-Dimensional Beam Steerable Semiconductor Laser Array

A typical application (e.g., source for an optical communication system) may call for the use of both types of electrooptic modulators: intracavity modulators (described in Section II), which fine-tune the oscillation frequency of the individual lasers in the array, thus making the phase locking possible, and external modulators (described in Section III), which electronically control the beam shape and deflection of the array.

Both modulators can be fabricated in the same processing procedure. It is worth noting that just by applying antireflection coating to different facets in the device, the modulator section shown in Fig. 5 can operate both inside and outside the laser cavity, thus performing both functions. Of course, other device configurations are also possible.

When operating as elements of an array, the individual devices are placed in close proximity to each other, typically about  $10 \mu\text{m}$  or less. Since the electrical contact of the total device must be in the size of at least  $50 \times 50 \mu\text{m}^2$ , a two-level metallization is needed for the contacts (as opposed to the one-level metallization used for single devices). Also the metal stripes that connect the devices themselves (especially the lasers) and the external contacts should not have high resistivity.

An example of a one-dimensional beam steerable semiconductor laser array is shown in Fig. 6. The figure shows a schematic configuration of one-half of a four-element array. Several technical details are omitted (as described in the figure caption), but the main ingredients of the device –

the laser section, the modulator – are clearly depicted. Extension of such arrays to more than four elements is straightforward. The functions of the various parts of each element of the array have been described in the previous sections, and the mechanism by which all the individual components operate in a coherent fashion was analyzed in Ref. 15.

## V. Conclusions

The operational principles and a possible device configuration of one-dimensional monolithically integrated semiconductor laser arrays have been described. Two electro-optic modulators accompany each laser-amplifier element of the array. One of the modulators is placed inside the laser cavity, making

fine-tuning of the laser frequency possible, thus alleviating the problem of maintaining phase-lock conditions across the array. The second modulator, which is external to the laser cavity, controls the phase of the optical wave emitted by the laser. By judiciously controlling the phases of all the elements, controlled beam steering capability of the array is expected.

Arrays of the types described in this report may be useful in applications which call for a single and stable mode operation of semiconductor light sources in applications where the amount of power needed is beyond the capability of a single injection laser device. Among the possible applications are deep-space, intersatellite and near-earth optical communication systems, and optical radars.

## References

1. Botez, D., and Herskowitz, G. J., "Components for Optical Communications Systems: A Review," *Proc. IEEE*, 68, pp. 689-731, 1981.
2. Takamiya, S., et al., "One Order Power Improvement of Single Mode TJS Laser Diodes by Crank Structure," 7th IEEE International Semiconductor Laser Conference, Brighton, England, Sept. 8-10, 1980.
3. Ueno, M., "Optimum Design Conditions for AlGaAs Window Stripe Lasers," *IEEE J. Quant. Electron.*, QE-17, pp. 2113-2122, 1981, and references therein.
4. Blauvelt, H., Margalit, S., and Yariv, S., "Large Optical Cavity AlGaAs Buried Heterostructure Window Lasers," Topical Meeting on Integrated and Guided Wave Optics, Pacific Grove, Calif., Jan. 6-8, 1982.
5. Katz, J., and Lesh, J. R., "Optical Communication for Deep Space Missions Using Integrated Semiconductor Injection Lasers," Technical Report (in preparation), Jet Propulsion Laboratory, Pasadena, Calif.
6. Katz, J., "High Power Semiconductor Lasers for Deep Space Communications," *TDA Progress Report 42-63*, pp. 40-50, Jet Propulsion Laboratory, Pasadena, Calif., 1981, and references therein.
7. Ackley, D. E., and Engleman, R. W. H., "High Power Leaky-Mode Multiple-Stripe Laser," *Appl. Phys. Lett.*, 39, pp. 27-29, 1981.
8. Small, M. B., and Lynch, R. T., Jr., "A New Structure for High-Powered Injection Lasers," *J. Appl. Phys.*, 52, pp. 6051-6053, 1981.
9. Rediker, R. H., Schloss, R. P., Mooradian, A., and Welford, D., "External Cavity Controlled Operation of a Semiconductor Diode Gain Element in Series with an Optical Fiber," Topical Meeting on Integrated and Guided Wave Optics, Pacific Grove, Calif., Jan. 6-8, 1982.
10. Birbeck, F. E., "A Gallium Arsenide Laser Array for Communications," *J. Sci. Instr. (J. Phys. E.)* 1, Series 2, pp. 788-790, 1968.

11. Weider, H., and Marianne, T. C., "Uniformly Polarized GaAs Laser Array," *Appl. Phys. Lett.*, 20, pp. 311-312, 1972.
12. Crow, J. D., et al., "GaAs Laser Array Source Package," *Opt. Lett.*, 1, pp. 40-42, 1977.
13. Allen, L. B., et al., "Linear Array Configuration and Applications of the Double-Sided Heat Sink Diode," *SPIE*, 247, pp. 100-105, 1980.
14. Laser Diode Laboratories, New Jersey; Data sheets on various incoherent arrays: LA-60, LA-160, and MH-160 series, LDF-163, LDF-167, LS-410 and LSA-410.
15. Katz, J., "Phase Locking of Semiconductor Injection Lasers," *TDA Progress Report 42-66*, pp. 101-114, Jet Propulsion Laboratory, Pasadena, Calif., 1981.
16. See, for example, A. Yariv, *Quantum Electronics*, Second Edition, Wiley, New York, 1975, Ch. 14, and references therein.
17. Reinhart, F. K., and Logan, R. A., "Integrated Electro-optic Intracavity Frequency Modulation of Double-Heterostructure Injection Laser," *Appl. Phys. Lett.*, 27, pp. 532-534, 1975.
18. Scifres, D. R., Streifer, W., and Burgham, R. D., "Beam Scanning and Wavelength Modulation with Branching Waveguide Stripe Injection Lasers," *Appl. Phys. Lett.*, 33, pp. 616-618, 1978.

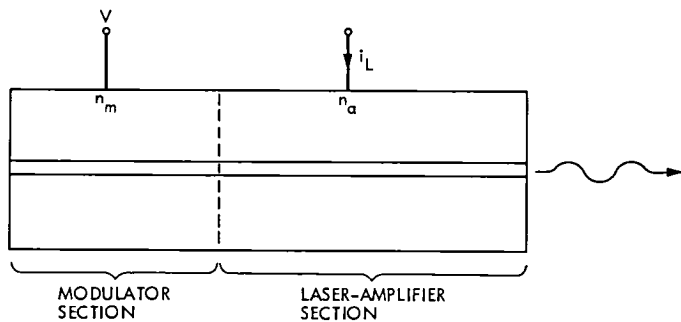


Fig. 1. Schematic cross section of a semiconductor laser with an intracavity modulator.  $n_a$  and  $n_m$  are the indices of refraction of the representative sections.

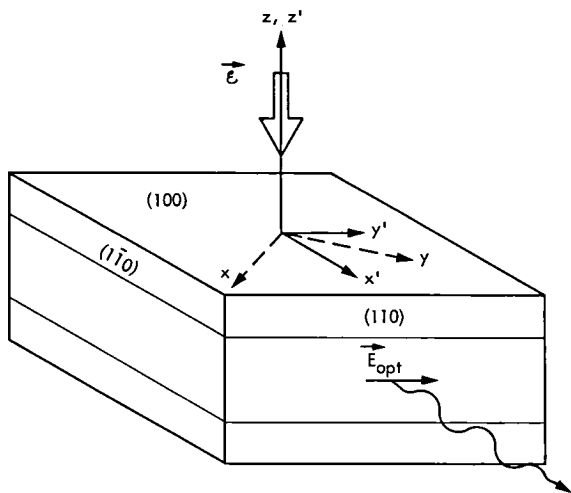
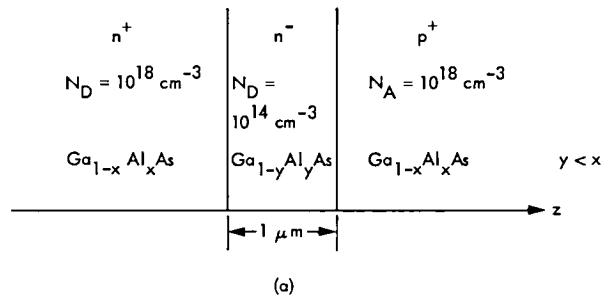
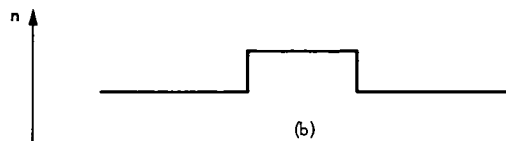


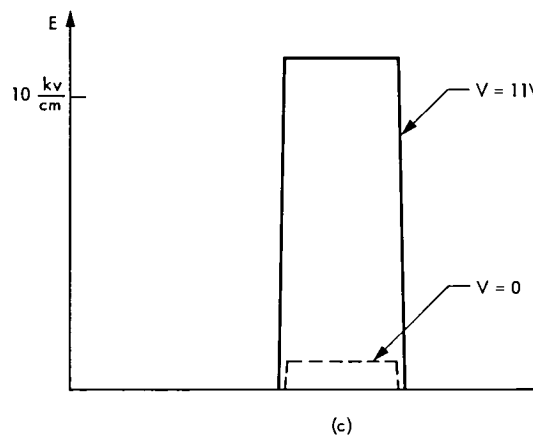
Fig. 2. GaAs electrooptic modulator. The GaAs crystal is cut in the same orientation used for fabrication of semiconductor lasers. (See test for details of coordinate systems.)  $\vec{E}$  is the electric modulation field and  $\vec{E}_{opt}$  is the electric TE field of the optical wave.



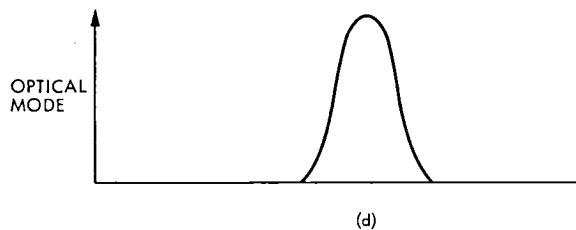
(a)



(b)



(c)



(d)

Fig. 3. Design example of an electrooptic modulator in a reverse biased pn junction configuration. a) Electrical structure. b) Index of refraction (almost unchanged by the applied field). c) Electric field distribution for various applied voltages. d) Intensity profile of the optical mode

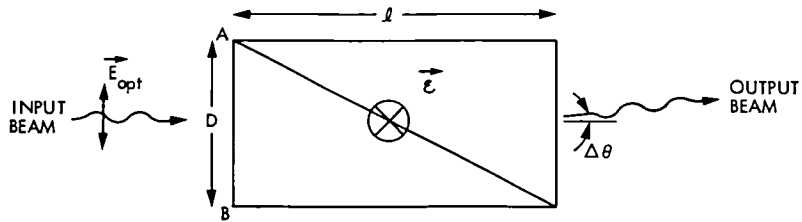


Fig. 4. Double-prism electrooptic beam deflector.  $\mathcal{E}$  is the applied electric field (Ref. 16). The optical path for waves entering the input plane (AB) at different points vary, thus causing a tilting of the wavefront by  $\Delta\theta$

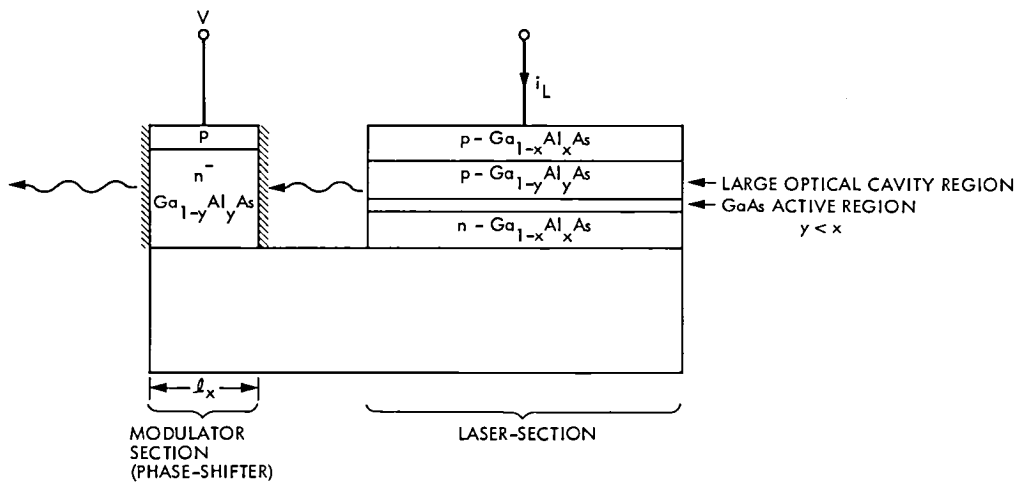


Fig. 5. Cross section of a possible monolithic implementation of a semiconductor laser and an external electrooptic phase-shifter. (The cross-hatched facets depict layers of antireflection coating to prevent coupling from the phase-shifter back to the laser.)

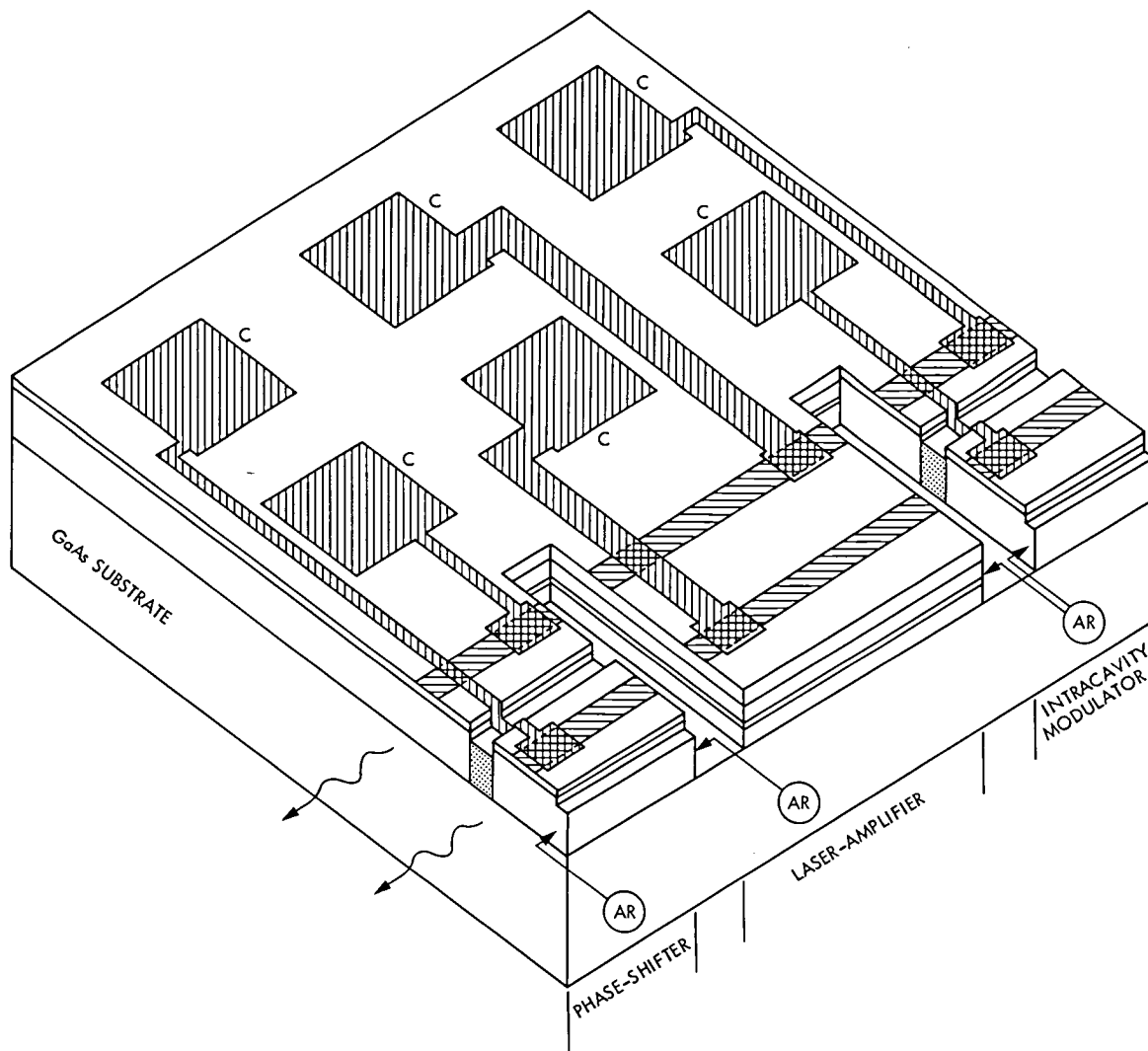


Fig. 6. Schematic layout of a one-dimensional four-element semiconductor laser array (only one-half of the symmetric array is shown). Each laser has an intracavity electrooptic modulator and an external electrooptic phase-shifter. Facets denoted by AR are antireflection-coated. Areas denoted by C are the contacts of the various elements to the external wiring. Dotted areas represent electrical isolation between neighboring elements, for example by proton-implantation. (Not shown in this schematic layout are the oxide layers used for isolation between the two levels of metallization, and also possible materials that can fill the gaps between the laser-amplifier and the modulator, thus increasing the coupling efficiency between them.)

# A PPM Modulator and Demodulator for the 2.5-Bit/Detected Photon Demonstration

W. K. Marshall

Communications Systems Research Section

*The design and operation of a 256-ary pulse position modulation (PPM) modulator and demodulator is described. The unit is an integral part of the 2.5-Bit/Detected Photon Demonstration Program.*

## I. Introduction

The use of quantized pulse position modulation over the photon channel has been much discussed (Refs. 1,2) but little practiced. This article gives a functional description of a hardware PPM modulator and demodulator/analyzer which has been built for use in a 2.5-bit/detected photon, 256-ary PPM demonstration project (Ref. 3). The basic setup is shown in Fig. 1.

In addition to performing the basic pulse position modulation and demodulation, the hardware described also indicates the occurrence of erasures and errors of various types. The "analyzer" portion of the circuit counts the number of pulses received in a word, demodulates a second input pulse (if one is received), indicates the occurrence of erasures, and detects PPM word errors. Word errors are detected by comparing the modulator input word to the corresponding demodulator output. These functions are provided mainly for testing and diagnosis of the system during the feasibility demonstration period.

The hardware consists of two circuit boards (the modulator and the demodulator/analyzer) and a power supply in a single

enclosure (see Figs. 2 and 3). The system was designed primarily for 8-bit (256-ary) PPM operation, but can be very easily modified for up to 12-bit (4096-ary) PPM operation. The maximum clock rate is 10 MHz (yielding 100-ns minimum slots), resulting in 256-ary PPM operation at up to

$$\frac{8 \text{ bits/word}}{256 \text{ slots/word} \times 100 \text{ ns/slot}} = 3.1 \times 10^5 \text{ bits/sec}$$

Hardware interfaces are at TTL logic levels — external circuitry must be provided to drive the laser and to convert the photomultiplier output (typically 10-ns pulses corresponding to individual photon or noise counts) to the required "count detected" decision for each slot.

## II. The Modulator and Demodulator Hardware

The modulator (Fig. 4) consists of a binary downcounter, a phase-locked loop clock multiplier, and a serial-to-parallel converter. The PPM output is a one-slot pulse, position-modulated over the 256-slot word time (slot 0 is first, 255 is last). Each

8-bit word transmitted is also hard-wired to the error detection circuit in the demodulator. The clock multiplier generates a slot clock running at 256 times the word rate, and also a one-slot-per-word synchronization pulse. Both signals are available at the front panel.

After passing through the laser, the optics, and the detector, the PPM pulse enters the demodulator as a logic "true" (actually a TTL '0') during the appropriate time slot. Erasure of the pulse in transmission or the introduction of noise may result in any number of slots being "true" during any given word time. In the demonstration setup, the timing from the modulator is wired to the detector circuitry and to the demodulator, bypassing the problem of slot and word synchronization at the receive end. The demodulator can be adjusted to account for any number of full slot delays (up to one word time) through the system.

The demodulator/analyzer (Fig. 5) consists of two demodulators each with a parallel-to-serial converter, a pulse counter and decoder, and an error detector. The error detector compares the 8 bits demodulated from the first input pulse received in a word to the 8 bits provided by the modulator. This tests the success or failure of the basic PPM modulation-transmission-demodulation sequence. Demodulation of the second input pulse received is provided for diagnosis of systematic errors in transmission. All outputs are available one slot time after the word ends.

The pulse counter output indicates the number of slots which were "true" during the previous word time. Decoded

outputs are available to indicate erasures (0 pulses received), normal PPM (1 pulse received), and error conditions (2 pulses received and  $> 2$  pulses received). In the demonstration setup, only the "single pulse received" output is used, to indicate an (assumed) normal transmission. In this case, a nondetected error occurs only when an erasure and one noise count occur during the same word.

### III. Remarks

The hardware provides the desired functions of PPM modulation and demodulation. Additional features are provided to increase the usefulness of the hardware in testing the system prior to use. Flexibility is provided by keeping the immediate interface to the optical channel external to the modulator/demodulator hardware.

The optical transmission and detection components will be connected soon in preparation for the 2.5-bit/detected photon phase III (uncoded PPM) demonstration. In this phase of the demonstration, a setup similar to that shown in Fig. 1 will be used.

Reed-Solomon coded PPM (phase IV of the demonstration) will be possible using the same modulator/demodulator hardware, by encoding data given to the modulator and decoding the output from the demodulator. In this setup, final verification of the 2.5-bit/detected photon transfer efficiency (at a reduced error rate from that of phase III) is expected.

## References

1. Pierce, J. R., "Optical Channels: Practical Limits with Photon Counting," *IEEE Transactions on Communications*, Vol. COM-26, No. 12, pp. 1819-1821, Dec. 1978.
2. McEliece, R. J., "Practical Codes for Photon Communications," *IEEE Transactions on Information Theory*, Vol. IT-27, No. 4, pp. 393-398, July 1981.
3. Lesh, J. R., Katz, J., Tan, H. H., and Zwilling, D., "2.5-Bit/Detected Photon Demonstration Program: Analysis and Phase I Results," *TDA Progress Report 42-66*, Jet Propulsion Laboratory, Pasadena, Calif., pp. 115-132, Nov. 1981.

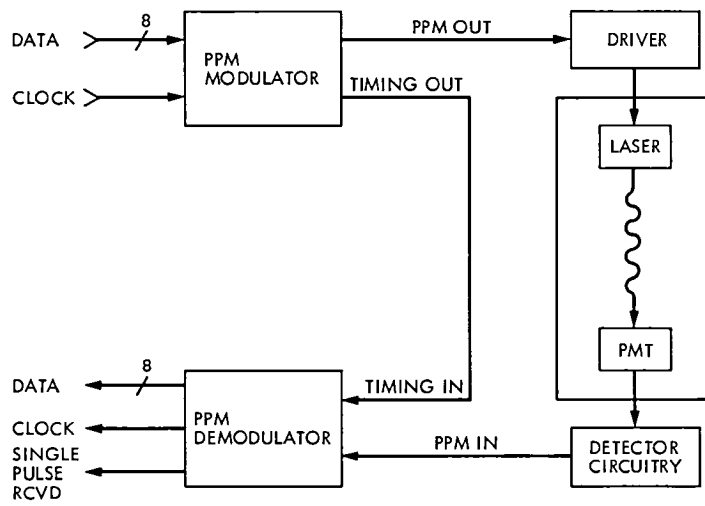


**Fig. 1. Basic setup for the 256-ary PPM optical channel**

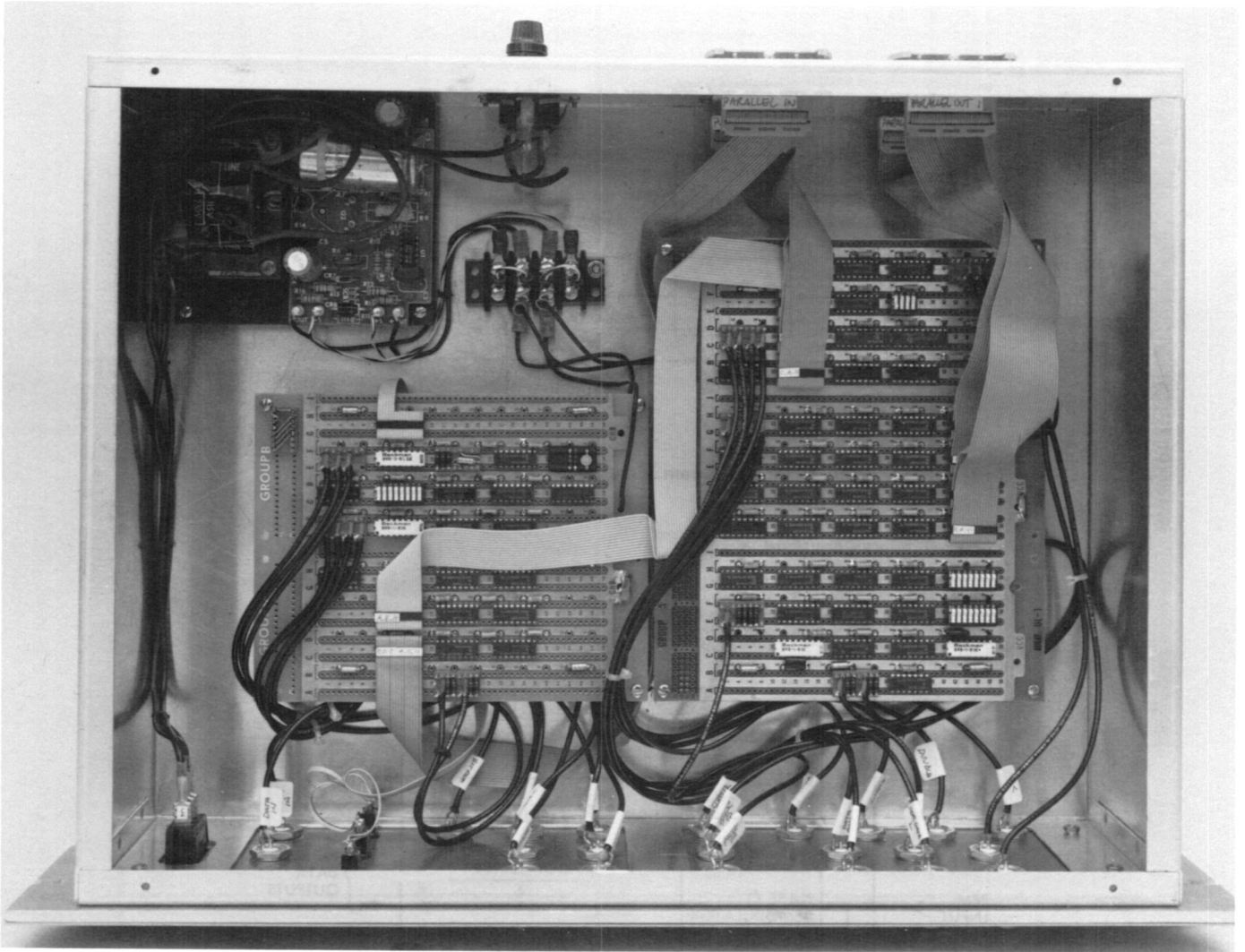


Fig. 2. Top view of the PPM modulator and demodulator hardware

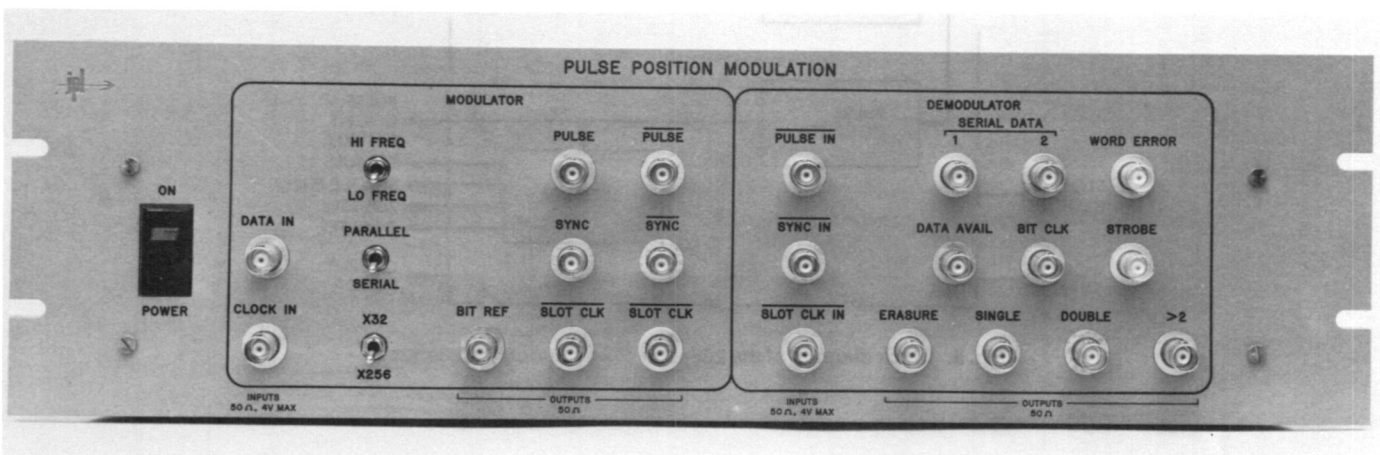


Fig. 3. Front panel of the PPM modulator and demodulator hardware

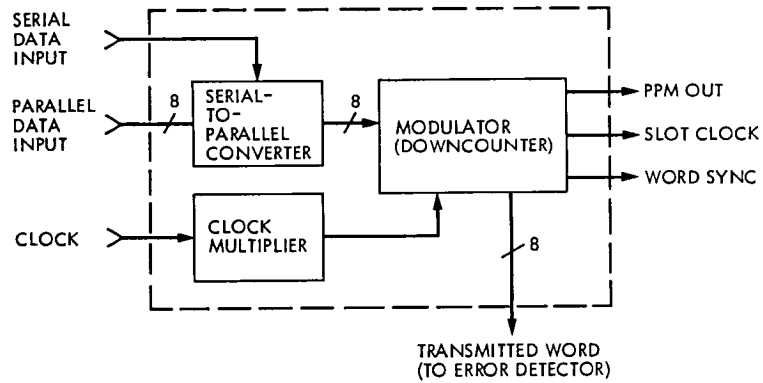


Fig. 4. Block diagram of the 256-ary PPM modulator

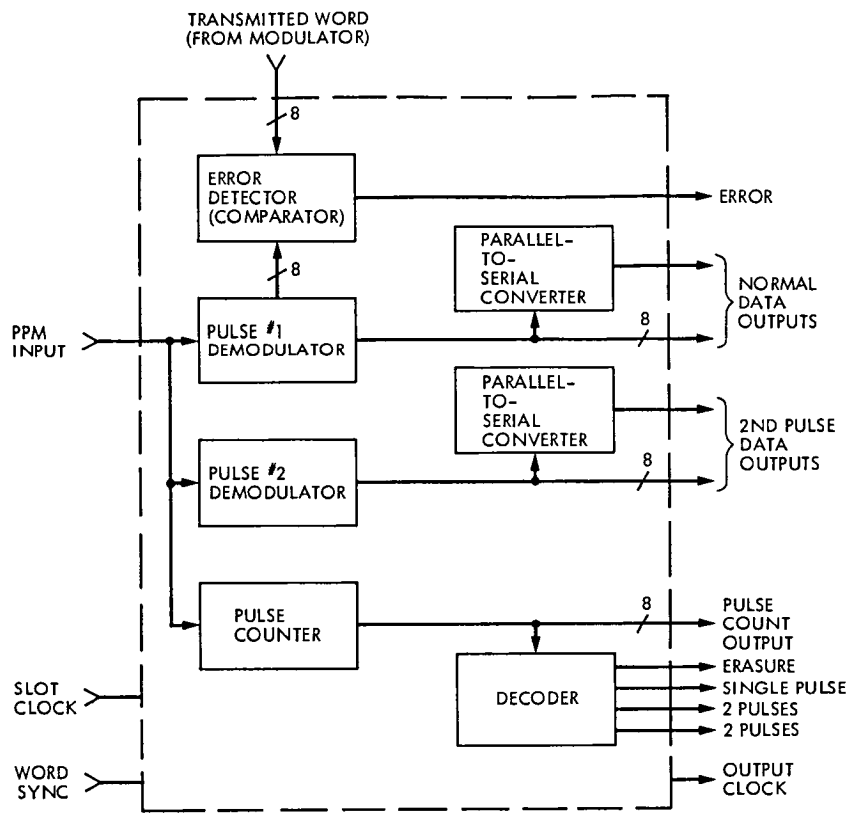


Fig. 5. Block diagram of the 256-ary PPM demodulator/analyser

# A Statistical Model of the Photomultiplier Gain Process With Applications to Optical Pulse Detection

H. H. Tan

Communications Systems Research Section

*The complete statistical behavior of the random gain of a photomultiplier tube (PMT) has not previously yielded to exact analysis. In this paper a Markov diffusion model is used to determine an approximate probability density for the random gain. This approximate density preserves the correct second-order statistics and appears to be in reasonably good agreement with previously reported experimental data. The receiver operating curve for a pulse counter detector of PMT cathode emission events is analyzed using this density. The error performance of a simple binary direct detection optical communication system is also derived.*

## I. Introduction

The photomultiplier tube (PMT) is an optical energy detector which has high enough internal gain to provide adequate output signal levels at low light levels. Electrons that are emitted at the cathode of a PMT are directed through a series of dynodes by an applied electric field. A single electron emitted at the cathode causes a number of secondary electrons to be emitted at the first dynode. These secondary electrons from the first dynode are in turn directed to a second dynode where this multiplication process is repeated for each impinging electron. This electron multiplication process is repeated through a series of several dynodes until the electrons from the last dynode are collected at the PMT anode, with the resulting anode current being the PMT output.

The PMT *gain* is defined to be the total number of electrons collected at the anode as a result of a single electron emission event at the cathode. Since the number of secondary electron

emissions at a dynode for each primary impinging electron is a random quantity, the overall PMT gain is a random variable. Thus the PMT output current signal resulting from a single electron emission event at the cathode is also random in nature.

In optical communications, direct detection receivers employ photodetectors with internal gain such as PMTs in low light level situations to overcome thermal noise in the amplification stages following the PMT. The probability distribution of the random PMT gain is then required to determine error performance in systems that use a PMT detector. It is well known (Refs. 1, 2) that the random electron multiplication process can be modelled by a Galton-Watson branching process (Ref. 3). Although the mean and variance of the gain can be readily determined using the branching process model, the problem of determining an explicit expression for its probability distribution appears to be intractable. An approach to

circumvent this intractable problem is to obtain an accurate approximation of the probability distribution of the PMT gain. This approximate distribution can then be used to evaluate the error performance of the direct detection digital communication system.

Feller (Ref. 4) was the first to suggest the use of a Markov diffusion process approximation to analyze the statistical behavior of a Galton-Watson branching process. As is well known, the Galton-Watson branching process is a discrete-time discrete-state Markov process that can be specified by its conditional state transition probability distribution. On the other hand, the diffusion process is a continuous-time continuous-state Markov process whose incremental state transition statistics are specified by conditional incremental mean and variance parameters called the infinitesimal mean and variance, respectively. Feller's approach is to use a diffusion process approximation whose infinitesimal mean and variance parameters simulate the mean and variance respectively of the branching process conditional state transition distribution. Thus the second-order incremental state transition statistics of the diffusion approximation are similar to those of the original branching process.

In this paper we employ Feller's approach to obtain a Markov diffusion process approximation of the PMT gain branching process. The resulting diffusion process then has a marginal probability density which is obtained by solving a Fokker-Planck partial differential equation. This density can then be regarded as an approximate density for the PMT gain. This approximate density of course yields the true mean and variance of the PMT gain. Moreover, the general shape of the approximate density appears to be in good agreement with experimental PMT gain data reported in the literature (Ref. 5).

The number of electrons emitted at the PMT cathode is also random in nature and can be assumed to be Poisson distributed. Thus the random nature of the number of electrons collected at the anode is a result of both the random electron emission process at the cathode and the random PMT gain. It is the probability distribution of the number of PMT anode electrons that is required for evaluating communication system error performance. In order to determine an explicit expression for this distribution, the distribution of the gain is again required. Hence the problem of determining an explicit expression for the distribution of the number of PMT anode electrons appears to be also intractable. In this paper we obtain an approximate density for the number of anode electrons by using the approximate density for the gain random variable derived from the diffusion approximation.

The number of PMT cathode electron emission events is often monitored by using a pulse counter. It is interesting to

determine the effect of the random PMT gain, thermal noise in the PMT output amplifier and the counter response time on successful cathode electron emission event detection. The receiver operating curve of this detection process is determined in this paper using the derived approximate PMT gain distribution.

Finally we analyze the error performance of a direct detection communication system with a PMT detector and an on-off binary signalling scheme. Here the laser transmitter light source is either on or off in a binary symbol time. We consider a simple receiver which integrates the PMT amplifier output over the symbol time period and compares the result to a threshold. Detection of the laser light is then declared if and only if the threshold is exceeded. The error performance of this system is analyzed, taking into account the random PMT gain and the thermal noise in the PMT output amplifier.

This paper is organized as follows. Section II describes the branching process model of the PMT gain and the diffusion approximation. Section III considers the detection performance of pulse counter monitoring of PMT cathode emission events using the approximate PMT gain density obtained in Section II. Section IV derives the approximate density of the number of electrons collected at the PMT anode for Poisson distributed cathode electron emissions. This density is then used to evaluate the error performance of the binary on-off direct detection communication system.

## II. Branching Process Model and the Diffusion Approximation

### A. Branching Process Model for the PMT Gain

A primary impinging electron at a dynode causes a random number of secondary electrons. In this paper it is assumed that the number of secondary electrons generated per primary electron is Poisson distributed with mean  $\mu$ , where

$$\mu = \text{average gain per dynode stage.}$$

Moreover, it is assumed that the average gain of each dynode stage is identical. The Poisson assumption can be regarded as being valid when the physical nonuniformities across the dynode surfaces are small (Refs. 6, 7). In the dynode electron multiplication process it can be assumed that the secondary electron emission process operates on each individual primary electron in a statistically independent manner (Refs. 1, 2, 5, 6, 7). Hence the number of secondary electrons resulting from different primary electrons are independent random variables. This independence assumption leads directly to a branching

process model for the overall PMT gain. Specifically for  $k \geq 1$  let

$S_k$  = total number of electrons emitted by the  $k$ th dynode.

Moreover, define

$$S_0 = 1$$

= number of electrons emitted by the cathode,

and

$G$  = total number of electrons collected at the anode as a result of a single electron emission at the cathode

$\Delta$   
= PMT gain.

Then for a PMT with  $\nu$  dynode stages,

$$G = S_\nu. \quad (1)$$

Also, we have, under the above assumptions,

$$S_k = \sum_{i=1}^{S_{k-1}} N_{ki}, \quad k \geq 1, \quad (2)$$

where  $\{N_{ki}, k \geq 1, i \geq 1\}$  are independent Poisson random variables each with mean  $\mu$ . The process  $\{S_k: k \geq 0\}$  is known as a Galton-Watson branching process (Ref. 3). The second-order statistics of  $S_k$  can be shown (Ref. 3, p. 6) to be given by

$$E[S_k] = \mu^k \quad (3)$$

$$\text{Var}(S_k) = \frac{\mu^k(\mu^k - 1)}{\mu - 1} \quad (4)$$

where  $\mu \neq 1$ . Thus from (1) and (3), a PMT with  $\nu$  dynode stages has average gain

$$\bar{G} \stackrel{\Delta}{=} E[G] = \mu^\nu. \quad (5)$$

A typical PMT such as the RCA C31034 has  $\nu = 11$  dynode stages with  $\bar{G} = 10^6$ . Hence  $\mu = 3.51$  here. In this case it can be seen from (4) that the standard deviation of the gain  $G$  is roughly half of the average gain  $\bar{G}$ . Hence the distribution of  $G$  can be expected to be quite widely spread about its mean. This

is the situation with many PMTs where the standard deviation of the gain is of the same order of magnitude as its mean.

In branching process theory, the probability generating function (pgf) of  $S_k$ :

$$f_k(z) = E[z^{S_k}] \quad (6)$$

can be shown (Ref. 3, p. 5] to be given by

$$f_k(z) = \underbrace{g(g(\cdots g(z)\cdots))}_{k \text{ times}}, \quad (7)$$

where

$$g(z) = E[z^{N_{ki}}] = e^{\mu(z-1)} \quad (8)$$

is the pgf of the Poisson random variable  $N_{ki}$  with mean  $\mu$ . So in view of (1), the pgf of the PMT gain can be explicitly determined using (7). However, it is not possible to invert the pgf analytically to obtain the distribution of the gain because the number of dynode stages is usually sufficiently large to render that problem intractable. Thus the problem of determining an explicit expression for the probability distribution of the gain  $G$  appears to be intractable.

## B. Diffusion Approximation

A viable alternative is to attempt to obtain an accurate approximation of the PMT gain probability distribution. We propose to accomplish this goal by using a diffusion approximation of the branching process gain model. Diffusion approximations have previously been successfully employed in many stochastic process problems such as in the analysis of queuing systems (Ref. 8). Feller (Ref. 4) was the first to suggest the use of diffusion approximations to analyze branching processes. We apply Feller's approach to obtain an approximate distribution for the PMT gain as follows. Let  $S(t)$  be a diffusion process satisfying the Ito differential equation (Ref. 9):

$$dS(t) = \beta(S(t), t) dt + \alpha(S(t), t) dW(t), \quad (9)$$

where  $W(t)$  is a Wiener process with zero mean and variance  $t$ . Here  $\beta$  is the infinitesimal mean or drift and  $\alpha$  is the infinitesimal variance of  $S(t)$ . That is, for small  $\Delta t$ ,

$$E[S(t + \Delta t) - S(t) | S(t) = x] \cong \beta(x, t) \Delta t, \quad (10)$$

$$\text{Var}[S(t + \Delta t) - S(t) | S(t) = x] \cong \alpha(x, t) \Delta t. \quad (11)$$

Since the PMT gain  $G$ , which is usually of the order of  $10^6$ , is large, we can represent it as a continuous random variable. Let us now approximate the branching processing gain model  $\{S_k\}$  given by (2) by the continuous-state continuous-time diffusion process  $S(t)$ . Moreover, this approximation shall be made so that the infinitesimal parameters (10) and (11) of  $S(t)$  possess the same behavior of the corresponding incremental mean and variance of  $S_k$ . Note from (2) that

$$E [S_{k+1} - S_k | S_k = n] = n(\mu - 1) \quad (12)$$

$$\text{Var} [S_{k+1} - S_k | S_k = n] = n\mu \quad (13)$$

are both proportional to the population size  $S_k = n$  of electrons emitted by the  $k$ th dynode. Thus, in order to preserve this behavior, we should set the infinitesimal parameters

$$\beta(x, t) = \beta x, \quad (14)$$

$$\alpha(x, t) = \alpha x, \quad (15)$$

to also linearly increase with population size  $x$ . We shall not at this time specify the constants  $\alpha$  and  $\beta$  in view of the difference in time scales between the processes  $S_k$  and  $S(t)$ . Let

$$p(x, t) = \text{marginal probability density of } S(t).$$

Then it follows from (14) and (15) and a well-known result (Ref. 9) on diffusions that  $p(x, t)$  satisfies the following Fokker-Planck equation:

$$\frac{\partial p(x, t)}{\partial t} = \frac{1}{2} \alpha \frac{\partial^2}{\partial x^2} [xp(x, t)] - \beta \frac{\partial}{\partial x} [xp(x, t)], \quad (16)$$

$$p(x, 0) = \delta(x - 1). \quad (17)$$

The solution  $p(x, t)$  of (16) and (17) can be obtained as follows. Instead of solving for  $p(x, t)$  directly, consider its moment generating function (mgf)

$$\phi(u, t) = E [e^{-uS(t)}] = \int_{-\infty}^{\infty} e^{-ux} p(x, t) dx.$$

A technique (Ref. 10, p. 83) for transforming Fokker-Planck equations then obtains the following equations for  $\phi(u, t)$  from (16) and (17):

$$\frac{\partial \phi(u, t)}{\partial t} = \left( \beta u - \frac{1}{2} \alpha u^2 \right) \frac{\partial \phi(u, t)}{\partial u}, \quad (18)$$

$$\phi(u, 0) = e^{-u}. \quad (19)$$

The solution of (18) and (19) can be shown to be

$$\phi(u, t) = \exp \left[ \frac{-Au}{1 + Bu} \right], \quad (20)$$

where

$$A = e^{\beta t}, \quad (21)$$

$$B = \frac{\alpha}{2\beta} (e^{\beta t} - 1). \quad (22)$$

Finally (20) is inverted to recover  $p(x, t)$  as follows. First rewrite (20) as

$$\begin{aligned} \phi(u, t) &= e^{-A/B} \exp \left[ \frac{A/B}{1 + Bu} \right] \\ &= e^{-A/B} \sum_{n=0}^{\infty} \frac{(A/B)^n}{n!} \frac{1}{(1 + Bu)^n}. \end{aligned} \quad (23)$$

Next note that  $1/(1 + Bu)^n$  is the mgf of the Gamma density:

$$\frac{1}{(1 + Bu)^n} = \int_0^{\infty} e^{-ux} \left[ \frac{B^{-n} x^{n-1}}{(n-1)!} e^{-x/B} \right] dx. \quad (24)$$

So (23) and (24) yield

$$\begin{aligned} p(x, t) &= e^{-A/B} \delta(x) + e^{-A/B} \sum_{n=1}^{\infty} \frac{(A/B^2)^n x^{n-1} e^{-x/B}}{n!(n-1)!} \\ &= e^{-A/B} \left[ \delta(x) + \frac{e^{-x/B} \sqrt{A/x}}{B} I_1 \left( \frac{2\sqrt{Ax}}{B} \right) \right], \end{aligned} \quad (25)$$

for  $x \geq 0$ , where  $I_1$  is the modified Bessel function of the first kind. Finally, we want to choose the parameters  $A$  and  $B$  so that  $S(t)$  represents the gain  $G = S_\nu$  of a  $\nu$ -stage PMT with average gain  $\bar{G}$ . In particular,  $A$  and  $B$  are chosen so that the respective means and variances of  $G$  and  $S(t)$  are equal. It follows from (1), (4) and (5) that

$$E[G] = \bar{G}, \quad (26)$$

$$\text{Var}[G] = \frac{\bar{G}(\bar{G} - 1)}{\nu \sqrt{\bar{G} - 1}} \quad (27)$$

Also, from (23) we have

$$E[S(t)] = - \left. \frac{\partial \phi(u, t)}{\partial u} \right|_{u=0} = A,$$

$$\text{Var}[S(t)] = \left. \frac{\partial^2 \phi(u, t)}{\partial u^2} \right|_{u=0} - A^2 \quad (28)$$

$$= 2AB \quad (29)$$

So in order that  $G$  and  $S(t)$  have the same second-order statistics, we require

$$A = \bar{G}, \quad (30)$$

$$B = \frac{1}{2} \left( \frac{\bar{G} - 1}{\nu \sqrt{\bar{G} - 1}} \right). \quad (31)$$

So we can conclude that an approximate probability density  $p_G(x)$  of the gain  $G$  of a PMT with average gain  $\bar{G}$  and  $\nu$  dynode stages is given by

$$p_G(x) = \begin{cases} e^{-A/B} \left[ \delta(x) + \frac{e^{-x/B} \sqrt{A/x}}{B} I_1 \left( \frac{2\sqrt{Ax}}{B} \right) \right], & x \geq 0 \\ 0, & x < 0 \end{cases} \quad (32)$$

where  $A$  and  $B$  are given by (30) and (31)

Let us consider the appropriateness of this approximate density (32). First, it is clear from (26) – (31) that (32) yields the correct mean and variance for  $G$ . It is also known (Ref. 3, pp. 13-16) that  $S_n/\mu^n$  converges to a nonnegative random variable  $W$  with probability one as  $n$  tends to infinity. Moreover, the distribution of this limiting random variable  $W$  has a point mass at 0 (delta function at 0) and is absolutely continuous (has a density) elsewhere. Thus the structural form of  $p_G(x)$  appears to be correct for PMTs with a large number of dynodes. As another indication of the appropriateness of (32), we note from (7) that

$$\begin{aligned} P(G = 0) &= P(S_\nu = 0) \\ &= \underbrace{g(\cdots g(0)\cdots)}_{\nu \text{ times}}, \end{aligned} \quad (33)$$

where  $g$  is given by (8). On the other hand (32) gives

$$P(G = 0) \cong e^{-A/B} \quad (34)$$

with  $A$  and  $B$  given by (30) and (31). For the RCA 31034 PMT with  $\nu = 11$  dynodes, (33) yields  $3.36 \times 10^{-2}$  and  $1.4 \times 10^{-2}$  for  $P(G = 0)$  when  $\bar{G} = 10^6$  and  $10^7$  respectively, whereas (34) yields  $6.6 \times 10^{-3}$  and  $1.3 \times 10^{-3}$ . Thus (32) also gives a fairly reasonable approximation of  $P(G = 0)$ .

The 11-dynode RCA 31034 PMT has usable average gain  $\bar{G}$  in a range from  $10^5$  to over  $10^7$ . Figures 1 and 2 show the approximate density (32) normalized to give a density for  $G/\bar{G}$  for  $\bar{G} = 10^6$  and  $10^7$ . As can be seen from these figures, the density is not symmetric about the mean and in fact peaks at a point below the mean value. Also there is considerable probability mass below the mean. These properties appear to be in good agreement with experimental PMT gain data reported in the literature (Ref. 5). In particular, the asymmetric nature of the density (32) appears in the experimental results. Also shown in these figures are corresponding density functions which are positive truncations of the Gaussian density with the same mean and variance as  $G$ . The truncated Gaussian approximation is sometimes used (Ref. 11) to simplify the analysis of systems using PMTs. However, the simpler truncated Gaussian approximation has a mean larger than  $\bar{G}$  and substantially more probability mass above the mean than (32). Hence, using the Gaussian approximation to analyze communication system performance could produce overly optimistic results.

### III. Pulse Counter Detection of Cathode Emissions

In many PMT experiments such as determining the dark current, cathode emission event data is required. The cathode emission events are usually recorded by monitoring the PMT output with a pulse counter. In this section the effect of the random PMT gain, thermal noise in the PMT output amplifier and the counter response time on successful emission event detection is determined. We shall derive the probability of successful emission event detection and the probability of false alarm to obtain the receiver operating curve for this detection process.

Suppose a single electron is emitted at the PMT cathode. Denote  $e$  = electron charge =  $1.6 \times 10^{-19}$  coulombs,  $W_p$  = PMT bandwidth and  $T_p = 1/W_p$  = PMT response time. Then a current pulse of  $GeW_p$  amps is generated at the PMT anode as a result of this single electron emission. Suppose the anode is terminated with resistance  $R$ . Then the voltage pulse signal

$S(t)$  across the resistor can be represented as

$$S(t) = (GeW_p R) p(t) \text{ volts,} \quad (35)$$

where  $p(t) \geq 0$  can be assumed to be a pulse of duration  $T_p = 1/W_p$  seconds satisfying

$$\frac{1}{T_p} \int_0^{T_p} p(t) dt = 1. \quad (36)$$

The requirement (36) arises because the total charge in the current pulse  $S(t)/R$  due to the single emitted electron must be equal to  $Ge$ . Here  $G$  is of course the random PMT gain. We assume that the amplified PMT output is monitored using a pulse counter. Let  $W_c$  = counter bandwidth and  $T_c = 1/W_c$  = counter response time. We assume that the counter bandwidth  $W_c$  is less than the PMT bandwidth  $W_p$  so that

$$T_c > T_p \quad (37)$$

The only degradation introduced by the PMT output amplifier is assumed to be additive thermal noise. As a first approximation we model the counter as a short-term averager of its input over the counter response time  $T_c$  seconds followed by a threshold comparator to determine whether a positive pulse has occurred. So the PMT amplifier – pulse counter combination first introduces an independent additive white Gaussian noise process  $V(t)$  to the PMT output and then integrates the PMT output signal plus  $V(t)$  process over  $T_c$  seconds. The result is first normalized by  $T_c$  and then compared to a decision threshold  $\gamma$ . An emission event is declared if and only if this threshold is exceeded. This model is shown in Fig. 3. Let  $H_1$  be the hypothesis of the occurrence of an emission event and  $H_0$  the null hypothesis. If  $X(t)$  is the PMT amplifier output, then under

$$H_1: X(t) = (e W_p R) G p(t) + V(t), \quad (38)$$

$$H_0: X(t) = V(t), \quad (39)$$

where  $V(t)$  has spectral density

$$N_0 = k \theta R \text{ (volts)}^2/\text{Hz.} \quad (40)$$

Here  $k$  = Boltzmann constant =  $1.38 \times 10^{-23}$  watts/Hz-°K,  $\theta$  = amplifier noise equivalent temperature (°K) and  $R$  = amplifier equivalent input resistance (assumed to be matched to the

PMT anode load resistance). Let  $X$  be the normalized integrator output:

$$X = \frac{1}{T_c} \int_0^{T_c} X(t) dt, \quad (41)$$

and denote

$$V = \frac{1}{T_c} \int_0^{T_c} V(t) dt. \quad (42)$$

So from (35) – (42), it follows that under

$$H_1: X = (e W_c R) G + V, \quad (43)$$

$$H_0: X = V, \quad (44)$$

where  $V$  is a  $N(0, \sigma^2)$  random variable independent of  $G$  with

$$\sigma^2 = N_0/T_c. \quad (45)$$

In order to assess the performance of this pulse counter detection of emission events, consider the probabilities:

$$\begin{aligned} P_d &= \text{probability of correctly detecting an emission event} \\ &= P((e W_c R) G + V \geq \gamma) \end{aligned} \quad (46)$$

and

$$\begin{aligned} P_f &= \text{false alarm probability of declaring an emission event} \\ &\quad \text{when it actually was absent} \\ &= P(V \geq \gamma). \end{aligned} \quad (47)$$

The statistics of the random PMT gain  $G$  are required to determine  $P_d$ . We shall use the approximate density (32) for this purpose. So it follows from (46) and (47) that

$$P_f = Q(\gamma/\sigma), \quad (48)$$

and

$$\begin{aligned} P_d &= \int_0^\infty P[V \geq \gamma - (e W_c R) x] p_G(x) dx \\ &= \int_0^\infty Q\left(\frac{\gamma - (e W_c R) x}{\sigma}\right) p_G(x) dx, \end{aligned} \quad (49)$$

where  $p_G(x)$  is given by (32) and

$$Q(x) \stackrel{\Delta}{=} \frac{1}{\sqrt{2\pi}} \int_x^{\infty} e^{-t^2/2} dt. \quad (50)$$

The plot of  $P_d$  versus  $P_f$  determines the receiver operating curve for this detection process. Figure 4 gives receiver operating curves for a 11-dynode PMT such as the RCA 31034 for various values of average gain  $\bar{G}$  when the counter bandwidth  $W_c$  and noise spectral density height  $N_0$  are fixed. The receiver operating curves improve with increasing average gain  $\bar{G}$  since the average pulse height increases with  $\bar{G}$ . Figure 5 shows receiver operating curves for fixed  $\bar{G}$  and  $N_0$  for various counter bandwidths  $W_c$ . Here the receiver operating curves improve with increasing  $W_c$  since the average pulse height increases linearly with  $W_c$  while the noise standard deviation  $\sigma$  increases only according to  $\sqrt{W_c}$ .

#### IV. Error Performance of a Binary Direct Detection Communication System

In this section we consider a direct detection optical communication system utilizing a PMT as a photodetector with a binary signalling scheme in which the signalling time period is divided into successive time slots of  $T_s$  seconds duration. A given slot is either a "noise slot", in which case no incident light from the transmitter light source is received at the PMT cathode, or a "signal slot," when incident light of constant intensity from the transmitter is received. The problem of concern here is to detect whether a given time slot is a signal slot or a noise slot based on the amplified PMT output in that time slot.

We shall consider a receiver which integrates the amplified PMT output during a slot time  $T_s$ , normalizes the integrator output by the integration time  $T_s$  and compares the result to a threshold  $\gamma$ . A signal slot is declared if and only if the threshold is exceeded. The error performance of this simple binary receiver shall be analyzed here.

A block diagram of this system is shown in Fig. 6. Let  $V(t)$  be the additive white Gaussian noise process with spectral density  $N_0$  given by (40) representing the thermal noise in the amplifier. Suppose

$N$  = number of electrons emitted at the photocathode during the slot time  $[0, T_s]$

and  $\{t_i\}_{i=1}^N$  are the emission times of those  $N$  electrons. Also suppose the electron emitted at time  $t_i$  undergoes a gain  $G_i$  through the PMT dynode chain. Since the PMT electron multi-

plication process operates independently on each electron emitted at the cathode, the gain random variables  $G_i$  are mutually independent. So, similar to (38), the PMT amplifier output process  $X(t)$  is given by

$$X(t) = (e W_p R) \sum_{i=1}^N G_i p(t - t_i) + V(t), \quad (51)$$

where  $p(t)$  is as before in (35). The number  $N$  of cathode emission events in the signal slot time can be assumed to be Poisson with intensity equal to the average number of electron emissions per slot time. In a noise slot, electron emissions are due to the PMT dark current, whereas in the signal slots they are due to both dark current and received light excitation. In particular, if  $H_1$  is the hypothesis of a signal slot and  $H_2$  is the hypothesis of a noise slot, then

$$P(N = n | H_i) = \frac{\alpha_i^n}{n!} e^{-\alpha_i}, n \geq 0, \quad (52)$$

where

$$\alpha_2 = \bar{N}_n$$

$$\stackrel{\Delta}{=} \text{average number of dark current cathode emissions per time slot}, \quad (53)$$

$$\alpha_1 = \bar{N}_n + \bar{N}_s, \quad (54)$$

and

$$\bar{N}_s = \text{average number of cathode emissions due to received light excitation per signal time slot}$$

$$= \frac{\eta P_s}{hf}. \quad (55)$$

In (55),  $\eta$  is the photocathode quantum efficiency,  $P_s$  is the incident signal light intensity at the cathode surface,  $h$  is Planck's constant and  $f$  the incident light center frequency.

It is reasonable to assume that the slot time  $T_s$  is greater than the PMT response time  $T_p$ . Then, since the detector statistic

$$X = \frac{1}{T_s} \int_0^{T_s} X(t) dt,$$

it follows from (36) and (51) that

$$X = \left( \frac{eR}{T_s} \right) \sum_{i=1}^N G_i + V, \quad (56)$$

where  $V$  is a  $N(0, \sigma_1^2)$  random variable with

$$\sigma_1^2 = \frac{N_0}{T_s}. \quad (57)$$

In order to determine the receiver's error performance, the distribution of

$$Y = \sum_{i=1}^N G_i \quad (58)$$

must be determined under each hypothesis  $H_i$ . This requires the PMT gain probability distribution, which is the common distribution of all the random variables  $G_i$  in (58). We shall use the approximate density (32) here. First consider the mgf  $\phi_Y(u|H_i)$  of  $Y$  under  $H_i$ :

$$\begin{aligned} \phi_Y(u|H_i) &= E(e^{-uY} | H_i) \\ &= E[E(e^{-uY} | N, H_i) | H_i]. \end{aligned} \quad (59)$$

Let  $\phi_G(u)$  be the mgf of each of the  $G_i$ s. Then

$$\begin{aligned} E(e^{-uY} | N=n, H_i) &= E \left[ e^{-u \sum_{i=1}^n G_i} \right] \\ &= [\phi_G(u)]^n. \end{aligned} \quad (60)$$

So (52), (59) and (60) yield

$$\begin{aligned} \phi_Y(u|H_i) &= \sum_{n=0}^{\infty} [\phi_G(u)]^n \frac{\alpha_i^n}{n!} e^{-\alpha_i} \\ &= e^{\alpha_i [\phi_G(u) - 1]}. \end{aligned} \quad (61)$$

Since we are using the density (32) as the density of each of the  $G_i$ s,  $\phi_G(u)$  is taken to be the mgf (20) of (32). So using (20) in (61) yields

$$\phi_Y(u|H_i) = e^{\alpha_i \left[ e^{-A/B} \exp\left(\frac{A/B}{1+Bu}\right) - 1 \right]}. \quad (62)$$

Finally we shall invert the mgf (62) to obtain the probability density  $p_Y(y|H_i)$  of  $Y$  under  $H_i$  by using a technique similar to (23) - (25). That is, rewrite (62) as

$$\begin{aligned} \phi_Y(u|H_i) &= e^{-\alpha_i} \sum_{n=0}^{\infty} \frac{(\alpha_i e^{-A/B})^n}{n!} \exp\left(\frac{nA/B}{1+Bu}\right) \\ &= e^{-\alpha_i} \sum_{n=0}^{\infty} \frac{(\alpha_i e^{-A/B})^n}{n!} \left[ 1 + \sum_{k=1}^{\infty} \frac{(nA/B)^k}{k!} \right. \\ &\quad \left. \cdot \frac{1}{(1+Bu)^k} \right] \\ &= e^{\alpha_i(e^{-A/B}-1)} + e^{-\alpha_i} \sum_{n=0}^{\infty} \sum_{k=1}^{\infty} \frac{(\alpha_i e^{-A/B})^n}{n!} \\ &\quad \cdot \frac{(nA/B)^k}{k!} \frac{1}{(1+Bu)^k}. \end{aligned} \quad (63)$$

Next, similar to (25), (63) is inverted by using (24) to yield

$$\begin{aligned} p_Y(y|H_i) &= e^{\alpha_i(e^{-A/B}-1)} \delta(y) + e^{-\alpha_i} \sum_{n=0}^{\infty} \frac{(\alpha_i e^{-A/B})^n}{n!} \\ &\quad \cdot \left[ \sum_{k=1}^{\infty} \frac{(nA/B^2)^k y^{k-1}}{k! (k-1)!} e^{-y/B} \right]. \end{aligned} \quad (64)$$

But, since

$$\begin{aligned} \sum_{k=1}^{\infty} \frac{(nA/B^2)^k y^{k-1}}{k! (k-1)!} e^{-y/B} &= e^{-y/B} \sqrt{\frac{nA}{y B^2}} \sum_{k=0}^{\infty} \\ &\quad \cdot \frac{\left( \frac{1}{2} \sqrt{4nAy/B^2} \right)^{2k+1}}{k! (k+1)!} \\ &= \frac{e^{-y/B} \sqrt{nA/y}}{B} I_1 \left( \frac{2\sqrt{nAy}}{B} \right), \end{aligned} \quad (65)$$

(64) and (65) together yield the following expression for  $p_Y(y|H_1)$ :

$$p_Y(y|H_1) = e^{\alpha_i(e^{-A/B}-1)} \delta(y) + \frac{\sqrt{A/y} e^{-(\alpha_i+y/B)}}{B} \sum_{n=0}^{\infty} \frac{\sqrt{n} (\alpha_i e^{-A/B})^n}{n!} I_1 \left( \frac{2\sqrt{nAy}}{B} \right), \quad (66)$$

where  $y \geq 0$ . Further reduction of (66) to a closed form expression does not appear to be possible.

The error performance of this binary communication system is specified by

$$\begin{aligned} P_{ds} &= \text{probability of correctly detecting a signal slot} \\ &= P(X \geq \gamma | H_1), \end{aligned} \quad (67)$$

and

$$\begin{aligned} P_{dn} &= \text{probability of correctly detecting a noise slot} \\ &= 1 - P(X \geq \gamma | H_2). \end{aligned} \quad (68)$$

So from (56) - (58), (67) and (68) we have

$$\begin{aligned} P_{ds} &= \int_0^{\infty} P \left( V \geq \gamma - \left( \frac{eR}{T_s} \right) y \right) p_Y(y|H_1) dy \\ &= \int_0^{\infty} Q \left( \frac{\gamma - \left( \frac{eR}{T_s} \right) y}{\sigma_1} \right) p_Y(y|H_1) dy, \end{aligned} \quad (69)$$

and similarly

$$P_{dn} = 1 - \int_0^{\infty} Q \left( \frac{\gamma - \left( \frac{eR}{T_s} \right) y}{\sigma_1} \right) p_Y(y|H_2) dy, \quad (70)$$

where  $\sigma_1$  is given by (57) and  $p_Y(y|H_i)$  is given by (66) with  $\alpha_i$  given by (53) and (54). Typical receiver operating curves of

$P_{ds}$  versus  $1 - P_{dn}$  are shown in Fig. 7 for various values of signal counts  $\bar{N}_s$  for fixed PMT average gain  $\bar{G}$ , slot time  $T_s$ , thermal noise spectral height  $N_0$  and dark current count  $\bar{N}_n$ . The receiver operating curve can be seen to improve with increasing  $\bar{N}_s$  as expected.

## V. Discussion

We have used a Markov diffusion approximation of the PMT electron multiplication process to obtain an approximate density for the PMT random gain. This approximate density was subsequently used to determine the receiver operating curve for a pulse counter detector of PMT cathode emission events. It was also used for analyzing the error performance of a simple on-off binary direct detection optical communication system. These latter results are used elsewhere (Ref. 13) to analyze the error performance of uncoded and coded PPM direct detection optical communication systems employing a PMT detector.

We have assumed here for simplicity that all the dynode stages in the PMT have identical average gain. In some applications, the first dynode stage has a higher average gain than the remaining stages, which have equal average gains. This is achieved by applying a higher interdynode voltage between the first two dynodes of the PMT. The methods in this paper can be extended to obtain an approximate density for the overall PMT gain in the situation as follows. Consider a  $\nu$ -stage PMT with overall average gain  $\bar{G}$  so that the first dynode stage average gain is  $\mu_1$ . Then the remaining  $\nu-1$  dynode stages have overall average gain equal to  $\bar{G}/\mu_1$ . Based on the assumptions discussed in Section II, it can be seen that the overall PMT gain has the same distribution as the number of collected anode electrons for a  $(\nu-1)$ -stage PMT with average gain  $\bar{G}/\mu_1$  when the number of cathode emissions is Poisson-distributed with mean  $\mu_1$ . Thus it follows from the results in Section IV that an approximate density for the overall PMT gain in this case is given by the density (66) with parameter  $\alpha_i = \mu_1$  and parameters  $A$  and  $B$  corresponding to the  $(\nu-1)$ -stage PMT with overall average gain  $\bar{G}/\mu_1$ . We note that for a PMT operated as such with higher first dynode stage gain, the probability density for the number of anode elections when the cathode emissions are Poisson-distributed is no longer represented by (66). However, the basic technique in Section IV can still be extended to obtain this latter density although yielding a more complex double series solution. It would be interesting to investigate ways of simplifying this series solution.

## References

1. Shockley, W., and Pierce, J. R., "A Theory of Noise for Electron Multipliers," *Proc. IPE*, Vol. 26, pp. 321-332, 1938.
2. Woodward, P.M., "A Statistical Theory of Cascade Multiplication," *Proc. Cambridge Phil. Soc.*, Vol. 44, pp. 404-412, 1948.
3. Harris, T. E., *The Theory of Branching Processes*, Springer-Verlag, Berlin, 1963.
4. Feller, W., "Diffusion Processes in Genetics," *Proc. Second Berkeley Symposium on Probability and Statistics*, Vol. II, 1951, pp. 227-246.
5. Delaney, C. G. F., and Walton, P. W., "Single Electron Spectra in Photomultipliers," *Nuclear Instruments and Methods*, Vol. 25, p. 353, 1964.
6. *RCA Photomultiplier Handbook*, 1980, p. 165.
7. Prescott, J. R., "A Statistical Model for Photomultiplier Single-Electron Statistics," *Nuclear Instruments and Methods*, Vol. 39, pp. 173-179, 1966.
8. Kobayashi, H., "Application of the Diffusion Approximation to Queueing Networks, I. Equilibrium Queue Distributions," *Journal of the Association for Computing Machinery*, Vol. 21, No. 2, pp. 316-328, 1974.
9. Wong, E., *Stochastic Processes in Information and Dynamical Systems*, McGraw Hill, New York, 1971.
10. Bartlett, M. S., *An Introduction to Stochastic Processes*, Cambridge Press, Cambridge, 1955.
11. Gagliardi, R., and Prati, G., "On Gaussian Error Probabilities in Optical Receivers," *IEEE Trans. Comm.*, Vol. 27, pp. 1742-1747, Sept. 1980.
12. Gagliardi, R., and Karp, S., *Optical Communications*, Wiley, New York, 1976.
13. Lesh, J., Katz, J., Tan, H., and Zwillinger, D., "The 2.5 Bit/Detected Photon Demonstration Program: Description, Analysis and Phase I Results," *TDA Progress Report 42-66*, pp. 115-132, 1981.

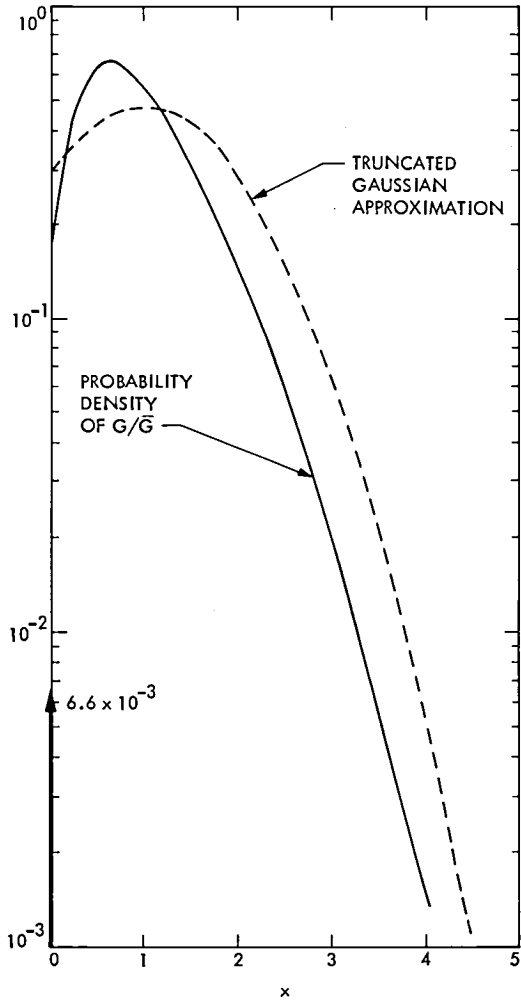


Fig. 1. Approximate probability density of  $G/\bar{G}$  for  $\bar{G} = 10^6$  and  $\nu = 11$

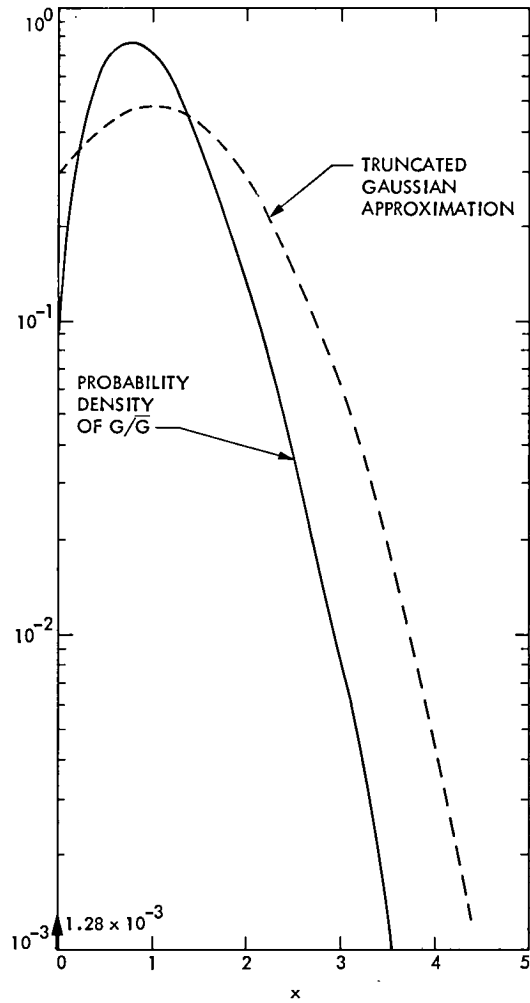


Fig. 2. Approximate probability density of  $G/\bar{G}$  for  $\bar{G} = 10^7$  and  $\nu = 11$

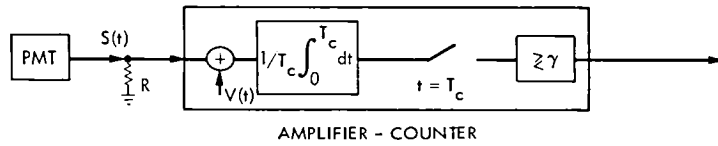


Fig. 3. Model for pulse counter detection of cathode emission events

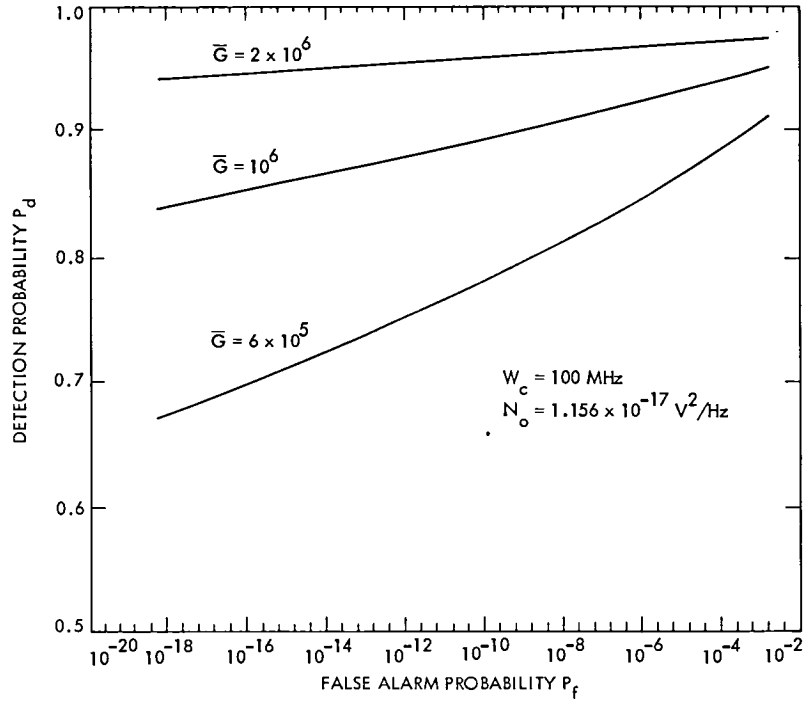


Fig. 4. Cathode emission event detection receiver operating curve as a function of PMT gain

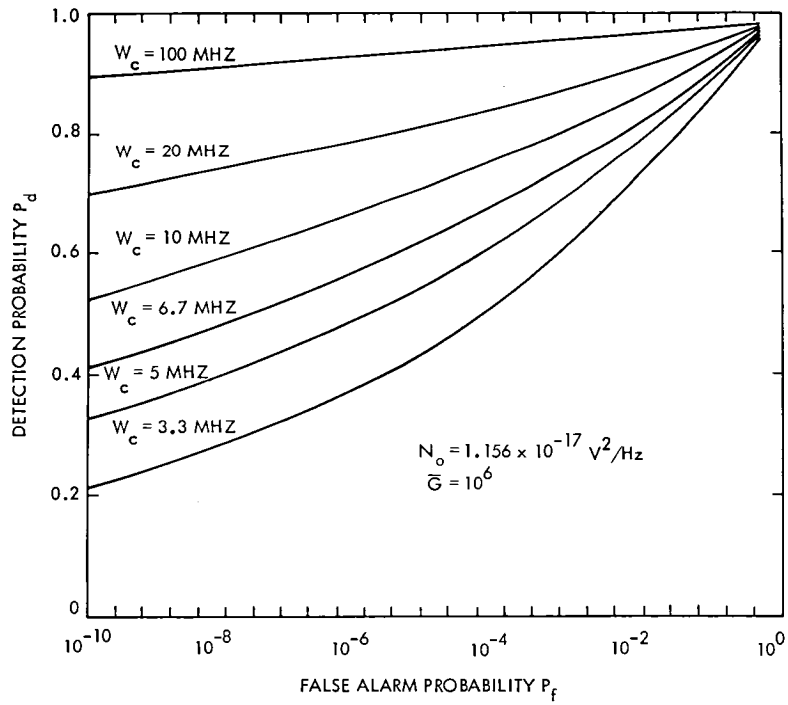


Fig. 5. Cathode emission event detection receiver operating curve as a function of counter bandwidth

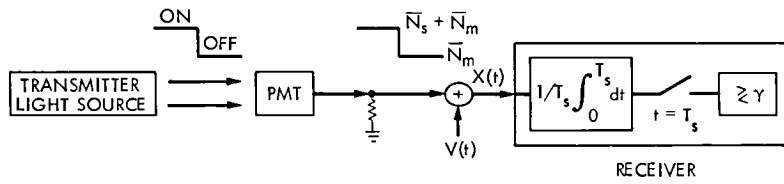


Fig. 6. Direct detection binary communication system

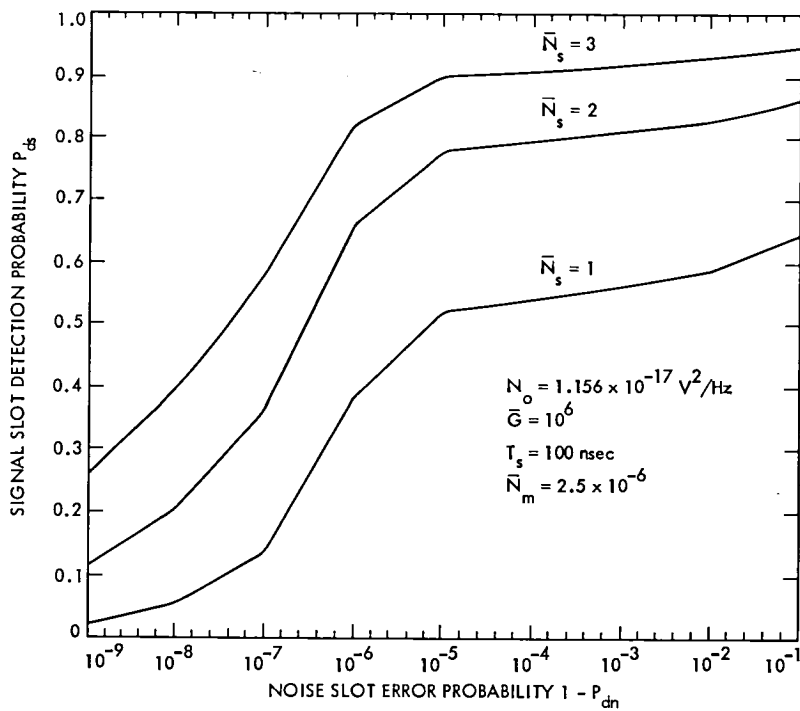


Fig. 7. Binary communication receiver operating curve as a function of  $\bar{N}_s$

# Evaluation of Waveguide Coating Materials

W. C. J. Chen and B. W. Baker  
Radio Frequency and Microwave Subsystems Section

*Waveguide coating materials were tested at 8470 MHz for insertion loss. Samples of these coatings on waveguide pieces without flanges were tested in an environmental chamber to simulate the effects of high power microwave heating.*

## I. Introduction

Stable high power handling is a requirement for some DSN tracking stations (Ref. 1). An improved X-band traveling wave resonant ring (Ref. 2) has been used in the past for high power tests and demonstrations. It was shown that stable (i.e., no arcing) CW high power could be obtained in the ring. However, copper waveguides without coating materials were used to construct the resonant ring, and no coating materials were evaluated at that time.

In a waveguide transmission system, surface finishes used for protection inside the waveguide play an important part in the value of attenuation measured. Cox and Rupp (Ref. 3) reported that good surface finish plus elimination of oxidation and corrosion are ways to minimize waveguide losses.

Acampora and Npioul (Ref. 4) studied the effects of surface roughness and particles on high power. They have observed that the presence of particles produces localized field enhancement and lowers the breakdown power.

This report covers three types of coating materials which were subjected to simulated high power and measured for insertion loss.

## II. Experimental Method

Insertion loss measurements were initially made to determine if there were any significant differences between coating materials. The measurement technique was the DC potentiometer microwave insertion loss method developed by Stelzried, Reid and Petty (Ref. 5).

A 60.96 centimeters (2 feet) piece sample of WR 112 waveguide was coated with one of the three coating materials and the insertion loss of the piece was measured. After each measurement the waveguide was stripped, cleaned and recoated with a different material. The three coating materials were Metcot 7<sup>1</sup>, BD-991<sup>2</sup> and Chemglaze R-104<sup>3</sup>.

A piece of clean waveguide without any coating and of the same length as the test samples was used as reference standard for calibration purposes.

The test input frequency was 8470 MHz. The experimental setup is shown in Fig. 1.

<sup>1</sup>Metcot 7, product of Allied-Kelite, Des Plaines Illinois.

<sup>2</sup>BD-991, product of National Chemsearch, Irving, Texas.

<sup>3</sup>Chemglaze R-104, product of Hughson Chemicals, Lord Corp., Erie, Pennsylvania.

WR 90 waveguides in the environmental chamber test were arranged for high power simulation. Sample waveguides with Metcot 7, BD-991, Chemglaze R-104 and plain waveguide cleaned with nitric acid for 15 seconds were cycled between 300°F (148.8°C) and 70°F (21.1°C) temperature for one month, which simulated DSN operation of the high power transmitters. Five ounce nitrogen gas flowed in the test chamber at all times. This simulates the nitrogen circulating in the waveguide in a field installation.

### III. Test Results

Each type of coating was measured consecutively 10 times. The standard plain waveguide was also measured 10 times for comparison. Results are shown as follows:

Waveguide samples	Average insertion loss, dB
Standard calibrated piece	0.04962
Metcot 7 coated	0.04727
BD-991 coated	0.04725
Chemglaze coated	0.04877

The plain waveguide without coating material has a rougher surface than the coated waveguide when examined with a microscope and the insertion loss is slightly higher than the coated guides, as expected. The insertion loss difference between the three types of coating is not considered significant.

The coated waveguides were examined by microscope before and after the environmental tests. The effects of the

RF heat simulation on the coated WR90 waveguides are summarized below and shown in Fig. 2.

Coated waveguide	Before test	After test
Metcot 7	Uniform coating surface, bright brown color	Coating surface nonuniformly distributed, color turns to deep brown gray; small peelings were observed
BD-991	Uniform coating distribution, bright brown color	Color turns to deep brown-gray; peelings were observed.
Chemglaze R-104	Uniform coating distribution, bright brown color	Coating still of uniform distribution, brown color; no peeling was observed.
Copper waveguide without coating, cleaned with nitric acid	Rough surface was observed, brown color	Color turns to dark gray; film was observed on the surface.

### IV. Conclusion

Test results indicated that three types of coating materials are acceptable with regard to insertion loss. However, simulated microwave heating caused debonding of Metcot 7 and BD-991 coatings, resulting in peelings in the waveguide. The higher cost Chemglaze R104 does not exhibit this problem.

### Acknowledgment

Vince Aneiro helped control the coating process.

## References

1. Hartop, R., and Bathker, D. A. "The High-Power X-Band Planetary Radar at Goldstone: Design, Development, and Early Results," *IEEE Trans. Microwave Theory and Techniques*, Vol. MTT-24, No. 12, pp. 958-963, Dec. 1976.
2. Chen, W. C. J., and Hartop R., "Improved Cooling Design for High Power Waveguide System," *The Telecommunications and Data Acquisition Progress Report 42-63, March and April 1981*, pp. 104-107, Jet Propulsion Laboratory, Pasadena, Calif., June 15, 1981.
3. Cox, R. M., and Rupp. W. E., "Fight Waveguide Losses 5 Ways," *Microwaves*, pp. 32-40, Aug. 1966.
4. Acampora, A. S., and Sproul, P. T., "Waveguide Breakdown Effects at High Average Power and Long Pulse Length," *The Bell System Technical Journal*, Vol. 51, No. 9, pp. 2065-2090, Nov. 1972.
5. Stelzried, C. T., Reid, M. S., and Petty, S. M., "A Precision DC Potentiometer Microwave Insertion Loss Test Set," *IEEE Trans. Instrumentation and Measurement*, Vol. IM-15 No. 3, pp. 98-106, Sept. 1966.

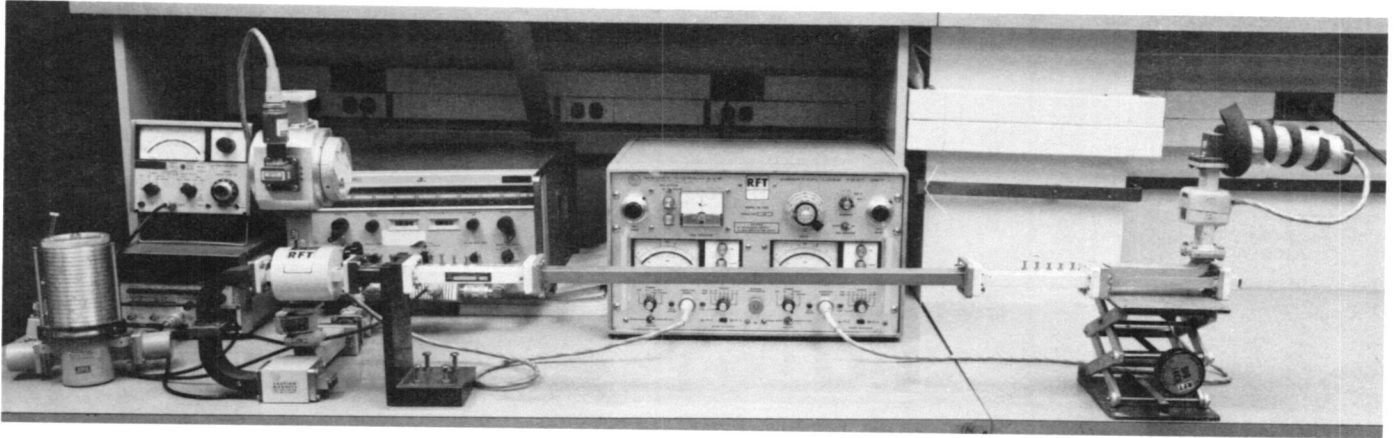


Fig. 1. Insertion loss measurement of sample X-band waveguide

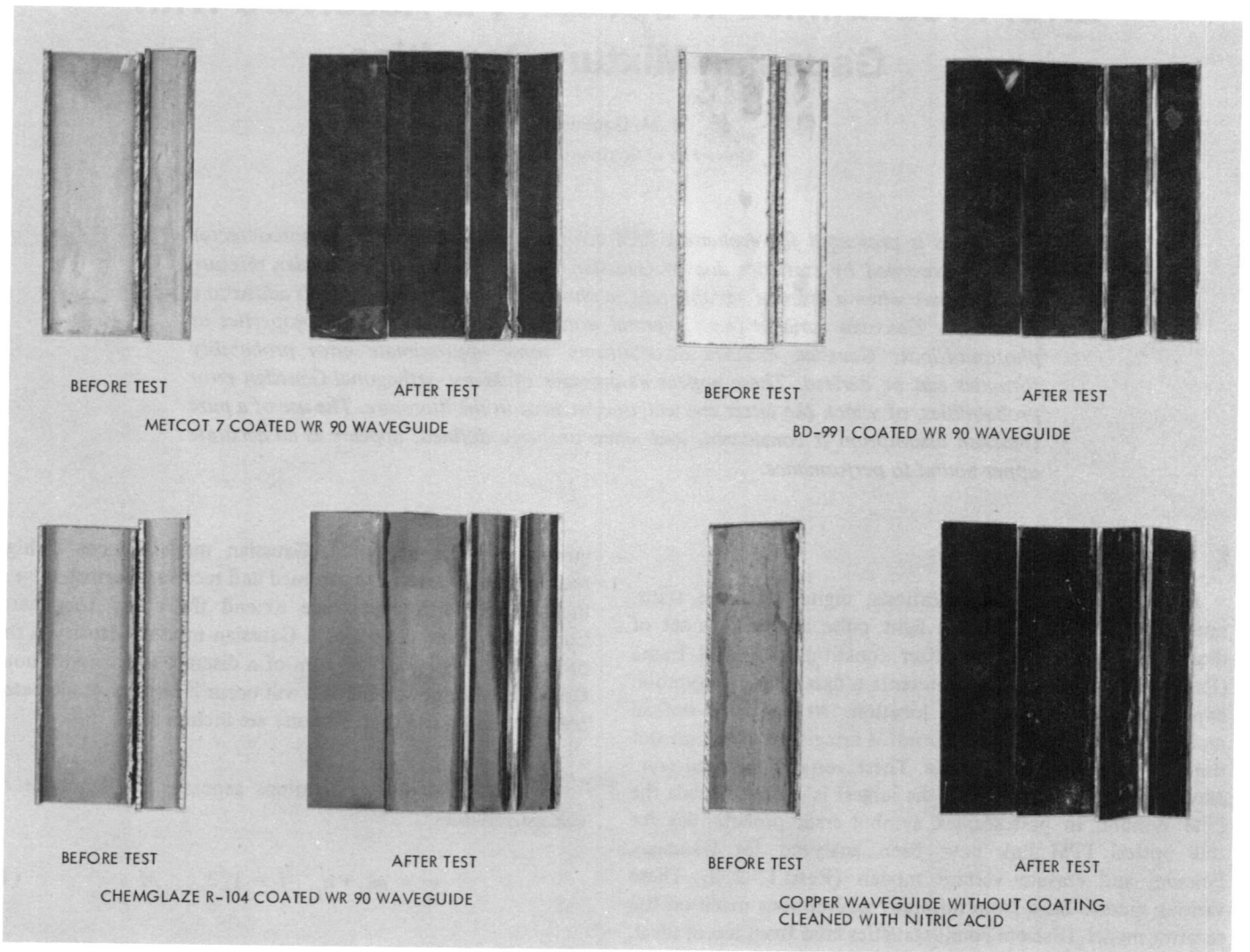


Fig. 2. Coated WR 90 waveguide samples before and after high power microwave heating simulation test

# Error Probabilities in Optical PPM Receivers With Gaussian Mixture Densities

R. M. Gagliardi  
University of Southern California

*Analysis is presented for evaluating PPM error probabilities in optical photodetector receivers governed by statistics due to Gaussian mixture densities. A Gaussian mixture density arises when a discrete variable (e.g., a photodetector count variable) is added to a continuous Gaussian variable (e.g., thermal noise). Making use of some properties of photomultiplier Gaussian mixture distributions, some approximate error probability formulas can be derived. These appear as averages of  $M$ -ary orthogonal Gaussian error probabilities, of which the latter are well documented in the literature. The use of a pure Gaussian assumption is considered, and when properly defined, appears as an accurate upper bound to performance.*

## I. Introduction

In optical PPM communications, digital data are transmitted by placing an optical light pulse in one of a set of designated pulse slots, the latter constituting a PPM frame (Ref. 1). Thus each pulse represents a data word, or symbol, depending on its pulse slot location. At the PPM optical receiver, the photodetected output is integrated over each slot time to generate a slot voltage. These voltages are then compared over a PPM frame, and the largest is used to decode the PPM symbol. In past studies, symbol error probabilities for this optical PPM link have been analyzed for Gaussian, Poisson, and erasure voltage models (Refs. 1, 2, 3). These various models arise from different assumptions made on the receiver model. Discrete count statistics arise from use of ideal, high-gain photomultipliers, for which receiver thermal noise is negligible, while erasure models occur if in addition back-

ground noise is neglected. Gaussian models occur if high receiver power levels are assumed and receiver thermal noise is included. In this report we extend the study to general Gaussian mixture densities. A Gaussian mixture density is the probability density of the sum of a discrete and a continuous Gaussian random variable and will occur if both photodetector count statistics and thermal noise are included.

Let the PPM slot integrations generate the sequence of voltage variables

$$y_j = ak_j + n_j, \quad j = 1, 2, \dots, M \quad (1)$$

where  $\{k_j\}$  is the discrete (count) sequence,  $M$  is the number of slots,  $a$  is a scalar, and  $\{n_j\}$  is a sequence of independent

Gaussian zero mean variables. The voltage variable  $y_j$  corresponds to that which would be generated from the integration of a photodetector output containing additive thermal noise. For this model the scalar corresponds to (Ref. 3)

$$a = eR_L/T \quad (2)$$

where

$e$  = electron charge

$R_L$  = photodetector load resistance

$T$  = slot integration time

The sequence  $k_j$  are independent count variables, in which the signaling slot has discrete count probabilities.

$$\text{Prob}(k_j = k) \stackrel{\Delta}{=} P_1(k) \quad (3)$$

while all other (nonsignaling) slots have

$$\text{Prob}(k_j = k) \stackrel{\Delta}{=} P_0(k) \quad (4)$$

The slots therefore generate a voltage  $y$  given by the mixture density

$$p_i(y) = \sum_{k=0}^{\infty} P_i(k) \Psi(y - ak), \quad i = 0, 1 \quad (5)$$

where

$$\Psi(y) = \frac{1}{\sqrt{2\pi}\sigma_n} e^{-y^2/2\sigma_n^2}$$

Here  $\sigma_n^2$  is the variance of the integrated Gaussian thermal noise variates. For the typical optical receiver at noise temperature  $T^\circ$

$$\sigma_n^2 = 4\kappa T^\circ R_L/T \quad (6)$$

where  $\kappa$  is Boltzmann's constant. We point out that, based on a true slot voltage comparison test among all slots, the PPM channel with mixture densities *cannot* be an erasure channel, since the probability of equal slot voltages (an erasure event) is always zero with continuous densities as in (5).

Although primary photoelectrons released from photo emissive surfaces are usually modeled as obeying a Poisson

process, secondary electrons generated via multi-anode secondary emissions as in photomultiplier vacuum tubes, or by avalanche mechanisms, as in avalanche photodetectors (APD), generally produce more symmetrical distributions. These photomultiplied electron distributions are usually modeled (Refs. 4, 5) with Gaussian-shaped discrete probabilities of the form

$$P_i(k) = \frac{C_i}{\sqrt{2\pi\sigma_{di}^2}} e^{-(k-Gm_i)^2/2\sigma_{di}^2}, \quad i = 0, 1 \quad (7)$$

where  $m_i$  is the mean primary count,  $G$  is the mean photodetector gain,  $C$  is a proportionately constant and  $\sigma_{di}$  is the standard deviation of the output counts. The parameter  $\sigma_{di}$  is often called the photodetector "spread," and typically

$$\sigma_{di}^2 = G^\delta m_i \quad (8)$$

where  $2 \leq \delta \leq 3$ . (For a photomultiplier tube  $\delta \cong 2$ , while for an APD,  $\delta \cong 3$ ). The coefficient  $C_i$  in (7) is defined by

$$C_i^{-1} = \frac{1}{\sqrt{2\pi\sigma_{di}^2}} \sum_{k=0}^{\infty} e^{-(k-Gm_i)^2/2\sigma_{di}^2} \quad (9)$$

For  $Gm_i \geq 10$ ,  $C$  is almost identically unity. The PPM symbol error probability, based on a comparison test among the  $M$  slot voltage, is then given by

$$\text{PSE} = 1 - \int_{-\infty}^{\infty} p_1(y) \left[ \int_{-\infty}^y p_0(x) dx \right]^{M-1} dy \quad (10)$$

The bracketed term corresponds to the distribution function of the mixture density  $p_0(x)$ . This distribution function can be written as

$$\int_{-\infty}^y p_0(x) dx = F\left(\frac{y - aGm_0}{\sigma_0}\right) [1 + \epsilon(y)] \quad (11)$$

where

$$F(y) = \int_{-\infty}^y \frac{1}{\sqrt{2\pi}} e^{-t^2/2} dt \quad (12)$$

$$\sigma_0^2 = a^2 \sigma_{d0}^2 + \sigma_n^2 \quad (13)$$

and  $\epsilon(y)$  is the fractional error in representing the left side of (11) by a Gaussian distribution function. Extensive studies

(Refs. 3, 6) have shown that  $|\epsilon(y)|$  is extremely small. Figure 1a, extracted from Ref. 4, shows how the magnitude  $|\epsilon(y)|$  behaves under the condition  $\sigma_{d0} = \sigma_n = \beta$  for  $y \geq 0$ . The magnitude function is monotonic in either  $\sigma_{d0}$  or  $\sigma_n$ , and is essentially constant for all  $y \geq 0$ . Figure 1b replots  $|\epsilon(y)|$  as a function of  $\beta$  for several values of  $y$ . These results simply state that if the variances of the discrete count and the continuous added noise are each large enough, the Gaussian mixture density loses its "discreteness" in integration. Furthermore the resulting integral is within  $|\epsilon|$  of integrating an equivalent Gaussian density with the same mean and combined variance. In essence, the Gaussian mixture density behaves as a continuous Gaussian density, as far as integration is concerned.

With (11), the PPM mixture error probability becomes

$$PSE = 1 - \int_{-\infty}^{\infty} p_1(y) \left[ F\left(\frac{y - aGm_0}{\sigma_0}\right) \right]^{M-1} [1 + \epsilon(y)]^{M-1} dy \quad (14)$$

where  $\epsilon(y)$  can be either positive or negative at each  $y$ , with its magnitude plotted in Fig. 1. We can immediately write

$$[1 + \epsilon(y)]^{M-1} \geq [1 - |\epsilon_\beta|]^{M-1} \quad (15)$$

where  $|\epsilon_\beta| = |\epsilon(\infty)|$ , and we use the subscript  $\beta$  to indicate that we have assumed  $\sigma_{d0} = \beta$  and  $\sigma_n/a = \beta$  in evaluating  $\epsilon(\infty)$ . (For all purposes  $\epsilon_\beta$  can be taken as the variable in the plot in Fig. 1b at  $y = 10$ ). We can therefore bound the integral in (14) as

$$\int_{-\infty}^{\infty} p_1(y) F^{M-1}\left(\frac{y - aGm_0}{\sigma_0}\right) [1 + \epsilon(y)]^{M-1} dy \geq [1 - |\epsilon_\beta|]^{M-1} P_c \quad (16)$$

where

$$P_c = \int_{-\infty}^{\infty} p_1(y) \left[ F\left(\frac{y - aGm_0}{\sigma_0}\right) \right]^{M-1} dy \quad (17)$$

This also means

$$PSE \leq 1 - [1 - |\epsilon_\beta|]^{M-1} P_c \quad (18)$$

Hence the right side serves as an upper bound to PSE. To evaluate this bound, we can write

$$P_c = \int_{-\infty}^{\infty} p_1(y) \left[ F\left(\frac{y - aGm_0}{\sigma_0}\right) \right]^{M-1} dy = \sum_{k=0}^{\infty} P_1(k) \Phi(M, k) \quad (19)$$

with

$$\Phi(M, k) \triangleq \int_{-\infty}^{\infty} \Psi\left(\frac{y - ak}{\sigma_n}\right) \left[ F\left(\frac{y - aGm_0}{\sigma_0}\right) \right]^{M-1} dy \quad (20)$$

We recognize  $\Phi(M, k)$  as the probability that a Gaussian variable with mean  $ak$  and variance  $\sigma_n^2$  exceeds  $M - 1$  independent Gaussian variable with mean  $aGm_0$  and variance  $\sigma_0^2$ . This  $\Phi$  is simply the detection probability associated with  $M$  Gaussian orthogonal variable, with the correct one having mean  $(ak - aGm_0)$ , all incorrect having mean zero, and all have variance  $(\sigma_n^2 + \sigma_0^2)$ . These detection probabilities are known (Ref. 7) to depend only on the number of variables  $M$  and the signal-to-noise ratio  $\rho$ , the latter defined by

$$\rho = \frac{(ak - aGm_0)^2}{\sigma_0^2 + \sigma_n^2} = \frac{(k - Gm_0)^2}{(\sigma_0^2 + \sigma_n^2)/a^2} \quad (21)$$

Thus we can rewrite (20) as simply

$$\Phi(M, k) = PD(M, \rho(k)) \quad (22)$$

where  $PD(M, \rho)$  is the  $M$ -ary Gaussian word detection probability at an  $E_b/N_0$  of  $\rho$ . This forms (19) as the average, over  $k$ , of a Gaussian  $M$ -ary word detection probability whose bit energy is  $(k - Gm_0)^2$ .

Some useful approximations to this  $PSE$  bound can be derived. For example, since  $(1 - \epsilon)^{M-1} \geq 1 - M\epsilon$  we can write

$$PSE \leq 1 - (1 - M|\epsilon_\beta|) P_c = (1 - P_c) + M|\epsilon_\beta| P_c \quad (23)$$

The first term is now an average word error probability, while the second appears as a correction term. Clearly, if  $M|\epsilon_\beta| \ll 1 - P_c$ , the correction term can be neglected. This simply requires the discrete integration error plotted in Fig. 1 to be significantly less than  $1/M$  times the desired word error probability. In this case, the bound  $1 - P_c$  can be evaluated by

simply averaging the Gaussian word error probabilities instead of evaluating (22). This means

$$PSE \leq \sum_{k=0}^{\infty} P_1(k) PWE(M, \rho(k)) \quad (24)$$

where  $PWE(M, \rho)$  is the Gaussian word error probabilities (Ref. 7) of an  $M$ -ary test with an  $E_b/N_0$  of  $\rho$ . Equation (24) can be further evaluated by introducing the union bound to the Gaussian  $PWE$ :

$$PWE(M, \rho) \leq \frac{M-1}{2} e^{-\rho/2} \quad (25)$$

Equation (24) becomes

$$PSE \leq \frac{M-1}{2} \sum_{k=0}^{\infty} P_1(k) e^{-(k-Gm_0)^2/2\sigma^2} \quad (26)$$

where we have used

$$\sigma^2 \triangleq \sigma_{d0}^2 + (2\sigma_n^2/a^2) \quad (27)$$

For the discrete count distribution of (7) we have

$$PSE \leq \left(\frac{M-1}{2}\right) \left(\frac{C_1}{\sqrt{2\pi\sigma_{d1}^2}}\right) \sum_{k=0}^{\infty} \exp - \left[ \frac{(k - aGm_1)^2}{2\sigma_{d1}^2} + \frac{(k - Gm_0)^2}{2\sigma^2} \right] \quad (28)$$

Algebraically combining inside the summand yields

$$PSE \leq \left\{ \left(\frac{M-1}{2}\right) \exp \left[ \frac{-G^2(m_1 - m_0)^2}{2(\sigma_{d1}^2 + \sigma_{d0}^2 + 2\sigma_n^2/a^2)} \right] \right\} g(m_1, m_0) \quad (29)$$

where

$$g(m_1, m_0) = \sum_{k=0}^{\infty} \frac{C_1}{\sqrt{2\pi B}} e^{-(k-A)^2/2B^2}$$

$$A = \frac{\sigma^2 G m_1 + \sigma_{d1}^2 G m_0}{\sigma_{d1}^2 + (\sigma^2/a^2)}$$

$$B^2 = \frac{\sigma^2 \sigma_{d1}^2 / a^2}{\sigma_{d1}^2 + (\sigma^2/a^2)} \quad (30)$$

The term in braces is simply the  $M$ -ary union bound based on the mean primary counts  $m_1$  and  $m_0$ . The  $g$  parameter represents a modification of this bound caused by the mixture density models. Again, if  $Gm_1$  and  $Gm_0$  are large,  $g(m_1, m_0)$  will be almost identically one. In this case the bracket accurately estimates performance and corresponds to the result that would be computed from a purely Gaussian assumption on all receiver statistics.

If we assume  $g = 1$ , substitute from (8) and divide through by  $G^2$  in the exponent of (29) we have

$$PSE \leq \frac{M-1}{2} \exp \left[ - \frac{(m_1 - m_0)^2/2}{F(m_1 + m_0) + 2\sigma_n^2/a^2 G^2} \right] \quad (31)$$

where  $F = G^\delta/G^2$  is referred to as the excess noise factor of the photomultiplier. Note that the denominator represents the usual shot noise-plus-thermal noise contributions obtained in optical receiver analysis.

## II. Conclusion

An analysis is presented for determining the symbol error probability of an optical, direct detection, PPM communication system when background noise, nonideal photomultipliers, and postdetection thermal noise are included. This study extends earlier studies based on pure count statistics and simple Gaussian noise models. The effect of the nonideal photomultiplication is to redistribute the count statistics into more symmetrical discrete distribution from those used earlier. The additive thermal noise adds to this density, providing a combined continuous density for the PPM slot integration variables. This combined discrete and Gaussian variable, referred to here as a mixture density, interconnects the earlier discrete count and Gaussian models. When the photomultiplier is high gain and ideal, the count statistics prevail. However, nonideal and low gain devices redistribute the counts, and additive noise can no longer be neglected.

Earlier published results have contended that the redistributed counts appear to have a discrete Gaussian envelope model. It is shown here that under this model the mixture densities begin to behave as a continuous Gaussian density as far as computing error probabilities is concerned. This allows Gaussian  $M$ -ary word error probabilities to be used to estimate performance, with signal-to-noise ratio obtained from the usual squared mean to variance ratios. Thus, even though detector statistics are not Gaussian, performance appears to be adequately obtained from Gaussian performance curves.

## References

1. Gagliardi, R., and Karp, S., *Optical Communications*, Wiley, 1976, Chapter 8.
2. Massey, J. L., "Capacity, Cut-off Rate, and Coding for a Direction Detection Optical Channel," *IEEE Trans. Comm.*, Vol. COM-26, Nov. 1981.
3. Gagliardi, R., and Prati, G., "On Gaussian Error Probabilities in Optical Receivers," *IEEE Trans Comm.*, pp. 1742-1747, Sept. 1980.
4. McIntyre, R., "Distribution of Gains in Avalanche Photodiodes: Theory," *IEEE Trans. Electron Devices*, pp. 703-712, June 1972.
5. Conradi, J., "Distribution of Gains in Avalanche Photodiodes: Experimental," *IEEE Trans. Electron Devices*, pp. 713-718, June 1972.
6. Prati, G., and Gagliardi, R., "Encoding and Decoding for Optical PPM Channel," *IEEE Trans. IT*, pp. 88-92, Jan. 1982.
7. Lindsey, W. and Simon, M., *Telecommunication System Engineering*, Prentice-Hall, Chapter 6.

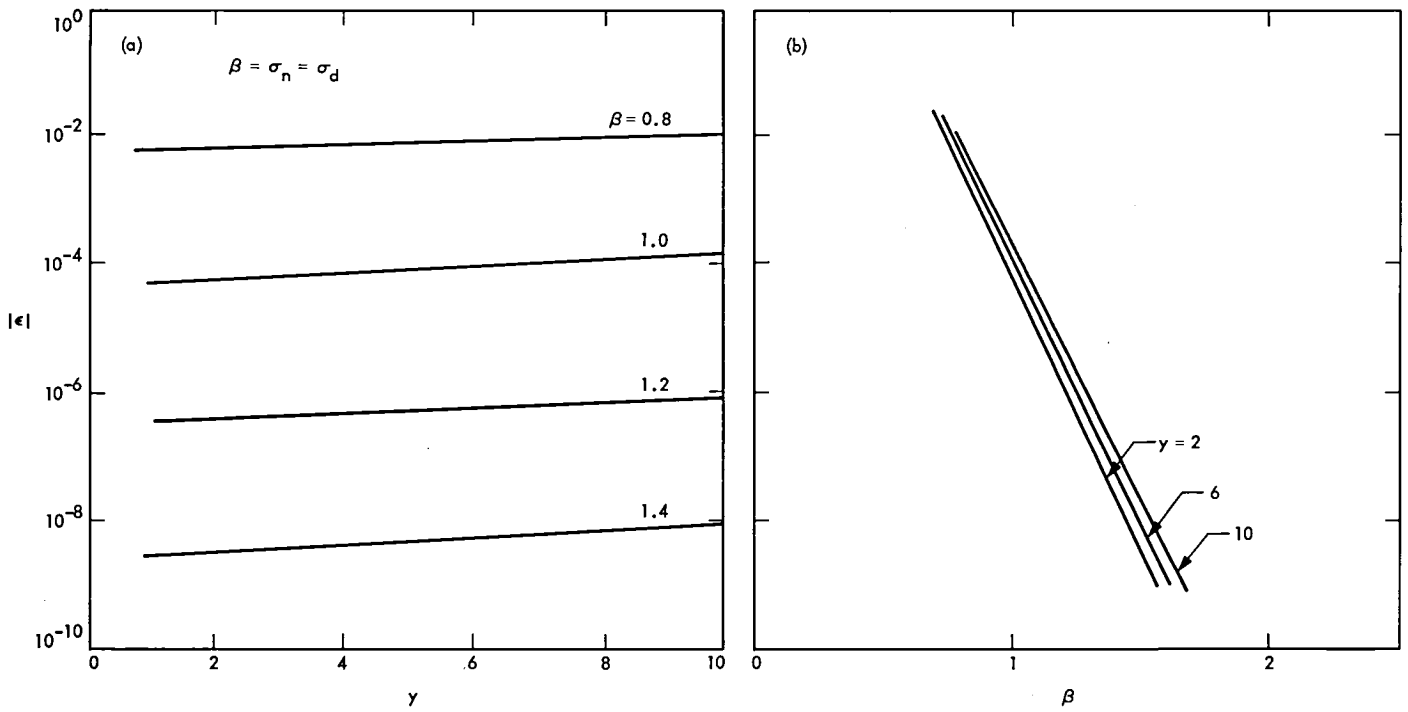


Fig. 1. Fractional error in replacing mixture distribution in  $y$  by Gaussian distribution with same mean and variance,  $\sigma_n^2 =$  thermal noise variance;  $\sigma_d =$  photon detector spread

# An Automated FORTRAN Documenter

T. Erickson

Tracking Systems and Applications Section

*We have written a set of programs designed to help R&D programmers document their FORTRAN programs more effectively. The central program reads FORTRAN source code and asks the programmer questions about things it has not heard of before. It inserts the answers to these questions as comments into the FORTRAN code. The comments, as well as extensive cross-reference information, are also written to an unformatted file. Other programs read this file to produce printed information or to act as an interactive document.*

## I. Introduction

Documentation is a continuing problem in software development: programmers don't like to produce it, much of it is never used, it takes up shelf space, time, and nervous energy. Yet we can't get along without it. We too easily forget how programs are put together and how to run them. After a week away from a program, undocumented variable names and subroutine calls may seem like hieroglyphics even to their well-intentioned author.

One solution has been to insist that programmers adhere to strict documentation standards in spite of the time required and the paper produced. Every routine must be flowcharted, every variable explained. This has been applied to implementa-

tion programming with some success, but it has never gained a foothold with programmers doing research and development (R&D).

Programs produced in an R&D environment still tend, as a rule, to be documented poorly. We cannot possibly calculate the time lost in program development due to forgetting, or the time lost when maintenance or implementation programmers can't figure out what the original author meant. Just why R&D programmers are so resistant to standardized programming practices is not clear. It may be their varied backgrounds: they can't be fit into the same molds. Maybe it's their academic histories: the programming techniques needed for thesis research seldom require documentation for other users or maintenance programmers. Perhaps it's natural stubbornness

reacting to a “waste of time,” or the eagerness to get on to the next problem “now that this routine is working.” As to flow-charting routines before coding, the R&D programmer often does not know what algorithm is going to solve a problem best until the program runs.

Whatever the reasons for poor R&D documentation, something must be done. RNDOC (an R&D DOCumenter) and its family are interactive tools especially designed to help R&D programmers document their programs effectively and painlessly. It is designed first to help the programmer remember things that need remembering. Later versions will pay more attention to the needs of other programmers and the users of the programs.

## II. How RNDOC Works

RNDOC is the name of the central program in this set of tools. It actually reads the FORTRAN code being documented; the other tools require output from RNDOC as well. It's being developed in FORTRAN 77 on a VAX 11/780 under the VMS operating system. It can be used to document programs written in FORTRAN and Structured FORTRAN. We will discuss its portability to other computers and other languages later.

RNDOC is basically a simple parser that decomposes lines of code into FORTRAN symbols and constants. We should briefly discuss the structures RNDOC can currently recognize in FORTRAN code. The first structure RNDOC recognizes is the whole *program*, whose name it gets from the user or from a PROGRAM statement. The program consists of one or more *modules* (functions, subroutines, and the main program), which in turn reside in one or more regions on the disk called *files*. Files may contain more than one module. For each module it encounters, RNDOC records the file it is in, so that it (and the user) will always know where to find the code. This is very simple, but even this saves time for a forgetful programmer. Within modules, RNDOC identifies arguments, common areas, I/O units, declared variables, and undeclared variables. For example, in the FORTRAN 77 code fragment

```
SUBROUTINE DISPLAY (lun)
character*6 symb
integer lunlim, x(10)
common/DISCOM/  lunlim, x
DO i = lun, lunlim
write (i, 100) x, symb (x(10))
END DO
```

RNDOC will recognize the beginning of module **DISPLAY**, its argument **lun**, the common area **DISCOM**, the declared variables **lunlim** and **x**, which are also recognized as an array, the undeclared variables **i** and **lun**, the I/O unit **lun**, and the function **symb**. It will also record obvious relationships between these names: **DISCOM** is found in **DISPLAY**, **symb** is called by **DISPLAY**, **lunlim** and **x** reside in **DISCOM**, **i** is local to **DISPLAY**, and so forth. To carry the example further, if RNDOC has not yet heard of **symb**, it will ask the user for a comment. Now RNDOC knows that the program uses the *module symb*, though it will not know what *file symb* is in until it comes across

Character\*6 FUNCTION Symb(j)

The user can set RNDOC to prompt for comments at various levels; RNDOC always requires comments for modules and arguments, but the user can choose whether to comment every variable. Furthermore, the user can “table” or postpone comments, or get a display of the section of code where a symbol was found.

At the end of a module, when RNDOC encounters a FORTRAN “END” statement, the user may quit, leaving RNDOC, or continue to other modules in the file. At the end of the file, the user can choose to write a new copy of the code with all new comments in place. Figure 1 shows schematically how RNDOC works.

## III. An Example

Imagine that we have written a FORTRAN program to calculate primes. It looks like this:

In file PRIME.FOR:

```
PROGRAM Prime
implicit integer (a-z)
dimension primes(1000)
call getnum(n, 'How many primes do you want to calculate?')
primes(1) = 2
DO i=2, n
call FindNextPrime(i, primes)
END DO
```

```

100      write(6,100) n,primes(n)
        format(' prime number ',i5,' is ',i6)
        call getnum(m,'How many primes do you want to type out?')
        DO i=1,m
          Write(6,100)i,primes(i)
        END DO
        call exit
        end

SUBROUTINE getnum(n,string)
character*(*) string
write (6,100) string
100      format('$',a,x)
        read (5,'(i10)') n
        return
        end

```

In file PRIMESUB.FOR:

```

SUBROUTINE FindNextPrime(i,Primes)
implicit integer (a-z)
dimension primes(1)
logical*1 IsTestPrime
test = primes(i-1)
DO WHILE (.true.)
  test = test + 1
  IF (IsTestPrime(test,primes,i)) THEN
    primes(i) = test
    return
  ENDIF
END DO
END

LOGICAL*1 FUNCTION IsTestPrime(test,primes,i)
implicit integer (a-z)
dimension primes(1)
DO j=1,i-1
  IF (mod(test,primes(j)) .eq. 0) THEN
    IsTestPrime = .false.
    return
  ELSE IF (primes(j)**2 .gt. test) THEN
    IsTestPrime = .true.
    return
  ENDIF
END DO
IsTestPrime = .true.
return
END

```

This program has been deliberately broken into subroutines for the purposes of this example. Let's see how parts of an RNDOC session would look at the terminal. In the following example, **boldface** text is typed by the user. Annotations appear in italics in the right hand column. On the VAX,

control-Z is the end-of-file character, and will be indicated by [^Z].

\$ run rndoc

enter name of program: **PRIME**

do you want to skip old comments? yes

Do you want to document variables other than arguments?  
no

CREATING A NEW DOCUMENTATION FILE: prime.rnd

```
-----  
----- CURRENT STATUS -----  
----- UNFOUND MODULES: -----  
                none  
-----
```

*RNDOC hasn't ever seen program PRIME before; it needs to create a new unformatted documentation file. Our next session will begin by reading the file we create here.*

Enter filename (ctrl-z to quit, SYS for system): prime.for

FOUND a reference to your main program, PRIME:  
PROGRAM PRIME

*RNDOC types the line of code where the reference is found.*

Type in your comment (ctrl-z ends):

**This is a program to calculate the first "n" primes, where "n" is a parameter typed in by the user. [^Z].**

OKAY. Thanks.

```
----- ENTERING MODULE PRIME -----
```

FOUND a reference to the routine GETNUM:

call getnum (n, 'How many primes do you want to calculate?')

Type in your comment (ctrl-z ends):

**This routine gets an integer from the keyboard, prompting the user with the string argument. [^Z]**

OKAY. Thanks.

*RNDOC types the line of code where the reference is found.*

*If we had answered simply with a control-z, RNDOC would have typed the section of code surrounding the reference. This goes on, getting comments for modules FindNextPrime and Exit, until. . .*

END encountered in module PRIME.

Do you want to quit looking at PRIME. FOR? no

```
----- ENTERING MODULE GETNUM -----
```

Reconciling variables in module GETNUM:

We need a comment for variable "n" in module GETNUM.

Type in your comment (ctrl-z ends):

**OUTPUT: the number returned as data to the calling program. [^Z]**

OKAY. Thanks.

*Routine GETNUM is in the same file as PRIME, the main program. As we've already commented this routine, and have asked to skip old comments, it doesn't ask us about it.*

*At the end of the module, RNDOC checks its list of variables to see which need commenting. Though we asked not to be bothered about ALL variables, it always requires comments for arguments.*

We need a comment for variable "string" in module GETNUM.

Type in your comment (ctrl-z ends):

**INPUT: the string used to prompt the terminal for the number. [^Z]**

OKAY. Thanks.

END encountered in module GETNUM.

Do you want to quit looking for PRIME.FOR? no

END OF FILE found in PRIME.FOR.

Do you want to write a new copy of it? Yes

*Here RNDOC writes the new copy of the code, which can be seen on the following page.*

```

-----
----- CURRENT STATUS -----
----- UNFOUND MODULES: -----
          FINDNEXTPRIME
          EXIT
          2 modules in all
-----

```

enter filename (ctrl-z to quit, SYS for system):

primesub.for

*This module was commented when its call was found in the main program. We aren't asked now, but RNDOC records that this module is found in file PRIMESUB.FOR.*

```

----- ENTERING MODULE FINDNEXTPRIME -----

```

FOUND a reference to some FUNCTION named INTEST-PRIME:

IF (IsTestPrime(test,primes,i)) THEN

Type in your comment (ctrl-z ends):

*This continues until the end of file, including comments for arguments.*

.  
.
.

END OF FILE found in PRIMESUB.FOR.

Do you want to write a new copy of it? Yes

```

-----
----- CURRENT STATUS -----
----- UNFOUND MODULES: -----
          EXIT
          MOD
          2 modules in all
-----

```

enter filename (ctrl-z to quit, SYS for system):

SYS

*The remaining "unfound" modules can be flagged as system routines.*

Is EXIT a system routine? yes

Is MOD a system routine? yes

```

-----
----- CURRENT STATUS -----
----- UNFOUND MODULES: -----
          none
-----

```

enter filename (ctrl-z to quit, SYS for system): [^Z]

and we are done.

Here is what the rewritten code looks like:

```
PROGRAM Prime
C.
C. MODULE PRIME
C. This is a program to calculate the first "n" primes, where
C. "n" is a parameter typed in by the user.
C.
C. .... ARGUMENTS. ....
C. --none--
C. .... MODULES CALLED. ....
C. EXIT closes all files and stops execution.
C.
C. FINDNEXTPRIME updates a list of the first (i-1) primes by
C. putting the ith prime in position i.
C.
C. GETNUM This routine gets an integer from the keyboard,
C. prompting the user with the string argument.
C.
C. .... COMMON BLOCKS. ....
C. --none--
C.
C processed by RNDQC 20-OCT-81 10:28:21 for program PRIME
implicit integer (a-z)
dimension primes(1000)
call getnum(n,'How many primes do you want to calculate?')
primes(1) = 2
DO i=2,n
call FindNextPrime(i,primes)
END DO
write(6,100) n,primes(n)
100 format(' prime number ',i5,' is ',i6)
call getnum(m,'How many primes do you want to type out?')
DO i=1,m
Write(6,100)i,primes(i)
END DO
call exit
end

SUBROUTINE getnum(n,string)
C.
C. MODULE GETNUM
C. This routine gets an integer from the keyboard, prompting
C. the user with the string argument.
C.
C. .... ARGUMENTS. ....
C. N OUTPUT: the number returned as data to the
C. calling program.
C.
C. STRING INPUT: the string used to prompt the terminal
C. for the number.
C.
C. .... MODULES CALLED. ....
C. --none--
C. .... ENTRY POINTS. ....
C. --none--
C. .... COMMON BLOCKS. ....
C. --none--
C.
C processed by RNDQC 20-OCT-81 10:28:21 for program PRIME
character*(*) string
write (6,100) string
100 format('$',a,x)
read (5,'(i10)') n
return
end
```

The other file, PRIMSUB.FOR, has been similarly commented. The unformatted documentation file, PRIME.RND, is now also on disk, and contains all the comments, module locations, and cross-reference information.

#### IV. Other Tools

We are designing and writing other tools to work with RNDOC to make R&D documentation easier. Generally, they read RNDOC's unformatted output and allow for code display if it is needed. They are interactive, and their displays are designed for a CRT. For the most part, these tools act as interactive documents without producing printout. Their functions include the following:

- (1) Module list: for each module in a program, lists the name of the file where it resides, its comment, the modules it calls, the modules that call it, its arguments, and the common areas it hosts.
- (2) Call tree: graphically displays which modules call which for all the modules in a program.
- (3) Comment editor: lets you change a particular comment without rerunning RNDOC.
- (4) Variable cross-reference: displays all lines of code in a program where a particular variable occurs.
- (5) Index searches: lets you look for a string or a word in all the comments and symbol names of a program in order to find some forgotten bit of information.

Here is an example of the use of such tools: suppose you have seen an output error in a large program. Instead of looking at the output routine to rediscover the name of the variable that is at least a symptom of the problem, you remember that it has something to do with "delay." You do an index search on "delay," and discover five variables whose comments contain that word. You probably recognize which one is the one you want from the names and comments. Having settled on **ZDLY** as the variable you are after, a variable cross-reference search will show all the lines *in all modules* of the program where **ZDLY** appears. You can use a general-purpose editor to make the appropriate changes to the code, and see if

your solution worked. If it did you make changes to affected comments using the comment-editing tool.

#### V. Portability

Portability has also influenced the design of RNDOC. It is the main reason to read code and not listings — even though listings have a lot of useful information in them — as listing format changes from compiler to compiler.

RNDOC should be easy to run under any virtual memory operating system that supports FORTRAN 77. For smaller systems without virtual memory, the job will be harder but not impossible. Basically, parameters governing the size of arrays should be reduced, and the most space-consuming arrays changed to functions reading scratch direct-access files. RNDOC's response time will grow accordingly. As to host language requirements, RNDOC and its family rely heavily on the FORTRAN "character" data type, so versions of FORTRAN which do not support it will not support these tools.

Structured FORTRAN code can be processed by RNDOC, through each version of Structured FORTRAN must be tested thoroughly to ensure that RNDOC understands its particular methods of describing IF-structures and procedure calls. RNDOC's techniques could be used on other languages, such as Pascal; that would require major changes in the parser, and besides, excellent off-the-shelf Pascal Development Systems make such a program unnecessary.

#### VI. Current Work and Future Plans

The RNDOC project is currently working to improve the processing of I/O references, to improve the portability to systems smaller than the VAX, and to ensure upward compatibility of current comments and unformatted files with future versions of RNDOC.

Future versions of this software will include run-time flow information and recognition of structured blocks of code (DO-or IF-blocks). We are also continuing to try to find out just what documentation R&D programmers and their maintenance and implementation heirs need to program more effectively.

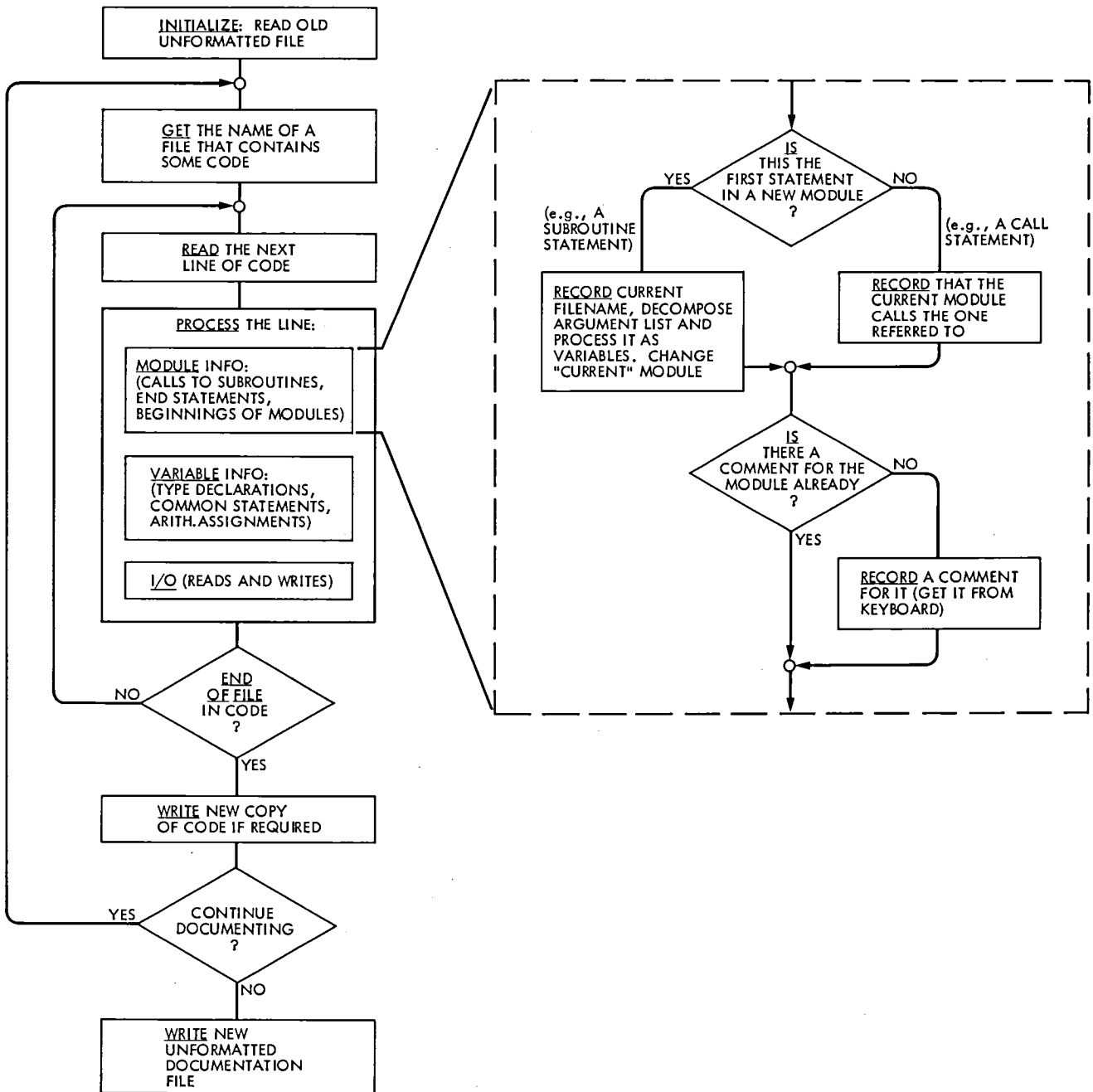


Fig. 1. Block diagram of RNDOC and expansion of one block (simplified)

## New CCIR Papers on Telecommunications for Deep Space Research

N. F. de Groot

Telecommunications System Section

*Eight JPL papers dealing with telecommunications for deep space research were recently adopted by Study Group 2 of the International Radio Consultative Committee (CCIR). In this article we present a brief description of the circumstances leading to the preparation and adoption of the papers. One of the papers is then presented. It deals with the selection of frequency bands that would be useful for deep space communication links in the 20 – 120 GHz range.*

The use of the radio frequency spectrum is regulated by international treaty. The treaty embodies the consensus of more than 150 nations that are members of the International Telecommunication Union (ITU). Technical aspects of the treaty are based upon reports and recommendation of the International Radio Consultative Committee (CCIR), a part of the ITU.

In recent years, JPL has played an increasingly active role in CCIR affairs. This participation is for the purpose of protecting and enhancing the regulations and agreements that permit and protect the telecommunication links associated with deep space research.

CCIR Study Group 2 deals with space research and radio astronomy. The study group held a three-week meeting in Geneva during October 1981. The purpose of the meeting was

to consider and approve Study Group 2 papers that will be published in the 1982 edition of the 13-volume set of Reports and Recommendations of the CCIR. Approximately 50 papers were submitted by six countries. Eight papers dealing with deep space telecommunications were approved. These papers were based on input documents prepared by the JPL Spectrum Engineering Group and are:

Doc. 5010 New Report	Frequency Bands in the 20-120 GHz Range That Are Preferred for Deep-Space Research.
Doc. 5007 New Recommendation	Protection Criteria and Sharing Considerations Relating to Deep-Space Research.
Doc. 5008 New Recommendation	Preferred Frequencies and Bandwidths for Deep-Space Research.

Doc. 5015 Revision of Report 683	Frequency Bands in the 1-20 GHz Range That Are Preferred for Deep- Space Research.
Doc. 5023 Modification of Question 14	Feasibility of Frequency Sharing Within and Among Space Research Systems.
Doc. 5024 Revision of Report 685	Protection Criteria and Sharing Con- siderations Relating to Deep-Space Research.
Doc. 5025 New Report	Potential Interference Between Deep- Space Telecommunications and the Fixed-Satellite and Broadcasting Satellite Services in Harmonically Related Bands.
Doc. 5026 Modification of Study Program 14B	Frequency Sharing Between Deep- Space and Other Space Research systems.

In this issue of the *TDA Progress Report* we begin the presentation of 6 of the adopted papers.<sup>1</sup> Document 5010 is a new CCIR report that identifies bands in the 20-120 GHz range that would be useful for deep-space research. The report summarizes work that was done in preparation for the 1979 World Administrative Radio Conference. The report is shown in its CCIR form and not in the usual TDA style.

Until it is adopted by a Plenary Assembly of the CCIR, the report is considered to be a draft. The next Plenary Assembly will be held in February 1982. Adoption of reports by that body is usually an administrative formality. Following the February meeting, the report will be published in Volume II of the 1982 edition of *Recommendations and Reports of the CCIR*.

---

<sup>1</sup>Documents 5015 and 5024 are revisions of material that appears in the 1978 edition of *Reports and Recommendations of the CCIR* (Ref. 1) and also in Refs. 2 and 3. The nature and scope of the revisions suggest that these documents need not be included in the TDA Progress Report.

## References

1. International Radio Consultative Committee, *Recommendations and Reports of the CCIR*, 1978, Vols. I-XIII, International Telecommunications Union, Geneva, 1978.
2. de Groot, N. F., "CCIR Papers on Telecommunications for Deep Space Research," *DSN Progress Report 42-43*, Jet Propulsion Laboratory, Pasadena, Calif., Feb 15, 1978.
3. de Groot, N. F., "CCIR Papers on Telecommunications for Deep Space Research," *DSN Progress Report 42-44*, Jet Propulsion Laboratory, Pasadena, Calif., Apr. 15, 1978.

Documents  
CCIR Study Groups  
Period 1978-1982

Doc. 2/5010-E  
(Ref. 2/192)  
15 October 1981  
Original: English/  
French/  
Spanish

Working Group 2-B

Draft REPORT AH/2  
FREQUENCY BANDS IN THE 20 - 120 GHz RANGE THAT ARE PREFERRED  
FOR DEEP-SPACE RESEARCH\*  
(Question 22/2, Study Programme 22A/2)

1. Introduction

This report pertains to the selection of preferred frequency bands for deep-space telecommunications in the 20-120 GHz range. The performance of links between earth stations and stations in deep-space is affected by the atmosphere of the Earth. Attenuation and emission by the atmosphere generally limits deep-space telecommunications to frequencies below 20 GHz. There are, however, certain frequency bands in the 20-120 GHz range where atmospheric attenuation is low enough to permit links between earth stations and deep-space stations. Additionally, there are certain other bands in the 20-120 GHz range that would be particularly suitable for links between an earth-orbiting relay station and deep-space stations.

The selection of preferred frequency bands below 20 GHz is given in Report 683 (2/139).

1.1 Performance Advantages of Higher Frequencies

Radio frequencies above 20 GHz can provide advantages for deep-space telecommunications. The advantages are higher link performance, reduced errors in measurements that depend on the velocity of propagation, and the possibility of shielding from terrestrial interference.

---

\*Information in this report is based on reports 205-4, 263-4, 563-1, 584-1, 718 and 721 from the 1978 Kyoto volumes. This report (5010) is brought to the attention of Study Groups 5 and 6 with a view towards their comment on how the analysis might be affected by recent changes in propagation data.

The net gain of a free space link between perfect antennae with fixed apertures varies in direct proportion to the frequency squared. For certain frequencies where the attenuation of the atmosphere is low, links between Earth and space can benefit from the use of frequencies above 20 GHz.

The increased performance of higher frequency links may be utilized for command, telemetering and radiometric functions. Alternatively, the higher performance may be traded for smaller and lighter spacecraft antennae and transmitters.

Accurate navigation of deep-space probes depends upon determination of their position and velocity by means of phase and group delay measurements of received signals. These measurements are influenced by the velocity of propagation along the transmission path. The velocity of propagation is a function of the presence of charged particles along the path. The effect of these particles varies inversely with the square of the frequency and hence higher frequencies are preferable for purposes of navigation and certain other radio measurements.

#### 1.2 Shielding from Terrestrial Interference

In the future it may be desirable to employ a geostationary relay station for signals to and from deep-space probes. The links between such a station and deep-space probes would be free of the perturbing effects of the atmosphere. These links could be protected from terrestrial interference by choosing frequencies where the atmosphere is relatively opaque to radio signals. There are such frequencies in the 20-120 GHz range.

#### 1.3 Basis for Frequency Selection

Selection of preferred frequencies is based on link performance as determined by propagation and equipment characteristics. In the next three sections of the report we examine the factors that influence frequency selection. Some of these factors provide the information needed to calculate an index of link performance. This index is expressed as  $P_R/N_0$ , the ratio of total received power to noise spectral density for a particular set of propagation conditions and equipment parameters.

## 2. Frequency Dependent Characteristics of Interplanetary Propagation

Interplanetary propagation characteristics determine the performance of links between a deep-space probe and a relay satellite located outside of the atmosphere of the Earth. These characteristics also affect the performance of links between Earth stations and deep-space.

### 2.1 Sky Noise Temperature

The sky noise temperature seen by a relay satellite will be determined by the cosmic background (3K) and quantum noise as shown in curve A of Figure 1, except when noise from the Earth, other planets or the Sun enters the antenna.

The sky noise temperature seen by a spacecraft will also be that shown in A of Figure 1. Earth will generally be within the main lobe of a spacecraft antenna pointed at a relay satellite. The presence of Earth within the antenna beam will contribute to the noise temperature. For example, for a spacecraft at  $4 \times 10^7$  km from the Earth (the minimum distance to Venus), the Earth subtends an angle of  $1.8 \times 10^{-2}$  degrees. If the spacecraft antenna is limited to a minimum beamwidth of 0.15 degrees by pointing accuracy, then the Earth can fill less than 1/69 of the antenna main lobe. The effect of the black body temperature of the Earth, (approximately 250 K at 2.3 GHz) is correspondingly reduced to a value that is small compared to the 600-1500 K noise temperature of a typical spacecraft receiving system.

The increase in noise temperature when an antenna is pointed at the Sun is large. This can affect the timing and design of some deep-space missions and experiments.

For calculation of  $P_R/N_0$  as a function of frequency, the sky noise temperature seen by a relay satellite or deep-space probe will be considered a negligible part of the system temperature.

### 2.2 Attenuation

A review of gaseous absorption and scattering by dust particles outside of planetary atmospheres indicates that neither will attenuate the signal by as much as 0.1 dB in the 20-120 GHz range as long as the propagation path is restricted to our solar system. Attenuation by interplanetary space will be considered a negligibly small factor in the selection of preferred bands.

Attenuation in dB due to charged particles varies as the inverse frequency squared ( $1/f^2$ ) and thus favours the highest frequency available.

### 2.3 Velocity of Propagation

Charged particles along the communication path cause changes in the velocity of propagation. Figure 2 shows an example of the apparent range measurement error as a function of frequency and of the angle between the ray path and a line between the Sun and the Earth station. This figure is based on the relationships described in Report 683 (2/139). It is apparent from Figure 2 that high frequencies are desirable for the most precise ranging.

### 2.4 Scintillation

Amplitude and phase scintillation from solar plasma will be a factor for ray paths close to the sun. The magnitude of the scintillation decreases with increase in frequency.

## 3. Frequency Dependent Characteristics of Propagation Through an Atmosphere

The foregoing interplanetary propagation factors affect links between deep-space and a relay station in the geosynchronous satellite orbit. For links between deep-space and Earth, the atmosphere plays a dominant role in the selection of preferred frequencies in the 20-120 GHz range.

Atmospheres of other planets can affect paths that graze or penetrate the atmosphere in question.

### 3.1 Attenuation

#### 3.1.1 Earth Atmosphere

Attenuation of signals passing through the ionosphere of the Earth is negligible at frequencies above 20 GHz, but the neutral atmosphere plays a major role at these frequencies. The attenuation for transmission through the atmosphere is shown in Figure 3 (Report 719). Above 20 GHz, minimum attenuation on links between Earth and spacecraft would be obtained at frequencies near 30 GHz.

The specific attenuation due to rain at rates greater than a few millimeters per hour is generally larger than that of the gaseous atmosphere and increases monotonically with frequency in the range of

interest. The rain rate for 0.001% of the time in rain climate 4 is 55 mm/hr (Report 563-1). The attenuation in the 20-120 GHz region during rain at this rate is so high that propagation is not practicable and will not be considered further as a determinant of preferred frequencies.

For the satellite-to-spacecraft links, the line-of-sight propagation paths will be obscured at times by the interposition of the Earth or some portion of the Earth's atmosphere. From the geostationary satellite orbit the solid Earth subtends an angle of 17.34 deg. If the atmosphere to 100 km altitude were opaque to radio waves the obscuration angle would increase by 0.27 deg., too small a difference to influence band selection.

The objective of protecting the paths between deep-space probes and an Earth orbiting satellite from terrestrial interference may be satisfied by taking advantage of the high atmospheric attenuation in the 60 and 119 GHz regions. Molecular oxygen absorption lines at these frequencies are responsible for the high attenuation observed in Figure 3.

A pair of links (deep-space to Earth satellite) could be accommodated in the high attenuation region between 54 and 64 GHz. A frequency separation of approximately 7% is required (Report 683 (2/139)). The absorption line at 119 GHz is much narrower and only one link of a pair could enjoy the maximum shielding. Shielding of the down-link is most important.

### 3.1.2 Planetary Atmospheres

From the standpoint of attenuation, the nature of planetary atmospheres does not influence the selection of communication frequencies in the 20-120 GHz range. This is not to say that the atmospheres of some planets do not contain spectral lines of scientific interest in the 20-120 GHz range, for example ammonia.

### 3.2 Sky Noise Temperature

Sky noise temperature as seen by an Earth station is a function of frequency and elevation angle. Noise temperature from absorption-related emission from the gaseous atmosphere of the Earth pertinent to the standard atmosphere and elevation angle of 30° is shown in Figure 1. Attenuation caused by rain also influences sky noise temperature in a manner analogous to gaseous absorption. The 0.001% curve of Figure 1 showing rain-related sky temperature has been computed from the attenuation experienced during 55 mm/hr rainfall.

When the Earth station antenna is pointed near the Sun, the noise temperature will increase.

### 3.3 Scintillation

Amplitude and phase scintillation from the neutral atmosphere of the Earth at frequencies in the 20-120 GHz range can cause fading at a parabolic receiving antenna of a few meters in diameter as shown below (Report 718).

Peak-to-Peak Fades for Clear Air

Elevation Angle (deg)	Fade at 35 GHz (dB)	Fade at 100 GHz (dB)
>45	±2	±4
10	±6	±12

Scintillation due to the Earth's ionosphere will not be a selection factor for frequencies above 20 GHz (Report 263), and the same conclusion can be drawn relative to planetary ionospheres. For some missions, scintillation caused by the solar corona could affect the choice of frequency.

### 4. Frequency Dependent Equipment Factors

Equipment characteristics which determine link performance include transmitter power, antenna size, surface accuracy and pointing accuracy, and receiver noise temperature. These characteristics usually depend upon frequency to some degree. In the frequency range 20-120 GHz, propagation factors influence the link performance so strongly that the frequency dependent equipment factors have only a minor effect on the selection of preferred frequencies. For this reason, only the propagation factors are considered in the following link analyses; the arbitrarily selected equipment parameters are assumed to be independent of frequency.

### 5. Link Performance

Figures 4-7 illustrate link performance as a function of frequency. Curves A are for a path in free space. Curves B include the

effect of the atmosphere of the Earth. The index of performance  $P_r/N_o$  was calculated on the basis of data in Figures 1 and 3 and the following parameter values:

Communication distance	8 x 10 <sup>8</sup> km
Earth station transmitter	100 kw
Satellite transmitter	100 watts
Spacecraft transmitter	25 watts

Antenna parameters used in the calculation are as shown in Figures 4-7. The antennae are assumed to be ideal with gain that is proportional to frequency squared.

These values are illustrative only; other values could be used. Different numerical results would be obtained, but the shape of the performance curves and the corresponding frequency selection would not change.

Comparison of curves A and B shows the advantage in link performance that results from utilizing higher frequencies when the path is entirely in space. This is a principal reason for establishing a relay station in a near-Earth satellite.

Curves B show that frequency bands within the 20-120 GHz range can provide for transmission through the atmosphere, and for the shielding of paths between a relay satellite and deep-space probes from terrestrial signals.

#### 6. Preferred Frequency Bands

The preferred frequency bands for deep-space research in the 20-120 GHz range are listed in Table 1. The bands were selected on the basis of the index of performance curves and the requirement to provide links between a satellite and a station in deep space that are shielded from terrestrial signals, and links that permit communication between a deep-space station and either a near Earth satellite or an Earth station. The feasibility of band sharing and the existing allocations in the Radio Regulations were not factors in the selection of bands. The frequency dependent characteristics of scintillation and velocity of propagation were not used as determinants of preferred frequency bands. These factors could influence the use of certain allocated bands for particular space research missions, but communication performance was considered the dominant factor in preferred band selection. Similarly, equipment characteristics that vary with frequency were not used to influence band selection. Bands that may be allocated will likely remain for many years, and equipment technology will develop to make best use of those frequencies, as limited by

natural phenomena. The bandwidth and frequency separation requirements are discussed in Report 536-1 (MOD I).

TABLE 1  
Preferred frequencies and their uses

Range of Preferred Frequencies	General Applicability	Other Requirements <sup>(1)</sup>
28.5-39 GHz	Deep-space-to Earth during clear weather, and deep-space-to satellite.	500 MHz bandwidth.
34-50 GHz	Earth-to-deep space during clear weather, and satellite-to-deep space.	500 MHz bandwidth, spaced at approximately 7% from the space-to-Earth band in the 28.5 - 39 GHz range.
56-64 GHz	Deep-space-to-satellite and satellite-to-deep space shielded from terrestrial signals.	A pair of 500 MHz wide bands spaced at approximately 7% within the 56-64 range.
117.7-119.8 GHz	Deep space-to-satellite shielded from terrestrial signals.	500 MHz bandwidth.
98-110 GHz	Satellite-to-deep space (uplink for 119 GHz downlink).	500 MHz bandwidth, spaced at approximately 7% from the space-to-satellite band in the 117.7 - 119.8 GHz range.

(1) The requirements shown are based on characteristics of telecommunication systems utilized or planned by several administrations.

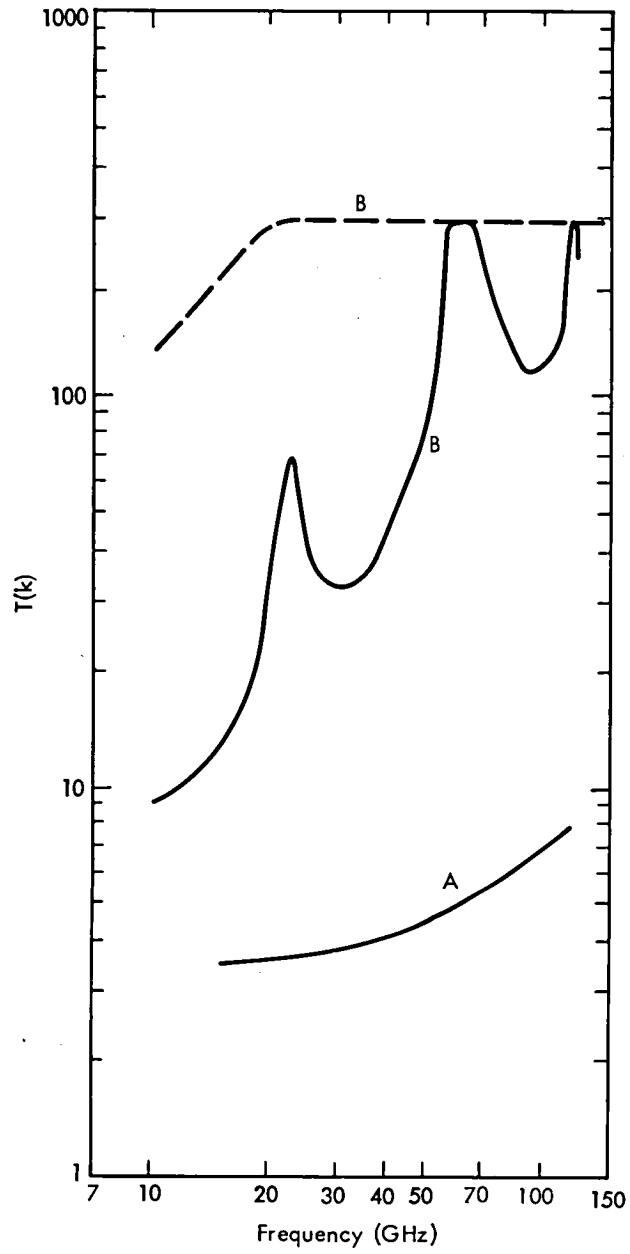


**FIGURE 1.**  
*Sky noise temperature*  
A: As seen by deep space station  
B: As seen by earth station, antenna  
at 30° elevation angle  
— Gaseous atmosphere  
- - - Composite of gaseous atmosphere plus rain  
exceeded 0.001% of time (55 mm/hr, rain  
climate 4)

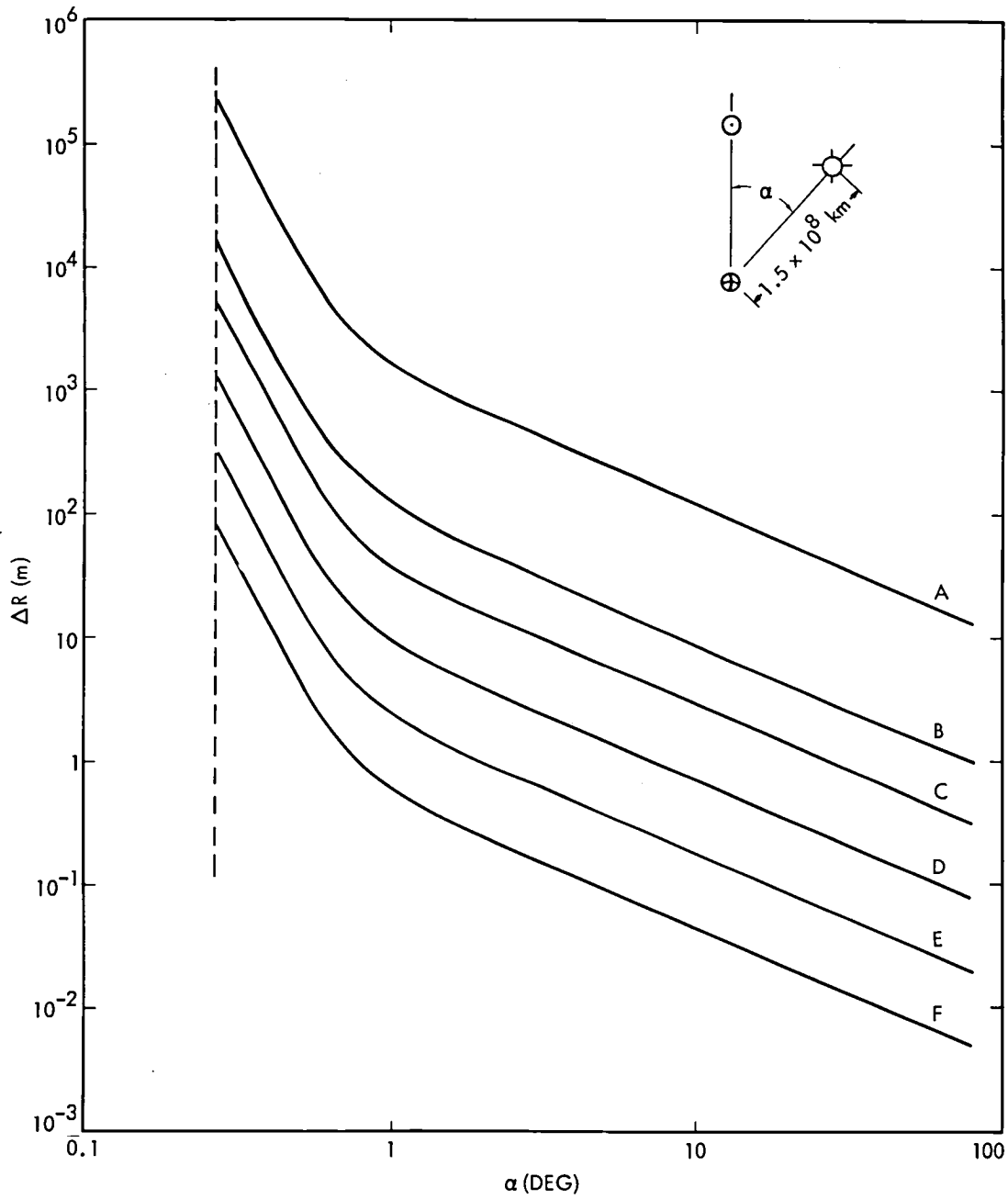
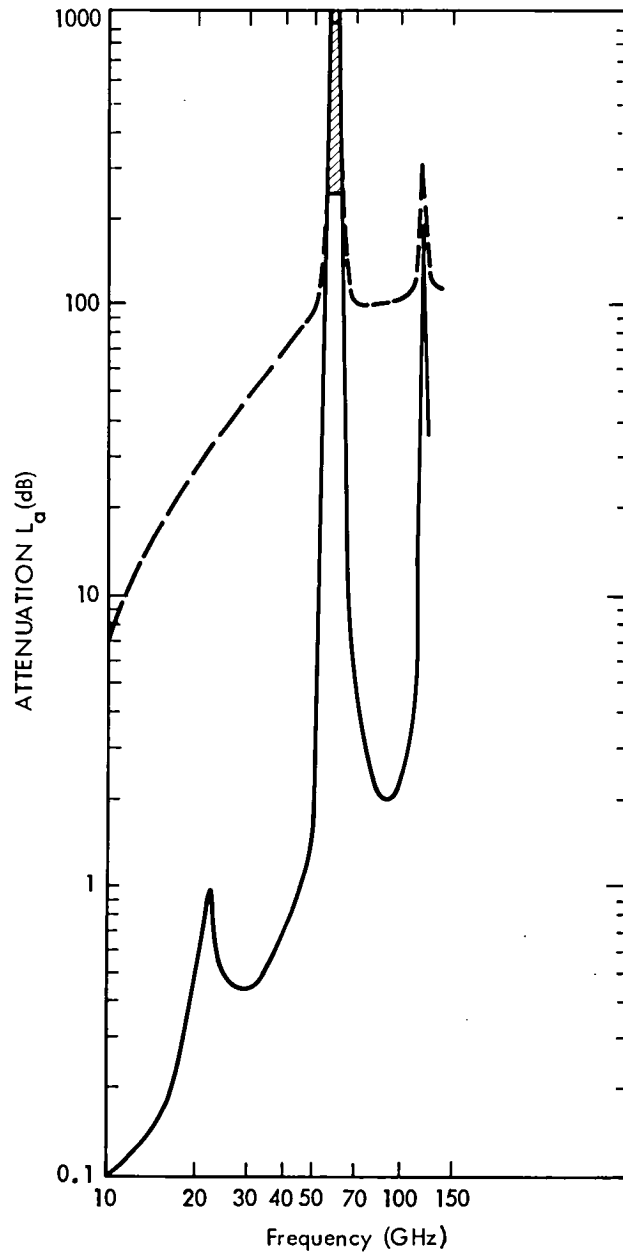


FIGURE 2.

Approximate error ( $\Delta R$ ) in measured spacecraft range caused by charged particles along a  $1.5 \times 10^8$  km path, as a function of angle from center of sun ( $\alpha$ )

A: 2.295 GHz	D: 30 GHz	☉: SUN
B: 8.450 GHz	E: 60 GHz	⊕: EARTH
C: 15.0 GHz	F: 120 GHz	☾: SPACECRAFT



**FIGURE 3.**  
*Attenuation due to the gaseous atmosphere and rain for an antenna elevation angle of  $30^\circ$  at an earth station*

- Gaseous atmosphere ( $7.5 \text{ g/m}^3$  water vapor at surface)
- - - Composite of gaseous atmosphere plus rain exceeded 0.001% of time (55 mm/hr, rain climate 4)

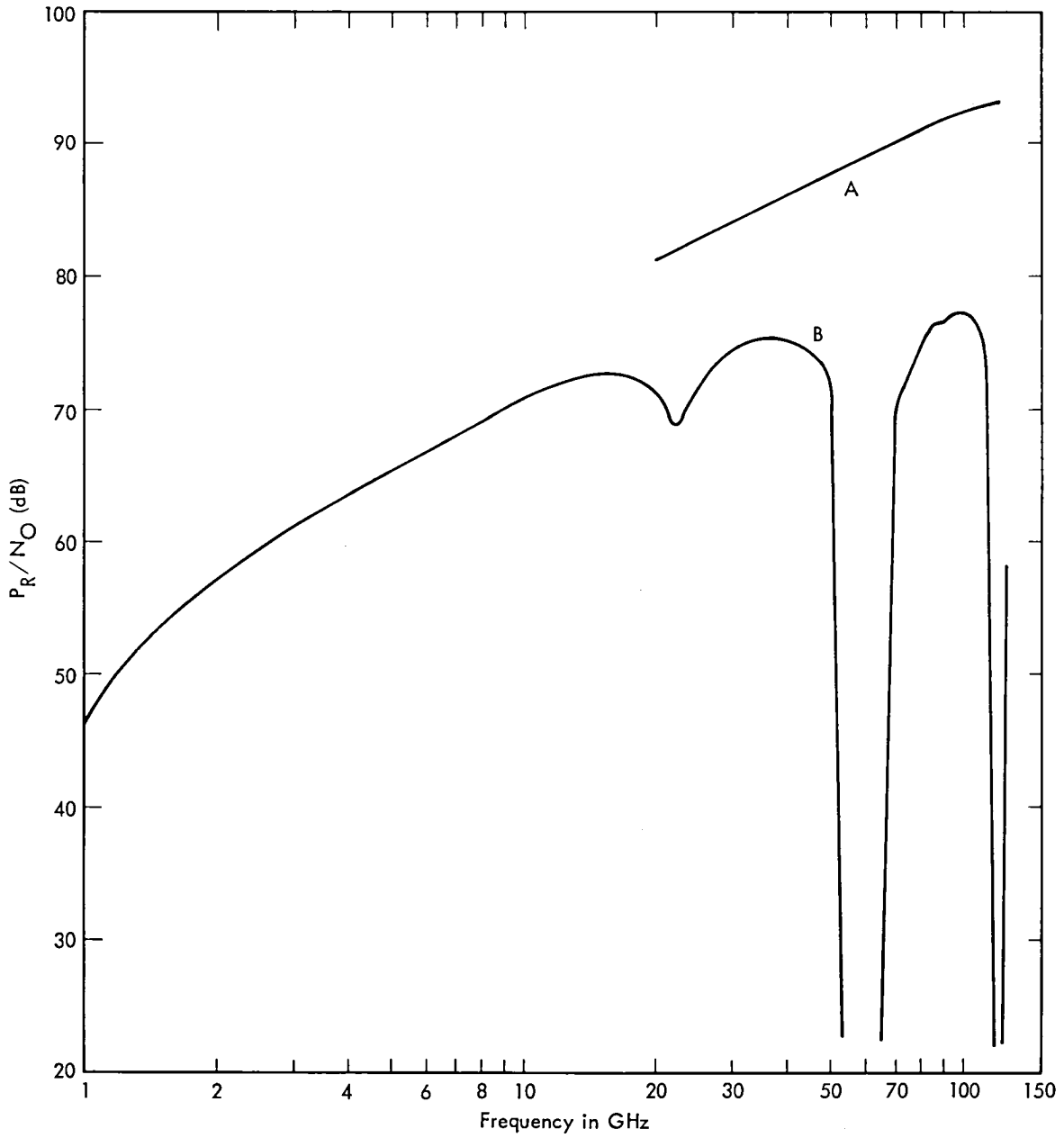


FIGURE 4.

Link performance ( $P_R/N_O$ ) limited by natural phenomena only.

Two fixed diameter antennas: 3.7m on deep space station, 64m at receiving station.

A: Deep space-to-satellite

B: Deep space-to-earth station

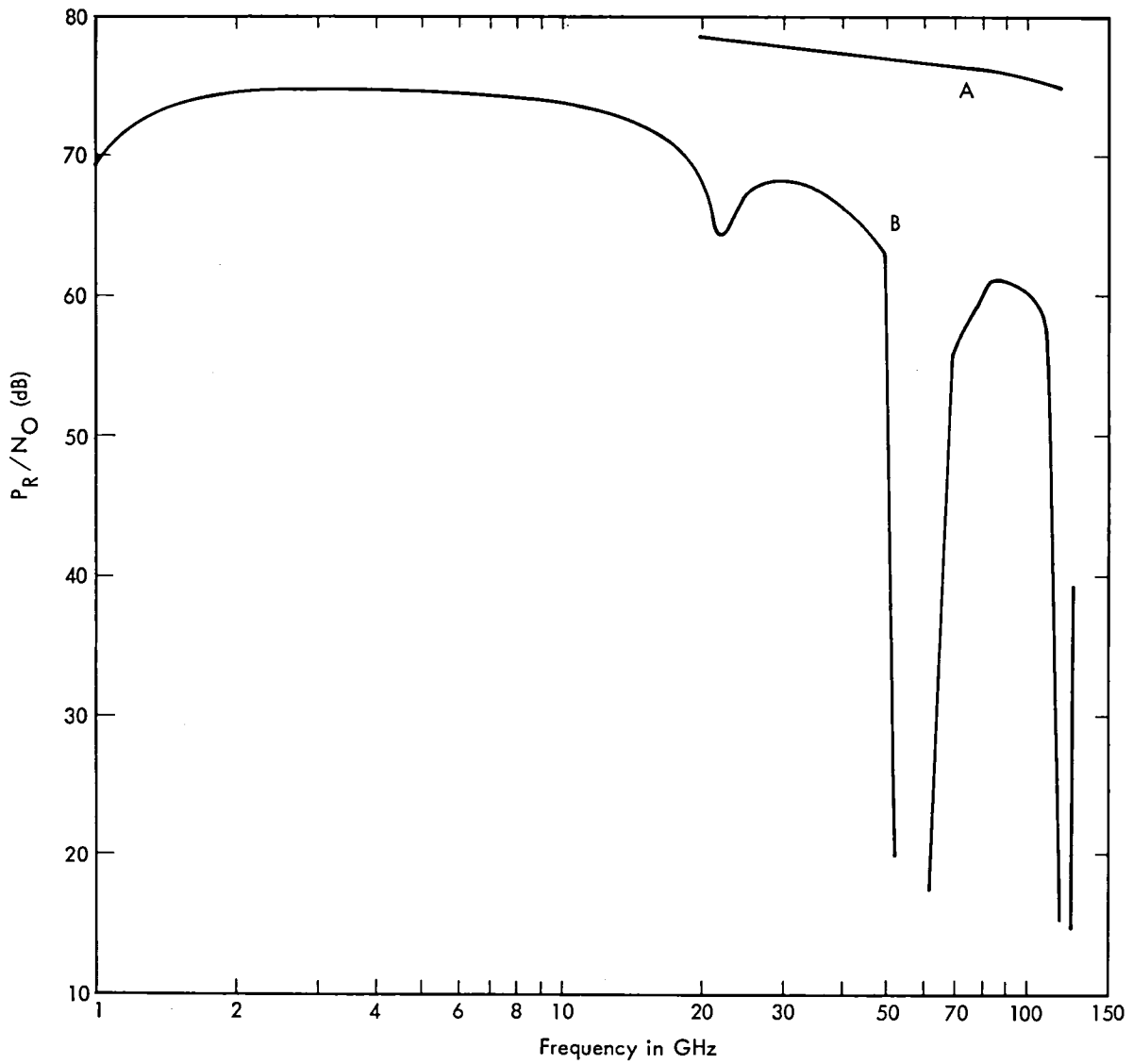


FIGURE 5.

*Link performance ( $P_R/N_O$ ) limited by natural phenomena only.  
Fixed beamwidth (55 dBi gain) antenna on deep space station.  
Fixed diameter (64m) antenna at receiving station.*

*A: Deep space-to-satellite*

*B: Deep space-to-earth*

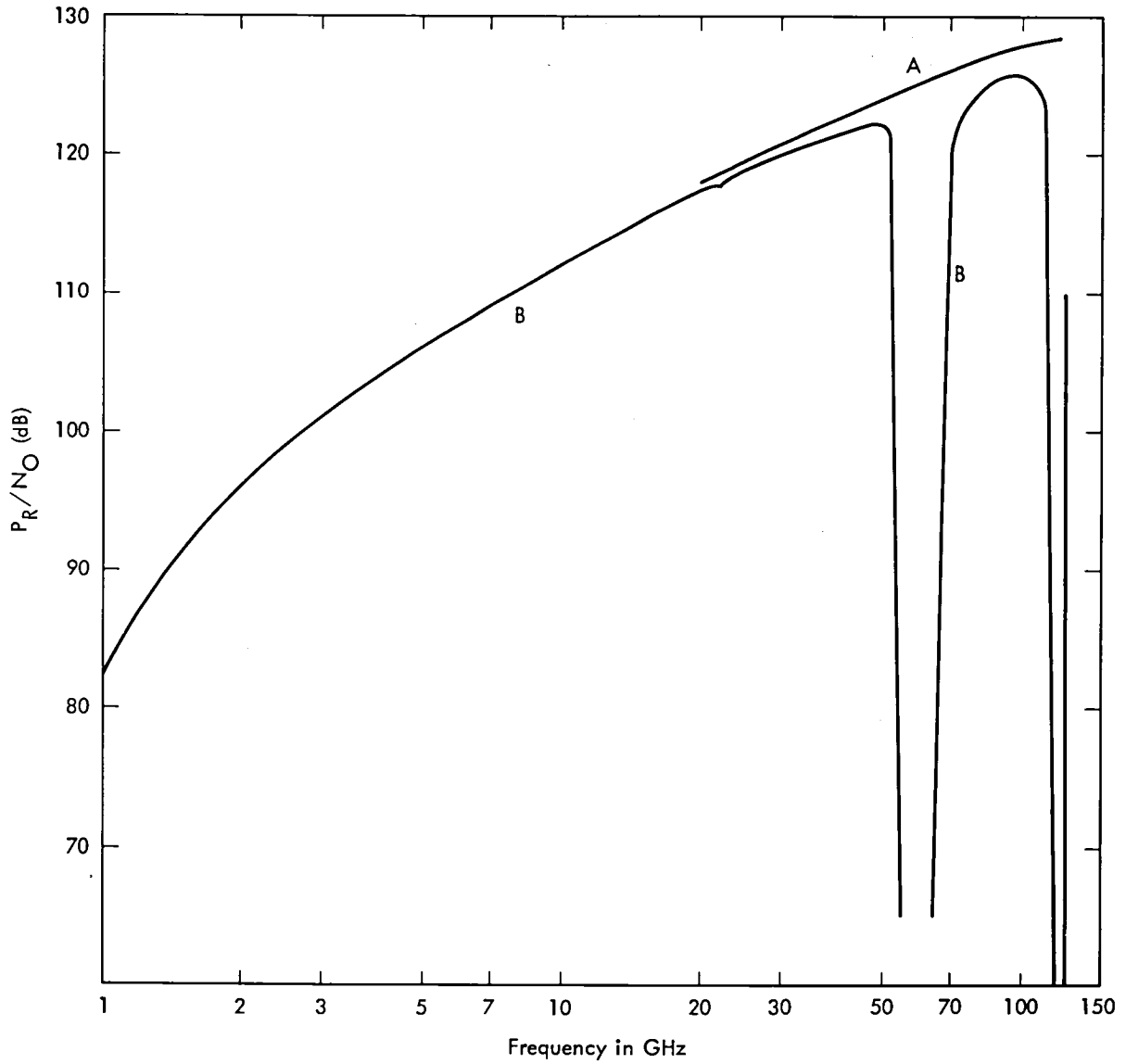


FIGURE 6.

*Link performance ( $P_R/N_0$ ) limited by natural phenomena only.*

*Two fixed diameter antennas: 3.7m on deep space station, 64m at transmitting station.*

*A: Satellite to deep space*

*B: Earth station to deep space*

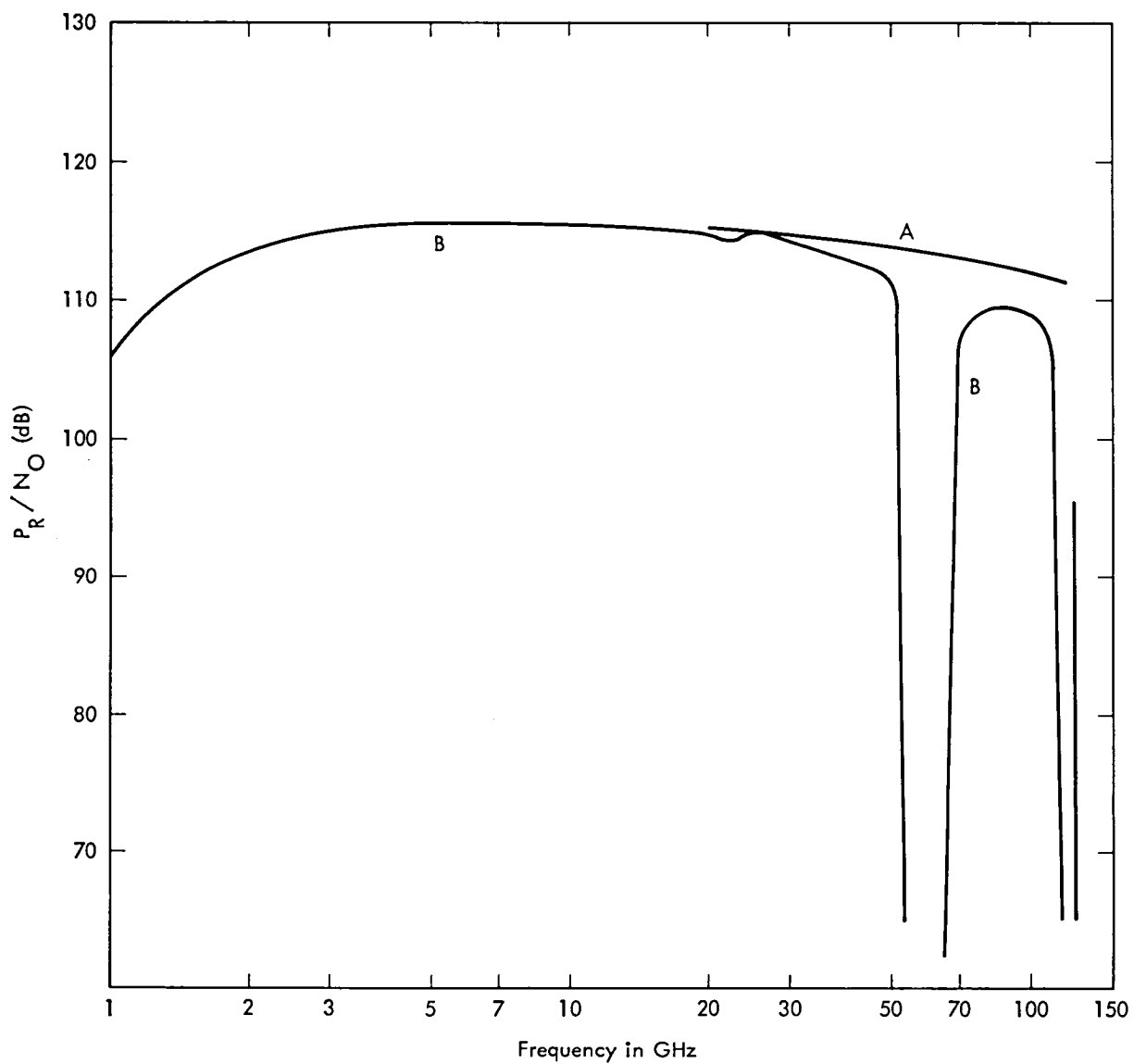


FIGURE 7

*Link performance ( $P_R/N_O$ ) limited by natural phenomena only.  
Fixed beamwidth (55 dBi gain) antenna on deep space station.  
Fixed diameter (64m) antenna at transmitting station.  
A: Satellite to deep space  
B: Earth station to deep space*

# DSN RFI Susceptibility Models Development Program Overview

M. K. Sue

Telecommunications Systems Section

*Earth stations employed for space exploration are often operated in an environment of man-made electromagnetic radiation. Such an environment can have the potential of radio frequency interference (RFI). To analytically determine and predict the effects of RFI it is necessary to have models that describe the response of the earth station receivers to various types of interference. The RFI model development described in this article is intended to provide an understanding of the interference susceptibility of DSN receivers. The article presents an overview of interference types and effects, analytic modelling and experimental verification, and work accomplished and work to be done.*

## I. Introduction

Growing usage of the radio frequency spectrum has increased the potential for interference to deep space communications. To allow successful operations in an environment of man-made electromagnetic radiation, it is necessary to know the susceptibility of the DSN stations to various forms of RFI. RFI model development is in response to this need and to the following specific requirements:

- (1) The obligation to provide the Department of Defense (DOD) with DSN RFI susceptibility data under the Memo of Understanding agreed upon by NASA and DOD.
- (2) The need to be capable of DSN operational RFI prediction.
- (3) The need for susceptibility information and protection criteria used in band and frequency sharing studies.

The RFI effects on the DSN receiving systems, the scope and approach of the model development, past achievements, and future direction are discussed in this article.

## II. Types of RFI and Their General Effects

For the purpose of developing RFI models, three types of interference may be considered:

- (1) CW interference.
- (2) Pulsed sinusoidal interference.
- (3) Wideband interference.

Most of the interference in the Fort Irwin-Goldstone area is of the pulse type. The source of this type of interference is a wide variety of radar equipment. All the RFIs considered are unintentional; the special problems that result from the characteristics of intentional jamming are not considered.

RFI can have various effects on the receiving system, depending on the power level and the frequency range of the interference. At weak-to-moderate power levels, an in-band<sup>1</sup> interference can result in an increase in the static phase error and the phase jitter of the carrier tracking loop, an increase in the telemetry bit error rate, or a loss of synchronization. These effects are referred to as performance degradation. Performance degradation caused by RFI can generally be expressed as an equivalent reduction in the signal-to-noise ratio and can be compensated by increasing the power level of the desired signal. At strong levels, an interference can result in a performance degradation and simultaneously drive one or more of the receiver components into a nonlinear region, resulting in gain compression and the generation of harmonics, spurious signals, and intermodulation products. These nonlinear effects are collectively referred to as saturation effects. Unlike performance degradation, saturation effects generally cannot be compensated by simply increasing the power level of the desired signal.

An interference with a strong power level and with a large frequency offset from the carrier of the desired signal generally tends to produce saturation effects. For an interference with a small frequency offset, the predominant effect is performance degradation, such as an increase in the telemetry bit error rate.

### III. RFI Effects to be Modeled

There are two classes of RFI effects that must be considered in model development, i.e., saturation and performance degradation. The subsystem that is responsible for saturation is the maser. It is the first element in the entire system to be saturated at strong interference levels (Ref. 1). Other parts of the system are not likely to have saturation because severe performance degradation would take place much before saturation effects became noticeable. A strong interference can cause the maser to saturate if the interference frequency is (Ref. 2): (1) in the maser passband, (2) near the maser passband, (3) in the maser mixing range, or the idler frequency range.

The second class of RFI effects includes the performance degradation of various receiver functions. RFI can result in: (1) telemetry channel performance degradation, (2) ranging channel performance degradation, and (3) doppler channel performance degradation. In order to evaluate these effects, it is necessary to also examine the performance of the carrier tracking loop because it directly affects the performance of the telemetry, ranging and doppler systems.

---

<sup>1</sup>An in-band interference is one that falls inside the desired channel bandwidth.

Carrier channel degradation occurs in the presence of an interference at or near the carrier frequency. Degradation to the telemetry channel can be caused by an interference in the telemetry channel, near the telemetry subcarrier odd harmonics, or in the carrier channel. Degradation to the ranging channel can be a result of an in-band interference or a carrier interference. Doppler channel degradation is directly caused by a carrier interference.

In addition, interference in the maser idler frequency range or mixing range can mix with the maser pump frequency and produce a mixing product at the desired signal frequency. This product, being frequency-modulated, is wide band and can produce one or more of the four possible performance degradations.

The response of the receiving system to an interference is a function of the interference type, interference power, interference frequency and the operating condition of the system. It is not feasible to completely specify the RFI characteristics of the system by a single model. Different models, each developed for a particular type of interference and a particular part of the system under a particular condition, are necessary.

### IV. Required RFI Models

Based on the RFI types and effects, three system level models are needed to completely define the RFI susceptibility characteristics of the receiving system: (1) CW RFI model, (2) pulse RFI model, and (3) wideband RFI model. Each of these system models contains two parts, one for the saturation effects and the other the performance degradation effects. The saturation part of the model contains a subsystem model that defines the saturation characteristics of the maser, i.e., maser saturation model. The performance degradation part of each system model contains five subsystem models: (1) carrier channel degradation, (2) telemetry channel degradation, (3) ranging channel degradation, (4) doppler channel degradation, and (5) maser mixing/conversion.

The first four subsystem models define the performance degradation of the four functions performed by the receiving system. The last subsystem model accounts for the possible performance degradation caused by interference having a frequency in the maser idler frequency range. An interference in idler frequency range or mixing range can mix, or multiply and mix, with maser pump frequencies and create an in-band interference through two mechanisms: electron spin resonances and reaction with linear elements in the maser.

The relationships between the interference frequency, the power level, the affected subsystems, the degradation effects, and the necessary models at the system and subsystem levels

are shown in Fig. 1 for the three types of interference. Since the system can operate in both S-band and X-band, each model in Fig. 1 generally has both S-band and X-band versions. A summary of the required models is shown in Table 1. These models are needed for all three interference types.

## V. Current Status and Future Direction in Model Development

Most of the model development effort in the past has been directed to CW interference. Table 2 shows the current status in CW RFI model development. Column 1 lists the subsystem models that make up the system model. Column 2 lists specific interference effects to be modeled for each subsystem model. Column 3 shows the required frequency bands and column 4 shows the current status. To complete the CW RFI model, several effects remain to be included:

- (1) Maser conversion loss in converting interference in the maser idler or mixing range to in-band interference due to nonlinear elements in the maser.
- (2) Ranging channel degradation due to RFI in (a) the carrier loop, and (b) the ranging channel.
- (3) Telemetry degradation due to interference (a) in the telemetry channel, and (b) in or near telemetry sub-carrier odd harmonics.

The model development for the CW RFI, pulse RFI and wideband RFI in theory can be handled simultaneously. In practice, it is convenient to complete the model development for the CW case, then the pulse case followed by the wideband case. There are two reasons that the CW case should precede the pulse case:

- (1) Effects of a pulse RFI can be approximated by a CW RFI under certain conditions.
- (2) Insight gained in developing CW RFI models may be helpful for the pulse case.

Effects of a wideband interference can be estimated by the traditional noise conversion technique where the interference is treated as extraneous noise. Models for this type of RFI are relatively simple and will be treated last.

The plan for the immediate future is to complete the model for the CW RFI case. Modelling for pulse RFI can then begin. The effects of pulse RFI are a function of pulse width, repetition rate and pulse carrier frequency. To bound the scope of modelling, it is necessary to determine these characteristics for the typical pulse interference encountered by DSN. Having determined these characteristics, pulse RFI models for the degradation of carrier loop, telemetry, ranging, doppler and saturation can then be developed in the order mentioned.

## VI. Model Application

The saturation model developed is based on a 1-dB gain compression criterion. This model allows one to predict whether a given interference violates the 1-dB gain compression criteria. This model does not predict the degree of performance degradation.

Unlike the saturation model, all performance degradation models are capable to predict for a given interference the degree of degradation. Performance degradation is measured by a variety of parameters and they are discussed in the following subparagraphs.

- (1) Carrier Channel Performance Degradation Model. This model allows one to predict the amount of static phase error and phase jitter in the tracking loop due to the presence of a CW interference in the carrier channel. It also predicts the lock and unlock behavior of the loop under strong interference.
- (2) Telemetry Channel Performance Degradation Model. Development of this model is yet to be completed. Upon completion, it will allow one to determine the error probability for the coded as well as the uncoded cases. Alternatively, it will predict the equivalent reduction in the signal energy to spectral density ratio. Currently, it is not planned to include the lock and unlock behavior of the telemetry system. It may be necessary to expand the model to include these effects in the future as needs arise.
- (3) Ranging Channel Performance Degradation. This model will determine the variance of range delay estimate and the equivalent reduction in signal-to-noise ratio.
- (4) Doppler Channel Degradation Model. This model can be derived directly from the carrier channel degradation model and it allows one to determine the equivalent doppler noise.
- (5) Maser Mixing/Conversion Model. This model will predict the amount of degradation on the carrier channel, telemetry channel, ranging channel and doppler channel due to interference in the maser idler frequency range or mixing range.

## VII. Conclusion

Efforts taken under the RFI susceptibility model development program in recent years have produced some limited but useful results. Further efforts are necessary to obtain a full set of RFI susceptibility data for the receiving system. In addition to fulfilling NASA's obligation to DOD, these data

can be useful in a variety of ways such as in the development of protection criteria for deep space communications and in the selection of frequency channels for future missions. They can also be applied to upgrade DISSIP2, an operational computer program used by DSN to predict interference from earth-orbiting satellites.

The use of RFI susceptibility models to protect deep space stations from harmful interference through coordination and control is only a first step to obtain RFI protection. In the future, it may be necessary to consider design changes in order to obtain RFI immunity, such as filtering and the use of different modulation techniques and coding schemes.

## References

1. Hersey, D. R., and Sue, M. K., "Maximum CW RFI Power Levels for Linear Operation of the DSN Block IV Receiver at S-Band Frequencies," *DSN Progress Report 42-56, January and February 1980*, Jet Propulsion Laboratory, Pasadena, Calif.
2. Clauss, R., "X- and K-Band Maser Development: Effects of Interfering Signals," *DSN Progress Report 42-42*, Jet Propulsion Laboratory, Pasadena, Calif.
3. Bautista, J. J., and Petty, S. M., "Cryogenic Filters for RFI Protection," *DSN Progress Report 42-65, July and August 1981*, Jet Propulsion Laboratory, Pasadena, Calif.
4. Sue, M. K., "Block IV Receiver Tracking Loop Performance in the Presence of a CW RFI," *TDA Progress Report 42-60, September and October 1980*, Jet Propulsion Laboratory, Pasadena, Calif.
5. Sue, M. K., "Telemetry Degradation Due to a CW RFI Induced Carrier Tracking Error for the Block IV Receiving System With Maximum Likelihood Convolutional Decoding," *JPL Progress Report 42-61, November and December 1980*, Jet Propulsion Laboratory, Pasadena, Calif.
6. Low, P. W., "Radio Frequency Interference Effects of Continuous Sinewave Signals on Telemetry Data," *DSN Progress Report 42-40, May-June 1977*, Jet Propulsion Laboratory, Pasadena, Calif.
7. Low, P. W., "Radio Frequency Interference Effects of Continuous Sinewave Signals on Telemetry Data - Part 2," *DSN Progress Report 42-51, March-April 1979*, Jet Propulsion Laboratory, Pasadena, Calif.

**Table 1. Required RFI susceptibility models  
(for a given type of interference)**

Type of system models	Subsystem models	Interference frequency
Saturation model	Maser saturation model	In or near maser passband Inside maser mixing range Inside maser idler frequency range or mixing range
Performance degradation models	Carrier channel degradation	Near carrier
	Telemetry channel degradation	Near carrier Near TLM subcarrier odd harmonics Near telemetry channel
	Ranging channel degradation	Near carrier Near ranging channel
	Doppler channel degradation	Near carrier
	Maser mixing/ conversion model	Inside maser idler frequency range or mixing range

**Table 2. Model development status for CW RFI**

Required subsystem models	Interference effects to be modeled	Required frequency bands	Status
Maser saturation	Maser saturation characteristics for X-band (BLK 1, 2) and S-band (BLK 3, 4):		
	(a) RFI in or near maser passband	S&X	Available in Refs. 1-3
	(b) RFI in the maser mixing range	S&X	Available in Refs. 1-3
	(c) RFI in the maser idler frequency range or mixing range	S&X	Available in Refs. 1-3
Maser mixing/ conversion loss	Loss incurred in converting idler frequency interference to in-band interference	S&X	Partially available in Refs. 2, 3. Conversion loss due to non-linearities not available.
Carrier channel degradation	PLL degradation due to RFI near the carrier	S&X	Completed (Ref. 4)
Doppler channel degradation	Doppler channel degradation due to interference in the carrier channel	S&X	Completed (Ref. 4)
Ranging channel degradation	Ranging channel degradation due to:		
	(a) carrier interference	S&X	TBD
	(b) ranging channel interference	S or X	TBD
Telemetry channel degradation	Telemetry channel degradation due to:		
	(a) carrier interference	S&X	Completed (Ref. 5)
	(b) interference in the telemetry channel	S or X	Currently under study
	(c) interference near telemetry subcarrier and harmonics	S or X	TBD

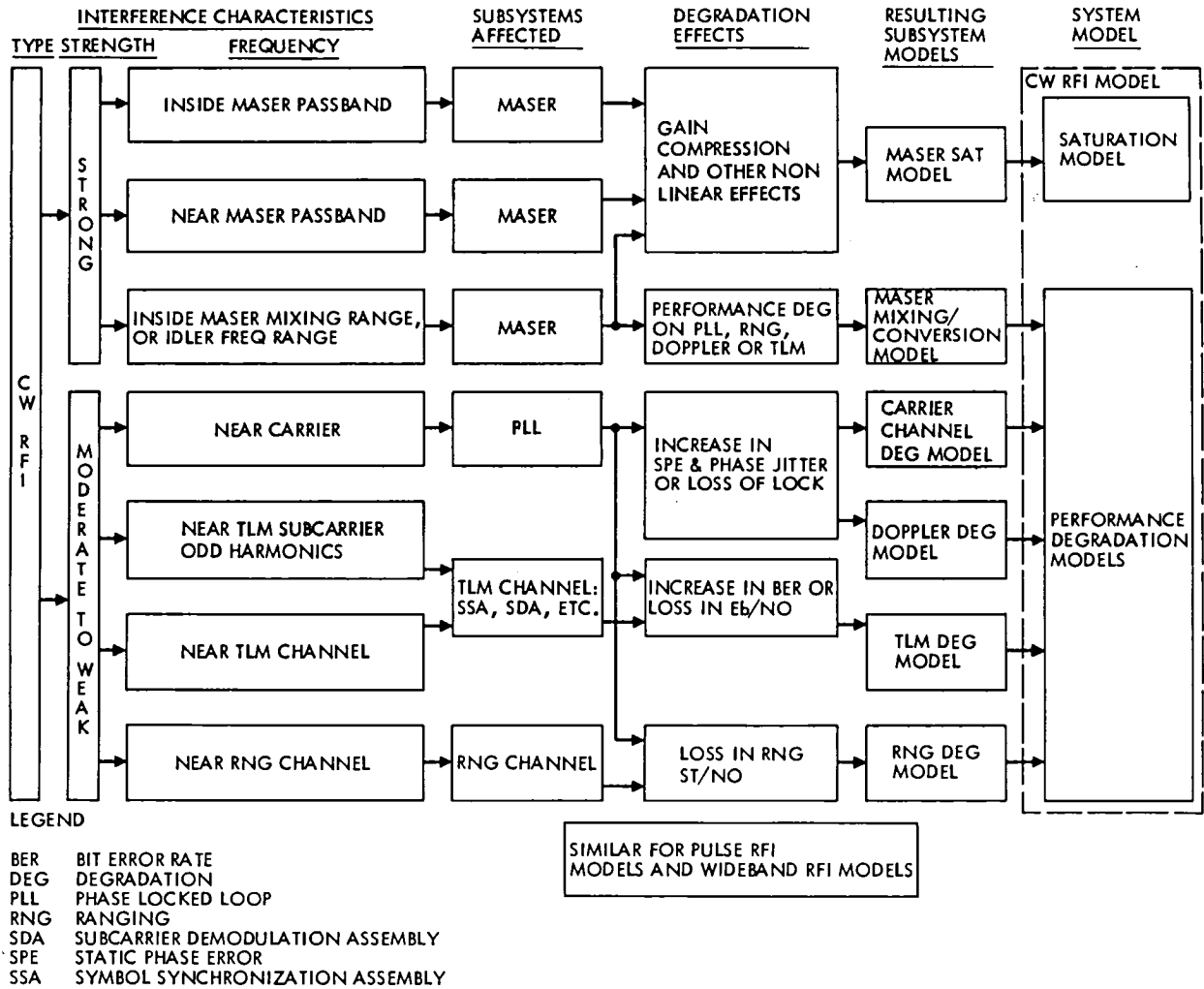


Fig. 1. RFI models

# RFI Measurement Survey at Goldstone in November and December 1981

R. M. Taylor  
TDA Mission Support

*The participation of Deep Space Network personnel in support of a measurement survey contracted with the Institute of Telecommunication Science is reported. The survey took place at Goldstone, California, in November and December 1981 and measures the emissions from the transmitters at Deep Space Station 14 and the Spaceflight Tracking and Data Network station.*

## I. Introduction

This survey was commissioned in order to inform the Deep Space Network (DSN) managers about the emissions, both intended and spurious, from DSN operational transmitters and about the quiescent (no DSN transmitters operating) electromagnetic environment at the Deep Space Communications Complex, Goldstone, California. The opportunity was taken to gather information about the emissions from the Spaceflight Tracking and Data Network (STDN) transmitters at the Apollo site at Goldstone and to compare the Institute of Telecommunications Science (ITS) survey van sensitivity with the operational Radio Spectrum Surveillance Station (RS3) at Goldstone. The timing of the survey was driven by two considerations: (1) the desirability of completing the measurements before the Army's National Training Center at Fort Irwin and the Air Force's Superior Valley Electronic Warfare Range became operational in late January 1982 and (2) the availability of the Radio Spectrum Measurement System (RSMS) van from ITS at Boulder, Colorado.

## II. Preparation

A team was formed at Jet Propulsion Laboratory and Goldstone to support this task. The team organization chart is

Fig. 1. A technical plan was drawn up (appendix) and furnished to ITS.

Mr. R. J. Matheson is the lead engineer in ITS responsible for the operations of the RSMS van. Working in concert with Mr. Matheson, the team honed the plan from desirables to practicable; the availability of the RSMS van was defined as being November 9, 1981, onwards and the period of observations was refined to five weeks. It was explained in detail to ITS that the nature of DSN and STDN operations and scheduling would leave no room for error — that is, transmitter measurements would have to be made during a specific, pre-scheduled time frame at both DSS 14 and the Apollo site.

The variables in the schedule from the network viewpoint were identified as (1) the second orbital flight test of the Space Transportation System (Space Shuttle) and (2) engineering maintenance work at DSS 14. As things transpired, the Space Shuttle's second flight was delayed by a week and, fortunately, DSS 14 was made inoperative from 5 October to 7 December for engineering repairs to be effected on the elevation drive gearboxes. This enforced inoperability of DSS 14 allowed for a long period of time during which schedules of transmitter on/off times could be adjusted to allow for possible problems with the ITS van or any other unfore-

seen circumstances which might have arisen. This was, then, a positive bonus in flexibility to the whole measurement program. A schedule (Fig. 2) was drawn up, in concert with ITS, to take advantage of this flexibility.

From the technical plan, ITS and Section 331 of JPL were requested to interface and organize some preparatory hardware and software to enable the RFI Surveillance System of the Advanced Technology program to be utilized in support of these measurements to produce a finer resolution and, hence, a higher order of sensitivity to the measurements.

### III. Operation

The observations, originally planned to commence on November 10, were delayed due to software and hardware problems arising in the ITS van and did not get under way until December 1, 1981. At a meeting on November 23 to discuss the scheduling difficulties caused by the inoperability of the RSMS van, it was agreed that the measurements would be rescheduled as shown in Fig. 3.

The measurements were, in fact, conducted at DSS 14 in a somewhat "piecemeal" fashion; that is to say that because the station had to become operational on December 7 and the measurements could not start before December 1 and pre-operational system performance tests had to be performed prior to tracking support commencement, some tests had to be performed at odd hours (non-daytime) and with low priority (NIB 3). Tests had to be shortened to exclude all but the *essential* elements and some tests were even postponed.

The measurements at STDN and the GOSR (Goldstone Operational Surveillance Radar) Hill seemed to go very well, although the ITS van sensitivity was questioned because of its inability to detect the test transmitter at DSS 11, without reconfiguration, from GOSR Hill. An offer was made by ITS, and accepted by JPL, for the van to return to Goldstone in March 1982 to finish measurements not completed in the initial visit.

### IV. Comments

This section represents an amalgam of the observations and comments of the several support team members at the conclusion of the ITS van survey.

The funding to ITS for the measurement was to be applied in three parts: (1) \$40,000 in FY 81 for hardware and software preparation and planning, (2) \$35,000 in FY 82 for the field

measurements, and (3) \$15,000 in FY 82 for the analysis and report writing.

Technical comments included the following: (1) lack of preventive maintenance of the van resulted in its breakdown; (2) lack of planning and preparation resulted in the inability to repeatedly survey the 2290-2300 MHz band without covering the whole "superband" 2000-3580 MHz; (3) the inaccuracy of the least significant (MHz) digit of the remote receiver center frequency readout provided to the RFI surveillance system; and (4) the failure of the IF from the ITS van to perform within advertised limits ( $\pm 3$  dB within any superband). Many spurs were noticed in this IF when examined with the higher resolution of the RFI trailer.

A comment on personnel management must mention the fact that many crew changes resulted in a noticeable lack of continuity due, in part, to the average skills "mix" being definitely biased toward software and away from RF and hardware. General impressions were that this preponderance of software experience has, over a number of years, led to the use of many workarounds and fixes which may be disguising some basic RF and IF hardware problems.

Despite the above it was felt that the personnel involved in the measurements were adaptive, creative and very willing to cooperate to ensure the success of this program. Their dedication and flexibility is very much appreciated and respected.

Some of the findings which raise interesting questions are (1) there is an apparent 20 dB or so difference in received signal strength at DSS 14 for different azimuths, and (2) apparently the high power (400 kW) S-band transmitter is "cleaner" than the DSN (20 kW) transmitter in the range 1-4 GHz.

One very successful feature of these tests was the utilization of the RFI surveillance system trailer at DSS 14. The trailer was in situ awaiting the arrival of the ITS van prior to November 10, having already accomplished a 6-day environmental search of S-band. Throughout the duration of this survey the trailer proved to be very reliable (one recorder failed for two days) and very operable. The hope is that this instrument will be available in the future when other RFI tests are scheduled to be performed.

Finally it seems that, despite several problems of a technical nature, the whole measurement has been worthwhile and will yield important information about transmitter emissions and the Goldstone environment. The total success of the venture will be assured by the upcoming analyses at JPL and ITS.

## Acknowledgment

The following personnel are commended for their efforts in behalf of this program:

P. E. Beyer, Performance Analysis Group, JPL  
D. R. Hersey, Spectrum Engineering Group, JPL  
M. J. Grimm, Digital Projects Group, JPL  
G. L. Stevens, Digital Projects Group, JPL  
T. R. Tesarek, High Power Transmitter Maintenance Group, Goldstone  
M. A. Gregg, High Power Transmitter Maintenance Group, Goldstone  
F. Tate, High Power Transmitter Maintenance Group, Goldstone  
C. A. Kodak, DSN Radio Astronomy Unit, Goldstone  
R. J. McConahy, DSN Radio Astronomy Unit, Goldstone  
J. McCoy, Maintenance and Integration Group, Goldstone  
G. Wischmeyer, DSN Research & Development Facility, Venus Station, Goldstone  
D. W. Call, GSFC  
R. Nuttall, GSFC  
A. Danessa, GSFC  
Personnel of the scheduling department of the STDN at GSFC  
Station operations personnel of the DSS 14 (Mars) station, Goldstone  
Station operations personnel of the STDN (Apollo) station, Goldstone

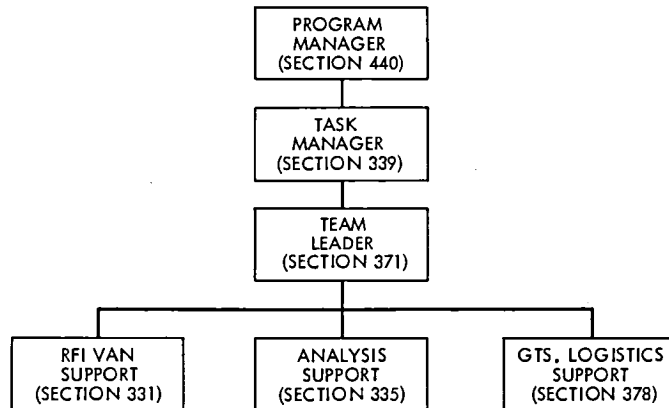


Fig. 1. JPL organization chart for RFI measurement task

MILESTONES	NOV												DEC													
	10	11	12	13	16	17	18	19	20	23	24	25	30	1	2	3	4	7	8	9	10	11	14	15	16	17
1																										
2 STDN 26-m TRANSMITTER	SU	↔																								
3																										
4 STDN 9-m TRANSMITTER			↔																							
5																										
6 HILLTOP (GOSR)			↔																							
7																										
8 HIGH-RESOLUTION ENVIRONMENTAL SURVEY						M	SU	←	→																	
9																										
10 DSS 14 TRANSMITTER (SUBREFLECTOR)												SU	←	→												
11																										
12 RFI TRAILER COUPLED								←	→																	
13																										
14																										
15																										
16																										

M - MOVE SU - SET UP

Fig. 2. ITS van survey schedule, Goldstone 1981

MILESTONES	NOV		DEC																					
	30	1	2	3	4	5	6	7*	8	9	10	11	12	13	14	15	16	17	18	19	20	21	22	
1																								
2																								
3																								
4																								
5																								
6																								
7																								
8																								
9																								
10																								
11																								
12																								
13																								
14																								
15																								
16																								

\* DSS 14 TRANSMITTER MEASUREMENTS MUST BE COMPLETED BY 1600 P.S.T. ON THIS DATE



EXTRA DAYS IN THE EVENT OF FURTHER EQUIPMENT FAILURES

Fig. 3. Revised ITS van survey schedule, Goldstone 1981

## Appendix

# Test Plan: Goldstone Transmitter Emissions and Radio Frequency Environment Measurements

### I. Introduction

This plan describes radio frequency measurements to be performed at the Goldstone Station Complex from the period of November 10 to December 17, 1981. The objectives of these measurements are to identify and quantify spurious emissions of the transmitters at DSS 14 and the Apollo station and to measure the ambient radio environments at DSS 14 and the Goldstone radar site. The information gained from these measurements will be used to assess the interference potential of the NASA stations to other stations operating in the Goldstone area, to verify assumptions made in estimating the RFI potential of colocating antennas as planned for the Network Consolidation Program and to better understand the Goldstone radio frequency environment.

### II. Test Description

The Department of Commerce Radio Frequency Measurement System (RSMS van) is required for all measurements. The JPL RFI van is to be used in conjunction with the RSMS van at DSS 14 to gain additional sensitivity. (Ideally, both vans would be used for all measurements; however, due to the time required for moving and preparing the RFI van it will only be possible to operate the two vans together at DSS 14).

### III. Apollo Station Transmitter Emissions

The purpose of these measurements is to measure the emissions from the Apollo station transmitters in order to provide emission characteristics to other Goldstone users. The RSMS van will be located 200 meters from the 9-meter and 26-meter antennas. A different location for the van will be required for each station antenna. The station antenna under test will point in azimuth at the van and as close as possible in elevation to the RSMS van's antenna.

#### WARNING

RADIATION LEVELS HAZARDOUS TO PERSONNEL ARE PRESENT WITHIN THE NEAR-FIELD TUBES OF THE STATION ANTENNAS. AT NO TIME MUST THE RSMS VAN OR PERSONNEL BE IN THE NEAR-FIELD TUBE OF A STATION ANTENNA. THIS TUBE IS CENTERED ON THE ANTENNA BORESIGHT AXIS AND HAS A DIAMETER EQUAL TO THE DIAMETER OF THE ANTENNA.

The RSMS van will perform measurements over a 1- to 12-GHz frequency range with each antenna operated at 1 kW with normal ranging modulation. The transmitter center frequency shall be approximately 2105 MHz; the major ranging tone shall be 500 kHz with a modulation index of 0.7 radian, peak. The minor ranging tone (4 kHz) shall have the same modulation index and be modulated with the normal range ambiguity resolving frequencies.

The RSMS van detection threshold (peak detection) for frequencies from 1 to 12 GHz shall be  $-97$  dBm/m<sup>2</sup> or lower except for frequencies from 2290 to 2300 MHz and 8400 to 8450 MHz, which shall be  $-116$  dBm/m<sup>2</sup> or lower. The expected received spectra are shown in Fig. A-1.

### IV. Goldstone Radar Site

The purpose of these measurements is to measure the ambient radio environment at a site which has large coverage of the Goldstone complex. If a signal measured from this location is also measured at the DSS 14 or Apollo station site an estimate of site shielding at these sites can be made.

The RSMS van will be located near the Goldstone radar facility and will perform a 360-degree horizon scan with a detection threshold of  $-109$  dBm/m<sup>2</sup> or lower over the frequency range of 2200 to 2300 MHz. At one azimuth (to be specified) the RSMS van will perform a 1- to 12-GHz search with a detection sensitivity of  $-97$  dBm/m<sup>2</sup> or better.

A comparison of indicated frequencies and received signal levels indicated by the RSMS van and Radio Spectrum Surveillance Station (RS<sup>3</sup>) for at least one airborne source and the RS<sup>3</sup> test source shall be made.

### V. Measurements at DSS 14

The measurements to be performed at DSS 14 are measurements of emissions from each of the station's transmitters and measurements of the DSS 14 radio environment with the station transmitter off. The purposes of the transmitter emission measurements are to identify spurious transmitter emissions which may interfere with future colocated stations and to obtain emission characteristics needed for frequency coordination with other agencies.

The measurements of the ambient radio environment will be performed with high-frequency resolution and sensitivity to determine the operating environment of the station. This information is needed for frequency coordination activities and to aid in the design of future DSN equipment.

The measurements will be performed using the RSMS van and RFI van operating together. The RSMS van will be located approximately 405 feet from the center of the base of DSS 14's antenna and as close as possible to the RFI van, which will be located approximately 100 feet east of the control building (see Fig. A-2).

The exact location of the RSMS van shall be selected by maximizing the signal level received at the van when the van's antenna is directed along a line from the center of the DSS 14 antenna subreflector to the edge of the antenna reflector, with the 20-kW S-band transmitter on and the station antenna in the stowed position. The maximum calculated radiation level at this location (with a 400-kW transmitter) is  $-14 \text{ dBm/cm}^2$ , so there is no hazard to personnel working in this location ( $0 \text{ dBm/cm}^2$  or higher is considered hazardous by JPL).

The interconnections of the vans shall provide:

- (1) A 330-MHz IF signal from the RSMS van receiver to the RFI van (3 dB bandwidth of 20 MHz).
- (2) An interrupt signal supplied from the RSMS van to initiate RFI van signal processing. This interrupt will occur after each 20 MHz frequency change of the RSMS van receiver center frequency.
- (3) An inhibit signal supplied by the RFI van to the RSMS van to inhibit changing the RSMS van receiver center frequency.
- (4) Digital signals for displaying the RSMS receiver center frequency in the RFI van (four most significant digits).
- (5) A voice communication link.

Using the described configuration and with the RSMS antenna directed at the DSS 14 subreflector, both vans shall measure the emissions of the DSS 14 transmitters in the frequency range of 1 to 12 GHz. The required transmitters, frequencies, and modulations are:

- (1) 20 kW S-band transmitter with DRVID ranging modulation, 9-dB carrier suppression. Center frequency, 2113.3 (DSN Channel 14).
- (2) 100 kW S-band transmitter same as 20-kW transmitter conditions.

- (3) 400 kW S-band radar transmitter modulated with 5.1 microsecond chipwidth PN code (length 2048 bits). Center frequency, 2320 MHz.
- (4) 400 kW X-band radar transmitter modulated with 5.1 microsecond chipwidth PN code. Center frequency, 8495 MHz.

Both vans will make hard copy records of the frequency and signal level of all detected signals.

The detection threshold of the RSMS van shall be  $-96 \text{ dBm/m}^2$  or lower over the range of 1 to 12 GHz except for frequencies between 2200 to 2300 MHz and 8400 to 8450 MHz. For frequencies in these ranges the detection threshold shall be  $-116 \text{ dBm/m}^2$  or lower. The detection threshold for the RFI van shall be  $-140 \text{ dBm/m}^2$  or lower for all frequencies from 1 to 12 GHz. Estimated spectra (near the carrier) for each transmitter are shown in Figs. A-3, A-4, and A-5.

The high-resolution environmental survey shall use the same configuration as for the emission measurements except that the RSMS van antenna will be pointed near the horizon and stepped 360 degrees in azimuth (time permitting). Due to limited manpower to staff the RSMS van, only the RFI van shall record the detected signals. The survey shall be made over the frequencies of 1 to 12 GHz with a detection threshold of  $-140 \text{ dBm/m}^2$  or lower.

## VI. Required Support

### A. Manpower

A minimum of two RSMS van operators shall be provided by the Institute of Telecommunications Sciences, Department of Commerce, for a 5-week period. A minimum of 1 RFI van operator will be provided by JPL for a 2-week period. Additional support, as required, will be provided by the DSN Radio Astronomy Unit.

Station personnel required are those necessary to operate the transmitters at DSS 14 and the transmitters and antennas at the Apollo station. Goldstone facility support personnel will be required to provide ac power and telephones for the RSMS and RFI vans. An RS<sup>3</sup> operator will be required for approximately 4 hours to assist in the RS<sup>3</sup> and RSMS comparisons.

### B. Power Requirements

The RFI van requires 45-kW, 3-phase power at 208 volts at DSS 14. The RSMS van requires 30 amps at 240 volts, rms, single-phase or 208 volts, rms, three phase at DSS 14, the Goldstone Radar Facility and the Apollo station.

### C. Communications

JPL will provide intercom equipment for voice communications between the RSMS van and RFI van. A telephone shall be installed in each van at DSS 14.

### D. Other Support

All electrical interfaces are shown in Table A-1. All interconnecting cables between vans and the power cables will be provided by JPL except the cable providing RSMS receiver frequency information, which will be furnished with the RSMS van. Interconnecting cables between the RFI and RSMS vans shall be 120 feet long and of the following type.

RG 214 for the 330 MHz IF signal  
RG 223 for the interrupt signal

RG 223 for the inhibit signal  
RG 223 for voice communication

## VII. Test Reports

The Institute of Telecommunications Sciences shall provide a test report describing the results of the RSMS van measurements by June 4, 1982. Copies of original hardcopy data will be supplied by JPL within 1 month of completion of the measurement. The test report shall include (1) the test configurations and pertinent system parameters, and (2) graphs of amplitude versus frequency and identification of signals where possible.

JPL Section 331 shall provide a report giving the results of the RFI van measurements within 60 days of the completion of the measurements. The report requirements are the same as in the above report.

**Table A-1. Electrical interfaces**

---

**IF signal**

Center frequency: 330 MHz  
Source impedance: 50 ohms  
3 dB bandwidth:  $\geq 20$  MHz  
Signal level: -50 dBm noise level

**RMS to RFI van interrupt**

Signal type: TTL levels  
Operation: Zero volts for ready condition

**RFI to RSMS van inhibit**

Signal type: Contact closure  
Switch excitation: +5 volts dc or ground  
Operation: Zero volts for inhibit receiver tuning

**Center frequency display**

Cable and display unit supplied with RSMS van

**Electrical power**

The power cord for the RSMS van mates with a Hubbel 50-amp female connector (No. 9450). Two phases of the three-phase power are used.

RSMS cable pin assignments are as shown.

---

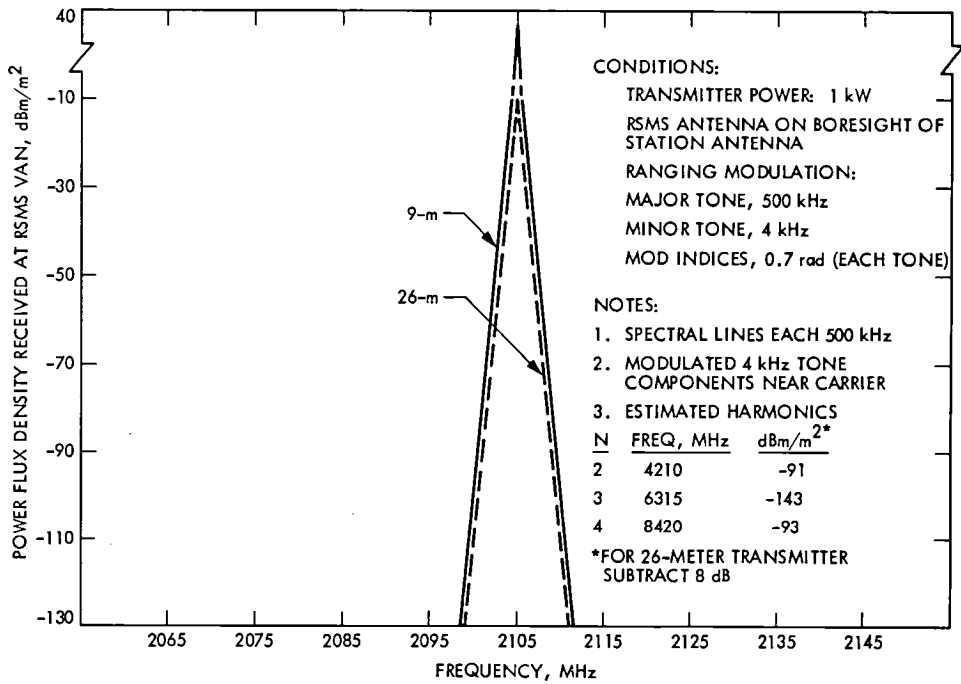


Fig. A-1. Expected emission envelope of STDN 9-meter and 26-meter transmitters

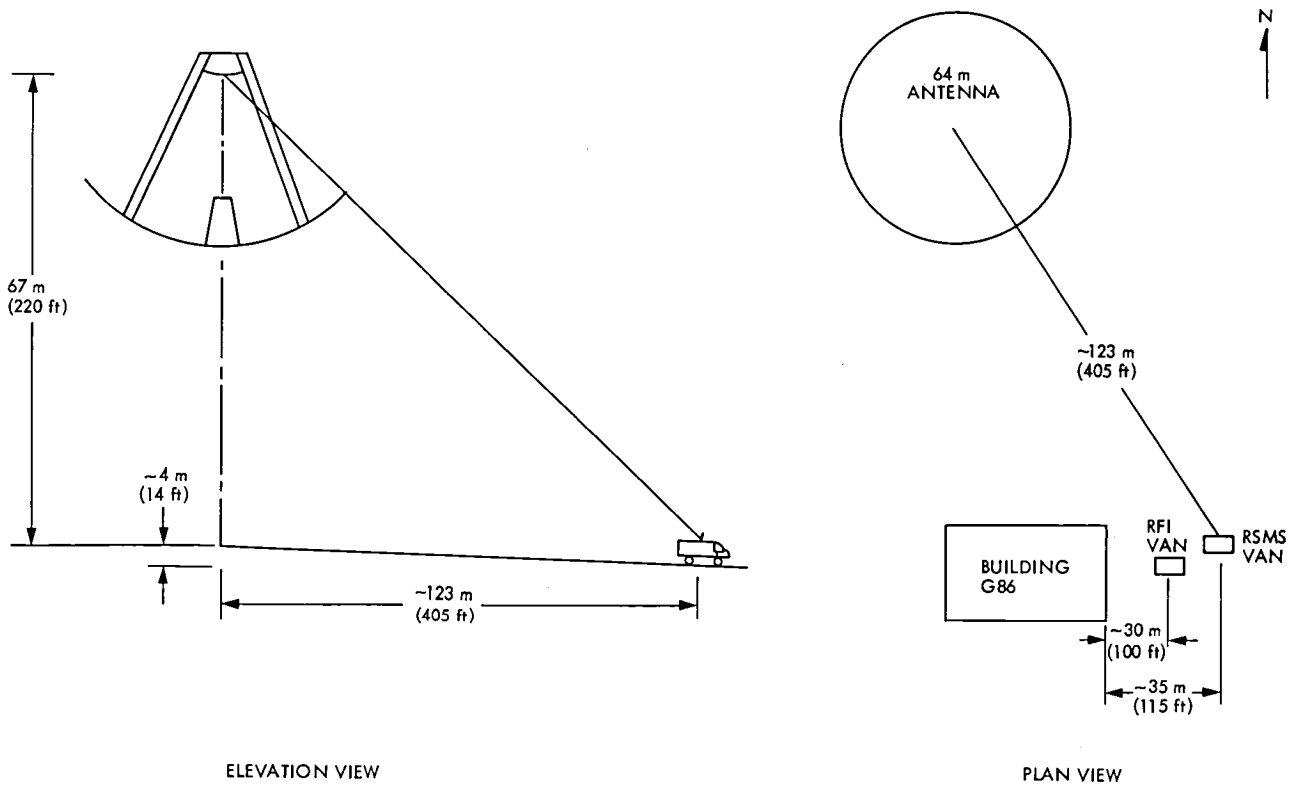


Fig. A-2. RMS van location at DSS 14

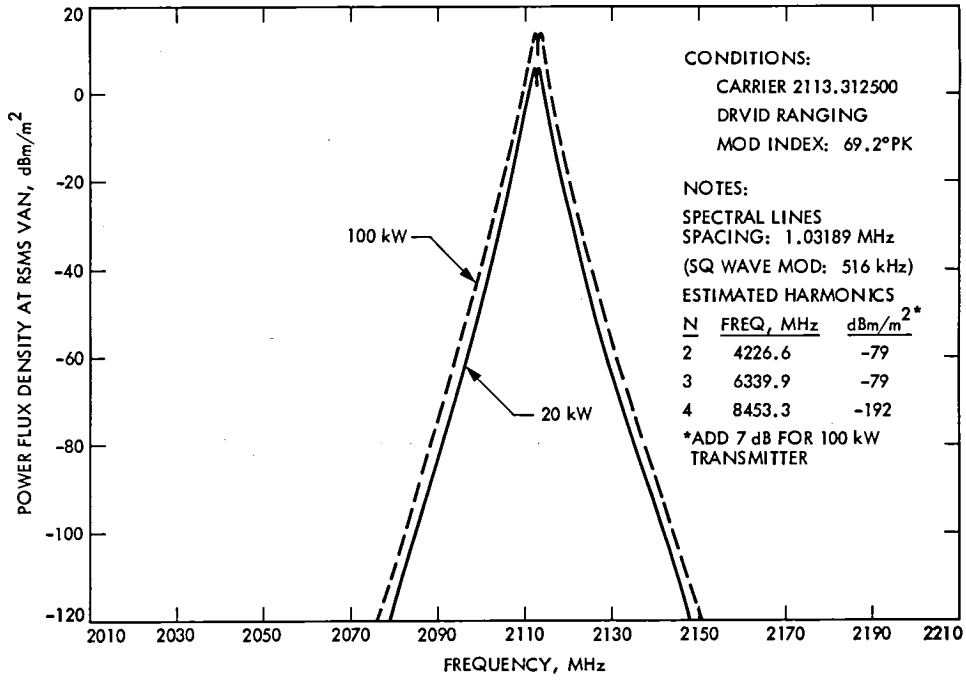


Fig. A-3. Expected emission envelopes of DSS 14 20- and 100-W transmitters

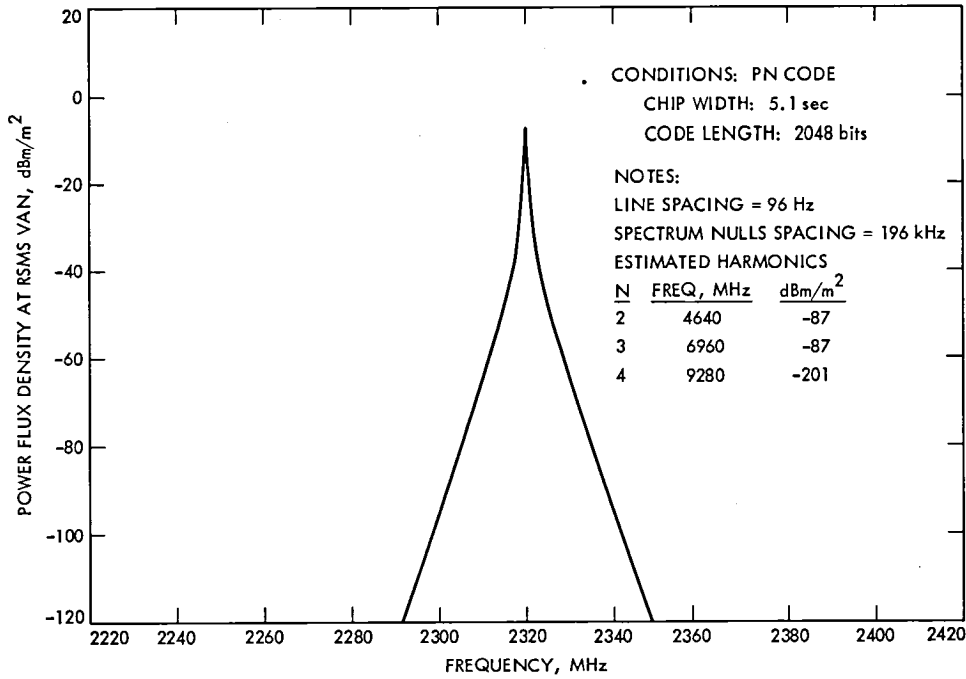
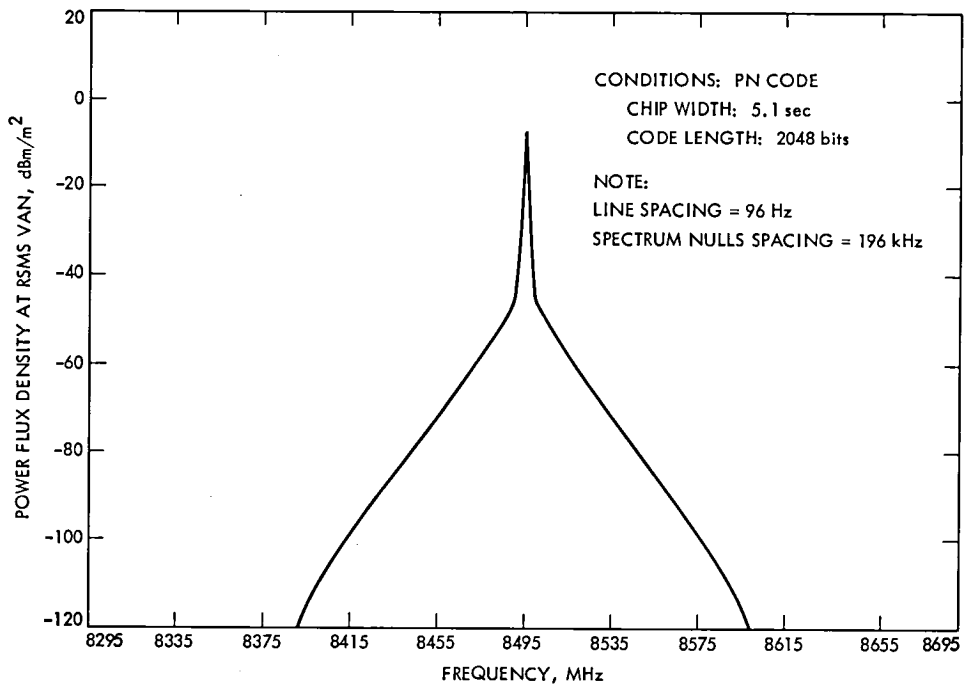


Fig. A-4. Expected emission envelope of DSS 14 400-kW S-band radar



**Fig. A-5. Expected emission envelope of DSS 14 400-kW X-band radar**

# Operations of the Reconfigured Ground Communications Facility Central Communications Terminal and the Network Operations Control Center

J. C. Santana and L. E. Jennings  
Control Center Operations Section

*The Ground Communications Facility (GCF) Central Communications Terminal and Network Operations Control Center (NOCC) hardware was rearranged, supplemented, and modified and software programs changed to provide an improved GCF and NOCC operational environment and capability. This report addresses Control Center Operations Section (371) activities required to make the 1981 changeover from the old to the new GCF and NOCC configuration.*

## I. Introduction

A requirement to reduce GCF and NOCC computer count and to provide for an improved operational capability led to the GCF-NOCC reconfiguration effort. The hardware and software changes required to implement the reconfiguration requirements were addressed in Refs. 1 to 3. As previously reported, the GCF-NOCC reconfiguration was essentially completed in April 1981 and provided the following:

- (1) A much improved operational capability to monitor and control GCF subsystems.
- (2) Reduction in minicomputers from 20 to 16.
- (3) Reduction in computer programs from 8 to 6.
- (4) Reduction in magnetic tape handling.
- (5) Reduction in operator workload due to centralized monitor and control capability, thereby providing a base for reduced manning in the Central Communications Terminal (CCT).

Personnel from DSN Data System Section (338), Control Center Operations Section (371), Deep Space Network Support Section (377), and TDA Engineering Office (430) worked together to develop and implement reconfiguration plans. The plans provided for the transition from the old to the new GCF-NOCC configuration to be accomplished without interruption of the GCF and Network Data Processing (NDP) operations support committed to Flight Projects and other DSN users. The changeover required extensive operator training and considerable integration and testing of equipment and software.

## II. Reconfiguration Implementation

To assure that ongoing projects and other DSN users were provided committed operational support it was necessary to implement the reconfiguration in phases which resulted in the coexistence in the CCT of the old and the new configuration. The original configuration of the elements of the GCF, CCT and NOCC involved in the reconfiguration is shown in Fig. 1. To provide for the development and testing of the new software programs and hardware interfaces two additional Mod-Comp minicomputers were installed (by Section 338) in the CCT. These computers became the temporary Error Correction and Switching (ECS) and Data Records Generation (DRG) assemblies and, along with the existing backup Central Communications Monitor (CCM) and Network Communication Equipment (NCE) computers, provided an interim ECS-DRG-CCM-NCE string which processed both high-speed and wideband data.

The interim string was used for development and testing and also provided for informal operator training and general familiarization with the new equipment and software programs. The additional ModComps were connected to the existing CCT equipment and to the Mission Control and Computing Center (MCCC) interfaces, thereby permitting development, testing, and training to be done in a realistic environment.

Beginning in July 1980 installation activities began to implement the GCF-NOCC Reconfiguration Engineering Change Order 79.112. As a result, operations simultaneously operated equipment and software in both the old and new configuration. The resultant configuration was the test configuration shown in Fig. 2. The test configurations improved the ability of operators to acquire on-the-job training in equipment and software which resembled the final GCF-NOCC configuration. From January-April 1981, installation activities took place which resulted in an operational version of the GCF-NOCC configuration. The reconfigured GCF-NOCC, shown in Fig. 3, was used to support Voyager 2 encounter with Saturn.

## III. Reconfiguration Operational Phases

The operation of the GCF-NOCC reconfiguration was accomplished in two phases, the first using the test configuration shown in Fig. 2 and the second using the operational configuration shown in Fig. 3. An orderly transition from the old to the new configuration required considerable planning by and coordination between personnel from Sections 338, 371, and 377 and Office 430. A GCF-NOCC Reconfiguration Project Team, headed by J. P. McClure, Section 338, developed and implemented reconfiguration installation, testing, training and support plans. Section 377 prepared two excellent Training Materials Packages (TMP). One of the TMPs covered

all of the GCF, CCT and NOCC subsystems and the other TMP applied specifically to the Central Communications Monitor Assembly. In addition, Section 371 prepared and implemented a GCF-NOCC Reconfiguration Operations Support Transition Plan and a Communications Operations Support and Training Plan. The Section 371 plans, supplemented by those prepared by the Reconfiguration Project Team, formed the basis for the operations of the reconfigured GCF-NOCC.

In May 1980, the Communications and Data Processing Operations Group (Section 371), in coordination with the GCF Subsystem Group (Section 338), established an interface which took advantage of operator training opportunities provided during the development phase of the ECS/DRG/CCM software programs. Participation by Operations personnel in the early stages of software testing resulted in their becoming familiar with the new configurations and provided a basis for the development of personnel training packages. During the hardware/software development phase, many GCF and NOCC subsystem verification and acceptance tests were supported by Communications and NDP Operations personnel, and they gained valuable operating experience. Unfortunately, Communications and NDP Operations personnel were unable to take maximum advantage of the training opportunities afforded during the development phase since the priority for limited operations resources was given to the task of preparing for the critical support of Voyager 2's encounter with Saturn.

As ECO 79.112 implementation activities progressed, Operations was able to operate the interim configuration in a parallel mode. Committed support was provided using the old configuration and at the same time the data were processed in the new configuration. The parallel mode of operations provided a means to verify the validity of the performance of the new hardware and software by allowing a comparison of the data processing results of the two configurations.

## IV. Flight Project and DSN User Support

The GCF-NOCC Reconfiguration Operations Support Transition Plan prepared by the Mission Coordination Group, Section 371 was implemented beginning on December 1, 1980. Operational support was provided to Flight Projects and other DSN users using the interim configuration.

### A. Pioneer Project Data Interfaces

The DSN to Pioneer Project Mission Operations Control Center (PMOCC) was the first interface verified. Telemetry/Command data from the DSSs were parallel-routed to both the Error Detection Correction (EDC) and Network Log Processor (NLP) computers and to the new ECS-DRG-CCM string. The preliminary testing verified that DSN support

committed to the Pioneer Project could be met using the new hardware and software programs.

The next step was to support the Pioneer Project using only the new configuration. This began on March 10, 1981, and verified the operational capability of the new/revised GCF and NOCC subsystems to support the Pioneer Project. The testing established the following:

- (1) That the new ECS, DRG, CCM, NCE, Digital Display Processor (DDP) and Video Assembly Processor (VAP) software and software interfaces operated properly.
- (2) That the new hardware interfaces were compatible and functional.
- (3) That Intermediate Data Records (IDR), a deliverable data product, could be properly generated in accordance with DSN-Pioneer Project IDR Interface Agreements.

The Pioneer Project evaluated the support provided by the new CCT configuration and concurred that DSN commitments to them were being met.

## **B. Helios Project Data Interfaces**

Development and implementation of the ECS to MCCC router interface was successfully completed and this allowed Helios Project testing to begin in mid-February 1981. Tests were scheduled which successfully verified the operational interface between the MCCC and the German Space Operations Center (GSOC), using the ECS to Router interface to pass high-speed data blocks between the MCCC and GSOC. The next step was the scheduling of Deep Space Station (DSS) to MCCC/GSOC demonstration passes. These tests successfully demonstrated that the new configuration could provide DSN committed support to the Helios Project.

## **C. Viking Project and DSN User Data Interfaces**

On April 5, DSS demonstration passes verified that the Viking Project could be supported using the new configuration. Also successfully demonstrated was the DSN's capability to support DSN users. Very Long Baseline Interferometry (VLBI) and Tracking Calibration Data (TCD) demonstration passes processed data using the new configuration. VLBI/TCD IDRs were generated and met IDR Interface Agreement commitments.

## **D. Voyager Project Data Interfaces**

Testing to verify the DSN's capability to meet its commitments to the Voyager Project using the new configuration was much more complex than for other flight projects and required

extensive planning and support from all elements of the DSN and MCCC.

**1. IDR generation test.** A Voyager Project IDR generation test was scheduled in August 1980 using the new ECS-DRG-CCM interim string and the ECS-MCCC Router interface. Telemetry data from DSS 12 support of Voyager 2, Spacecraft 32, were processed. The test had as objectives the following:

- (a) Error Correction Switching Computer:
  - (1) Process high-speed data from Station 12.
  - (2) Log all data on magnetic tape generating Front End Records (FER).
  - (3) Transmit data to the DRG across GCF Star Switch Controllers (SSC).
  - (4) Transmit data to MCCC Routers (RTR) across GCF MCCC SSCs.
  - (5) Receive/transmit Automatic Total Recall System (ATRS) messages to Station 12 during postpass ATRS activities.
  - (6) Generate and transmit CCM report.
- (b) Data Records Generator Computer:
  - (1) Log high-speed data from ECS on big disc by data stream.
  - (2) Provide data throughput status reports in real-time.
  - (3) At end of pass, recall missing data from station using ATRS and log on big disc.
  - (4) Merge real-time and recall data from big disc to magnetic tape; generate an IDR.
  - (5) Generate and transmit CCM report.
- (c) Central Communications Monitor Computer:
  - (1) Receive ECS-DRG reports and generate displays.
- (d) MCCC Router:
  - (1) Receive data from ECS across the GCF MCCC SSCs.

Analysis of the test results, including Voyager Data Management Team processing of the IDR, established that Voyager data could be processed by the new hardware and software and that DSN to MCCC high-speed data interfaces were satisfactory.

**2. MCCC Router interface.** The extensive development, testing, and training requirements placed a great demand on the limited ECS-DRG-CCM-Router capability. Close coordi-

nation was necessary to assure maximum and efficient utilization of the new equipment/software programs. After considerable DSN and MCCC testing, the ECS-MCCC Router interface was successfully established with the MCCC Router software transferred from Development to MCCC Operations on March 20, 1981.

3. **Ground data system tests.** Voyager Ground Data System (GDS) tests to validate telemetry, monitor, tracking, and command data end-to-end system operations were successfully supported. The facilities of CTA-21 (Compatibility Test Area, JPL) were used for the April 1 and April 6 GDS tests. On April 13, a third GDS test was completed with DSS 43. The Voyager Project considered the tests very successful and with all GDS test objectives met all further testing was cancelled.

## V. GCF Wideband Subsystem

ECO 79.112 also provided for changes to the GCF WB subsystem and those changes were implemented simultaneously with the changes to the NOCC Display Subsystem and other GCF subsystems. Wideband Network Encoder Decoders (NED) replaced Coded Multiplexer Demultiplexers (CMDs) in the CCT. The NED installation along with installation of new WB unbalanced switches, WB customer interfaces, customer distribution assemblies, and other changes to the WB subsystem allowed wideband data to be processed by the old system or the new system or both at the same time. The interim wideband capability was used to support Voyager and VLBI wideband tests.

## VI. Cutover to New Configuration

The testing necessary to verify that the new GCF-NOCC configuration could meet the DSN's committed support requirements was now complete and it was mutually agreed that the cutover to the new configuration could take place. At 8:30 a.m. April 20, all flight support was assigned to the new configuration and the old configuration decommitted. Ten of the 16 computers that were part of the new configuration were placed on-line. Yet to be converted were three EDC Computers, which were to become ECSs 1, 2, and 3, and one High Speed Switch (HSW) Computer and two NLPs, which were to become DRGs 1, 2, and 3. The conversion began immediately after the old equipment was decommitted, and at the end of April 20 all but one EDC and the two NLPs were converted to their new configuration. The two NLPs were converted to DRGs the week of April 20, but due to hardware malfunctions difficulty was experienced converting EDC 4 to become ECS 4. After considerable coordinated effort by Sections 371 and 338 the EDC was finally converted to ECS 4 on May 31.

With communications and NDP support being provided using the new configuration, Operations began experiencing problems that had not been evident when they operated the interim configuration. Operations initiated approximately 120 Discrepancy Reports, from April 20 to June 4, which described problems/failures with the ECS hardware/software/interfaces.

The DRGs also experienced problems, but to a much lesser degree. The operational performance of the new GCF CCT-NOCC configuration became a matter of concern because of the inordinate amounts of problems/failures. With DSN committed to support Voyager 2 encounter with Saturn in the new configuration, it was essential that the operational performance of the reconfigured GCF CCT-NOCC improve considerably. To this end, Section 338 reactivated the GCF-NOCC Reconfiguration Task Team to systematically define the problems, to determine the reasons for the problems, and to implement solutions.

The team meetings began June 10 and continued on a weekly basis until August 13. The team's activities resulted in minor software and hardware changes and operational procedure revisions which when implemented resulted in a decided improvement in the operational performance of the new configuration. That the team's efforts paid off was evident by the fact that Voyager 2's encounter with Saturn was an outstanding success. Contributing to that success was the excellent communications and network data processing operations support provided using the new configuration.

## VII. Summary

The GCF-NOCC reconfiguration effort was very complex and required extensive coordination and planning by Sections 371, 338, and 377 and Office 430. Many implementation problems were encountered and were resolved by a coordinated effort of all concerned. The implementation challenges were met and the operational support committed to flight projects and DSN users was successfully accomplished using the reconfigured GCF-NOCC.

DSN Engineering and DSN Operations learned many important lessons during the long period required to develop, test, and implement the GCF-NOCC reconfiguration. DSN Engineering/Operations agree that the lessons learned should be applied to future implementation activities. Summaries of the lessons learned are:

- (1) Need for close coordination between Engineering and Operations beginning early in the development of major implementation tasks.

- (2) Need for documented operational testing and training plans early in the implementation phase. Early knowledge by Operations of testing/training requirements can provide time needed to properly develop the resources required to train/test operations personnel to operate complex new systems.
- (3) Need for early development of documentation which describes the new hardware and software capabilities and functions.
- (4) Need to implement means for testing new capability, to the maximum extent, independent of the use of operational equipment.
- (5) Need to form combined Engineering/Operations teams early in the implementation phase. The team's objectives to be the development and implementation of detailed plans which document the steps necessary to take a major new capability from the development to the operational support phase.

## References

1. McClure, J. P., "GCF-NOCC Reconfiguration," in *The Deep Space Network Progress Report 42-55*, pp. 86-89, Jet Propulsion Laboratory, Pasadena, Calif., Feb. 1980.
2. Bremner, D. S., and Hung, C. K., "Ground Communications Facility and Network Operations Control Center Reconfiguration," in *The Deep Space Network Progress Report 42-58*, pp. 108-109, Jet Propulsion Laboratory, Pasadena, Calif., Aug. 1980.
3. McClure, J. P., "GCF-NOCC Reconfiguration," in *The Deep Space Network Progress Report 42-66*, pp. 288-290, Jet Propulsion Laboratory, Pasadena, Calif., Dec. 1981.

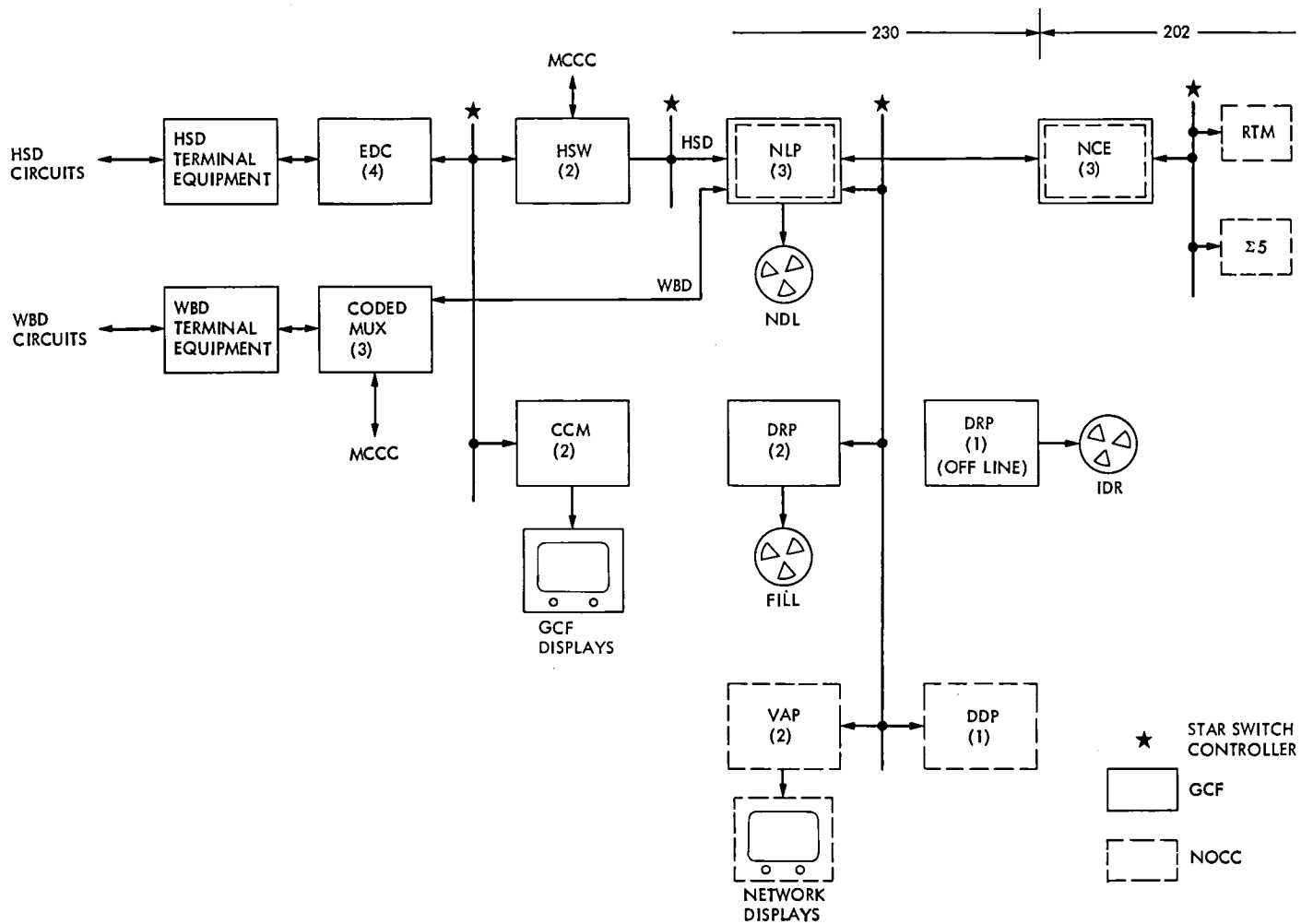


Fig. 1. Original GCF CCT-NOCC configuration

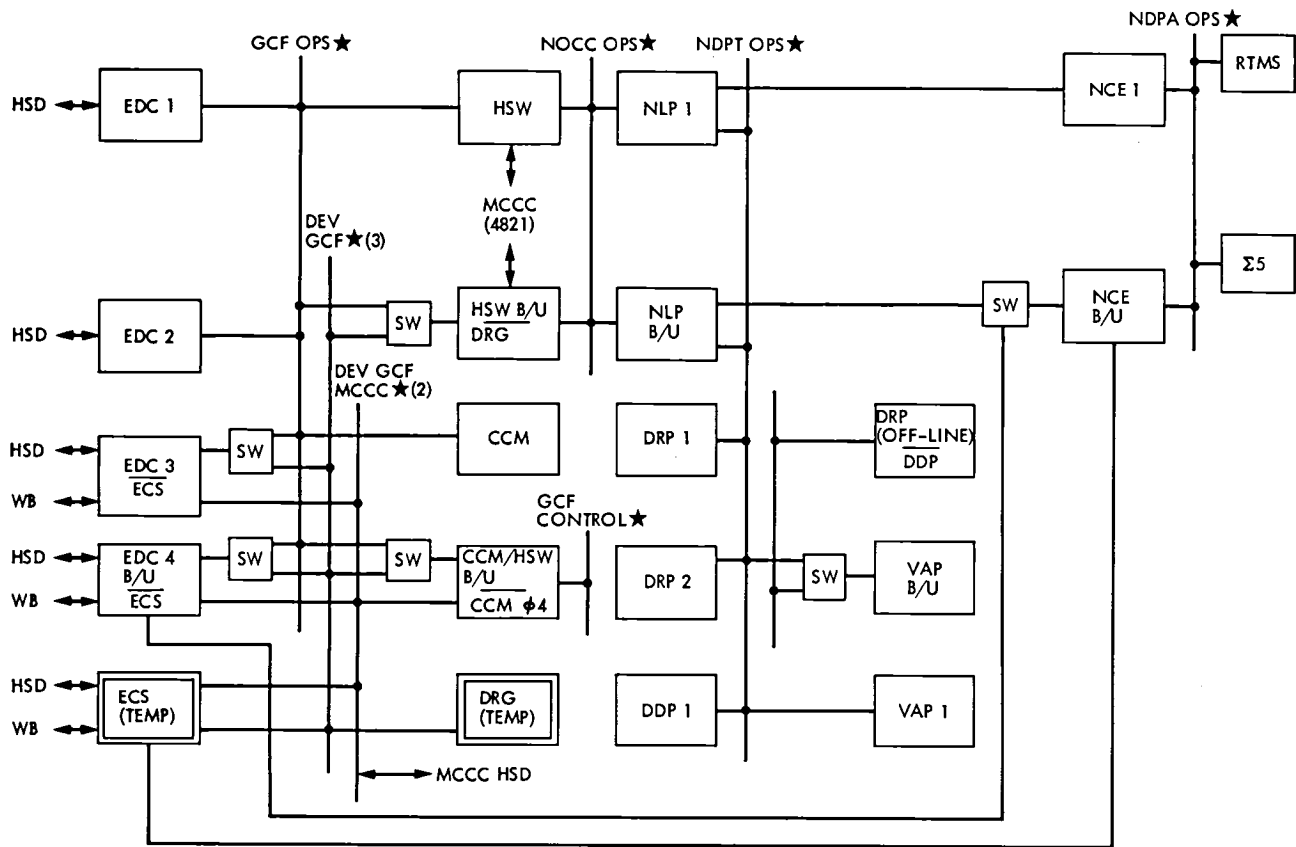


Fig. 2. Test configuration

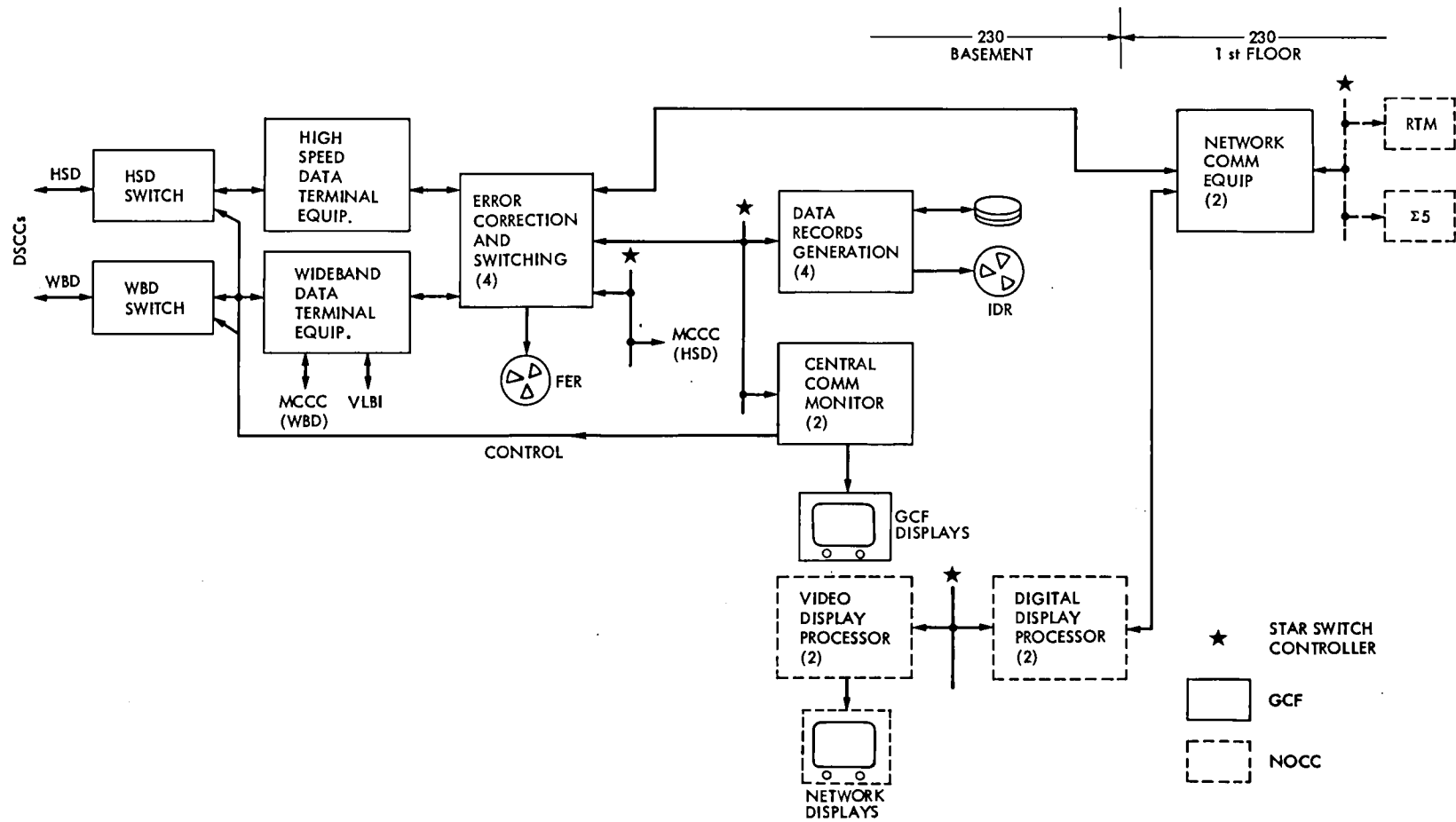


Fig. 3. Reconfigured GCF-NOCC

# Mark IV-A DSCC Telemetry System Description

R. Burt  
TDA Engineering Office

*This article provides an update to the description of the Deep Space Communications Complex (DSCC) portion of the Mark IV-A Telemetry System. This system, first described a year ago in this document, is currently being designed as a replacement for the Mark III.*

## I. Introduction

The present DSN Telemetry System, the Mark III, is described in Ref. 1. The DSN is undertaking a major modification of the Mark III. The modified Network, described in Ref. 2, will be called the Mark IV-A and will be implemented between 1983 and 1985. The DSCC portion of the DSN Telemetry System will be changed in two major ways as a result of the Mark IV-A DSN implementation:

- (1) Two 34-meter antennas will be added to each Deep Space Communications Complex (DSCC). The arraying of those antennas with the existing 64- and 34-meter antennas will provide the equivalent of two separate 64-meter antennas or two 64-meter antennas arrayed together. To accomplish this, the DSCC will be modified to provide baseband combining of three 34-meter antennas and one 64-meter antenna.
- (2) The Telemetry System will be configured to support either two deep space missions and one highly elliptical orbiter or two highly elliptical orbiters and one deep space mission. Highly elliptical orbiter (HEO) missions will have data rates up to 202 kbps modulated directly on the carrier.

Implementation of these changes, when combined with the existing capabilities, will prepare the network to support both DSN and HEO missions.

The DSN missions will be the following:

Pioneers 6 through 9

Pioneers 10 and 11

Pioneer Venus

Viking

Voyager

Galileo

ISPM (ESA) (International Solar Polar (European Space Agency))

The Highly Elliptical Orbiter (HEO) missions will be the following:

ISEE-C (International Sun Earth Explorer)

AMPTE (Active Magnetospheric Particle Tracer Experiment)

— CCE (Charge Composition Explorer)

- IRM (Ion Release Module)
- UKS (United Kingdom Spacecraft)

TDRS (Tracking Data Relay Satellite)

GOES G, H, I (Geostationary Operational Environmental Satellite)

## II. Key Characteristics

The key characteristics of the DSCC portion of the Mark IV-A Telemetry System are:

- (1) *Data rates up to 500 kilosymbols per sec (ksp/s).*
- (2) *Baseband combining for up to 7 antennas.*
- (3) *Deletion of analog recording.*
- (4) *Four complete groups of telemetry equipment at each complex, each with the capacity to support one of the above missions.*
- (5) *Demodulation of Manchester coded (Bi $\phi$ -L) or NRZ-L data modulated directly on the carrier.*
- (6) Maximum likelihood decoding of short-constraint-length convolutional codes and sequential decoding of long-constraint-length convolutional codes.
- (7) Precise measurement of received signal level and system noise temperature.
- (8) Centralized control by (and real-time reporting to) the Monitor and Control Subsystem.
- (9) Production of a digital telemetry Original Data Record (ODR) at each telemetry group with playback via local manual control or in automatic response to GCF inputs; reduced playback rate for higher data rates as required.

The characteristics that reflect new or modified capabilities due to Mark IV-A design requirements are italicized. The handling of increased data rates and demodulation of NRZ or biphase data modulated directly on the carrier directly responds to a requirement for telemetry support of HEO spacecraft. Baseband combining provides for improved sensitivity to high data rate X-band signals in support of deep space telemetry and is driven by the Voyager project requirement for support of 19.2 kbps at Uranus encounter. New equipment for baseband combining allows a data rate increase to 500 kps from the previous high of 250 kps. The provision for four groups of telemetry equipment at each SPC responds to the requirement to provide telemetry support to three projects concurrently. The absence of project requirements for analog recording allows that function to be removed. Characteristics

which are not italicized exist presently in the Mark III and are discussed in Ref. 1.

## III. Project Data Rate and Coding Requirements

HEO missions are compatible with the existing DSN capabilities. This is illustrated in Table 1, which defines the single link data handling requirements for the HEO projects included in the Mark IV-A mission set. A telemetry single link can be defined as all of the functional elements, from the antenna(s) through an SPC telemetry group, that have been selected for support of a project. The requirement to detect Bi $\phi$ -L (Manchester coding) modulated directly on the carrier is not supportable by existing DSN capabilities.

Requirements for new and existing deep space missions are listed in Table 2. The new missions to be supported during Mark IV-A are Galileo and ISPM-ESA. The next section shows how HEO and deep space mission requirements will be met.

## IV. DSCC Conceptual Description

The DSCC block diagram in Fig. 1 provides a conceptual description of the portion of the Mark IV-A Telemetry System to be located at the DSCC. At each complex there will be one 64-meter antenna, three 34-meter antennas, and a 9-meter antenna. The 64-meter and 34-meter transmit/receive antennas will be able to receive an S-band plus an X-band carrier simultaneously. One of the 34-meter Listen-Only antennas will receive either one S-band or one X-band carrier; the other will receive one X-band carrier. The 9-meter will receive 2 S-band carriers. Table 3 gives the RF reception characteristics for these antennas and indicates the distribution of masers, FETs and Paramps. The 64-meter antennas will be equipped exclusively with masers whereas the 34-meter antennas will also have FETs. At the 34s the masers will provide deep space support and the S-band FETs will support HEOs with their broader (2200-2300 Mhz) reception bandwidth requirements. The 9-meter antennas will be provided exclusively with Paramps. New Block II-A X-band masers will be provided, giving lower X-band system temperatures than in the Mark III DSN. Also, the new 34-meter antennas will provide increased gain compared with the existing 34-meter transmit-receive antennas.

Existing Block III and Block IV receivers will be used to receive the baseband signals. They will be modified to support HEO frequencies and provide a broad (~8 MHz) baseband output to the Telemetry Subsystem. The Telemetry Subsystem is arranged to provide four telemetry groups, any of

which can process data from either an HEO or deep space spacecraft. All groups will include the Mark III Maximum Likelihood Convolutional Decoder (MCD) and Telemetry Processor Assembly (TPA). Telemetry Groups 1 and 2 will also be equipped with a new Baseband Assembly (BBA) which will include the functions of baseband combining, subcarrier demodulation and symbol synchronization. Figure 2 is a functional block diagram of the BBA. Any combined set of receiver outputs can be input to either subcarrier demodulator; or any single receiver output can be routed to either subcarrier demodulator, bypassing the combining function. The monitor and control function will be performed from the TPA with no manual intervention required. The BBA will be designed to accommodate NRZ-L, M or Bi $\phi$ -L symbol formats, subcarriers up to 2 MHz and data rates from 4 s/s to 1 Ms/s without subcarrier or up to 4 Ms/s (NRZ) with subcarrier. Operation with the BBA, including combining the 64-m and all three 34-m antenna basebands, will result in a nominal system degradation at the highest data rates of about 0.3 dB. This includes an allowance for waveform, spectrum correlation and symbol timing losses and represents an improvement over the Mark III system of several tenths of a dB. Telemetry Groups 3 and 4 will include Mark III Subcarrier Demodulator Assemblies (SDA) and Symbol Synchronizer Assemblies (SSA) as well as an MCD and TPA. Therefore, hardware in Group 3 and Group 4 will closely resemble the Mark III Telemetry Subsystem. The SDAs will be modified to decode Bi $\phi$ -L (Manchester coded) data so that Groups 3 and 4 can support HEO missions without using Spaceflight Tracking and Data Network (STDN)

bit synchronizers as proposed in Ref. 3. New software will be provided for the TPAs.

The 64- and 34-meter antennas can be arrayed by combining baseband signals and performing subcarrier demodulation and symbol synchronization in the BBA in either Telemetry Group 1 or Telemetry Group 2. The combined signal is then decoded in the Maximum Likelihood Convolutional Decoder and formatted for transmission to JPL in the Telemetry Processor Assembly. When combining is not required, outputs from an antenna may also be routed to a Subcarrier Demodulator Assembly (Groups 3 and 4) or to either Baseband Assemblies (Groups 1 and 2).

Any of the telemetry equipment groups can accept two data streams. In any group, one data stream is processed by Channel 1 and one by Channel 2. The performance parameters for Channels 1 and 2 are listed in Tables 4 and Table 5, respectively. Comparing Table 1 with Tables 4 and 5, it may be noted that Data Stream 1 in Table 1 is processed by Channel 2, while Data Stream 2 is processed in Channel 2. Also note that Groups 1 and 2 provide higher data rate capability (500 ks/s vs 250 ks/s and higher subcarrier frequency capability (2 MHz vs 1.2 MHz). This improvement is due to the BBA and wider receiver passband. However, the overall system will not support the highest BBA/receiver data rate capability until further improvements are made, including MCD replacement and provision for high rate recording and quick look. Future planned missions will require these additional improvements.

## References

1. Gatz, E. C., "DSN Telemetry System Mark III-77," in *DSN Progress Report 42-49*, Jet Propulsion Laboratory, Pasadena, Calif., Feb. 15, 1979.
2. Gatz, E. C., "Networks Consolidation Program System Design," in *TDA Progress Report 42-63, March and April 1981*, Jet Propulsion Laboratory, Pasadena, Calif., June 15, 1981.
3. Burt, R. W., "Mark IV-A DSCC Telemetry System Description," in *TDA Progress Report, 42-63, March and April 1981*, Jet Propulsion Laboratory, Pasadena, Calif., June 15, 1981.

**Table 1. Single link requirements for HEO missions**

Mission	Data Stream 1	Data Stream 2
I SEE-C	Convolutionally coded; K=24, R=1/2; NRZ-L; 64 b/s; Subcarrier: 1024 Hz  or Convolutionally coded; K=24, R=1/2; 512 to 2048 b/s; Bi $\phi$ -L	
AMPTE-CCE	Convolutionally coded; K=7, R=1/2; Bi $\phi$ -L 101,000 b/s	Uncoded NRZ-L; 3300 b/s; subcarrier: 404 kHz
AMPTE-IRM	Convolutionally coded; K=7, R=1/2; NRZ-L; 1.024 kb/s, 2.048 kb/s, 4.096 kb/s, or 8.192 kb/s; subcarrier: 131,072 Hz	
AMPTE-UKS	Convolutionally coded; K=7, R=1/2, or uncoded; Bi $\phi$ -L; 1024 b/s, 2048 b/s, 4096 b/s, 8192 b/s, 16384 b/s, 32768 b/s	
TDRS		Uncoded; 250 b/s, 1000 b/s, 4000 b/s, NRZ; subcarrier: 1.024 MHz
GOES-G,H,I		Uncoded; 2000 b/s, Bi $\phi$ -L

**Table 2. Single link requirements for deep space missions**

Mission	Data Stream 1	Data Stream 2
Pioneers 6-9	Uncoded; NRZ-M; 8 to 512 b/s; subcarrier: 512 Hz for 8 to 64 b/s, 2048 Hz for $\geq 128$ b/s; S-band	
Pioneers 10/11	Uncoded; NRZ-L; 8 to 2048 b/s; subcarrier: 32 kHz; S-band  or Convolutionally coded; K=32, R=1/2, NRZ-L; 8 to 2048 b/s; subcarrier: 32 kHz; S-band	
Pioneer Venus	Uncoded; NRZ-L; 8 to 4096 b/s; subcarrier: 16 kHz; S-band  or Convolutionally coded; K=32, R=1/2; NRZ-L; 8 to 2048 b/s; subcarrier: 16 kHz; S-band	
Voyager	Convolutionally coded; K=7, R=1/2; NRZ-L; 10 to 115,000 b/s; combined X-band; subcarrier: 360 kHz	Uncoded; NRZ-L; 40 b/s; subcarrier: 360 kHz; combined X-band  or Uncoded; NRZ-L; 40 b/s; subcarrier: 22.5 kHz; S-band
Galileo	Convolutionally coded; K=7, R=1/2; NRZ-L; up to 134.4 kb/s; subcarrier: 360 kHz; combined X-band  or Convolutionally coded; K=7, R=1/2; NRZ-L; up to 40 kb/s; subcarrier: 22.5 kHz for data rates up to 7.68 kb/s, 360 kHz for rates $\geq 7.68$ kb/s; S-band	Uncoded; NRZ-L; 40 b/s; subcarrier: 22.5 kHz; S-band
ISPM-ESA	Convolutionally coded; NRZ-L; K=7, R=1/2; 128 b/s-8,192 b/s; subcarrier: 65,536 Hz for rates up to 1,024 b/s, 131,072 Hz for rates of 2,048 b/s or greater; X-band	
Viking	Block coded; NRZ-L; 250 b/s to 1 kb/s; subcarrier: 228 kHz; S-band	Uncoded; NRZ-L; 8-1/3 or 33-1/3 b/s; subcarrier: 48 kHz; S-band

**Table 3. RF reception characteristics**

Parameter	Antenna			
	64-meter	34-meter Transmit/ Receive	9-meter	34-meter Listen- Only
Frequency range, MHz				
S-band	2270-2300	2200-2300	2200-2300	2200-2300 <sup>a</sup>
X-band	8400-8440	8400-8440		8400-8435
Gain, dBi				
S-band	61.7 <sup>+0.3</sup> <sub>-0.4</sub>	56.1 <sup>+0.3</sup> <sub>-0.7</sub>	43.8 <sup>+0.4</sup> <sub>-0.8</sub>	55.8 <sup>+0.0</sup> <sub>-0.5</sub>
X-band	72.1 <sup>+0.6</sup> <sub>-0.6</sub>	66.5 <sup>+0.3</sup> <sub>-0.9</sub>		67.3 <sup>+0.5</sup> <sub>-0.8</sub>
System noise temp, K zenith				
S-band with maser				
Diplex	18.5 ±3	27.5 ±2.5		
Listen-Only	14.5 ±3	21.5 ±2.5		
S-band with paramp <sup>b</sup>				
Prime			125 ±25	
S-band with FET				
Diplex		130 ±10		
Listen-Only				115 ±10 <sup>a</sup>
X-band with maser	20 ±3	21.5 ±3		18.5 ±2

<sup>a</sup>One 34-m Listen-Only antenna per complex has this capability. Others are 2290-2300, X-band only.

<sup>b</sup>Diplexed operation.

**Table 4. DSCC Telemetry Subsystem channel capabilities (Telemetry Groups 1 and 2)**

Functions	Channel 1	Channel 2
Baseband combining	Up to six receivers	N/A
Subcarrier demodulation	Approximately 10 kHz to 2 MHz, squarewave or sine wave	Approximately 10 kHz to 2 MHz squarewave or sine wave
Sequential decoding	K=24, 32; R=1/2; frame length= variable 6 s/s to 10 ks/s	N/A
Maximum-likelihood	K=7; R=1/2 or 1/3	N/A
Convolutional decoding	10 b/s to 250 kb/s	N/A
Block decoding	Reed-Muller 32/6; up to 2 kb/s	N/A
Symbol rate	4 s/s – 500 ks/s <sup>a</sup>	4 s/s to 500 ks/s <sup>a</sup>
Uncoded rate	4 b/s – 600 kb/s <sup>a</sup>	4 b/s to 500 kb/s <sup>a</sup>
Data format	NRZ-L, M, Biφ-L	NRZ-L, Biφ-L

<sup>a</sup>Record with non-real-time playback from 250 to 500 ks/s.

**Table 5. DSCC Telemetry Subsystem channel capabilities (Telemetry Groups 3 and 4)**

Functions	Channel 1	Channel 2
Subcarrier demodulation	100 Hz to 1.00 MHz squarewave or sine wave	100 Hz to 1.00 MHz, squarewave or sine wave
Baseband combining	N/A	N/A
Sequential decoding	K=24, 32; R=1/2; frame length: variable, 6 s/s to 10 ks/s	N/A
Maximum-likelihood	K=7, R=1/2 or 1/3	N/A
Convolutional decoding	Reed-Muller 32/6, up to 2 kb/s	N/A
Symbol rate	6 s/s to 250 ks/s	6 s/s to 250 ks/s
Uncoded rate	6 b/s to 250 kb/s	6 b/s to 250 kb/s
Data format	NRZ-L, NRZ-M, Biφ-L	NRZ-L, NRZ-M, Biφ-L

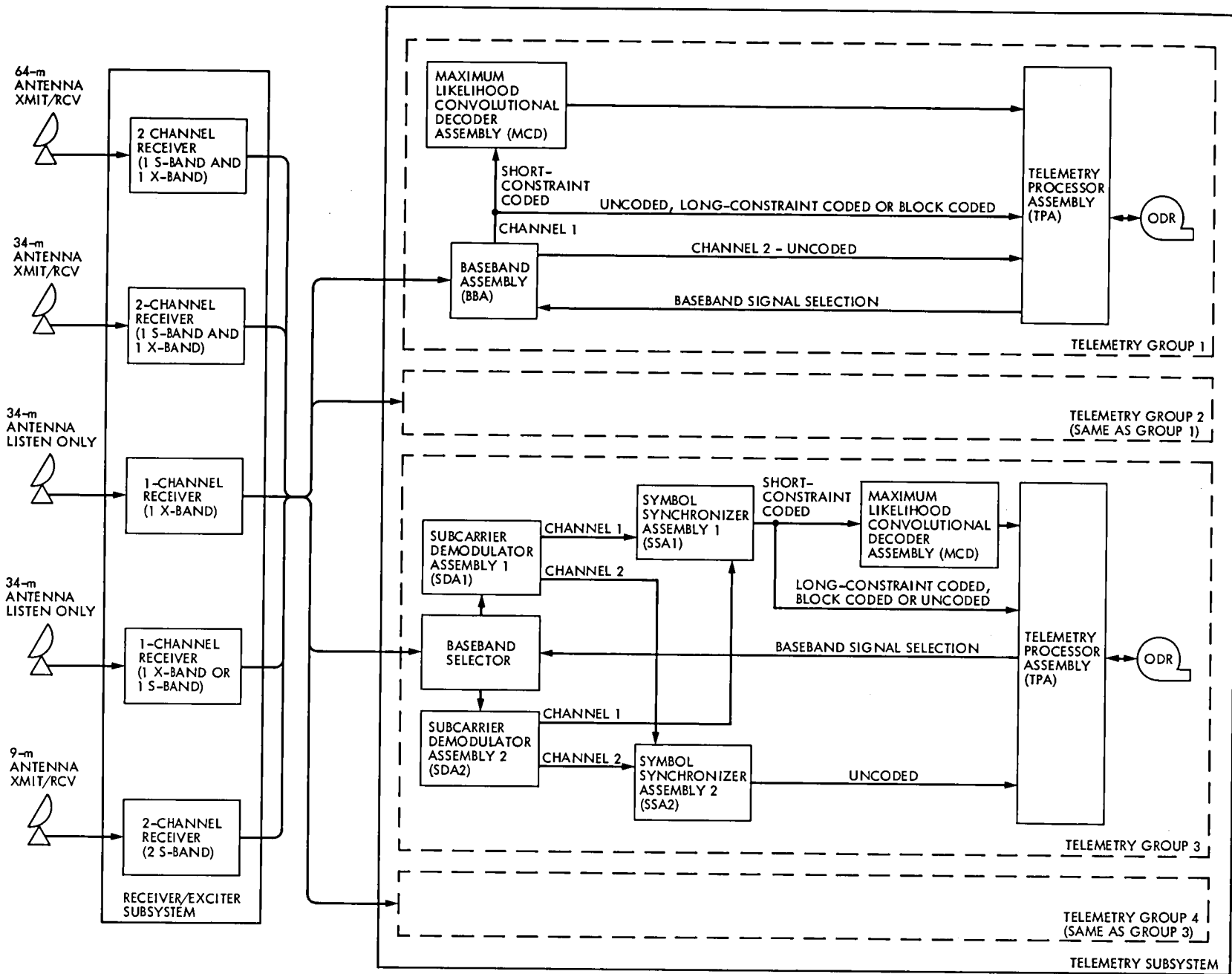


Fig. 1. Telemetry System: DSCC block diagram

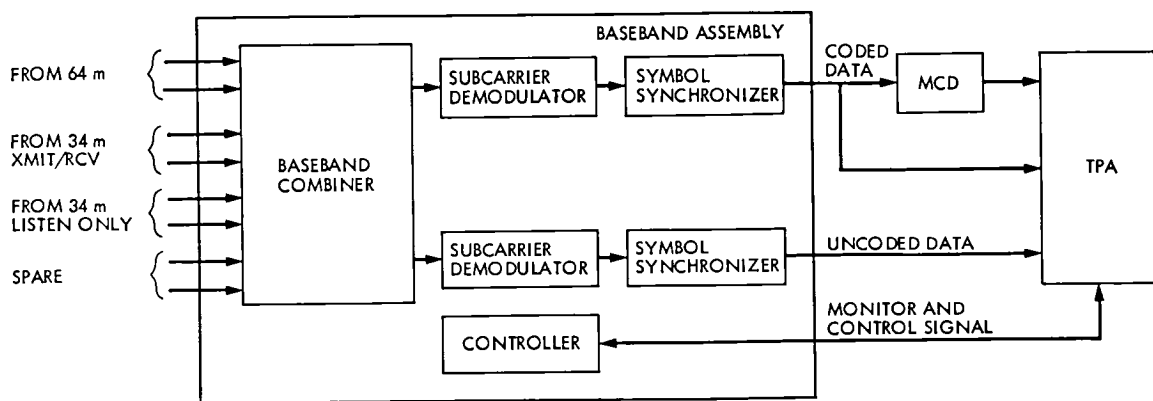


Fig. 2. Baseband Assembly functional block diagram

# Analysis of DSN PPM Support During Voyager 2 Saturn Encounter

C. D. Bartok  
Control Center Operations

*The Precision Power Monitor (PPM) is a precision radiometric instrument used to improve the efficiency of signal reception by the Deep Space Network. Real-time estimates of the system operating temperature, the present (signal + noise)-to-noise ratio, and the signal power are utilized to increase the accuracy and resolution of the received spacecraft signal.*

*Due to the critical nature of Radio Science data returning from Voyager 2 at Saturn Encounter, PPM support was required. The task was undertaken to validate the performance of equipment technically under research and development in time to meet the encounter deadline. Initial studies revealed PPM performance to be out of tolerance. Action was immediately taken to identify the system problems. Using data analysis as feedback, the system failures were identified and corrected in time to contribute to the encounter support efforts. As a result, the Radio Science data were collected successfully.*

## I. Background

The Precision Power Monitor, or PPM, functions as a precision radiometric instrument for the Receiver-Exciter Subsystem. The PPM is used to furnish real-time estimates of the system operating temperature ( $T_{op}$ ), the present (signal + noise)-to-noise ratio  $(S + N)/N$ , and the signal power  $S$  of the received spacecraft signal. The main components comprising the PPM are the S-band and X-band noise diode assemblies, the noise-adding radiometer (NAR), and the Precision Signal Power Monitor (PSPM).

The Deep Space Network (DSN) mode of operation is the primary application function of the PPM. The PPM uses the

intermediate frequency (IF) output from either the Block III or Block IV System Receivers as input (see Figs. 1 and 2). From this input the noise temperature is obtained by using NAR techniques. These are designed such that the noise added by the NAR does not degrade  $T_{op}$  by more than 0.1 dB.

From the same input the PSPM utilizes a fast Fourier transform (FFT) algorithm to measure the spectrum of the spacecraft signal. This spectrum is operated upon to form the (signal + noise)-to-noise ratio. Knowledge of this ratio and the noise temperature is used to calculate the noise power. From these data the signal power  $S$  is measured. The resultant PPM output provides continuously updated display and communication of  $T_{op}$ ,  $(S + N)/N$ , and  $S$  to the station.

## II. S-Band and X-Band Noise Diode Assemblies

The S-band and X-band noise diode oven assembly and power supply assembly provide a modulated stable noise signal at any one of seven preset levels. The noise is injected into the low-noise input coupler through the calibration assembly for the respective traveling wave maser (TWM), as shown in Figs. 1 and 3. The composite signal is extracted from the DSN receiver at IF and processed by the PPM to provide real-time system temperatures and signal level measurements.

The seven diode levels are calibrated against a precision ambient termination using a Y-factor method with the antenna looking at the cold sky in the zenith position and the maser input switching from the antenna to the ambient load (see Fig. 3). After calibration, the diode noise levels are used to provide reference values for NAR and PSPM processing.

## III. NAR Subassembly

The NAR function measures the S-band or X-band operating temperature  $T_{op}$  of a Deep Space Station (DSS). The temperature can be measured over a range of 10 to 400 K with a specified accuracy of 0.3 K and signal resolution of 0.1 dB<sub>m</sub>.

The fundamental equation describing the operation of the NAR is:

$$T_{op} = \frac{T_N}{(Y - 1)}$$

where

$T_{op}$  = system operating noise temperature, kelvin  
(defined at system input reference plane)

$T_N$  = noise diode injected noise temperature, kelvin  
(defined at system input reference plane)

$Y$  = Y-factor =  $(V_2 + \alpha V_2^2)/(V_1 + \alpha V_1^2)$

$V_2$  = square law detector output voltage, diode on,  
volts

$V_1$  = square law detector output voltage, diode off,  
volts

$\alpha$  = detector nonlinearity constant, volts<sup>-1</sup> (= 0 in an  
ideal detector)

The NAR noise temperature measurement resolution is given by:

$$\Delta T = 2T_{op} (1 + T_{op}/T_N) (B\tau)^{1/2}$$

where

$B$  = predetection bandwidth, hertz

$\tau$  = integration time, seconds

The PPM software provides for automatic operation of the NAR. The NAR channel receives the "counts" from the voltage-to-frequency converter that are proportional to the product of the system operating temperature and the system gain (see Fig. 3). An assumption of  $T_{op} = 40$  K is initially made which caused the NAR to select the  $T_N = 0.50$  K noise diode and to integrate for 56 seconds. Once the measured value is available, the NAR makes a decision on which of the seven preset noise diodes to use and how long to integrate (see Fig. 4). This reiteration allows the noise temperature measurement accuracy and resolution to be 0.1 dB and offers the data in the minimum possible time.

Concurrently, the NAR monitors the output to insure that it is within the expected temperature range. The output,  $T_{op}$ , becomes an operator display which updates automatically as frequently as the existing noise temperatures change.

## IV. PSPM Subassembly

The PSPM provides knowledge of received spacecraft signal power. By observing changes in power level from predicted performance, spacecraft anomalies can be diagnosed and examined. In addition, as each DSN station is brought into view of the spacecraft by the Earth's rotation, the measurement of received signal power serves to validate individual station performance by comparison of station-to-station readings.

The technique for power measurement consists first of measuring the power spectrum of the received signal in a bandwidth just wide enough to observe the background noise. A typical power spectrum is shown in Fig. 5. Suitable manipulation of the power spectrum utilizing a FFT algorithm yields the (signal + noise)-to-noise ratio:

$$R = (S + N)/N.$$

Since  $T_{op}$  is known, as is the NAR prediction bandwidth  $B$ , the noise power is calculated as

$$P_N = kT_{op}B$$

where  $k$  = Boltzman's constant. The signal power is then determined:

$$S = P_N(R - 1),$$

but substituting the expression for  $P_N$  yields

$$S = kT_{op} B(R - 1).$$

The PSPM function measures either the S-band or X-band carrier power over a system temperature operating range from 10 to 400 K, and a signal power range from  $-120 \text{ dB}_m$  to  $-165 \text{ dB}_m$ . The PSPM operates automatically by first assuming a signal power. After the first measurement of the signal, the known signal level is used to set the integration time for improved signal power measurement resolution  $\Delta S$  (see Fig. 6). The measurement procedure is reiterated for maximum resolution and accuracy. The outputs  $(S + N)/N$  and  $S$  are provided to the station as continuously updating displays.

## V. PPM Performance

During the Voyager 2 Saturn Encounter the PPM supported Radio Science data collection. The PPM was considered to be under research and development prior to this encounter. However, since the critical nature of the Radio Science data returning from Voyager 2 required PPM support, the task was undertaken to validate the performance of the PPM in time to meet the encounter deadline.

Although the three 64-meter-diameter antenna sites of the DSN were equipped with PPM hardware, only the NAR sub-assembly was utilized for support procedures. An intensive effort was launched to develop a method of analyzing the operating temperature of the antenna system. Each 64-meter station tracking Voyager 2 for 10- to 12-hour periods recorded

NAR temperature data points every five seconds throughout those periods. The resultant data files were plotted so that the operating temperature could be visualized as a function of time.

A tracking pass corresponds to the time span as the spacecraft comes into view near the horizon and continues as it crosses the local sky until it travels out of view near the horizon. Thus, the data plots inherently illustrate operating temperature as a function of elevation as well as a function of time. Comparing the curvature of the data plots with nominal system noise temperature versus elevation test plots further confirms this relationship (see Figs. 7, 8 and 9). These test plots indicate acceptable PPM system temperatures under ideal test conditions for each 64-meter station operating at X-band frequencies. Nominal system temperatures at S-band operation average about three degrees less.

The actual data plots (Figs. 10-12) showed interesting results. The initial data plots for each of the stations revealed PPM performance out of tolerance. Encounter support was not possible with the evident PPM problems. Action was immediately taken to locate the source of the system problems. Using the data plots as feedback, the system failures were identified, located and corrected one by one. Analysis continued up until encounter to monitor the condition of the PPM performance. As the plots depict, the PPM was brought up to acceptable standards and validated in time to contribute to encounter support. PPM plots at all three 64-meter DSS sites showed system noise temperature within performance specifications and relatively unperturbed during encounter. Radio Science data collection was successful.

## Acknowledgment

A special thanks is due Dorin M. Lascu for developing software enabling the manipulation and reduction of vast quantities of data into manageable files.

## Bibliography

Winkelstein, R., "Precision Signal Power Measurement," *JPL Quarterly Technical Review*, Volume 2, Number 2, July 1972, pp. 18-24.

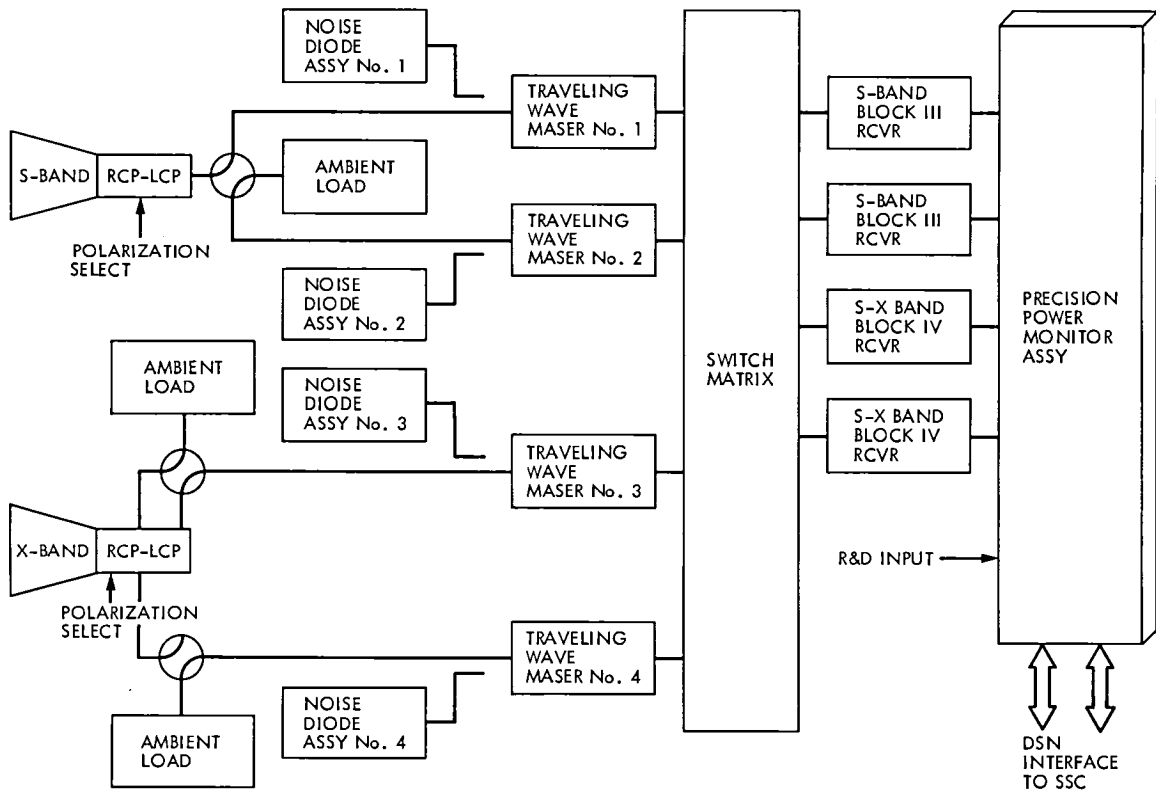


Fig. 1. System block diagram

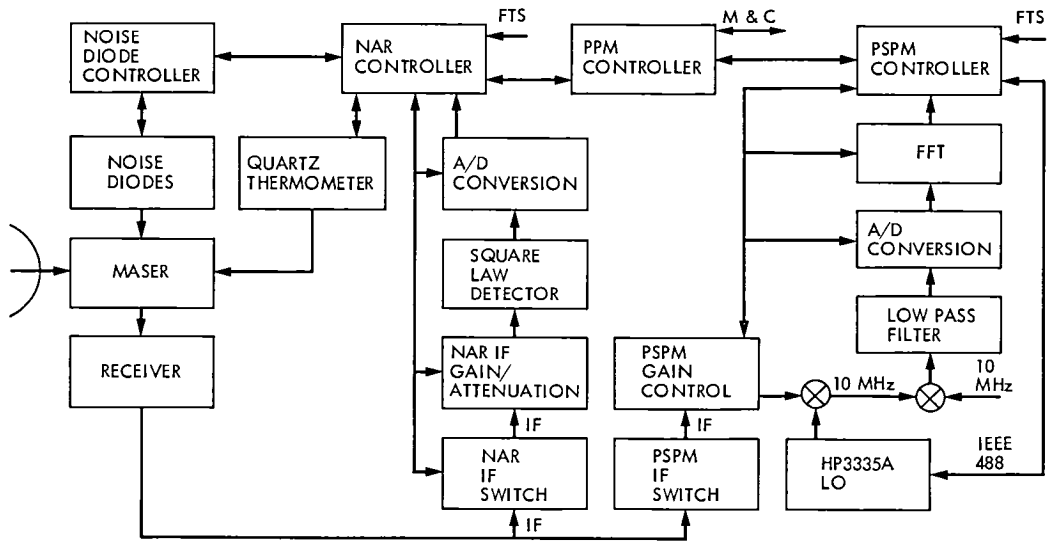


Fig. 2. PPM functional block diagram

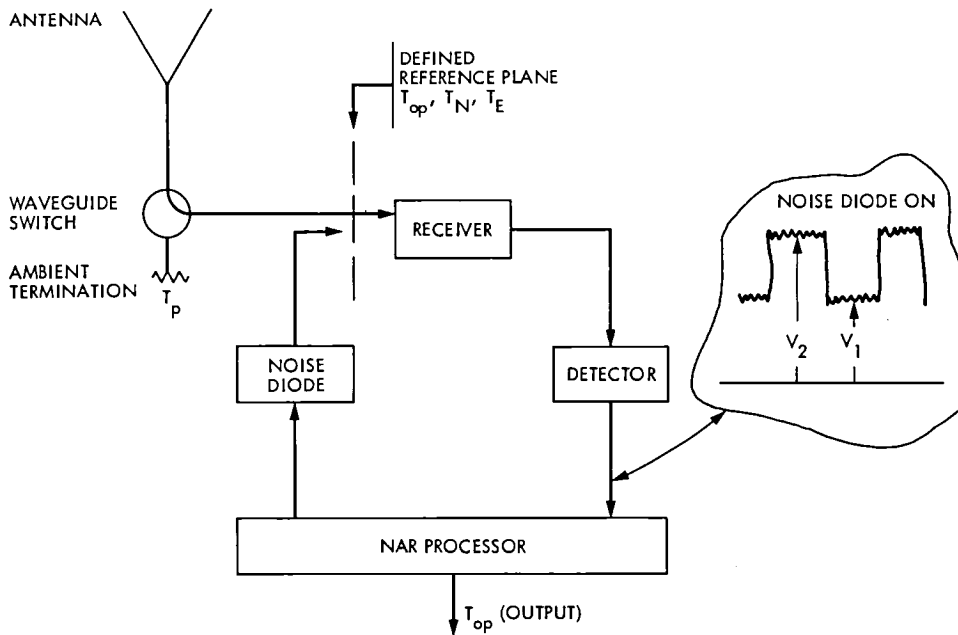


Fig. 3. Microwave receiving system showing NAR configuration

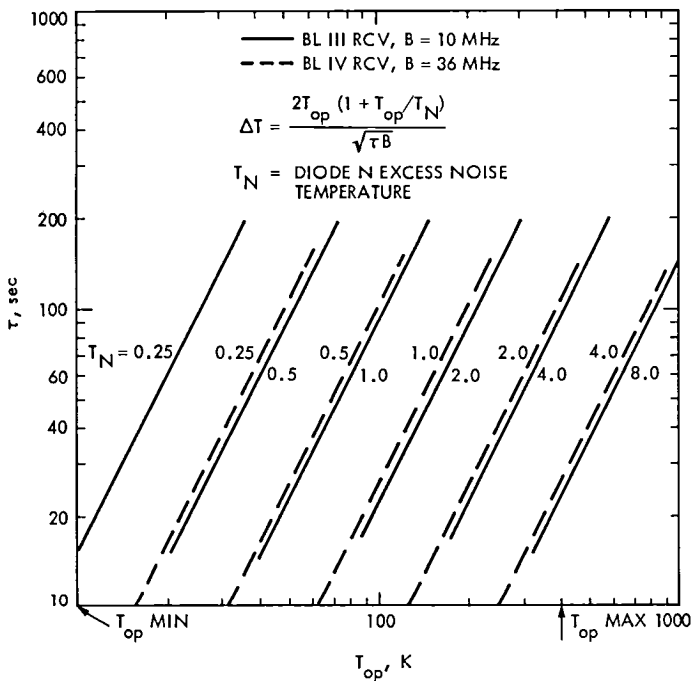


Fig. 4. Integration time  $\tau$  required for 2% accuracy versus  $T_{op}$  as a function of IF bandwidth

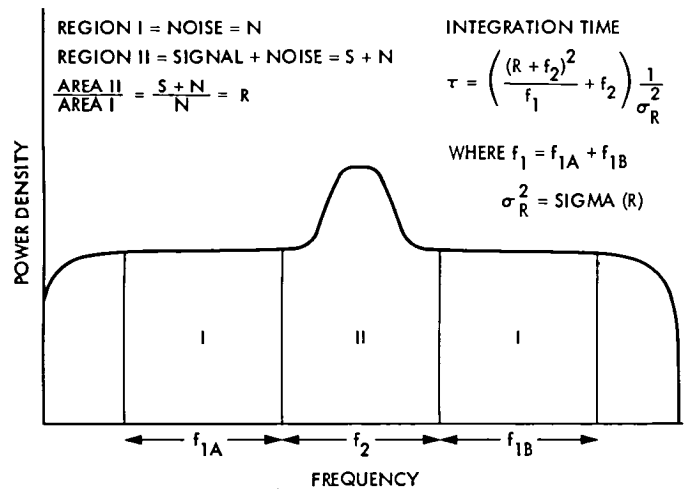


Fig. 5. Precision signal power measurement

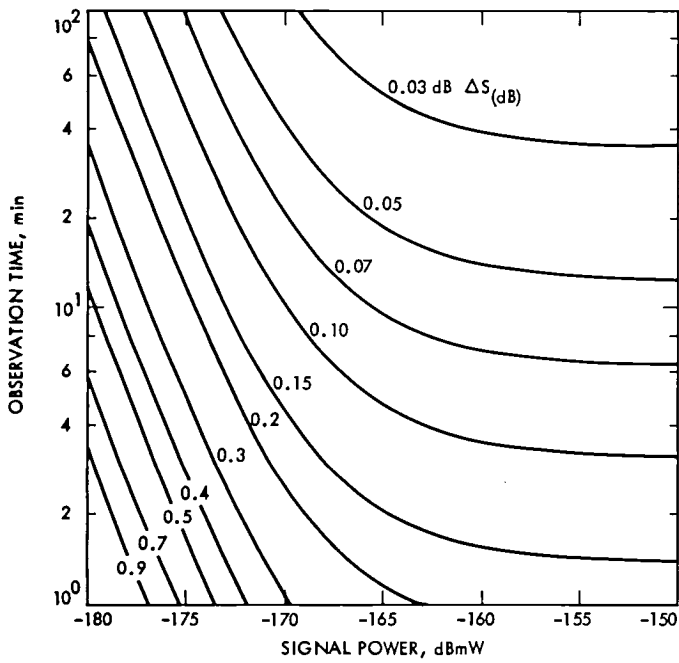


Fig. 6. PSPM required observation time

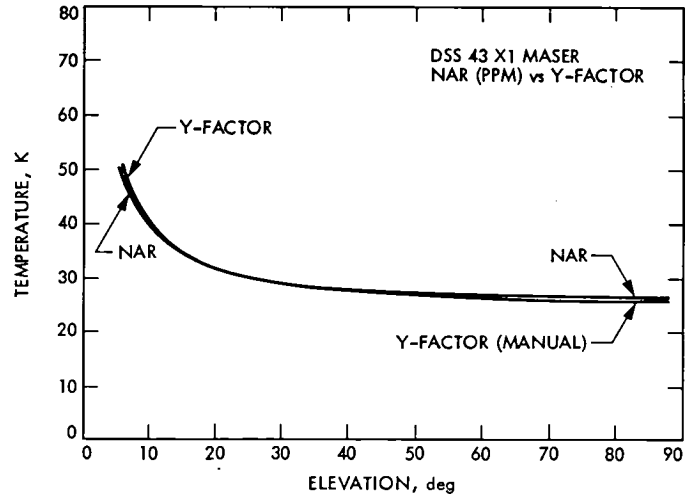


Fig. 8. System temperature versus antenna elevation, X-band, DSS 43

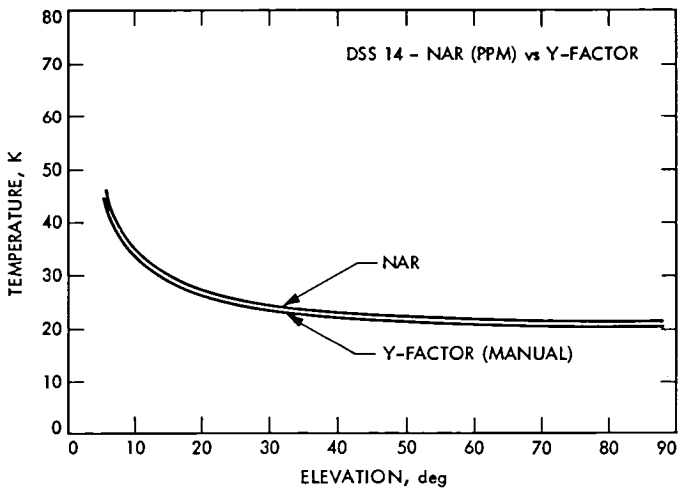


Fig. 7. System temperature versus antenna elevation, X-band, DSS 14

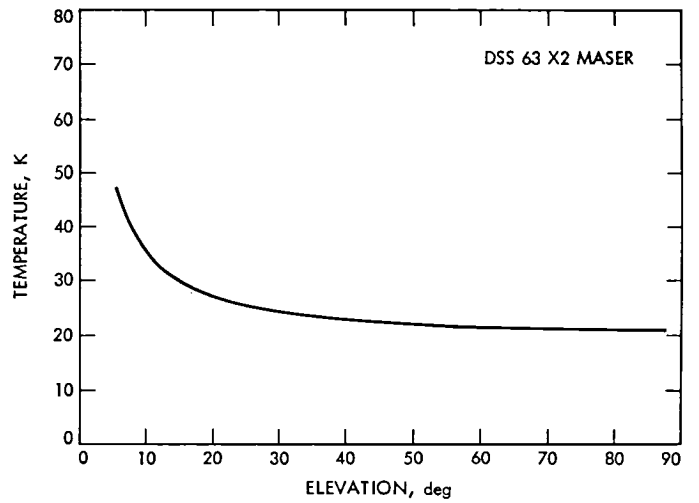


Fig. 9. System temperature versus antenna elevation, X-band, DSS 63

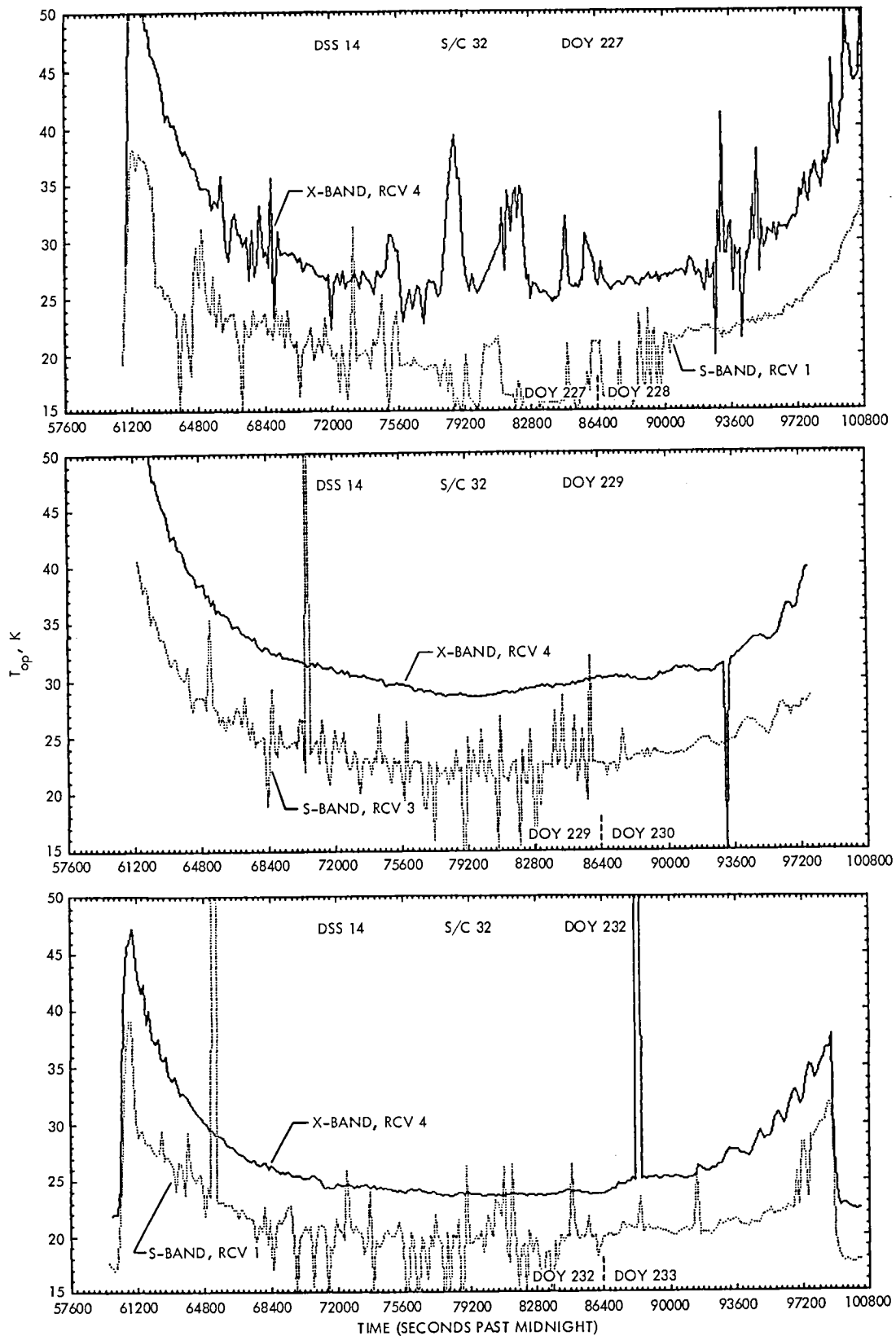


Fig. 10. System noise temperature plot—Goldstone, California

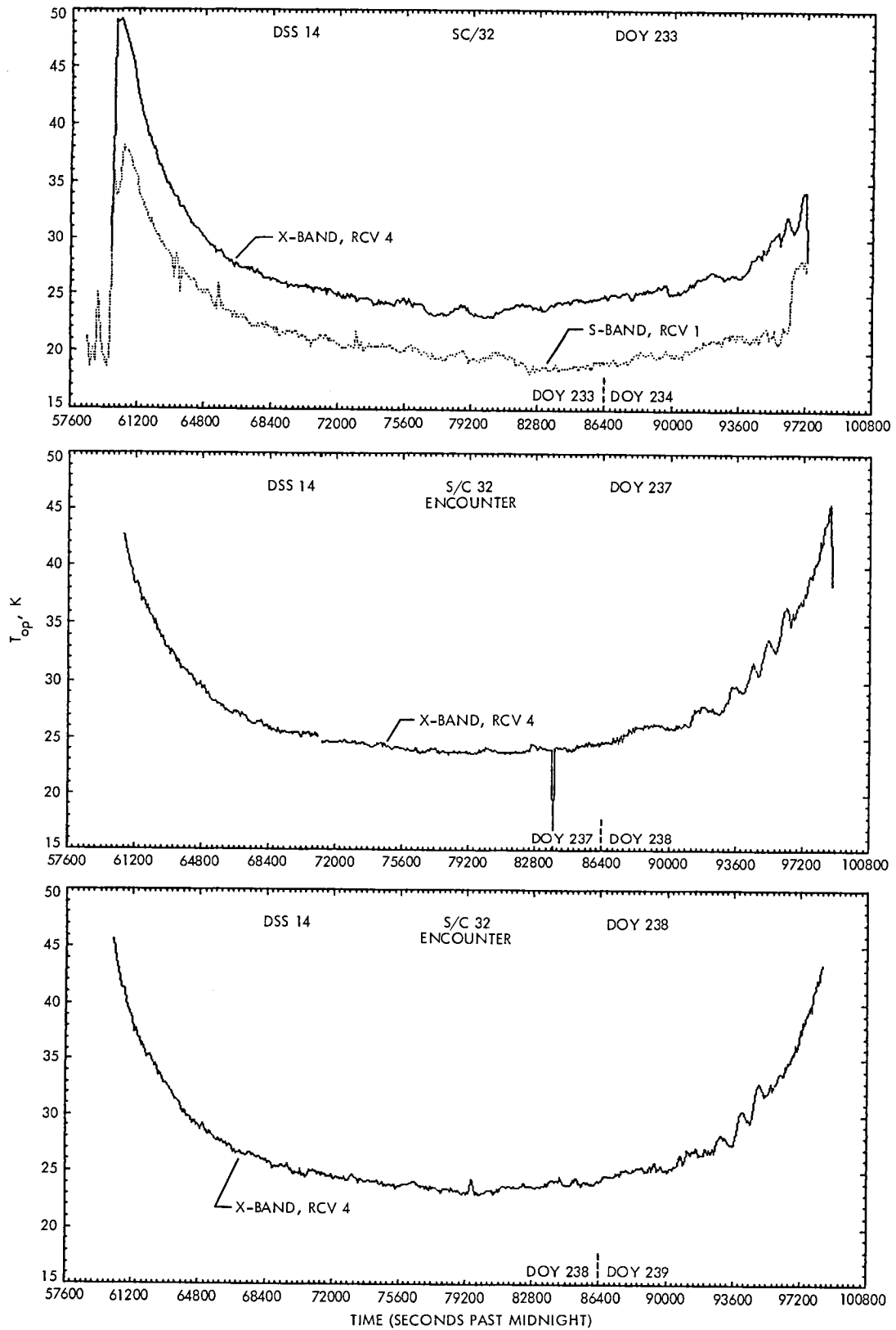


Fig. 10 (contd)

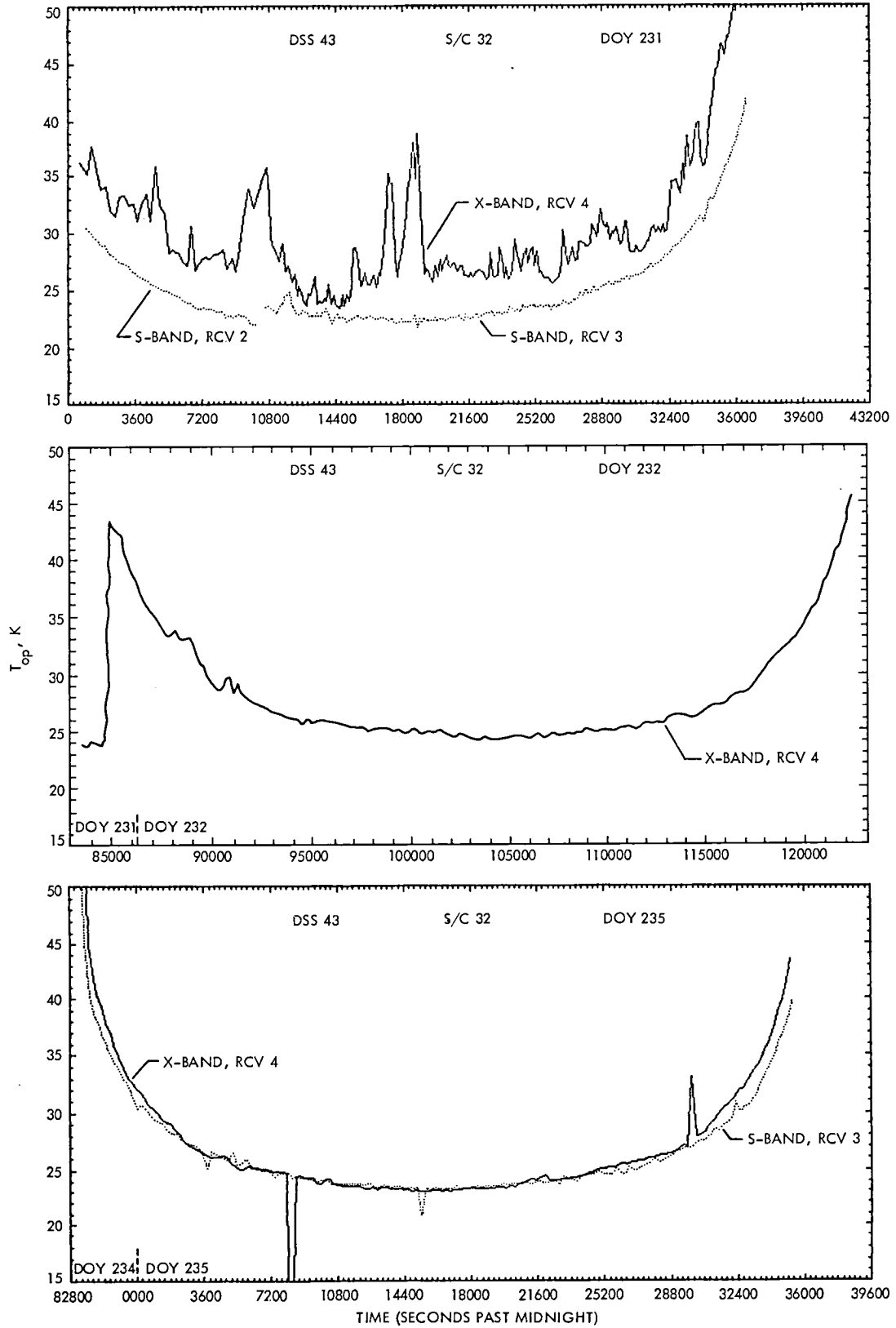


Fig. 11. System noise temperature plot—Australia

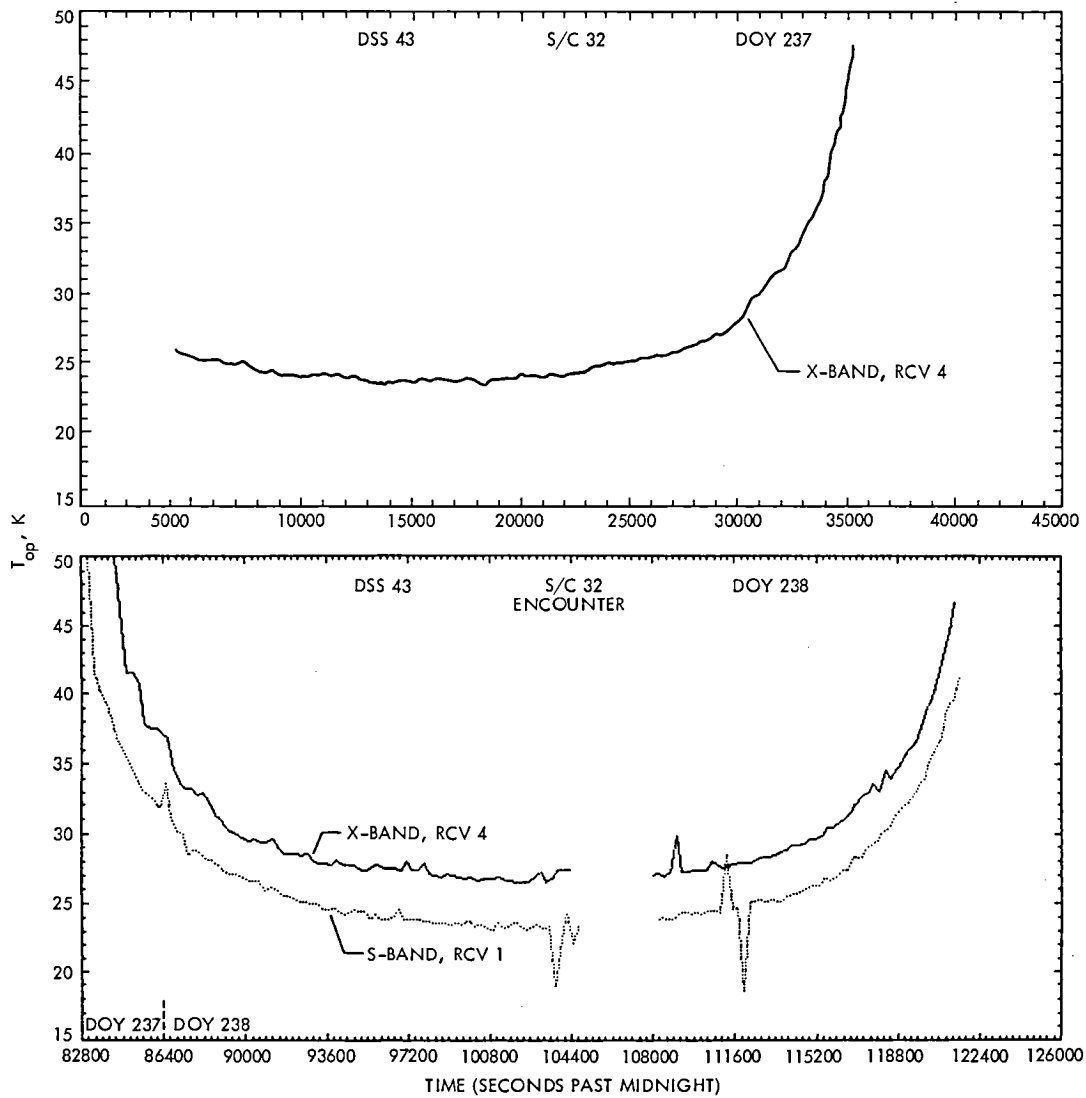


Fig. 11 (contd)

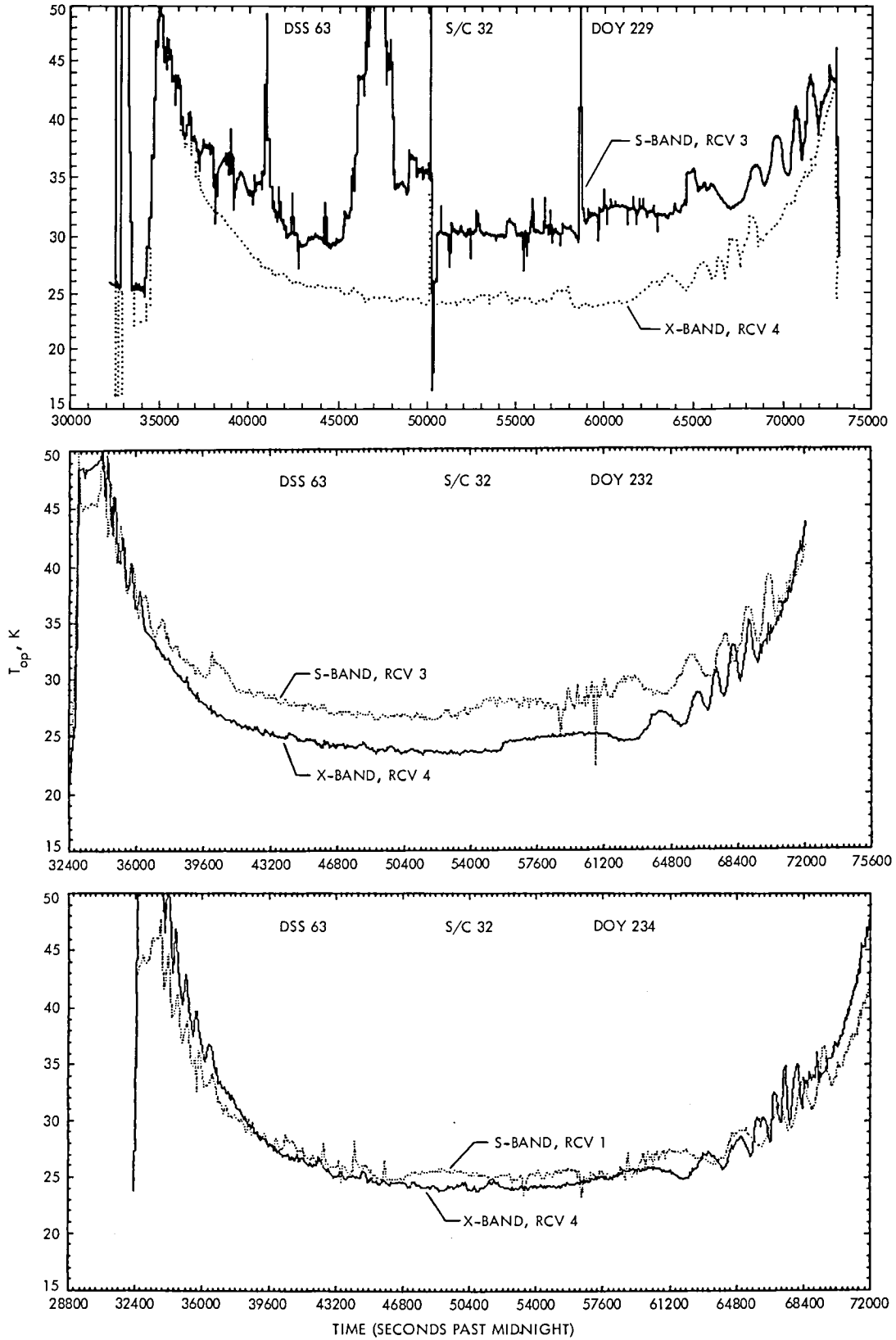


Fig. 12. System noise temperature plot—Spain

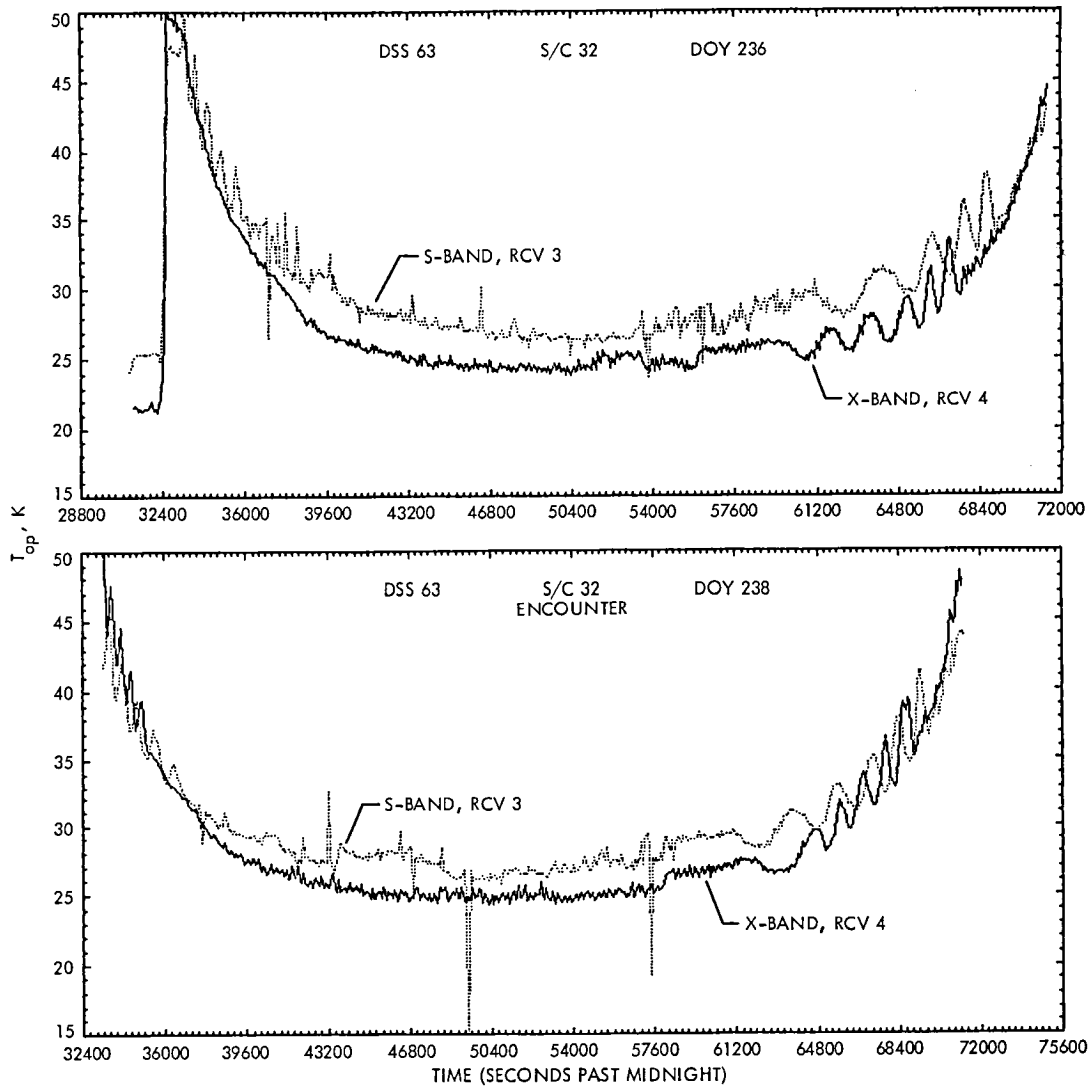


Fig. 12 (contd)

## Potential Reduction of DSN Uplink Energy Cost

S. Dolinsky and N. F. de Groot  
Telecommunications Systems Section

*DSN earth stations typically transmit more power than that required to meet minimum specifications for uplink performance. This article presents the results of a study of energy and cost savings that could result from matching the uplink power to the amount required for specified performance. The Galileo mission was selected as a case study.*

*Although substantial reduction in transmitted energy is possible, potential savings in source energy (oil or electricity) savings are much less. This is because of the rising inefficiency in power conversion and radio frequency power generation that accompanies reduced power output.*

*The work described in this report is part of a continuing study intended to guide future development and management of the DSN in the changing environment of space exploration.*

### I. Introduction

DSN earth stations typically transmit more power than that required to meet minimum specifications for uplink performance. The reason for this is the operational simplicity of selecting from one or two power settings, each of which can be used for a lengthy period of time. Excessive power also provides an additional margin of safety in performing the required uplink functions. If the uplink transmitter power was always adjusted to the minimum needed, a saving in electric energy would be expected. This report is the result of a study to assess the potential saving. Motivation for the study was the rapidly escalating energy cost at DSN stations.

To determine the potential cost savings that could result from more careful management of uplink power, the required power over the life of a mission was compared with the power that would be expected to result from station operation that is typical of past practice. The Galileo mission was selected as a case study.

Electric power for the earth station transmitter comes from either a commercial source or from diesel generator sets. The potential saving in transmitted power was converted to savings in electricity billings or fuel costs by considering the efficiencies of intervening equipment: transmitter power amplifier, motor/generator, and for the fuel oil case, the diesel generator.

## II. Required Uplink Power

### A. Uplink Modes

Four functions are performed via the uplink:

- (1) Transmission of spacecraft commands.
- (2) The uplink portion of turnaround ranging.
- (3) The uplink portion of two-way doppler tracking.
- (4) The provision of a carrier reference for downlink telemetry.

These functions may be required singly or in combination.

### B. Required Uplink Power

For each mode or mode combination there is a required input power at the spacecraft receiver. A selected set of modes and their corresponding power requirements are shown in Table 1 (Ref. 1). These modes were selected for analysis because they are representative of the range of required power and because they are expected to be extensively utilized. To relate the receiver input power to the corresponding earth station transmitter power, it is necessary to consider the antenna gains, space loss, and various atmospheric losses and noise temperature effects. The parameter with the largest variation during a mission is the space loss, which is proportional to the distance squared.

To determine the variation of required transmitter power during the Galileo mission and as a function of mode and antenna size, it was found convenient to first compute the power for a single mode and antenna. The -120-dBm and 34-m case was selected and the result is shown in Fig. 1. Power profiles for other levels of received power are related to this curve by an appropriate multiplication factor. Data for the curve were computed by means of telecommunications design control tables and graphs (see Appendix).

By considering the difference between the -120-dBm value and the other required powers shown in Table 1, it is then simple to create the family of curves shown in Fig. 2. Taking into account the higher gain of the 64-m antenna, Fig. 3 was prepared. Note that Fig. 1 is in terms of kilowatts, while Figs. 2 and 3 are in terms of dBW. The logarithmic scale of Figs. 2 and 3 is needed to show meaningful relationships between mode power requirements; the lower power curves would be lost on the kilowatt scale of Fig. 1.

### C. Typical DSN Operation

Based on past experience it may be assumed that earth station transmitter power to support Galileo would be ad-

justed to 10 kW for the first 300 days and then 18 kW until the end of mission. This typical operation is shown in Figs. 1, 2 and 3.

### D. Comparison of Typical and Required Energy

The area under each curve in Figs. 1, 2 and 3 is representative of the number of kilowatt days needed for that mode or mode combination. The energy for the assumed typical DSN operation is

$$10 \times 300 + 18 (1480 - 300) = 24,240 \text{ kW days}$$

The energy to provide -120 dBm at Galileo from a 34-m station was obtained by "counting the squares" under the curve in Fig. 1 and is 14,900 kW days. Energy required for the other modes was obtained by adjusting the value for the -120-dBm, 34-m case by an amount taken from Table 1. For example, the command mode requires 1/7.9 (9 dB) less power, or 3050 kW days. The ratio of required power to typical (assumed) power is presented in Table 2. Remember that the energy and energy ratios determined so far are for the transmitter radio frequency output, not the electric or fuel oil energy that must be purchased. To estimate the dollar value of net energy savings, the efficiency of generating the transmitted power must be considered. In addition, there is a minimum practical RF power from DSN transmitters, and this factor must be included when determining potential savings.

## III. Transmitter and Power Source Efficiencies

In the previous section it was shown that uplink RF power can usually be reduced from typical values while still meeting required link performance. It is, however, the reduction of source power and hence energy cost that is the subject of this study. How much power is saved at the source when the RF power is reduced? In this section we consider the efficiency of the typical end-to-end power system which drives the 20 kW RF klystron transmitter. Figure 4 shows the power system, Ref. 2. Diesel generators and/or commercial power provide a 60-Hz source which drives a motor/generator (M/G). The 400-Hz voltage generated by the M/G is converted into dc, which in turn drives the klystron. During uplink transmissions, basic support equipment for the klystron must remain on at all times. This equipment includes a heat exchanger (18 kW dc); cathode, control and monitoring instrumentation and safety devices (2 kW); and the magnet (6 kW). In all, this amounts to 26 kW dc, which cannot be reduced, regardless of the output RF power of the klystron amplifier.

The end-to-end efficiency of the system depends on three efficiency factors.

### A. Klystron Amplifier Efficiency

The klystron is operated in saturation at all times so as to prevent amplitude instabilities. Below 2 kW it is not possible to saturate the tube and so the klystron is not operated below this level. For the saturated condition, the beam power efficiency as a function of beam voltage is shown in Fig. 5. For 20-kW RF, the beam power efficiency is typically 43%. The klystron efficiency as a function of RF output is shown in Fig. 6.

The relationship between RF power and the beam voltage is

$$P_{RF} = \eta KV^{5/2}$$

where  $K = 0.825 \times 10^{-6}$ ,  $V$  is the beam voltage in volts and  $\eta$  is the beam power efficiency.

The total klystron amplifier efficiency is

$$\frac{P_{RF}}{\frac{P_{RF}}{\eta} + 26 \text{ kW}}$$

These relationships determine the data shown in Table 3 and Fig. 6.

### B. Motor/Generator Efficiency

Motor/generators like those at DSN sites work at a combined efficiency of 86% when the motor and generator each operate at a typical 93% efficiency. Using Refs. 3 and 4, a typical efficiency curve has been constructed and is shown in Fig. 7.

### C. Efficiency of Converting 60 Hz Power to RF Output

The end-to-end efficiency from a 60-Hz source to RF output is shown in Table 4 and in Fig. 8.

### D. Diesel Generator Efficiency

Either commercial power or on-site diesel generators may act as the 60-Hz source for the motor generator sets. There are 500-kW and 750-kW diesel generators at the DSN sites. Fuel consumption for these is nearly linear with electric power output and is approximately 1.9 gallons per kW-day for a 500-kW generator, 1.8 gallons per kW-day for a 750 kW generator. In this article, 1.9 gallons per kW-day will be used for calculation of cost savings.

## IV. Estimated Energy and Cost Saving

In the example discussed earlier, the DSN was assumed to operate at 10 kW RF (12.1% total M/G plus klystron efficiency) to day 300 of the Galileo mission and then at 18 kW RF (19.2% total efficiency) for the remainder of the mission. The energy required for this case is

$$300 \text{ days} \times \frac{10}{0.121} = 24,800 \text{ kW days}$$

$$(1480-300) \text{ days} \times \frac{18}{0.192} = 110,600 \text{ kW days}$$

Total energy for typical operation = 135,400 kW days.

If the transmitter were to operate at the 2-kW minimum level for the mission duration, the total power would be  $2 \times 1480 \div 0.029 = 102,100$  kW days.

Galileo will not operate continuously in any one mode for the entire mission. The potential for energy savings depends on the mix of modes. To estimate an aggregate energy saving, it is necessary to assume a mix. For example, a mission profile at a 64-m station might include:

Mode	Days	% of mission days
Doppler	800	54
Command	380	26
Carrier reference	300	20

By referring to Fig. 2 or 3, depending on the antenna to be used, an average power for the majority of the mission may be estimated for each mode. The source energy required for each mode to be used during the mission according to the assumed profile is then

$$E_{mode} = \text{days of mode operation} \times \text{average power} \div \text{efficiency}$$

The minimum allowable value for the average power is 2 kW.

The accuracy of this calculation depends upon the assumption that use of each of the several modes is more or less uniformly distributed over the life of the mission, and upon the estimate of the average power. Net savings are not very sensitive to these assumptions because of the linear relationship between efficiency and RF power output. A more elegant calculation is therefore not warranted. Table 5 shows the results of calculations for the assumed mix of modes, expressed

in terms of gallons of fuel oil and kW-days of commercial power. Also shown are dollar savings at estimated 1985 rates.

## V. Discussion

The study of potential savings in uplink energy cost was motivated by the observation that required performance margins are substantially exceeded in many instances. As shown in Table 2, less RF power could be used while meeting Galileo performance requirements. Depending upon the uplink mode, power reduction of 40 to 99% could be enjoyed, compared to typical past practice.

In reality, the potential for dollar and energy savings is much less. This is because of the efficiency with which 60-Hz source power is converted to RF output power. The overall efficiency is roughly proportional to output power: along with reduced power we have reduced efficiency. This is the result of decreasing klystron and motor-generator efficiencies that accompany decreases in output power. An additional factor is the fixed power overhead required to operate the amplifier regardless of RF output.

The nature of the klystron amplifier is such that there is a minimum output power below which saturation cannot be obtained. Saturated operation is needed for typical DSN applications, and is obtainable only above 2 kW. Even when the link doesn't need it, 2 kW must be generated, at the expense of 26 kW of support power.

Table 6 compares the percentage savings in RF and source energy for the selected mix of Galileo mission modes studied in this report. The difference between the energy required for assumed typical DSN profile (10 kW for 300 days and 18 kW for the remainder of the mission) and that needed for the 2-kW minimum for the same length of time is 135,400 -

102,100 = 33,300 kW-days. The potential savings over mission life cannot greatly exceed this value.<sup>1</sup> Accordingly, since the spread between typical and minimum energy is relatively small, the potential for savings is not critically dependent upon the mix of modes that could or would be used during the Galileo mission. For the mix chosen in the Galileo study, the savings is 29,200 kW-days at a 34-m station and 32,700 kW-days at a 64-m station.

The analysis presented above presumes a single mission, Galileo, being supported continuously by means of stations at the U.S. and overseas DSN sites. Additional savings could accrue if other missions were supported by these stations during periods when Galileo was not in view.

The estimate of potential savings is based on the normal operating characteristics of existing DSN stations. These characteristics include maximum and minimum values of transmitter power. It has been shown that uplink functions can often be accomplished with less than the minimum power available from existing DSN transmitters. The saving that could result from the use of new, low-power transmitters, or from use of existing exciters without further amplification, is not treated in this report.

The maximum required power is usually determined by the need for spacecraft command under emergency condition. While normal operations may suggest the use of lower power transmitters, the emergency capability must be maintained. More economical means of providing this capability were not examined and are beyond the scope of this report.

---

<sup>1</sup>Because the efficiency values used in the study are approximate, computed energy consumption for some mode mixes may be less than that estimated for the 2-kW case.

## Acknowledgments

Thanks are due Jim Taylor and John Rider for their suggestions regarding this study.

## References

1. Taylor, F. H. J., Section 339, private communication.
2. Rayburn, J., Section 333, private communication.
3. "Standard Handbook for Electrical Engineers," editor A. E. Knowlton, 7th Edition, McGraw-Hill.
4. "Standard Handbook for Electrical Engineers," editors D. G. Fink and H. W. Beaty, McGraw-Hill, 1978.
5. Data from Utility Cost Analysis (FY 81-85), DSN Goldstone Complex, supplied by S. Friesema, Section 420.

**Table 1. Power required at spacecraft receiver input**

Uplink mode	Required power, dBm
Carrier tracking for doppler <sup>a</sup>	-142
Command	-129
Command plus ranging	-128
Carrier reference for telemetry <sup>b</sup>	-120

<sup>a</sup>S up, S down.<sup>b</sup>S up, X down.**Table 2. Ratio of required transmitter power (kW days) to typical DSN practice (24,240 kW days)**

Mode	Ratio	
	34-m Antenna	64-m Antenna
Carrier tracking for doppler	0.004	0.001
Command	0.077	0.022
Command plus ranging	0.097	0.028
Carrier reference for telemetry	0.615	0.178

**Table 3. Klystron RF power out vs efficiency (RF power/total power)**

RF power, kW	Total power consumed by klystron amplifier, kW	Efficiency (RF power/total power), %
2	33.6	6.0
4	38.6	10.4
6	43.4	13.8
8	47.6	16.8
10	51.5	19.4
12	55.8	21.5
14	60.1	23.3
16	64.4	24.9
18	68.7	26.2
20	72.6	27.6

**Table 4. End-to-end efficiency from 60-Hz power source to RF output**

RF power, kW	Klystron efficiency, %	Motor generator efficiency, %	Total efficiency, %
2	5.9	25	2.9
4	10.3	35	5.6
6	13.8	44	7.9
8	16.8	49	10.2
10	19.4	52	12.1
12	21.4	58	14.4
14	23.2	61	16.1
16	24.8	64	17.7
18	26.2	67	19.2
20	27.6	71	21.0

Note: Of the fixed 26 kW needed to support the klystron amplifier, 18 kW comes directly from the 60-Hz source and not through the motor/generator. The total efficiency is therefore not a simple product of the klystron and motor generator efficiency values given in the table.

**Table 5. Potential source energy savings at 34-m and 64-m stations for selected profile of three Galileo mission modes**

Antenna station	Electricity or fuel required	Electricity or fuel expended for 10-kW/18-kW profile	Saving	Cost <sup>a</sup> saving, \$
34m station:				
Diesel generator	201,700 gal	257,300 gal	55,600 gal	94,300
Commercial power	106,200 kW-days	135,400 kW-days	29,200 kW-days	95,700
64m station:				
Diesel generator	195,000 gal	257,300 gal	62,300 gal	105,700
Commercial power	102,700 kW-days	135,400 kW-days	32,470 kW-days	107,500

<sup>a</sup>Estimated 1985 costs: \$1.696/gal; \$0.137/kWh. (Ref. 5)

**Table 6. Comparison of RF and source energy savings**

Antenna station	Potential RF saving, %	Estimated source energy saving, %
34 m	78	22
64 m	87	24

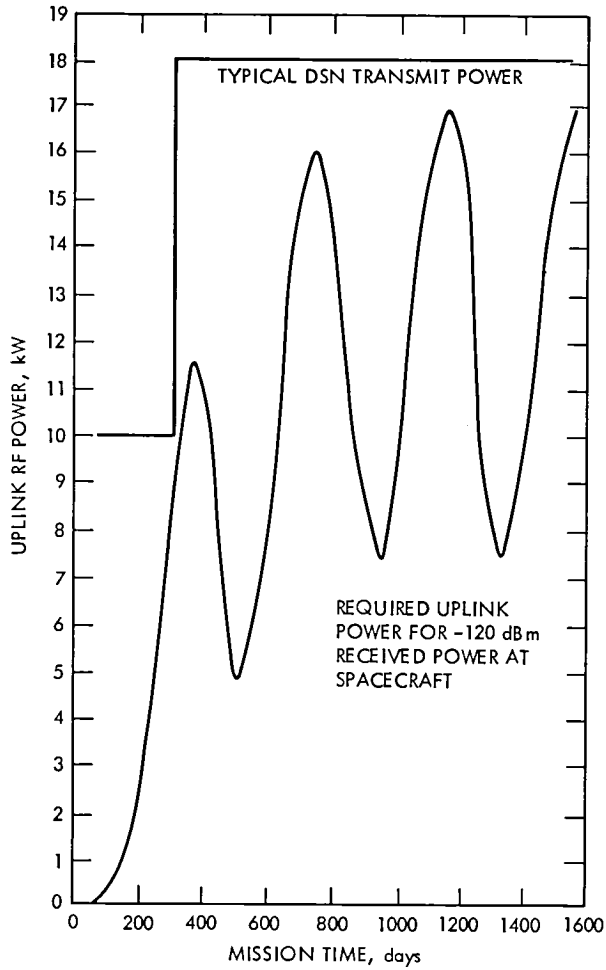
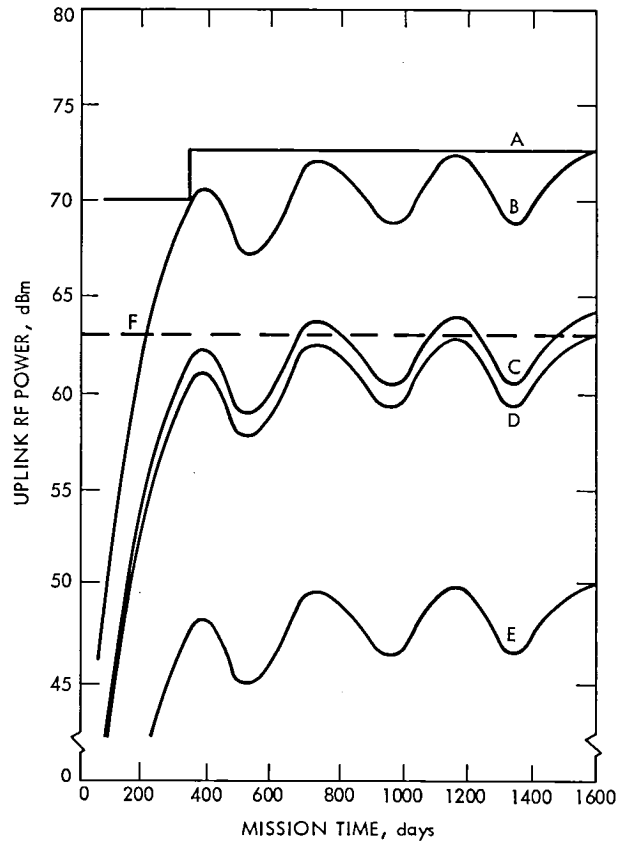
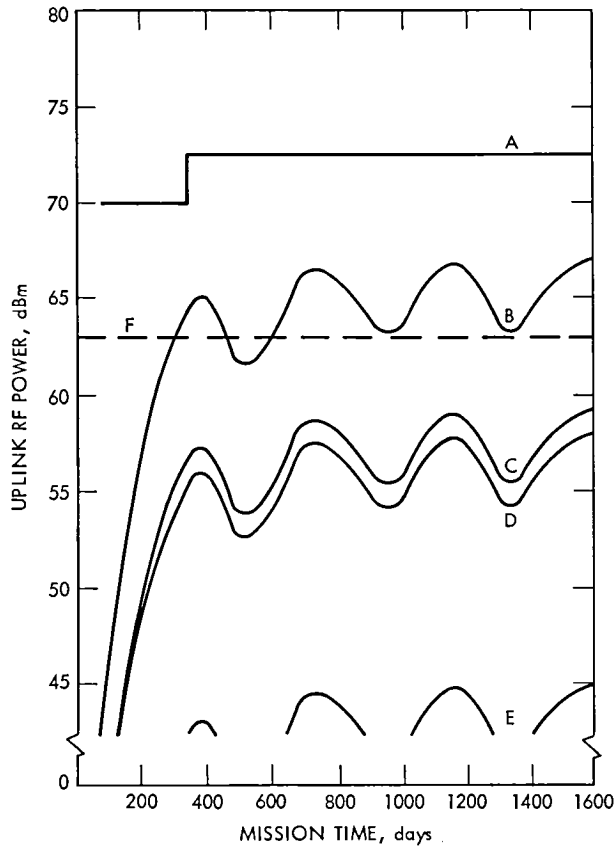


Fig. 1. Typical and required uplink power vs time for Galileo, 34-m antenna



- A. TYPICAL DSN OPERATION
- B. CARRIER REFERENCE
- C. COMMAND PLUS RANGING
- D. COMMAND
- E. DOPPLER
- F. 2 kW MINIMUM DSN POWER LEVEL

Fig. 2. 34-m uplink power vs time for typical DSN operation and for selected Galileo mode requirements



- A. TYPICAL DSN OPERATION
- B. CARRIER REFERENCE
- C. COMMAND PLUS RANGING
- D. COMMAND
- E. DOPPLER
- F. 2 kW MINIMUM DSN POWER LEVEL

Fig. 3. 64-m uplink power vs time for typical DSN operation and for selected Galileo mode requirements

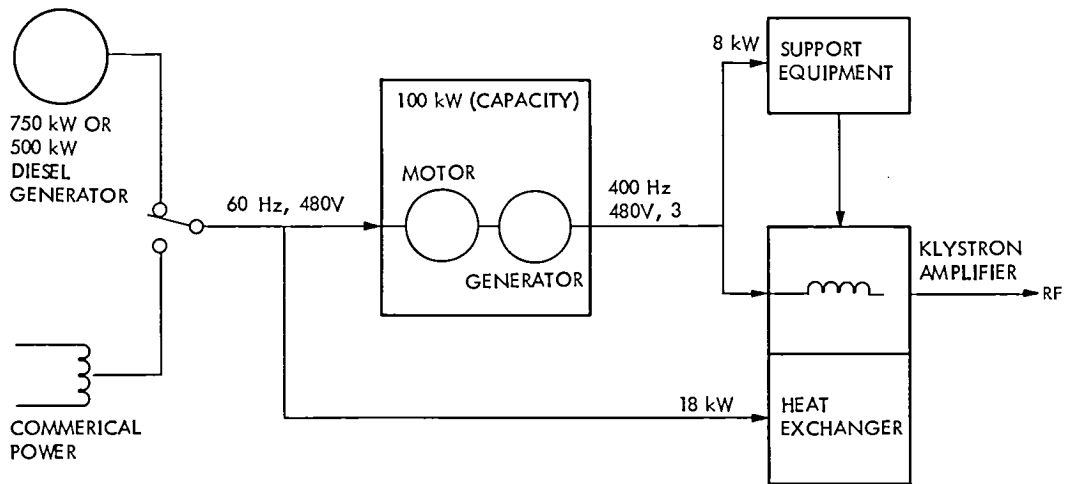


Fig. 4. End-to-end power flow diagram for Goldstone DSS 14/12

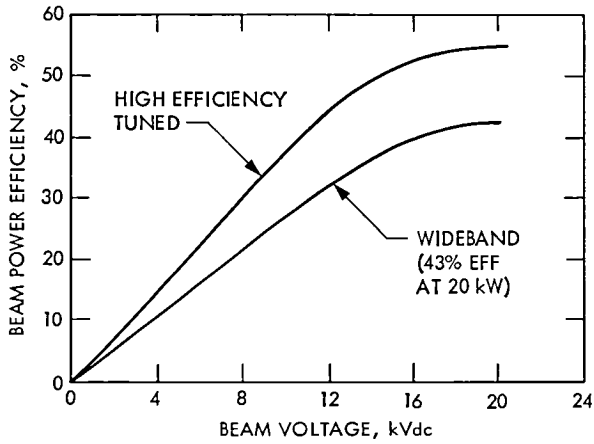


Fig. 5. Typical klystron beam power efficiency vs beam voltage

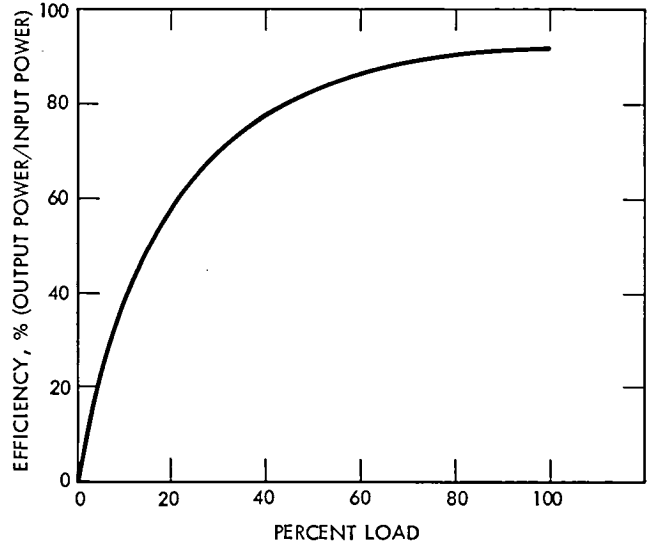


Fig. 7. Typical efficiency for 100-kW motor or generator

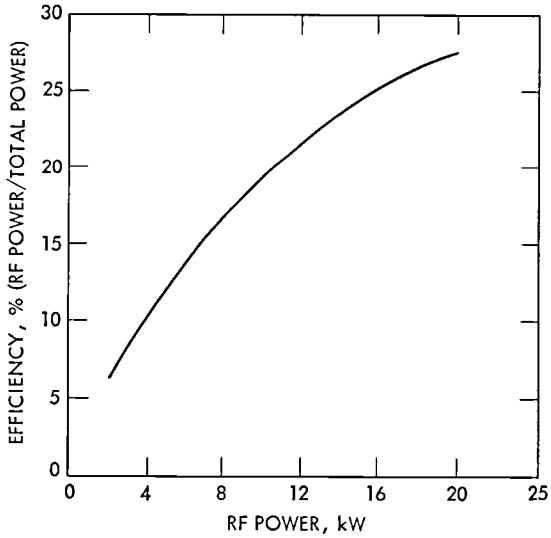


Fig. 6. Typical klystron efficiency vs RF power output

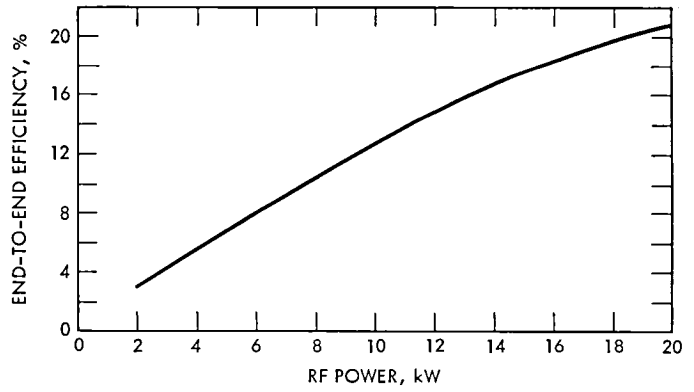


Fig. 8. End-to-end efficiency vs RF power output

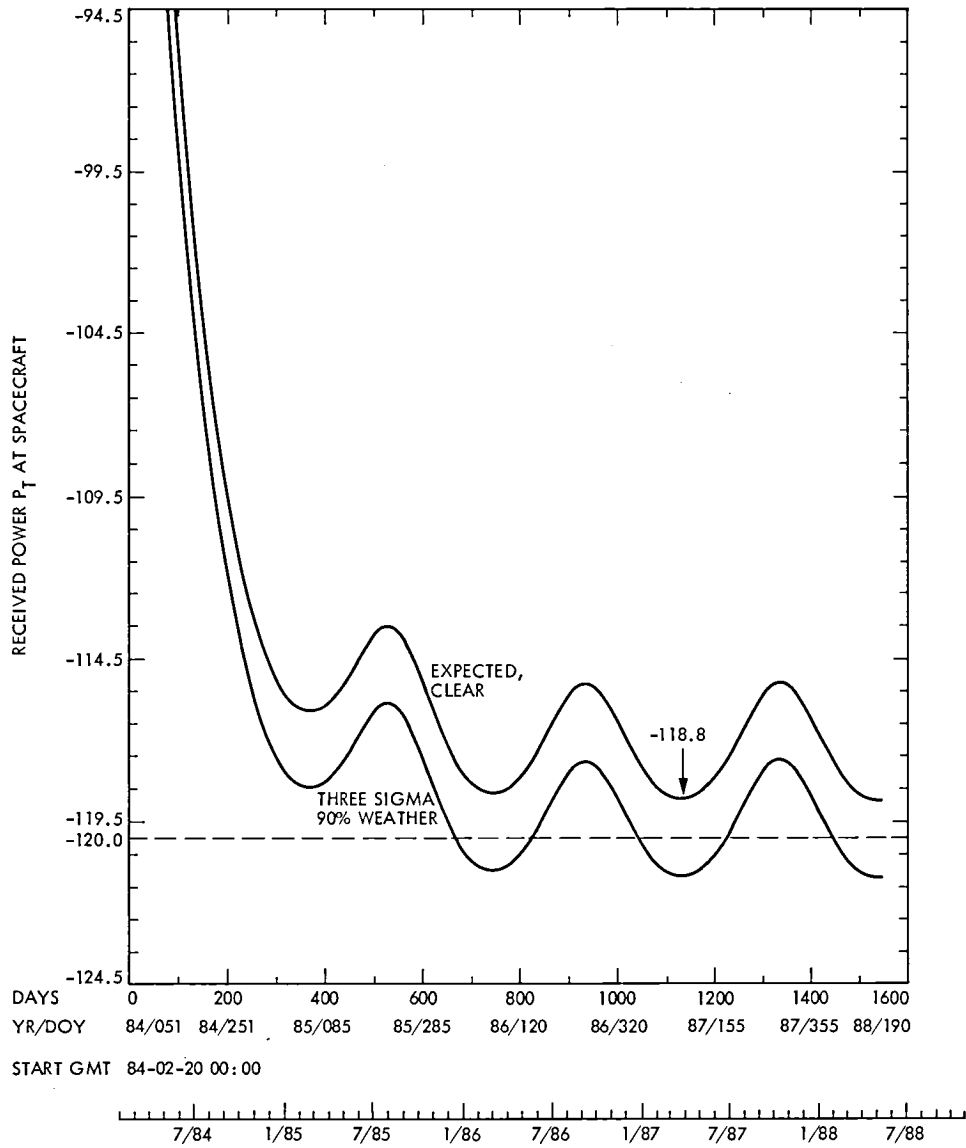


Fig. 9. Received power at spacecraft

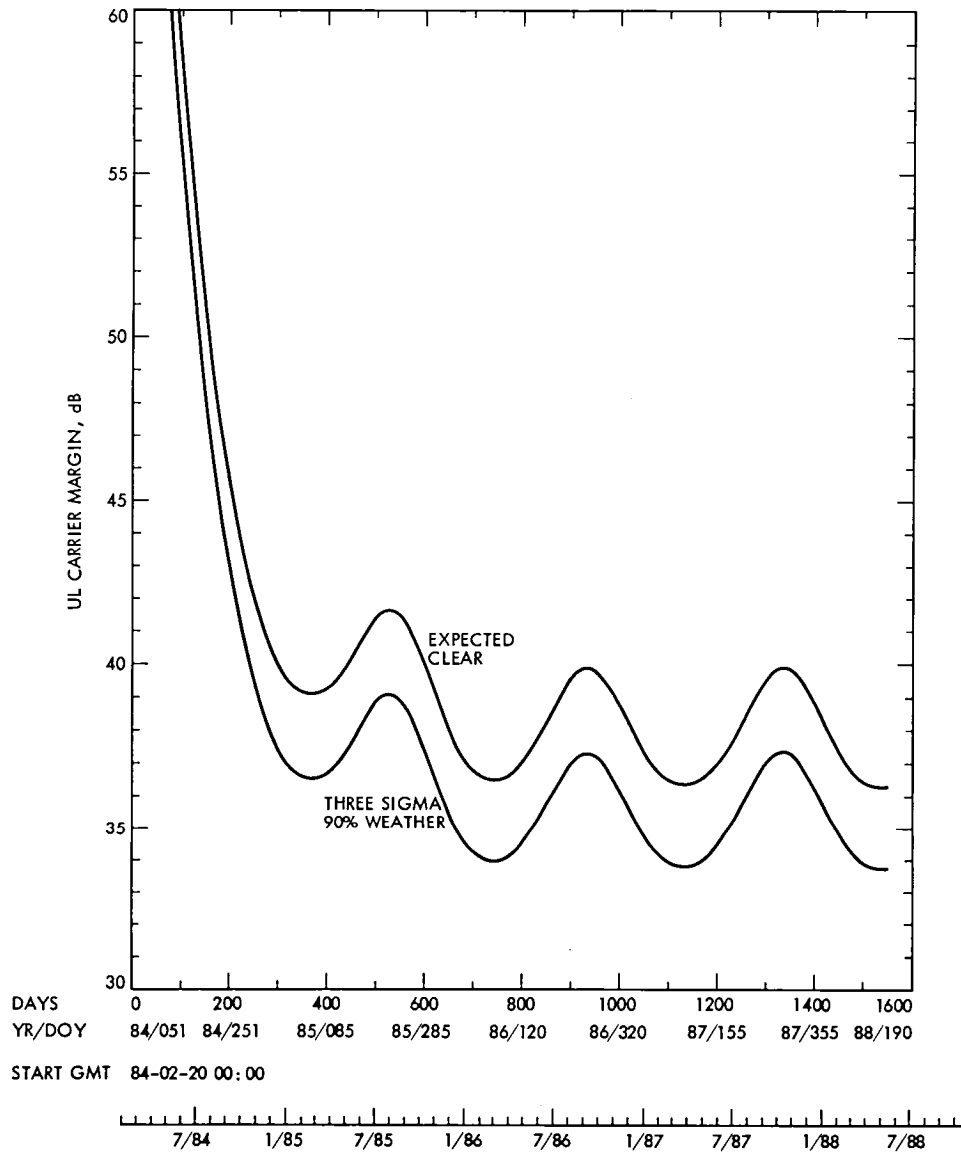


Fig. 10. Uplink carrier margin

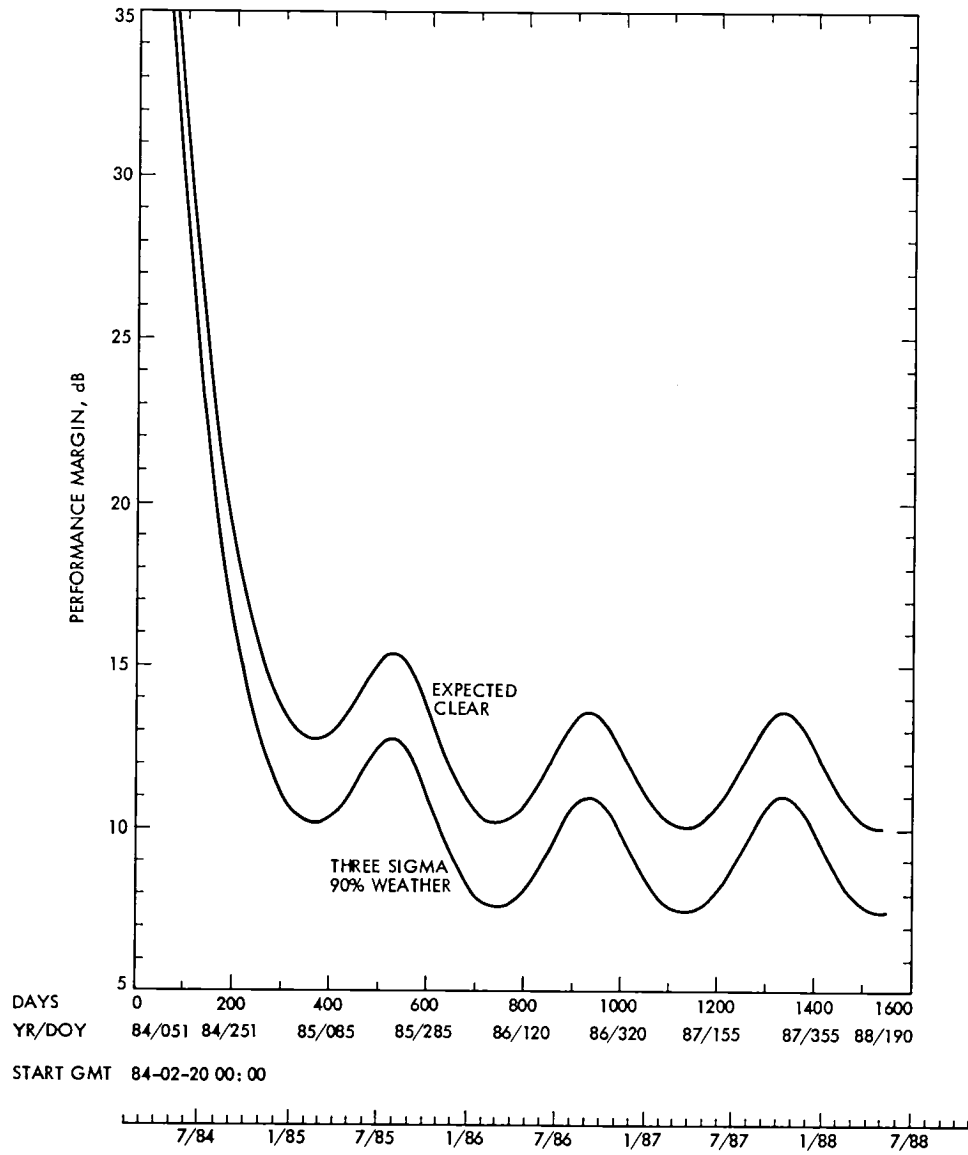


Fig. 11. Command performance margin

## **Appendix**

### **Design Control Tables**

Design Control Tables (DCT) are used to predict performance of a communications link. A DCT describes the link for a particular set of parameters at one point in the mission. Table A-1 is an example and is for the Galileo command link at Jupiter distance. To see the performance throughout the mission, certain performance parameters from the DCT are presented graphically. Figures A-1, 2, 3 are examples showing the received power, uplink carrier performance margin and command performance margin. The upper curve shows expected or mean link conditions. The lower curve takes into account a statistical estimate of weather effects plus the adverse tolerances of the link parameters. With approximately 99% confidence, the link will operate above the curve.

Each parameter listed in the DCT affects the link. By varying the bit rate, bit error rate, modulation index, coding, antenna size, transmitter power, and pointing error allowance the link performance will change.

The result of each DCT calculation is a performance margin. This margin is the amount by which the link varies from that required to give a specified performance. For the uplink power study the parameter of interest is the power required to just meet a specified required performance, not the margin resulting from a given uplink power. DCT results were adjusted accordingly. A new configuration, for example, 64-m rather than 34-m antenna, may be calculated from previous DCTs by adding the appropriate gain or loss into the table.

Table A-1. Galileo uplink carrier design control table

GALILEO CMD/34M/CLR DSGN/90PCT 2-SIG/RNG OFF/20 DEG MI HGA, 1985 BASELINE, STANDARD CASE #2, RUN 11/11/81						
EPOCH	85/120/00/00	SPACECRAFT	0	STATION	43	
DATE	89-06-13	DDY	164	HH:MM	00:00	DAYS FROM EPOCH
						1505 00:00
		DESIGN	FAV TOL	ADV TOL	MEAN	VAR
TRANSMITTER PARAMETERS						
1) RF POWER, DBM		73.00	.50	-.50	73.0	.04
POWER OUTPUT = 20.0 KW						
XMITR CIRCT LOSS, DB		.00	.00	.00	.0	.00
2) ANTENNA GAIN, DBI		55.30	.30	-.70	55.1	.08
ELEV ANGLE = 25.00 DEG						
3) POINTING LOSS, DB		.00	.00	-.10		
PATH PARAMETERS						
4) SPACE LOSS, DB		-278.16			-278.2	.00
FREQ = 2114.68 MHZ						
RANGE = 9.124+08 KM						
= 6.10 AU						
5) ATMOSPHERIC ATTENUATION, DB		-.11	.00	.00	-.1	.00
WTHR MODEL IS 810-5.						
RECEIVER PARAMETERS						
6) POLARIZATION LOSS, DB		-4.25	1.22	-1.55		
7) ANTENNA GAIN, DBI		36.30	.30	-.30	31.9	.34
CONE ANGLE = .69 DEG						
8) POINTING LOSS, DB		-.18	.18	-.07	-.1	.00
9) REC CIRCUIT LOSS, DB		-1.90	.40	-.50	-2.0	.07
10) NOISE SPEC DENS, DBM/HZ		-167.92	-.23	.79	-167.6	.03
OPERATING TEMP, K		1170.00	-60.00	235.00		
HOT BODY NOISE, K		.00	.00	.00		
11) 2-SIDED THRESHOLD LOOP NOISE BANDWIDTH, DB-HZ		12.00	-.70	.60	12.0	.07
POWER SUMMARY						
12) RCVD POWER, PT, DBM (1+2+3+4+5+6+7+8+9)					-120.3	.53
13) RCVD PT/NO, DB-HZ (12-10)					47.3	.56
14) RANGING SUPPRESSION, DB		.00	.00	.00	.0	.00
15) COMMAND SUPPRESSION, DB		-.55	.10	-.10	-.5	.00
16) CARR PWR/TOT PWR, DB (14+15)					-.5	.00
17) RCVD CARR PWR, DBM (12+16)					-120.9	.53
18) CARRIER MARGIN, DB (17-10-11)					34.8	.63
					---	

Table A-1 (contd)

	DESIGN	FAV TOL	ADV TOL	MEAN	VAR
DATA CHANNEL PERFORMANCE					
19) DATA BIT RATE, DB BIT RATE = 32.0 BPS	15.05	.00	.00	15.1	.00
20) DATA PWR/TOTAL PWR, DB	-9.25	.68	-.82	-9.3	.09
21) DATA PWR TO RCVR, DBM (12+14+20)				-129.6	.63
22) ST/NO TO RCVR, DB (21-19-10)				23.0	.66
23) SYSTEM LOSSES, DB RADIO LOSS, DB DEMOD, DETECT LOSS, DB	-1.20	.40	-.40	-1.2	.03
24) ST/NO OUTPUT, DB (22+23)				21.8	.68
25) THRESHOLD ST/NO, DB	9.59	.00	.00	9.6	.00
26) PERFORMANCE MARGIN, DB (24-25)				12.2	.68
				3.08 = 2.48	

# A Simplified Solar Cell Array Modelling Program

R. D. Hughes  
DSN Engineering Section

*As part of the energy conservation/self-sufficiency efforts of DSN Engineering, it was necessary to have a simplified computer model of a solar photovoltaic (PV) system. This article describes the analysis and simplifications employed in the development of a PV cell array computer model. The analysis of the incident solar radiation, steady-state cell temperature, and the current-voltage characteristics of a cell array are discussed. A sample cell array was modelled and the results are presented.*

## I. Introduction

As part of the Deep Space Network (DSN) effort in energy conservation and energy self-sufficiency at DSN tracking stations, the use of photovoltaic (PV) systems is being considered as a means of supplying cost-effective electrical power to these facilities. Flat-plate PV systems offer the advantages of relatively high efficiency, compactness, mechanical simplicity, high reliability, and adaptability to a variety of installation locations such as roof-top, ground, etc.

In order to have an analysis tool which could be used in conjunction with present computer models that quantify facility energy consumption, it was necessary to have a PV system computer model which operates with a minimum of computer storage space, is inexpensive to execute, and which can be easily interfaced with this existing software.

Several existing computer programs which model PV systems were investigated and were found to contain far more computational details and associated nonessential features than are required for the DSN engineering applications. For instance, the SOLCEL program developed by Sandia Laboratories is capable of performing a complex financial analysis

which takes into account the ratio of preferred stock to total capitalization, the annual rate of return on common stock, investment tax credits, etc. Other PV computer models were surveyed, among which was a program developed by the Low-Cost Solar Array (LSA) Project at JPL. This model, which addresses the cell reliability and failure modes, provides a basic cell array operation and maintenance analysis capability.

The requirement by DSN engineering to have design-oriented analysis procedures emphasized the need to develop, using a minimum effort, a simplified PV system computer model to support ongoing predesign studies. This article describes the first phase of this effort, which involved developing a computer model of only the PV cell array. The development of the entire system model, which will include such components as batteries, dc - ac inverters, and voltage regulators, which enable the system to generate maximum power and perform load-following, will be described in a subsequent article.

The emphasis in this work has been on using existing analysis tools, such as the ASHRAE solar radiation model (Ref. 1),

and on developing a simplified solar cell model. The result was a compact, low cost, and relatively accurate computer program.

## II. Technical Approach

The program analyzes flat-plate solar cells with a varied selection of tracking types, from stationary to double-axis (direct pointing) tracking. Hourly values for solar radiation and solar angles may either be input from data or calculated by an internal model. An approximate heat transfer analysis is performed to calculate the solar cell temperature, which determines cell efficiency. An iterative scheme is used, since cell temperature and efficiency are interdependent. Tables of current-voltage (I-V) performance curves as a function of temperature must be supplied to the program for the cell efficiency calculations.

The electrical circuit calculations are straightforward, since the main purpose is to analyze a PV array that is used to charge electrical batteries. A system voltage must be specified, and the power calculations are performed at this voltage.

In this fashion, relatively few PV cell properties are required from the user. The program is easy to operate and the results are quite accurate when compared to other photovoltaic programs which are much larger and more complicated to use.

A typical PV system, ARCO Model No. 104106, was selected to be analyzed, since cell array property data were available for this device from the LSA Project documentation (Ref. 4).

## III. Technical Analysis

The analysis is performed on a monthly basis using "typical" values of ambient and solar conditions for each month. Any single month or succession of months may be analyzed. A complete cell array performance summary which consists of 24 hourly conditions may be printed out. At the user's option, a short printout may be selected which prints only the total dc power for the "typical day" of each month and the total of all these "typical days" for the study period.

All calculations are performed in SI metric units. The computations are divided into the following segments:

### A. Solar Radiation Calculations

The solar radiation intensity  $I_t$  incident on the flat surface of a PV panel consists in general of three components: direct solar radiation  $I_D$ , diffuse sky radiation  $I_d$ , and the solar

radiation reflected from surroundings  $I_r$ . The direct component is expressed as:

$$I_D = I_{dN} \cos \theta \quad (1)$$

where  $I_{dN}$  is the direct normal insolation in  $W/m^2$ , and  $\theta$  is the angle of incidence between incoming solar rays and a line normal to the surface, as shown in Fig. 1. For a planar, tilted surface, the angle  $\theta$  is determined (Ref. 1) from the relation

$$\cos \theta = \cos \beta \cos \gamma \sin \Sigma + \sin \beta \cos \Sigma \quad (2)$$

where  $\beta$  is the solar altitude angle, the angle between the sun's ray and the projection of the ray on a horizontal surface;  $\gamma$  is the surface-solar azimuth angle, the angle between the projection of the normal to the surface on the horizontal plane and the projection of the sun's ray on the horizontal plane; and  $\Sigma$  is the angle the surface makes with the horizontal plane;  $\Sigma$  can be either fixed or changing each hour according to the tracking mechanism (single-axis, double-axis).

The surface-solar azimuth angle can be written as:

$$\gamma = \phi + \psi \quad (3)$$

where  $\psi$  is the surface azimuth angle, the angle between the projection of the normal to the surface on the horizontal plane and the direction south ( $\psi$  is taken positive for an angle west of south);  $\phi$  is the solar azimuth angle, the angle between the south direction and the projection of the sun's ray on the horizontal surface.

Furthermore, the solar angles  $\beta$  and  $\phi$  are obtained from

$$\sin \beta = \cos L \cos \delta \cos H + \sin L \sin \delta \quad (4)$$

$$\sin \phi = \cos \delta \sin H / \cos \beta \quad (5)$$

where  $L$  is the site latitude angle,  $\delta$  is the solar declination angle, and  $H$  is the hour angle of the sun. Since this model assumes that the local solar time equals the local civil time, and the longitude correction and equation of time (about +14 minutes) can be neglected, then the hour angle  $H$  is expressed by

$$H = 0.25 \times (\text{number of minutes from solar noon}) \quad (6)$$

The declination angle  $\delta$  is expressed by a Fourier series that is obtained by curvefitting data contained in Ref. 1.

$$\delta = (\pi/180) \left[ 0.2833 - 23.188 \cos\left(\frac{M\pi}{6}\right) - 0.15 \cos\left(\frac{M\pi}{3}\right) - 0.211 \sin\left(\frac{M\pi}{6}\right) + 0.1155 \sin\left(\frac{M\pi}{3}\right) \right] \quad (7)$$

where  $M$  is the month index (1, 2, 3 ... 12).

The diffuse sky radiation is expressed as (Ref. 1):

$$I_d = I_{Hd} (1 + \cos \Sigma)/2 \quad (8)$$

where  $I_{Hd}$  is the diffuse sky radiation falling on a horizontal surface.

The reflected solar radiation is expressed as:

$$I_r = \rho I_H (1 - \cos \Sigma)/2 \quad (9)$$

where  $I_H$  is the total radiation falling on a horizontal surface and  $\rho$  is the average reflectivity of the ground and surrounding surfaces.  $I_H$  is given by:

$$I_H = I_{Hd} + I_{dN} \sin \beta \quad (10)$$

Therefore, the total radiation  $I_t$  is given by

$$I_t = I_{dN} \cos \theta + I_{Hd} (1 + \cos \Sigma)/2 + \rho I_H (1 - \cos \Sigma)/2 \quad (11)$$

If measured solar data are supplied,  $I_{dN}$  and  $I_H$  are given and the expression for total insolation becomes:

$$I_t = I_{dN} \cos \theta + (I_H - I_{dN} \sin \beta) (1 + \cos \Sigma)/2 + \rho I_H (1 - \cos \Sigma)/2 \quad (12)$$

If the model described in Ref. 1 is used,  $I_{dN}$  for clear sky conditions is expressed as

$$I_{dN} = A/e^{B \sin \beta}$$

and  $I_{Hd}$  is expressed as

$$I_{Hd} = CI_{dN}$$

where  $A$ ,  $B$  and  $C$  are coefficients that vary throughout the year in a periodical shape. The coefficients  $A$ ,  $B$ , and  $C$  are curve-fitted with Fourier series using the data of Ref. 1:

$$A = 3.1538 \left[ 3.685 + 23.98 \cos\left(\frac{M\pi}{6}\right) - 1.083 \cos\left(\frac{M\pi}{3}\right) + 4.893 \sin\left(\frac{M\pi}{6}\right) - 0.722 \sin\left(\frac{M\pi}{3}\right) \right] \quad (13)$$

$$B = \left[ 1.7158 - 33.08 \cos\left(\frac{M\pi}{6}\right) + 3.08 \cos\left(\frac{M\pi}{3}\right) - 10.34 \sin\left(\frac{M\pi}{6}\right) + 1.3 \sin\left(\frac{M\pi}{3}\right) \right] (.001) \quad (14)$$

$$C = \left[ 90.333 - 39.63 \cos\left(\frac{M\pi}{6}\right) + 6.83 \cos\left(\frac{M\pi}{3}\right) - 10.651 \sin\left(\frac{M\pi}{6}\right) + 3.17 \sin\left(\frac{M\pi}{3}\right) \right] (.001) \quad (15)$$

The coefficient  $A$  is expressed in  $W/m^2$ ; the coefficients  $B$  and  $C$  are dimensionless. For non-clear sky conditions (clouds, fog, etc.), a cloud cover factor must be used. This cloud cover factor represents the fraction of clear sky insolation which occurs at ground level by multiplying the total insolation  $I_t$ . Five solar-tracking options are available to the user and are selected through an input parameter:

- (1) The PV panels are stationary with surface tilt angle specified. Panels are facing south (north for southern hemisphere); in this case:

$$\psi = 0$$

- (2) The PV panels are single-axis tracking about a horizontal east-west axis (ie., panels pivoting on a horizontal rod oriented east-west); in this case:

$$\gamma = \phi$$

$$\Sigma = \tan^{-1} (\cos \phi / \tan \beta)$$

$$\psi = 0$$

- (3) The PV panels are single-axis tracking about a horizontal north-south axis; here:

$$\psi = \frac{\pi}{2}$$

$$\Sigma = \tan^{-1} (\sin |\phi| / \tan \beta)$$

- (4) The PV panels are single-axis tracking about a vertical axis (i.e., tilted at a constant angle to the ground and mounted on a vertical rod which rotates); here:

$$\psi = \tan^{-1} \{ \cos \beta \sin \phi / [\sin |L| \cos (x - |L|)] \}$$

where  $x = \tan^{-1} (\cos \phi / \tan \beta)$ , and  $\Sigma = \tan^{-1} (\tan |L| / \cos \psi)$

- (5) Double-axis tracking, PV panels normal to sun vector ( $\theta = 0$ ).

## B. Cell Temperature Analysis

For all tracking options the cell array is assumed to be passively cooled by ambient air on the front surface only, with the rear surface insulated. The heat flux which is deposited in the cell is expressed as:

$$Q = I_t (\alpha - \eta) \quad (16)$$

where  $\alpha$  is the product of cell visible light absorbance and cell encapsulation transmittance (the fraction of incident energy which enters the cells), and  $\eta$  is the cell efficiency, fraction of incident insolation which is converted into dc electricity.

Figure 2 shows the equilibrium heat flux condition for the approximate heat transfer model used in this analysis. At equilibrium, the heat flux  $Q$  will be equal to the sum of heat lost from the cell outer surface by both convection and radiation; i.e.,

$$Q = (h_c + h_r) (T_c - T_a) \quad (17)$$

where  $h_c$  and  $h_r$  are the convective and radiative heat transfer coefficients, respectively. Equations (16) and (17) give the temperature  $T_c$  as:

$$T_c = T_a + \frac{Q}{(h_c + h_r)} \quad (18)$$

The following empirical relationships for the heat transfer coefficients  $h_c$  and  $h_r$  are taken from Ref. 2. The convective heat transfer coefficient  $h_c$  consists of two parts: a free con-

vection coefficient  $h_1$  and a forced convection coefficient  $h_2$ , for a flat plate in a moving airstream:

$$h_c = h_1 + h_2$$

The free convection heat transfer coefficient,  $h_1$ , is expressed in  $W/m^2 K$  as

$$h_1 = (k/x) (0.13) (GrPr)^{-0.333} \quad (19)$$

where  $k$ , the thermal conductivity of air, is expressed in  $W/m - K$  as

$$k = 3.623 \times 10^{-4} T_m^{.7488} \quad (20)$$

$T_m$  is the average of the air and cell temperatures (K);  $x$  is the characteristic panel length (m); and  $Gr$  is the Grashof number:

$$Gr = 9.8 \beta_\tau (\Delta T) x^3 / \nu^2$$

where  $\beta_\tau$  is the thermal expansion coefficient of air in  $(K^{-1})$ :

$$\beta_\tau = 1/T$$

$$\Delta T = |T_{air} - T_{plate}|$$

$\nu$  is the kinematic viscosity of air in  $m^2/s$ :

$$\nu = 9.253 \times 10^{-10} (T^{1.709})$$

$Pr$  = Prandtl number (0.72 for air)

The forced convection heat transfer coefficient  $h_2$  is given in  $W/m^2 - K$  as

$$h_2 = \frac{0.664 kPr^{.333} \sqrt{Re}}{x} [Re \leq 5 \times 10^5]_{\text{Laminar}}$$

or (21)

$$h_2 = \frac{0.036 kPr (Re^{.8} - 23000)}{x} [Re > 5 \times 10^5]_{\text{Turbulent}}$$

where  $Re = \text{Reynold's number} = Vx/\nu$ , and  $V$  is wind speed in m/s.

The radiation heat transfer coefficient  $h_r$  is linearized and given as

$$h_r = 5.688 \times 10^{-8} \epsilon (T_c^4 - T_r^4)/T_c - T_a \quad (22)$$

where  $\epsilon$  is the infrared emittance of the cell encapsulant;  $T_c$  is the cell temperature, taken as the plate surface temperature (K);  $T_a$  is the ambient air temperature (K);  $T_r$  is the "effective" radiative temperature, which is taken as the average of apparent sky temperature and ambient air temperature:

$$\begin{aligned} T_r &= (T_{sky} + T_a)/2 \\ T_{sky} &= 0.0552 T_a^{1.5} \end{aligned} \quad (23)$$

The cell temperature calculation procedure is started by assuming an initial guess for both  $T_c$  and  $\eta$ . Then calculate  $Q$  from Eq. (16) and calculate  $h_1$ ,  $h_2$ ,  $h_r$  from Eqs. (19), (21), and (22). The cell temperature  $T_c$  is calculated from Eq. (18) to check on  $\eta = \eta(T_c)$ . If  $\eta$  is inconsistent, repeat starting with Eq. (16). This iteration is found to converge within two to three steps, and therefore it is performed only four times in the program.

### C. Cell Efficiency Analysis

The method for calculating cell efficiency is based on the assumption that the efficiency is a strong function of cell temperature and a weak function of insolation within normal operating conditions. Consequently,  $\eta$  may be derived by interpolating among a family of reference I-V curves, as shown in Fig. 3, in which each curve represents a particular cell temperature. Once the voltage is given by the user, the current will be determined for a given cell temperature and cell efficiency. Hence,

$$\eta = IV/Cr \quad (24)$$

where  $Cr$  is a reference insolation. Note that this current is a representative value corresponding to a reference insolation and is used only for calculating efficiency. A justification for the above assumption may be made according to the circuit analysis (Ref. 3) as follows.

An equivalent circuit for a solar cell is shown in Fig. 4, where  $R_s$  = series resistance of the cell,  $I_L$  = light-generated current,  $I_D$  = dark current,  $V_D$  = diode voltage,  $I$  = net output current, and  $V$  = cell voltage. By writing

$$I = I_L + I_D \quad (I_L \gg I_D) \quad (25)$$

$$V_D = IR_s + V \quad (26)$$

$I_D$  may be expressed as (Ref. 3)

$$I_D = I_0 (1 - e^{-(q/kT)V_D}) \quad (27)$$

where  $I_0$  is the reverse saturation current.

Thus, by combining Eqs. (25), (26), and (27), we obtain

$$I = I_L + I_0 [1 - e^{-(q/kT)(V + IR_s)}] \quad (28)$$

Since cell efficiency is the ratio of dc power output to total incident insolation,  $\eta = IV/AI_t$ , then

$$\eta = I_L V/AI_t + (I_0 V/AI_t) [1 - e^{-(q/kT)(V + IR_s)}] \quad (29)$$

where  $A$  is the cell area.

For normal operating conditions (i.e., when voltage does not approach the cell's open-circuit voltage) the light-generated current is known to be proportional to insolation (Ref. 3). Thus, it can be seen that the first term is independent of  $I_t$  and the second term is linearly dependent on  $I_t$  and exponentially dependent on  $T^{-1}$  since  $R_s$  is usually small. This reasoning then supports the assumption that efficiency is primarily a function of temperature for a given voltage, and may be interpolated from a family of I-V curves.

### D. PV Array Power Output

The net dc power output, in kW, for any hour of the analysis is:

$$P_{net} = \frac{I_t \eta \bar{A} f N}{1000} \quad (30)$$

where  $\bar{A}$  is the area of each module of cells in  $m^2$ ,  $f$  is the packing factor of cells (ratio of cell area to module area), and  $N$  is the number of modules in the system. The sum of the hourly values of  $P_{net}$  represents the total dc power obtained for the typical day of each month under study.

## IV. Program Description

The cell array program is written in FORTRAN and consists of three routines.

- (1) The MAIN routine reads input data, performs initializations, and controls the overall simulation.
- (2) The PWR subroutine performs the insolation calculations, the thermal analysis, and the power analysis; PWR is called by MAIN.
- (3) The EFF subroutine is called by PWR to calculate the cell efficiency for a given voltage and temperature.

Program input consists of three parts:

- (1) The namelist "CDAT", which contains current-voltage (I-V) curve data.
- (2) The namelist "PVIN," which contains various system parameters and program operation flags.
- (3) A formatted input file which contains data about ambient and insolation conditions.

Note that the last input is not needed if the internal insolation model is used. The output is described for the sample case in the following section.

## V. Sample Case Analysis

The sample solar photovoltaic module chosen to be analyzed was the ARCO Solar Module, Model Type 10699-C, Module Serial No. 104108. A drawing of the module which illustrates pertinent physical features and electrical connections is shown in Fig. 5 (Ref. 4).

For this case, the program's internal solar model was used, since complete hourly data for direct normal insolation was not available for the Los Angeles site. Hourly data are now being recorded for the Los Angeles site by the National Oceanic and Atmospheric Administration (NOAA) and computer tapes should be available in late 1982.

A listing of both the long and short versions of output for this case are shown in the Appendix. The primary input parameters which describe the ARCO solar module are listed under the headings "SYSTEM PARAMETERS" and "SITE DESCRIPTION." The voltage was selected to be regulated at 15 volts dc since the cell efficiency is relatively high at this voltage and also excess charging voltage is allowed for charging a 12-volt battery system.

The tilt angle of the panels was fixed at 24 degrees from horizontal, the ground reflectivity was 0.2, the product of cell absorbance and encapsulant transmittance was 0.9, the infrared emittance of the cell encapsulant was 0.526, the surface area of each PV panel module was 0.2701 m<sup>2</sup>, the cell packing factor was 0.692, there were 100 modules, the site

was Los Angeles, California, and the latitude was 33.56° north. Also, the I-V curve data were taken from Fig. 3. The cloud cover factors for the 12 months of the year were 0.82, 0.75, 0.78, 0.78, 0.80, 0.82, 0.87, 0.9, 0.91, 0.92, 0.88, 0.86.

The first page of the Appendix is a summary of the input. The analysis results are shown in the following pages of the Appendix for both a long print version and a short print version of the output. An interpretation of the output is as follows: Under the column heading "HOUR," the integer number indicates the hourly period starting from midnight; subsequent columns are hourly averages. "AMBIENT TEMPERATURE" and "WIND SPEED" are as taken from input; "TOTAL INSOLATION" is the amount of insolation incident on the cells (not on the entire module area) during the hourly period; "CELL TEMPERATURE" is the calculated cell temperature; and "POWER OUTPUT" is the calculated power output for the hourly period. At the bottom, "TOTAL POWER FOR A TYPICAL DAY IN JAN" is the total of all hourly power outputs in the last column above. Note that this power is rated at the specified voltage, and the corresponding current may be calculated accordingly.

A parametric study was performed in which the panel tilt angle was varied over the range 10-70 degrees to determine the optimum angle for each month. Table 1 shows the results of this study in terms of power as a function of month and tilt angle. Table 2 shows the optimum tilt angles for each month and the resulting power for each typical day. The single tilt angle which gave the maximum total power for the entire year was approximately 35 degrees, which is equal to the site latitude, as expected. The trend in Table 2, which shows peak optimum power in the summer months is a result of the cloud cover factor.

The benefit of changing tilt angle to the monthly optimums instead of keeping a fixed angle of 35 degrees results in an increase of only about 5% in net power output over a one-year period (14443.83 kWh compared to 137.7 kWh) for 12 "typical days." Thus it would not seem reasonable to implement this feature in such a system unless a very simple and inexpensive way to do so was devised. The average daily power output for the entire year for the system of 100 panels is about 11.9 kWh.

## VI. Summary

The analysis result was compared to the photovoltaic computer program SOLCEL and found to predict very similar results. SOLCEL has more capabilities than SCAMP, but it is very large and somewhat difficult to use. In the sample case, which consisted of a system of panels mounted at a selected

angle, the results showed that a fixed tilt angle of 35 degrees, approximately the site latitude, was the optimum single angle for an entire year. The performance improvement realized by selecting an optimum angle for each month was only about a 5% gain in net power. Also, the system of 100 panels will have an annual average power output of 11.9 kWh per day.

The simplified model has been developed to fill a specific need. It is applicable to the design decision-making process and will be incorporated into a PV system model. A subsequent article will describe the overall PV system model that is currently being developed and will have the ability to interface with existing energy conservation analysis tools.

## References

1. *American Society of Heating, Refrigeration and Air Conditioning Engineer (ASHRAE) Handbook of Fundamentals*, ASHRAE Inc., New York, 1977.
2. Kreith, F., *Principles of Heat Transfer*, 2nd edn., International Textbook Co., Scranton, Pa., 1965.
3. Angrist, S. W., *Direct Energy Conversion*, 3rd edn., Allyn and Bacon Inc., Boston, Ma., 1977.
4. Smokler, M. I., "User Handbook for Block III Silicon Solar Cell Modules," Low Cost Solar Array Project Document 5101-82, Jet Propulsion Laboratory, Pasadena, Calif. 1979.

**Table 1. PV array power output (kWh) as a function of month and tilt angle for sample analysis case**

Month	Angle, deg						
	10	20	30	40	50	60	70
Jan	7.63	8.77	9.67	10.28	10.64	10.75	10.61
Feb	8.53	9.43	10.09	10.47	10.60	10.48	10.08
Mar	10.63	11.18	11.45	11.49	11.15	10.58	9.74
Apr	11.80	11.92	11.75	11.31	10.59	9.61	8.39
May	12.84	12.77	12.39	11.72	10.77	9.55	8.09
Jun	13.23	13.12	12.70	11.98	10.97	9.70	8.18
Jul	13.47	13.39	13.03	12.38	10.38	10.11	8.59
Aug	12.90	12.98	12.79	12.33	11.60	10.58	9.25
Sep	11.70	12.19	12.42	12.38	12.08	11.52	10.66
Oct	10.03	10.98	11.64	12.03	12.16	12.02	11.61
Nov	7.95	9.11	9.97	10.53	10.93	11.04	10.90
Dec	7.27	8.51	9.52	10.23	10.67	10.87	10.81
Total	127.98	134.36	137.43	137.14	133.55	126.79	116.91

**Table 2. Optimum tilt angles for sample analysis case**

Month	Angle, deg	Power, kWh
Jan	60	10.75
Feb	50	10.60
Mar	35	11.48
Apr	20	11.94
May	13	12.85
Jun	11	13.23
Jul	12	13.48
Aug	18	12.99
Sep	34	12.44
Oct	50	12.16
Nov	59	11.04
Dec	62	10.87
Total		143.83

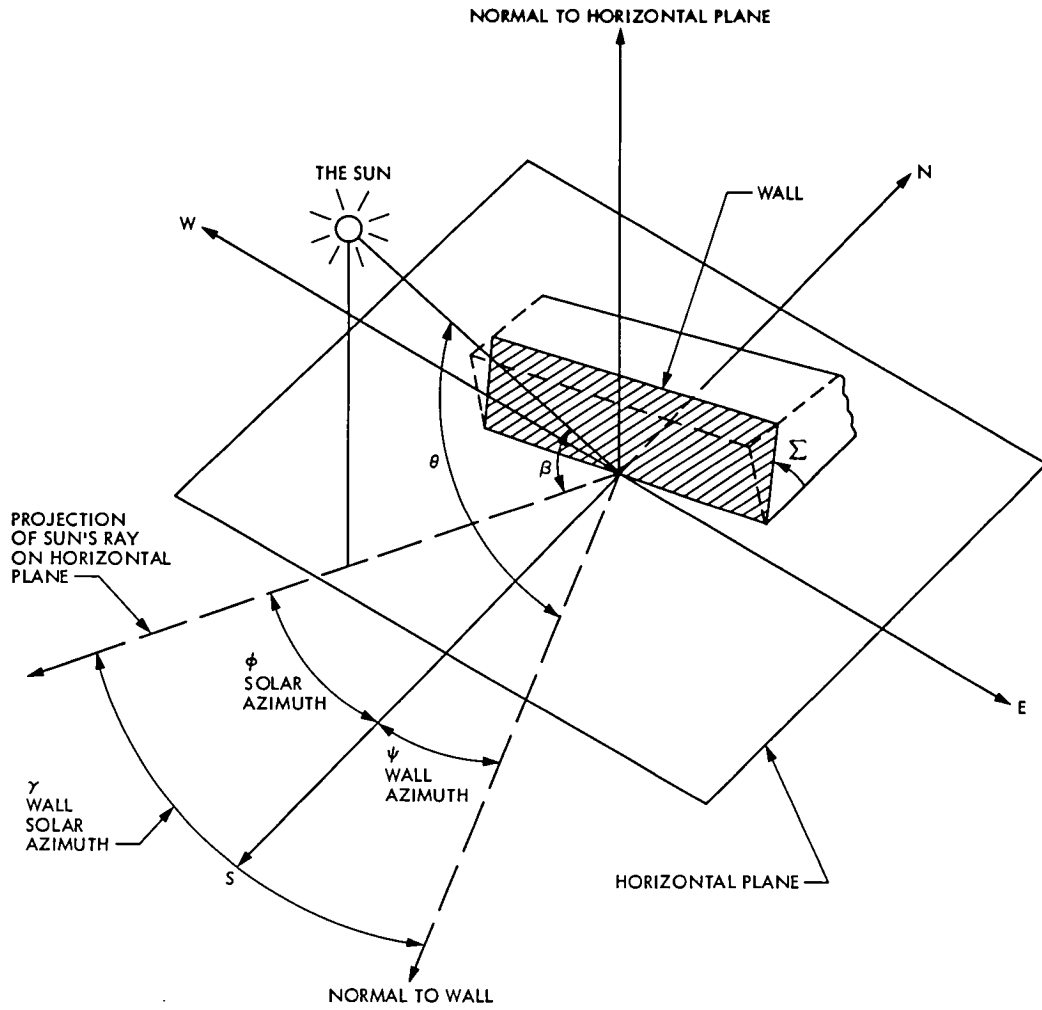


Fig. 1. Solar angles on a tilted plane

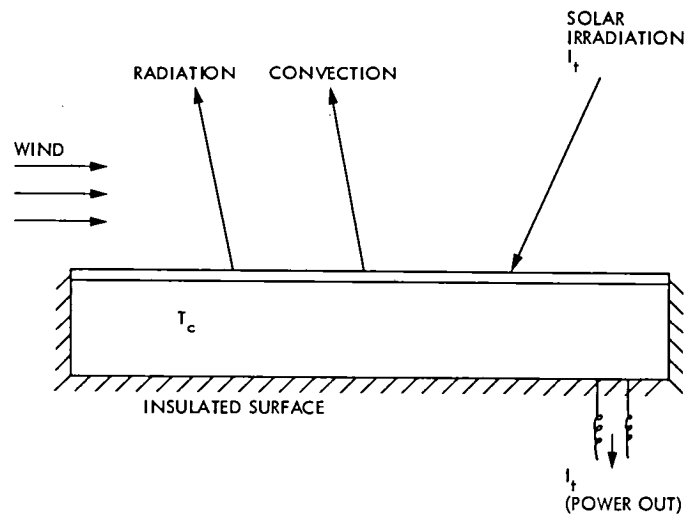


Fig. 2. Equilibrium heat transfer in TV panel

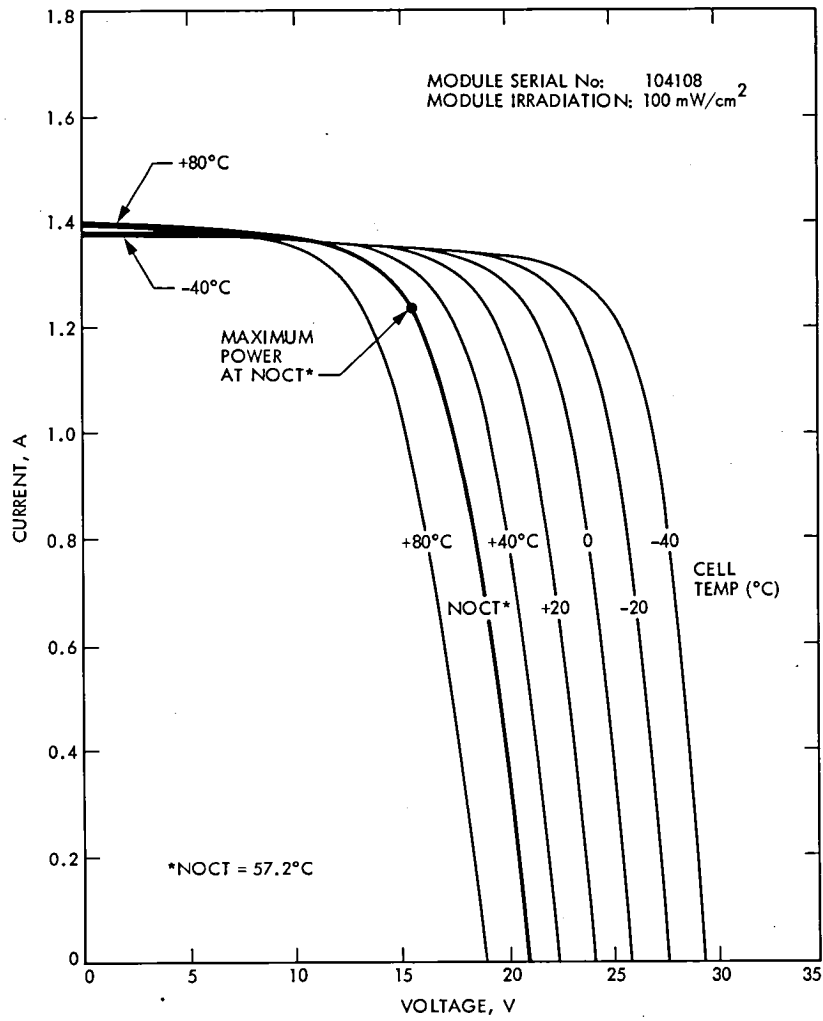


Fig. 3. I-V curves of a sample solar module (manufactured by ARCO)

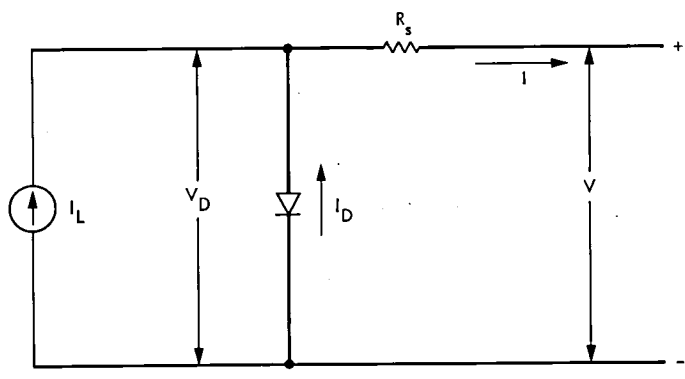
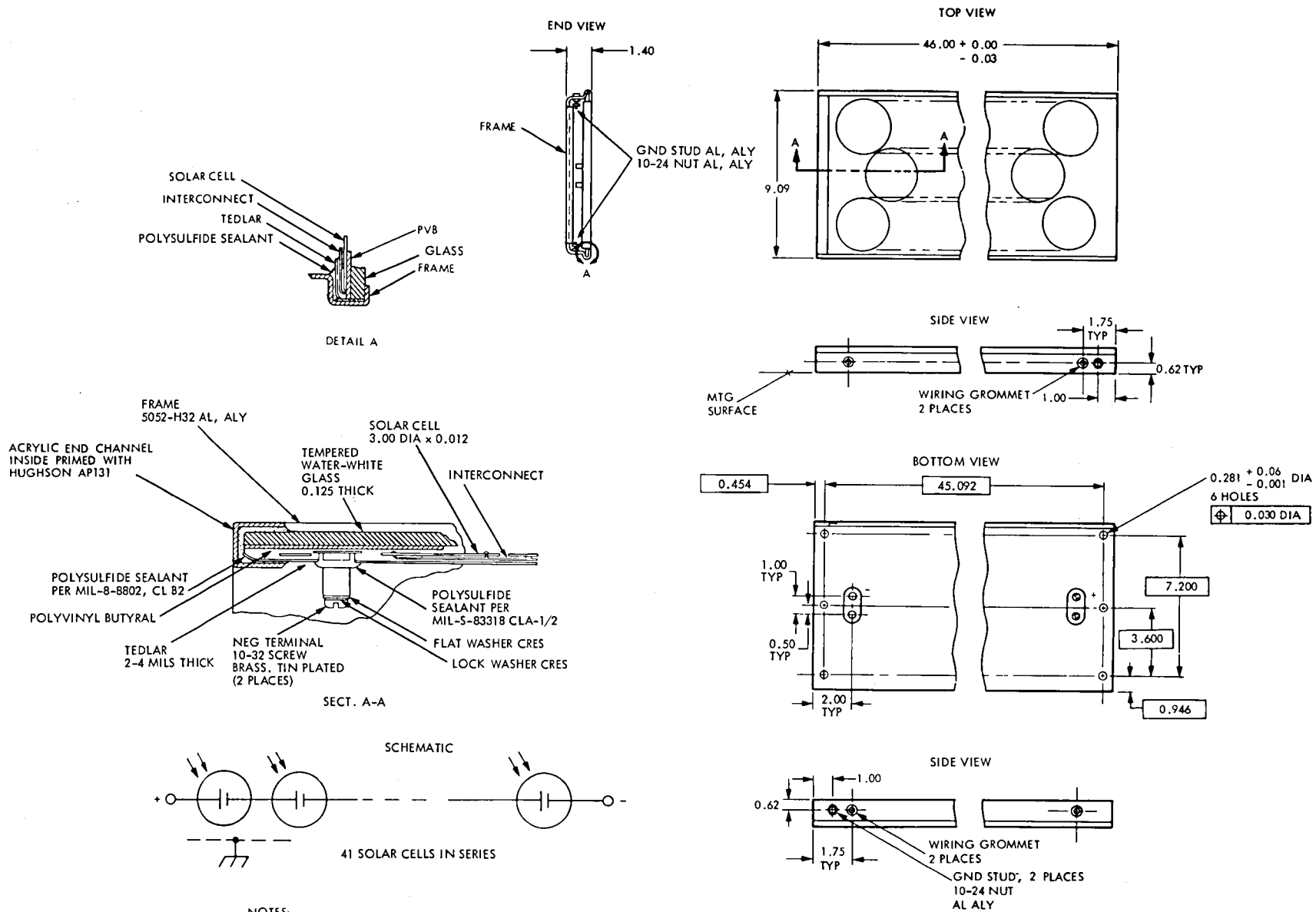


Fig. 4. An equivalent circuit for a solar cell



NOTES:

1. DO NOT SCALE
2. DIMENSIONS ARE IN INCHES
3. TOLERANCES ARE  $\pm 0.03$  UNLESS OTHERWISE SPECIFIED
4. MOUNTING PLANE OF SUBARRAY MUST NOT EXCEED ONE QUARTER INCH PER FOOT DEVIATION FROM PLANARITY

Fig. 5. ARCO solar module (from Ref. 4)

# Appendix

## Sample Case Output

\*\*\*\*\* PHOTOVOLTAIC CELL ARRAY MODEL \*\*\*\*\*  
ARCO SOLAR MODULE NO. 104108

\*\*\*\*\*

### SYSTEM PARAMETERS:

REGULATED VOLTAGE=15.00 VOLTS DC  
TILT ANGLE FROM HORIZONTAL=24.00 DEGREES  
GROUND REFLECTIVITY=.200  
CELL ABSORPTANCE \* ENCAPSULENT TRANSMITTANCE=.900  
IR EMITTANCE OF CELL ENCAPSULENT=.526  
INDIVIDUAL MODULE AREA=.2701 M\*\*2  
CELL PACKING FACTOR=.692  
NUMBER OF MODULES=100

### SITE DESCRIPTION:

LOCATION--LOS ANGELES, CA.  
LATITUDE = 33.560 DEG NORTH

\*\*\*\*\*

SYSTEM ANALYSIS FOR THE MONTH OF JAN

```

*****
    HOUR      AMBIENT      WIND      TOTAL      CELL      POWER
           AIR TEMP      SPEED      INSOLATION  TEMPERATURE  OUTPUT
           (DEG C)      (M/S)      (WATTS)      (DEG C)      (WATTS)

    1         12.0         1.9         .0000         12.0         .0000
    2         11.4         1.9         .0000         11.4         .0000
    3         10.9         1.6         .0000         10.9         .0000
    4         10.5         1.6         .0000         10.5         .0000
    5         10.3         1.9         .0000         10.3         .0000
    6         10.1         1.8         .0000         10.1         .0000
    7         10.3         1.7         .3769+00         10.3         .4020-01
    8         10.9         2.0         .4399+04         24.2         .4673+03
    9         12.7         2.3         .8458+04         37.4         .8931+03
   10         14.5         2.3         .1143+05         47.4         .1182+04
   11         16.2         1.4         .1326+05         57.1         .1335+04
   12         17.3         2.5         .1388+05         56.0         .1402+04
   13         18.0         3.1         .1326+05         53.6         .1349+04
   14         18.0         3.6         .1143+05         48.0         .1180+04
   15         17.5         4.5         .8458+04         38.9         .8925+03
   16         16.7         4.1         .4399+04         28.0         .4665+03
   17         15.7         3.6         .3769+00         15.7         .4015-01
   18         14.6         3.5         .0000         14.6         .0000
   19         14.3         3.5         .0000         14.3         .0000
   20         14.1         2.8         .0000         14.1         .0000
   21         13.9         2.3         .0000         13.9         .0000
   22         13.3         2.4         .0000         13.3         .0000
   23         12.9         2.6         .0000         12.9         .0000
   24         12.5         2.1         .0000         12.5         .0000
*****

```

TOTAL POWER FOR A TYPICAL DAY IN JAN = 9.17 KWH

SYSTEM ANALYSIS FOR THE MONTH OF FEB

```

*****
    HOUR      AMBIENT      WIND      TOTAL      CELL      POWER
           AIR TEMP      SPEED      INSOLATION  TEMPERATURE  OUTPUT
           (DEG C)      (M/S)      (WATTS)      (DEG C)      (WATTS)

    1         12.6         1.5         .0000         12.6         .0000
    2         12.2         1.8         .0000         12.2         .0000
    3         11.6         1.5         .0000         11.6         .0000
    4         11.3         1.8         .0000         11.3         .0000
    5         11.3         1.6         .0000         11.3         .0000
    6         10.8         1.4         .0000         10.8         .0000
    7         10.6         1.8         .1147+04         12.9         .1222+03
    8         12.3         2.1         .5359+04         28.4         .5682+03
    9         15.1         2.0         .8899+04         41.7         .9343+03
   10         17.6         2.5         .1158+05         50.3         .1188+04
   11         19.3         3.0         .1326+05         55.1         .1343+04
   12         20.0         3.5         .1383+05         56.1         .1397+04
   13         19.6         4.3         .1326+05         52.8         .1351+04
   14         19.3         4.5         .1158+05         48.2         .1195+04
   15         18.6         5.0         .8899+04         40.5         .9374+03
   16         17.8         5.0         .5359+04         31.0         .5675+03
   17         16.6         4.3         .1147+04         18.7         .1220+03
   18         15.3         3.5         .0000         15.3         .0000
   19         14.8         3.3         .0000         14.8         .0000
   20         14.8         3.0         .0000         14.8         .0000
   21         14.5         2.2         .0000         14.5         .0000
   22         14.0         1.7         .0000         14.0         .0000
   23         13.6         1.9         .0000         13.6         .0000
   24         13.3         1.9         .0000         13.3         .0000
*****

```

TOTAL POWER FOR A TYPICAL DAY IN FEB = 9.73 KWH

SYSTEM ANALYSIS FOR THE MONTH OF MARCH

```

*****
HOUR      AMBIENT      WIND      TOTAL      CELL      POWER
          AIR TEMP    SPEED    INSOLATION  TEMPERATURE  OUTPUT
          (DEG C)    (M/S)    (WATTS)    (DEG C)    (WATTS)

  1         10.9        2.6      .0000        10.9        .0000
  2         10.6        2.3      .0000        10.6        .0000
  3         9.9         2.5      .0000         9.9        .0000
  4         9.7         2.2      .0000         9.7        .0000
  5         9.3         2.5      .0000         9.3        .0000
  6         9.1         2.4      .1165-28     9.1        .1165-29
  7         9.6         3.1      .2733+04     16.7       .2911+03
  8        11.9        3.4      .6700+04     30.1       .7098+03
  9        14.0        3.3      .1019+05     41.5       .1071+04
 10        15.5        3.6      .1289+05     49.1       .1326+04
 11        16.7        4.1      .1459+05     53.4       .1484+04
 12        17.2        5.2      .1517+05     53.3       .1543+04
 13        17.3        5.6      .1459+05     51.5       .1492+04
 14        17.0        5.9      .1289+05     47.0       .1334+04
 15        16.8        6.4      .1019+05     40.3       .1074+04
 16        16.3        5.8      .6700+04     32.2       .7091+03
 17        15.6        5.3      .2733+04     21.8       .2906+03
 18        14.0        5.3      .1165-28     14.0       .1238-29
 19        13.1        4.3      .0000        13.1       .0000
 20        12.8        3.7      .0000        12.8       .0000
 21        12.4        2.9      .0000        12.4       .0000
 22        12.0        2.9      .0000        12.0       .0000
 23        11.6        2.7      .0000        11.6       .0000
 24        11.2        2.6      .0000        11.2       .0000
*****

```

TOTAL POWER FOR A TYPICAL DAY IN MARCH= 11.32 KWH

SYSTEM ANALYSIS FOR THE MONTH OF APRIL

```

*****
HOUR      AMBIENT      WIND      TOTAL      CELL      POWER
          AIR TEMP    SPEED    INSOLATION  TEMPERATURE  OUTPUT
          (DEG C)    (M/S)    (WATTS)    (DEG C)    (WATTS)

  1         13.3        1.7      .0000        13.3        .0000
  2         13.0        1.5      .0000        13.0        .0000
  3         12.8        1.4      .0000        12.8        .0000
  4         12.6        1.6      .0000        12.6        .0000
  5         12.5        1.4      .0000        12.5        .0000
  6         12.5        1.5      .9026+03     14.0       .9619+02
  7         13.3        1.8      .3864+04     25.1       .4102+03
  8         15.0        1.9      .7257+04     37.1       .7664+03
  9         16.8        2.5      .1048+05     46.6       .1086+04
 10         18.0        2.9      .1299+05     53.4       .1322+04
 11         18.6        4.5      .1458+05     54.6       .1478+04
 12         18.9        5.1      .1512+05     55.1       .1531+04
 13         18.9        5.7      .1458+05     52.9       .1485+04
 14         18.7        5.9      .1299+05     49.0       .1338+04
 15         18.1        6.1      .1048+05     42.5       .1098+04
 16         17.5        6.0      .7257+04     34.6       .7673+03
 17         16.7        5.5      .3864+04     25.8       .4101+03
 18         15.7        4.8      .9026+03     16.9       .9612+02
 19         14.8        4.2      .0000        14.8       .0000
 20         14.4        3.6      .0000        14.4       .0000
 21         14.0        2.8      .0000        14.0       .0000
 22         13.8        2.6      .0000        13.8       .0000
 23         13.7        1.9      .0000        13.7       .0000
 24         13.5        1.8      .0000        13.5       .0000
*****

```

TOTAL POWER FOR A TYPICAL DAY IN APRIL= 11.88 KWH

SYSTEM ANALYSIS FOR THE MONTH OF MAY

```

*****
    HOUR      AMBIENT      WIND      TOTAL      CELL      POWER
            AIR TEMP      SPEED      INSOLATION  TEMPERATURE  OUTPUT
            (DEG C)      (M/S)      (WATTS)      (DEG C)      (WATTS)

    1         13.7         2.3         .0000         13.7         .0000
    2         13.5         2.1         .0000         13.5         .0000
    3         13.3         2.4         .0000         13.3         .0000
    4         13.0         2.4         .0000         13.0         .0000
    5         12.9         2.1         .0000         12.9         .0000
    6         13.2         2.4         .2401+04         19.7         .2555+03
    7         14.6         2.6         .5414+04         30.2         .5736+03
    8         16.0         3.1         .7819+04         37.6         .8256+03
    9         16.8         3.3         .1059+05         45.3         .1102+04
   10         17.6         4.1         .1295+05         50.5         .1329+04
   11         18.0         4.6         .1445+05         53.5         .1470+04
   12         18.3         5.4         .1496+05         53.7         .1521+04
   13         18.5         6.0         .1445+05         51.9         .1476+04
   14         18.5         6.4         .1295+05         48.1         .1337+04
   15         18.0         6.4         .1059+05         42.4         .1110+04
   16         17.6         5.9         .7819+04         36.1         .8262+03
   17         17.1         5.6         .5414+04         30.0         .5736+03
   18         16.3         5.0         .2401+04         21.7         .2553+03
   19         15.4         4.8         .0000         15.4         .0000
   20         15.0         4.2         .0000         15.0         .0000
   21         14.6         3.6         .0000         14.6         .0000
   22         14.4         3.2         .0000         14.4         .0000
   23         14.2         2.8         .0000         14.2         .0000
   24         13.9         2.4         .0000         13.9         .0000
*****

```

TOTAL POWER FOR A TYPICAL DAY IN MAY = 12.65 KWH

SYSTEM ANALYSIS FOR THE MONTH OF JUNE

```

*****
    HOUR      AMBIENT      WIND      TOTAL      CELL      POWER
            AIR TEMP      SPEED      INSOLATION  TEMPERATURE  OUTPUT
            (DEG C)      (M/S)      (WATTS)      (DEG C)      (WATTS)

    1         15.7         2.0         .0000         15.7         .0000
    2         15.6         1.9         .0000         15.6         .0000
    3         15.7         1.7         .0000         15.7         .0000
    4         15.6         2.2         .0000         15.6         .0000
    5         15.6         2.3         .2440+00         15.6         .2440-01
    6         15.8         2.1         .3006+04         24.5         .3192+03
    7         16.6         2.5         .6024+04         34.1         .6370+03
    8         17.7         2.4         .8435+04         42.1         .8847+03
    9         18.8         3.0         .1067+05         48.0         .1101+04
   10         19.6         3.8         .1298+05         53.0         .1322+04
   11         20.2         4.7         .1444+05         55.5         .1461+04
   12         20.5         5.2         .1494+05         56.1         .1509+04
   13         20.6         5.9         .1444+05         54.1         .1467+04
   14         20.6         5.9         .1298+05         50.8         .1330+04
   15         20.3         6.2         .1067+05         45.0         .1110+04
   16         19.8         6.0         .8435+04         39.6         .8898+03
   17         18.9         5.7         .6024+04         33.3         .6372+03
   18         18.0         5.1         .3006+04         25.0         .3191+03
   19         16.9         4.6         .2440+00         16.9         .2591-01
   20         16.4         4.2         .0000         16.4         .0000
   21         16.2         3.6         .0000         16.2         .0000
   22         16.0         3.1         .0000         16.0         .0000
   23         16.0         2.5         .0000         16.0         .0000
   24         15.8         2.1         .0000         15.8         .0000
*****

```

TOTAL POWER FOR A TYPICAL DAY IN JUNE = 12.99 KWH

SYSTEM ANALYSIS FOR THE MONTH OF JULY

```

*****
HOUR      AMBIENT      WIND      TOTAL      CELL      POWER
          AIR TEMP     SPEED     INSOLATION  TEMPERATURE  OUTPUT
          (DEG C)      (M/S)     (WATTS)    (DEG C)      (WATTS)

1         17.4         2.2       .0000       17.4         .0000
2         17.3         1.7       .0000       17.3         .0000
3         17.1         1.5       .0000       17.1         .0000
4         17.0         1.7       .0000       17.0         .0000
5         16.9         1.3       .2440+00    16.9         .2440-01
6         17.1         1.5       .2580+04    25.0         .2740+03
7         18.4         2.1       .5844+04    35.9         .6175+03
8         20.3         2.3       .8444+04    44.9         .8789+03
9         21.5         3.1       .1134+05    52.2         .1157+04
10        22.5         4.2       .1385+05    57.3         .1394+04
11        22.8         4.7       .1544+05    60.4         .1518+04
12        22.9         5.3       .1599+05    60.7         .1568+04
13        23.1         5.6       .1544+05    59.2         .1532+04
14        23.0         6.0       .1385+05    55.0         .1403+04
15        22.6         5.7       .1134+05    49.4         .1166+04
16        22.1         5.7       .8444+04    42.2         .8853+03
17        21.3         5.5       .5844+04    35.4         .6177+03
18        20.2         4.7       .2580+04    26.2         .2738+03
19        19.1         4.4       .2440+00    19.1         .2590-01
20        18.6         3.8       .0000       18.6         .0000
21        18.2         3.0       .0000       18.2         .0000
22        18.0         2.6       .0000       18.0         .0000
23        17.8         2.3       .0000       17.8         .0000
24        17.6         1.9       .0000       17.6         .0000
*****

```

TOTAL POWER FOR A TYPICAL DAY IN JULY = 13.28 KWH

SYSTEM ANALYSIS FOR THE MONTH OF AUG

```

*****
HOUR      AMBIENT      WIND      TOTAL      CELL      POWER
          AIR TEMP     SPEED     INSOLATION  TEMPERATURE  OUTPUT
          (DEG C)      (M/S)     (WATTS)    (DEG C)      (WATTS)

1         19.3         2.0       .0000       19.3         .0000
2         19.1         1.7       .0000       19.1         .0000
3         19.0         1.7       .0000       19.0         .0000
4         18.8         1.9       .0000       18.8         .0000
5         18.8         1.9       .2440+00    18.8         .2440-01
6         18.8         2.1       .1026+04    20.7         .1091+03
7         19.9         2.0       .4431+04    33.3         .4688+03
8         21.2         2.3       .8169+04    45.1         .8501+03
9         22.4         3.0       .1178+05    54.4         .1195+04
10        23.1         3.7       .1459+05    60.6         .1431+04
11        23.4         4.3       .1636+05    63.9         .1565+04
12        23.5         5.2       .1697+05    63.7         .1626+04
13        23.5         5.4       .1636+05    62.0         .1589+04
14        23.6         5.8       .1459+05    57.5         .1465+04
15        23.5         5.8       .1178+05    51.2         .1206+04
16        23.0         5.7       .8169+04    42.5         .8560+03
17        22.3         5.4       .4431+04    32.9         .4688+03
18        21.3         4.7       .1026+04    22.9         .1090+03
19        20.3         4.2       .2440+00    20.3         .2594-01
20        20.0         3.5       .0000       20.0         .0000
21        19.6         3.2       .0000       19.6         .0000
22        19.5         2.9       .0000       19.5         .0000
23        19.4         2.5       .0000       19.4         .0000
24        19.2         2.9       .0000       19.2         .0000
*****

```

TOTAL POWER FOR A TYPICAL DAY IN AUG = 12.94 KWH

SYSTEM ANALYSIS FOR THE MONTH OF SEPT

```

*****
HOUR      AMBIENT      WIND      TOTAL      CELL      POWER
          AIR TEMP      SPEED      INSOLATION  TEMPERATURE  OUTPUT
          (DEG C)      (M/S)      (WATTS)      (DEG C)      (WATTS)
1         17.8         1.8         .0000         17.8         .0000
2         17.8         1.4         .0000         17.8         .0000
3         17.6         1.2         .0000         17.6         .0000
4         17.5         .7          .0000         17.5         .0000
5         17.4         1.3         .2440+00      17.4         .2440-01
6         17.5         1.5         .6227-09      17.5         .6227-10
7         18.1         2.0         .3058+04      27.1         .3243+03
8         19.1         2.0         .7555+04      41.8         .7930+03
9         20.6         2.3         .1152+05      53.6         .1171+04
10        21.7         3.2         .1458+05      60.4         .1434+04
11        22.4         3.8         .1651+05      64.4         .1574+04
12        22.9         4.8         .1717+05      64.3         .1637+04
13        22.9         5.4         .1651+05      61.7         .1606+04
14        22.8         5.8         .1458+05      56.7         .1470+04
15        22.5         6.1         .1152+05      49.3         .1185+04
16        22.1         5.9         .7555+04      40.0         .7969+03
17        21.3         5.6         .3058+04      28.3         .3242+03
18        19.8         4.9         .6227-09      19.8         .6602-10
19        19.3         4.5         .2440+00      19.3         .2587-01
20        19.0         3.8         .0000         19.0         .0000
21        18.8         3.4         .0000         18.8         .0000
22        18.7         2.8         .0000         18.7         .0000
23        18.5         2.0         .0000         18.5         .0000
24        18.2         2.0         .0000         18.2         .0000
*****

```

TOTAL POWER FOR A TYPICAL DAY IN SEPT = 12.32 KWH

SYSTEM ANALYSIS FOR THE MONTH OF OCT

```

*****
HOUR      AMBIENT      WIND      TOTAL      CELL      POWER
          AIR TEMP      SPEED      INSOLATION  TEMPERATURE  OUTPUT
          (DEG C)      (M/S)      (WATTS)      (DEG C)      (WATTS)
1         16.5         1.4         .0000         16.5         .0000
2         16.3         1.1         .0000         16.3         .0000
3         16.0         1.1         .0000         16.0         .0000
4         15.8         .7          .0000         15.8         .0000
5         15.8         1.0         .2440+00      15.8         .2440-01
6         15.8         1.5         .6227-09      15.8         .6227-10
7         16.1         1.7         .1273+04      19.0         .1355+03
8         17.5         1.9         .6301+04      36.8         .6656+03
9         19.3         1.9         .1057+05      50.9         .1083+04
10        20.7         2.9         .1380+05      58.1         .1380+04
11        21.5         3.8         .1583+05      61.8         .1539+04
12        21.7         4.7         .1652+05      61.8         .1606+04
13        21.7         5.1         .1583+05      59.5         .1567+04
14        21.4         5.6         .1380+05      53.9         .1403+04
15        20.9         5.7         .1057+05      45.9         .1097+04
16        20.1         5.7         .6301+04      35.1         .6661+03
17        19.1         4.9         .1273+04      21.4         .1354+03
18        18.3         4.0         .6227-09      18.3         .6623-10
19        17.9         3.5         .2440+00      17.9         .2595-01
20        17.7         2.8         .0000         17.7         .0000
21        17.5         2.0         .0000         17.5         .0000
22        17.3         1.7         .0000         17.3         .0000
23        17.2         1.6         .0000         17.2         .0000
24        16.8         1.4         .0000         16.8         .0000
*****

```

TOTAL POWER FOR A TYPICAL DAY IN OCT = 11.28 KWH

SYSTEM ANALYSIS FOR THE MONTH OF NOV

```

*****
HOUR      AMBIENT      WIND      TOTAL      CELL      POWER
          AIR TEMP     SPEED     INSOLATION  TEMPERATURE  OUTPUT
          (DEG C)      (M/S)     (WATTS)    (DEG C)     (WATTS)

  1         15.1         2.0       .0000       15.1       .0000
  2         14.3         1.9       .0000       14.3       .0000
  3         13.9         1.7       .0000       13.9       .0000
  4         13.6         2.0       .0000       13.6       .0000
  5         13.4         1.9       .2440+00    13.4       .2440-01
  6         13.2         2.3       .6227-09    13.2       .6227-10
  7         13.2         2.1       .2567+00    13.2       .2567-01
  8         15.5         2.6       .4546+04    28.5       .4820+03
  9         18.2         2.7       .8865+04    43.2       .9270+03
 10        20.5         2.7       .1203+05    53.9       .1222+04
 11        22.5         2.9       .1398+05    60.4       .1374+04
 12        22.8         3.6       .1464+05    60.7       .1436+04
 13        22.4         4.5       .1398+05    56.9       .1409+04
 14        21.9         4.6       .1203+05    51.7       .1229+04
 15        21.2         4.8       .8865+04    43.2       .9270+03
 16        20.5         4.9       .4546+04    31.7       .4813+03
 17        18.9         4.1       .2567+00    18.9       .2718-01
 18        18.0         3.2       .6227-09    18.0       .6592-10
 19        17.8         2.6       .2440+00    17.8       .2584-01
 20        17.8         2.7       .0000       17.8       .0000
 21        17.2         1.9       .0000       17.2       .0000
 22        17.2         2.1       .0000       17.2       .0000
 23        16.7         2.1       .0000       16.7       .0000
 24        16.2         2.3       .0000       16.2       .0000
*****

```

TOTAL POWER FOR A TYPICAL DAY IN NOV = 9.49 KWH

SYSTEM ANALYSIS FOR THE MONTH OF DEC

```

*****
HOUR      AMBIENT      WIND      TOTAL      CELL      POWER
          AIR TEMP     SPEED     INSOLATION  TEMPERATURE  OUTPUT
          (DEG C)      (M/S)     (WATTS)    (DEG C)     (WATTS)

  1         14.4         1.5       .0000       14.4       .0000
  2         13.9         1.7       .0000       13.9       .0000
  3         13.8         1.8       .0000       13.8       .0000
  4         13.5         1.6       .0000       13.5       .0000
  5         13.4         1.6       .2440+00    13.4       .2440-01
  6         13.2         2.0       .6227-09    13.2       .6227-10
  7         13.1         2.0       .2567+00    13.1       .2567-01
  8         13.8         2.1       .3789+04    25.0       .4023+03
  9         15.0         2.5       .8159+04    38.5       .8611+03
 10        16.4         2.4       .1128+05    48.6       .1163+04
 11        17.8         2.6       .1320+05    54.5       .1339+04
 12        18.4         3.5       .1385+05    54.6       .1404+04
 13        18.6         3.5       .1320+05    53.2       .1344+04
 14        18.4         4.1       .1128+05    47.2       .1167+04
 15        18.0         3.8       .8159+04    39.5       .8608+03
 16        17.3         3.8       .3789+04    27.1       .4019+03
 17        16.4         3.5       .2567+00    16.4       .2723-01
 18        15.8         2.6       .6227-09    15.8       .6606-10
 19        15.7         2.0       .2440+00    15.7       .2589-01
 20        15.7         2.3       .0000       15.7       .0000
 21        15.4         2.0       .0000       15.4       .0000
 22        15.2         2.1       .0000       15.2       .0000
 23        15.0         2.1       .0000       15.0       .0000
 24        14.7         1.8       .0000       14.7       .0000
*****

```

TOTAL POWER FOR A TYPICAL DAY IN DEC = 8.94 KWH

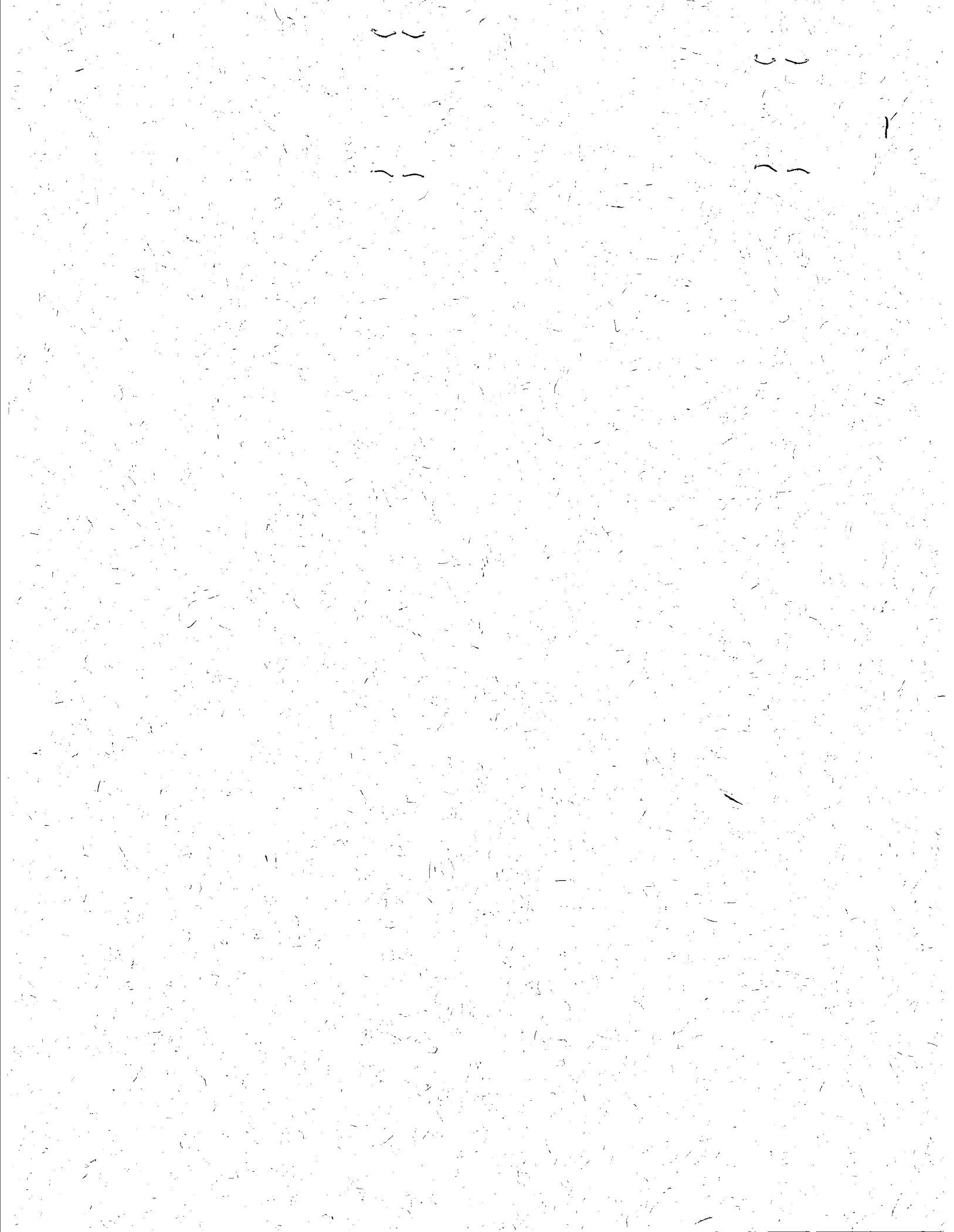
\*\*\*\*\*  
TOTAL POWER FOR SUM OF 12 TYPICAL DAYS IN THIS SIMULATION= 135.99 KWH

```

*****
TOTAL POWER FOR A TYPICAL DAY IN JAN = 9.17 KWH
*****
TOTAL POWER FOR A TYPICAL DAY IN FEB = 9.73 KWH
*****
TOTAL POWER FOR A TYPICAL DAY IN MARCH= 11.32 KWH
*****
TOTAL POWER FOR A TYPICAL DAY IN APRIL= 11.88 KWH
*****
TOTAL POWER FOR A TYPICAL DAY IN MAY = 12.65 KWH
*****
TOTAL POWER FOR A TYPICAL DAY IN JUNE = 12.99 KWH
*****
TOTAL POWER FOR A TYPICAL DAY IN JULY = 13.28 KWH
*****
TOTAL POWER FOR A TYPICAL DAY IN AUG = 12.94 KWH
*****
TOTAL POWER FOR A TYPICAL DAY IN SEPT = 12.32 KWH
*****
TOTAL POWER FOR A TYPICAL DAY IN OCT = 11.28 KWH
*****
TOTAL POWER FOR A TYPICAL DAY IN NOV = 9.49 KWH
*****
TOTAL POWER FOR A TYPICAL DAY IN DEC = 8.94 KWH
*****
TOTAL POWER FOR SUM OF 12 TYPICAL DAYS IN THIS SIMULATION= 135.99 KWH

```





LANGLEY RESEARCH CENTER



3 1176 00504 0218

